Faculté des Sciences Appliquées
Génie Civil et Géologie
Département de Mécanique des matériaux et Structures
Secteur Mécanique des Solides et des Matériaux

FEM Study of Metal Sheets with a Texture based, Local Description of the Yield Locus

Thèse présentée en vue de l'obtention du grade de
Docteur en Sciences Appliquées
par Laurent Duchêne

Année académique 2002-2003

Membres du Jury : A. Magnée (Prof ULG, président du jury)
S. Cescotto (Prof ULG)
A. M. Habraken (Maître de recherches FNRS, promoteur)
J. Lecomte-Beckers (Chargée de cours ULG)
P. Van Houtte (Prof KUL)
G. Cailletaud (Prof Ecole des Mines de Paris)
X. Lemoine (Ledepp, Arcelor R&D)
F. Barlat (Materials Science Division, ALCOA technical center)

Coordonnées de l'auteur : Duchêne Laurent
Département M&S
Université de Liège
1, chemin des Chevreuils
4000 Liège
Belgique
e-mail : l.duchene@ulg.ac.be

Acknowledgements

I would like to thank the Région Wallonne for its support. The steel research centre RDCS is acknowledged for performing the experimental deep drawing tests.

I also express my grateful thanks to:

- Anne Marie Habraken, André Godinas and Serge Cescotto for their help in the development of the presented model;
- The research team of professor Paul Van Houtte for providing us the texture treatment modules and for performing the texture measurements;
- The members of the jury who accepted to judge my work.

contents

Chapter 1: Introduction, research goal and method

1 *The general context of the thesis*

Nowadays, considerable numerical techniques are more and more used, by the mechanical component manufacturers, for the analysis of forming processes. Formerly, expensive experimental studies were required to control and optimise these processes. Now, several researches and developments are carried out to bring new knowledge and new numerical tools to fill up the increasing industrial need. The manufacturing of mechanical components with an increasing technicality is made possible with the help of numerical simulations. These simulations allow, on one hand, a better understanding of the phenomena taking place during the forming process and on the other hand, a better control of the quality of the product. The quality of the product is of course its geometry but also its material state: the metallurgical and mechanical properties of the final product. This point is essential for the prediction of the behaviour of a mechanical component during its later use.

This is the framework of the present thesis work, which has been achieved at the M&S department of the University of Liège. M&S department has early performed researches in the steel domain. These researches have been initiated by professor Massonnet more than 50 years ago. His pioneer works have oriented his team towards numerical methods to predict the behaviour of steel structures or steel pieces. His successors have mainly developed two different topics. The first one is related to the use of steel for civil engineering structures; the FINELG finite element code has been developed for the analysis of the behaviour of these structures. The second approach focuses on the numerical simulations of forming processes involving large displacements and large plastic strains. The LAGAMINE finite element code has therefore been developed.

The first results obtained with LAGAMINE, although satisfactory, rapidly highlighted the limitations of a constitutive law based on an isotropic material hypothesis. Several phenomenological constitutive laws based on an anisotropic material behaviour have been investigated. But it appeared that the texture of the material is an important feature if the anisotropy of the material is studied. The goal of the present thesis is the implementation into the finite element code LAGAMINE of a constitutive law which can take the texture of the material into account. Yet the texture is linked to microscopic measurements and metallurgical data rather than to the macroscopic approach of solid mechanics. This work is placed at the boundary between these two scientific fields and contributes to link them.

Texture can be seen as the volume distribution of the different grains or crystals constituting the material under investigation, each grain being characterised by its crystallographic lattice orientation. The implementation of a constitutive law based on texture is very important because the isotropic or anisotropic behaviour of the material directly derives from the more or less random distribution of the different grain orientations, i.e. from the texture. Indeed, each individual grain is highly anisotropic but a set of grains can yield to a more or less isotropic global behaviour.

The first stage required to be able to take texture into account during a finite element simulation is the measurement of the texture using, for example, a X-ray diffraction based technique. A microscopic model is then required to compute the mechanical behaviour of

each crystal. The main assumption of most microscopic models consists in considering that the plastic strains are achieved through dislocation glide at the crystal lattice level. So, other microscopic events like twinning or recrystallization are not present in these models. The texture is used to perform the micro-macro transition: the global behaviour of the material is computed from the microscopic behaviour using the distribution of the crystals as a micro-macro link.

The micro-macro approaches are naturally more predictive than phenomenological models in the sense that microscopic physical events occurring during plastic deformation are incorporated into the model. Contrarily to phenomenological models which must continuously be improved each time a new experimental observation is sought to be taken into account, the micro-macro models are intrinsically linked to the material behaviour.

2 *The objectives of the thesis*

An important difficulty frequently encountered when micro-macro approaches are investigated in the framework of finite element codes is the increasing computation time required when more and more complex models are developed. Indeed, the microscopic analysis must be performed at the crystallographic level while the macroscopic approach involves quite larger dimensions.

Several methods have already been investigated to overcome the computation time problem. A commonly used method is to fit a predefined representation of the yield locus on the micro-macro based computation. Munhoven et al. (1996) and Winters (1996) have developed a complex analytical representation of the yield locus while Maudlin et al. (1996) used a representation of the yield locus based on a set composed of a large number of simple linear functions. These two representations of the yield locus are fitted at the beginning of the finite element simulation on points computed by the micro-macro model. These models are qualified of **global** yield locus approaches because the whole yield locus is computed on the basis of the micro-macro technique.

A completely different approach not based on yield locus but on averaging crystals behaviour is proposed by different authors. See Crumbach et al. (2001), Anand et al. (1997), Kalidindi and Anand (1994), Mathur and Dawson (1989) or Delannay et al. (2002). In this case, each integration point of the finite element mesh is associated with a set of representative crystals. The mechanical state of each crystal is computed at the microscopic level then an averaging procedure provides the macroscopic state. These models propose different methods to identify the strain distribution in the crystals but also to compute crystal plasticity. Even if parallel computers allow this type of simulations, the CPU time is much larger than the models based on yield loci. So, they have not been investigated in our research. A quantitative idea of CPU time reduction reached with the model proposed in this thesis is presented later in this text section. This thesis is focussed on a texture based yield locus.
In addition to the use of the initial texture of the material to compute its mechanical behaviour, the prediction of the evolution of the texture during the forming process is also investigated. Indeed, during forming processes of steel sheets, the plastic strains undergone by the material, through crystallographic dislocation glides, will make the texture evolve. Depending on the steel grade and the forming process, the texture evolution can be neglected or not (see Imbault and Arminjon (1993) and Hoferlin (2001)). One goal of this thesis is to quantify for some deep drawing processes of different steel grades the effect of texture

evolution in the FEM model prediction. The phenomena are highly coupled as plastic strains induce texture evolution which indeed modifies the mechanical behaviour.

The texture evolution can hardly be taken into consideration with global yield locus approaches. Indeed, the computation time reduction obtained by the use of an analytical yield locus representation in the FEM analysis is lost if the fitting procedure must be repeated frequently.

The originality of our model is to use a **local** yield locus representation. Only the interesting small part of the yield locus is computed on the basis of the micro-macro technique. This method allows to compute rapidly a new yield locus representation (an updating of the local yield locus) when the mechanical behaviour has changed due to texture evolution. A drawback of the local yield locus approach is that the small part of the yield locus must also be updated when the interesting part has changed, i.e. when the stress state evolves.

The local yield locus approach would not be attractive if the texture remained constant or if the stress were often submitted to sharp changes. However, at least in the most deformed zones of the mechanical component under forming, a significant texture evolution is noticed and, as it is generally the case, the stress state appears to evolve smoothly during forming process.

The texture based constitutive law using the local yield locus presented here allows to achieve actual forming process simulations taking microscopic physical events into account and computing the texture evolution throughout the simulation within acceptable computation time.

The choice of the microscopic model used to describe the plastic behaviour at the crystallographic level and the choice of method used for the micro-macro transition is not imposed by our local yield locus approach. At this stage, Taylor's microscopic model is used for the microscopic plasticity and, for the micro-macro transition, Taylor's classical assumption is adopted: the equality of the macroscopic and the microscopic velocity gradients is assumed. The computation of the crystallographic slip rates necessary for the computation of the texture evolution is also based on the microscopic Taylor's model and the micro-macro Taylor's assumption.

The Taylor's hypotheses have been chosen because they are the most simple ones able to solve such problems providing satisfactory results and because they are less computation time consuming than more complicated models.
However, any other microscopic model or micro-macro transition model can be used for the finite element simulation of actual mechanical components. The computation time remains anyway sensitive to the complexity of the microscopic model.

Just to give an idea of the effectiveness of our local yield locus approach, for the deep drawing simulation presented in chapter 4 paragraph 4, the gain of our model compared to the direct use of Taylor's micro-macro assumption and microscopic model without any yield locus representation is summarised hereafter. If the texture evolution is not taken into consideration, when the Taylor's model is called once with the developed local yield locus approach, it is called 158 times with the direct Taylor's model approach. If the texture evolution is computed during the simulation, the gain decreases to 62 calls to Taylor's model for the direct approach for one call with the local yield locus approach. As the calls to the

Taylor's model constitute a very important part of the computer time, the gain obtained proves the large interest of the local yield locus approach.

The satisfactory results presented in this thesis have been obtained by overcoming several numerical problems linked to the local yield locus approach. For instance, a first local yield locus approach (called the hyperplanes method and described in chapter 3 paragraph 6) has been developed but had to be replaced due to numerous numerical problems.
The second local yield locus approach (called the stress-strain interpolation) is also described in chapter 3. Even if the basic concept is rather different from the hyperplanes method, the stress-strain interpolation method had to be successively improved according to the numerical problems encountered, but it finally provided a fully satisfactory method.

The model has been applied to different experimental cup deep drawings. Of course, we have validated the prediction ability of the model. However our main goal is not to reach a perfect numerical code able to predict with less than *x%* the final geometry or texture of a drawn steel sheet. If one focuses on one geometry, one steel grade, there exists enough parameters such as FEM element choice (shell or solid), friction model, to obtain numerical results as close as one wants from experimental measurements. Our objective was to identify the relative importance of the anisotropic constitutive law in earing prediction, punch force, strain field, final texture. What are the effects of replacing Hill's model by a texture based model with or without texture updating? Is the solid constitutive model more important than the friction model or the finite element choice?
As such general questions could not be answered with only one steel grade, 4 different cases have been analysed. They go from one steel with low anisotropic characteristics, for which the importance of other factors seems to be dominant towards other steel grades where anisotropy is the main factor.

3 *The content of the thesis*

This thesis is divided into 5 chapters; the first one is the present introduction.

The second chapter presents the state of the art in the field of the microscopic behaviour of metals and the different methods developed for the micro-macro transition. These features are used as tools required by our local yield locus approach for the characterisation of the metallurgical based behaviour of the metal.

First, the behaviour of a single monocrystal or, more generally, the behaviour of one crystal extracted from the polycrystal is examined. Taylor's microscopic model and Bishop-Hill's microscopic model are described; they constitute a primal-dual approach for the determination of the yield locus of one crystal.
The behaviour of the polycrystal, i.e. the macroscopic behaviour of the material is deduced from the microscopic behaviour thanks to a micro-macro transition. To do so, the texture of the material must be quantified; the Orientation Distribution Function (ODF) is a commonly used method for the representation of texture. However, Taylor's micro-macro assumption requires, for the description of texture, the computation of a representative set of crystals. It is a finite number of crystallographic orientations that is assumed to be representative of the actual texture of the material. Several methods have been developed to compute such representative set of crystals; some are described. The number of crystals included in the representative set is a crucial parameter; its influence on some computed results is investigated.

The elasticity of the polycrystal is briefly examined. As we focus on forming processes involving large strains, the plasticity of the polycrystal, i.e. the yield locus, is more largely investigated. Several micro-macro transition techniques are presented; the Taylor's assumptions used in the present work are described. But, other more sophisticated models with less restrictive assumptions could also be used at the cost of larger computation time. Finally, the hardening behaviour of the polycrystal is described.

Chapter 3 presents the mathematical tools required for the development of a local yield locus approach. The details of the implementation of the two investigated local approaches into the finite element code LAGAMINE are described.

As the local yield locus approaches are defined in the 5-dimensional deviatoric stress space, theory about the *n*-dimensional space geometry is recalled (*n* being chosen equal to 5 for the applications). The properties of the domain in which the local yield locus is defined are explained; the method used for the computation of this domain and the link between adjacent domains are described. Once the domain is defined, some theoretical methods for the interpolation of a local yield locus inside the domain, among which the hyperplanes method and the stress-strain interpolation method, are presented.
The hyperplanes method can be visualised in a 2-dimensional representation as a linear interpolation in Cartesian coordinates defined in the stress space. The points on the actual yield locus defining the boundaries of the local domain are simply linked by straight lines.
Similarly, the stress-strain interpolation method corresponds to a linear interpolation in polar coordinates in the stress space. The points on the actual yield locus are connected by curves. Due to the intrinsic curve shape of the yield locus of any metal, it is expected that the stress-strain interpolation method is better adapted for its implementation into a finite element code. Note that the von Mises yield locus assumed to model a perfectly isotropic metal corresponds to a hypersphere (a sphere in the 5-dimensional deviatoric stress space) which can be exactly represented with the stress-strain interpolation method. As it is an important point for the outcome of a local yield locus approach, the continuity between adjacent domains is also examined.

Another method which has only been theoretically investigated is the fitting of a usual global yield locus formulation (Hill's model or Tsai's model) on a small part of the actual yield locus; the zone of the global yield locus outside the small domain of interest is not used for the computation.

Due to its large importance for the implementation in a finite element code, the normal to the yield locus has to be clearly defined. Several problems were indeed encountered for the definition of a normal when a local yield locus approach is investigated. The definition of the normal inside the local domain is treated and the continuity of the normal to the yield locus between adjacent domains is also analysed.

Some particular points linked to the implementation of the hyperplanes method in the finite element code are presented: the discontinuities of the local yield locus and of its normals between adjacent domains is shown. Three stress integration algorithms were successively developed to overcome the numerical problems linked to the lack of continuity of the hyperplanes method. Anyway, this local yield locus approach had to be replaced by the stress-strain interpolation method. The details of the implementation of this second method into the finite element code are also presented: formulation of the method, introduction of the work

hardening and the tangent stiffness matrix required for the convergence of the finite element code. The stress integration algorithm is also presented.

Details of the FORTRAN subroutines linked to the stress-strain interpolation method are given and their flowchart is presented.

The implementation of the texture evolution is then treated. The rotation of the crystal lattice of each grain of the representative set is computed according to the plastic strain history obtained from the finite element code at each integration point of the mesh. These rotations must then be taken into account for the updating of the representative set of crystallographic orientations.

Chapter 3 ends by a small paragraph which analyses the accuracy and the robustness of the stress-strain interpolation method outside the finite element code. The stress integration scheme is tested in the case of complex loading paths. Elastic and plastic loadings are tested; elastic unloading followed by plastic reloading is investigated. The accuracy of the stress-strain interpolation local yield locus approach is verified by comparison with the direct Taylor's model based yield locus. The accuracy of the hyperplanes method is also tested.

The fourth chapter presents the validations achieved with the local yield locus approach and more particularly with the stress-strain interpolation method. Three academic validations are presented: the first one is the prediction of the texture evolution during rolling. The simulation is achieved with only one finite element submitted to plane strain loading.

The second academic validation is the prediction of the Swift effect. It consists in an axial extension of a tube or a cylinder submitted to severe torsion around its axis. Several experimental and numerical results found in the literature are presented. Unfortunately, the too basic hardening model that we have implemented does not allow us to predict the Swift effect. The torsion test was then simulated with a more complex but not physically based hardening law. The prediction of the Swift effect is then obtained.

The third academic validation is the comparison of the compressive and the torsional behaviour of isotropic face centred cubic and body centred cubic metals.

The first real shape validation is the deep drawing of cylindrical cups. Experimental results useful for comparison purposes are available for two different steels. The mechanical and metallurgical properties of these two steels are presented. The X-ray measurement of the initial texture had to be achieved for the use of our model. The geometry of the process as well as the measurement of the experimental results and the numerical parameters used for the simulations are largely detailed. The validation of our model is possible thanks to the comparison of the experimentally measured results with the ones predicted by the finite element code. The results under investigation are: the plastic strains at the end of the process, the punch force during the deep drawing process and the earing profile. The texture at the end of the process is also used for the validation. The experimentally measured textures on the deformed cups are compared to predicted ones.
The effects of some numerical parameters (number of element layers, friction and penalty coefficients, the constitutive law used, the procedure used to compute the representative set of crystals, the fitting procedure for Hill's law and the finite element type) on the computed results are also investigated to define the relative importance of the constitutive law on the results.

A second deep drawing process with a different geometry and a more anisotropic steel is investigated. For this process, the earing profile was particularly examined. It is indeed a direct consequence of the anisotropy of the steel sheet which is aimed to be accurately represented by our texture based model. The springback due to the removing of the drawing tools is examined in order to complete this deep drawing process analysis.

The results obtained for the deep drawing simulations compare generally favourably with experimental results. The earing profile prediction is however very sensitive and larger disagreements between experimental and numerical results were observed for this particular point.
That is the main reason why the second deep drawing process was investigated. Indeed, a more anisotropic steel conducted to a better prediction of the earing profile due to a lower influence of other numerical parameters in the FEM simulations.

The computation time needed for the deep drawing simulations is rather high (up to 300 hours for a simulation with 2252 solid finite elements). Anyway, thanks to parallel computation, it is not prohibitive. Furthermore, without the local yield locus approach, the computation time would be even larger.
The improvement of computer speeds will even allow to replace Taylor's model by a more computation time consuming model for the finite element simulations of complex industrial forming processes.

The validations proposed in this work forced us to better understand the studied forming processes. The microscopic physical events responsible for the Swift effect had to be understood. The experimental and the numerical results for the deep drawing processes also had to be deeply investigated.

A better modelling of the anisotropy of the steel sheets thanks to a texture based model allows a more accurate prediction of the earing profile. The numerical simulations are also very interesting when new deep drawing tools are set down. This is expected to produce a direct benefit during industrial forming processes by reducing the cost of experimental tests.

The industrial processes aimed up to now are principally the manufacturing of car body parts by deep drawing forming processes and cans. For these processes, the earing is particularly inconvenient. However, other industrial forming processes can be investigated thanks to the flexibility of the finite element code.

Chapter five proposes conclusions about the main objectives of the thesis. Some directions of further studies are finally described.

Chapter 2: State of the art

1 *Introduction*

This chapter presents the basic concepts concerning the analysis of the microscopic behaviour of polycrystalline metals. The polycrystalline behaviour is obtained thanks to the so-called micro-macro transition. Several micro-macro models are presented. This chapter is almost completely inspired from literature. Only a few personal investigations are presented. The polycrystalline behaviour is the basic tool used by our local yield locus approach developed in chapter 3.

2 *Monocrystal behaviour*

Metals plasticity at macroscopic scale results from complex microscopic phenomena. Experimental studies have permitted to understand that plastic deformation of metal is caused by 5 microscopic mechanisms:

- dislocation glide;
- mechanical twinning;
- stress-induced phase transformation;
- grain boundary sliding;
- superplasticity.

Depending on the material and the temperature range, some mechanisms can appear or not. Grain boundary sliding, for instance, requires a lot of energy and is only noticeable at high temperature (for steels and aluminium).
In the forming of steel sheets at room temperature, the dislocation glide is the main plastic deformation mechanism. It is characterised by shear strains acting on particular crystallographic planes and along particular crystallographic directions (each direction being parallel to the corresponding plane). These planes and directions are called slip systems and are such that the plastic deformation is achieved along the most dense directions of the crystal lattice. The dislocation glide is indeed easier along those directions. The dense directions and planes depend on the crystal structure:

- for face centred cubic (fcc) metals (aluminium, copper, austenite γ phase of steel, brass, silver, gold,…), using the Miller indices (see ref. Magnée) the main slip systems are:
  - plane $(1\ 1\ 1)$ with directions $[0\ 1\ \bar{1}]$, $[1\ 0\ \bar{1}]$, $[1\ \bar{1}\ 0]$;
  - plane $(\bar{1}\ 1\ 1)$ with directions $[0\ 1\ \bar{1}]$, $[1\ 0\ 1]$, $[1\ 1\ 0]$;
  - plane $(1\ \bar{1}\ 1)$ with directions $[0\ 1\ 1]$, $[1\ 0\ \bar{1}]$, $[1\ 1\ 0]$;
  - plane $(1\ 1\ \bar{1})$ with directions $[0\ 1\ 1]$, $[1\ 0\ 1]$, $[1\ \bar{1}\ 0]$.

  12 slip systems are listed hereabove. They are equivalent due to the symmetry of the crystal lattice and they are called the $\{1\ 1\ 1\}\langle 1\ 1\ 0\rangle$ slip systems.
- for body centred cubic (bcc) metals (ferrite α phase of steel, Tungsten, β-brass, β-Ti,…), the 24 main slip systems are:
  - planes $(0\ 1\ \bar{1})$, $(1\ 0\ \bar{1})$, $(1\ \bar{1}\ 0)$, $(\bar{2}\ 1\ 1)$, $(1\ \bar{2}\ 1)$, $(1\ 1\ \bar{2})$ with direction $[1\ 1\ 1]$;

- planes $(0\ 1\ \bar{1}), (1\ 0\ 1), (1\ 1\ 0), (2\ 1\ 1), (\bar{1}\ \bar{2}\ 1), (\bar{1}\ 1\ \bar{2})$ with direction $[\bar{1}\ 1\ 1]$;
- planes $(0\ 1\ 1), (1\ 0\ \bar{1}), (1\ 1\ 0), (\bar{2}\ \bar{1}\ 1), (1\ 2\ 1), (1\ \bar{1}\ \bar{2})$ with direction $[1\ \bar{1}\ 1]$;
- planes $(0\ 1\ 1), (1\ 0\ 1), (1\ \bar{1}\ 0), (\bar{2}\ 1\ \bar{1}), (1\ \bar{2}\ \bar{1}), (1\ 1\ 2)$ with direction $[1\ 1\ \bar{1}]$.

They are called the $\{1\ 1\ 0\}\langle 1\ 1\ 1\rangle$ and $\{1\ 1\ 2\}\langle 1\ 1\ 1\rangle$ slip systems. In the literature, other slip planes are also cited: $\{1\ 2\ 3\}$ (see Gil Sevillano et al. (1980); Turkmen et al. (2002) have also investigated the influence of the number of slip systems on the mechanical behaviour of bcc metals)

- for hexagonal closed packed (hcp) metals (α-titanium, zinc, zircalloy,…), the $(0\ 0\ 0\ 1)$ plane, i.e. the basal plane is responsible for the main dislocation glide along the 3 directions (comprised in the plane): $\langle 1\ 0\ \bar{1}\ 0\rangle$.

2.1 Taylor's model and Bishop-Hill's model for a single crystal

The deformation mechanisms involved in dislocation glide can be taken into account thanks to Taylor's model, which is described hereafter.

The velocity gradient $\underline{\underline{L}}$ of a single crystal can be decomposed into a slip induced part and a rate of crystal lattice rotation $\underline{\underline{\omega}}^L$:

$$\underline{\underline{L}} = \underline{\underline{K}}_S \cdot \dot{\gamma}_S + \underline{\underline{\omega}}^L \qquad (1)$$

S = 1, 24 in b.c.c. crystals
1, 12 in f.c.c. crystals

where $\underline{\underline{K}}_S$ represents the Schmid tensor defining the plastic deformation induced by a particular slip system. $\dot{\gamma}_S$ is the associated slip rate. Einstein's summation is applied on *S* indices representing one slip system. This approach neglects elastic crystal behaviour.

The $\underline{\underline{K}}_S$ matrices are constructed from the normal to the slip plane ($\underline{n}_S$) and the slip direction ($\underline{b}_S$) of each slip system *S*:

$$\underline{\underline{K}}_{S,ij} = \underline{b}_{S,i}\,\underline{n}_{S,j} \qquad (2)$$

(with no summation on *S*).

The velocity gradient $\underline{\underline{L}}$ may be split into a deviatoric plastic strain rate $\underline{\underline{\dot{\varepsilon}}}$ and a rate of rigid body rotation $\underline{\underline{\omega}}$:

$$\begin{cases} \underline{\underline{\dot{\varepsilon}}} = sym(\underline{\underline{L}}) = \underline{\underline{A}}_S \cdot \dot{\gamma}_S \\ \underline{\underline{\omega}} = skw(\underline{\underline{L}}) = \underbrace{\underline{\underline{Z}}_S \cdot \dot{\gamma}_S}_{=\underline{\underline{\omega}}^P} + \underline{\underline{\omega}}^L \end{cases} \qquad (3)$$

with $\underline{\underline{A}}_S = sym(\underline{\underline{K}}_S)$ and $\underline{\underline{Z}}_S = skw(\underline{\underline{K}}_S)$.

The resolved shear stress acting on a slip system can be derived by projecting the microscopic stress on the corresponding $\underline{\underline{A}}_S$ matrix (Van Houtte (1988)):

$$\tau_S = \underline{\underline{A}}_S \circ \underline{\underline{\sigma}} \tag{4}$$

The shear stress which will yield to dislocation glide will depend on several parameters hard to identify: stress field, activity of other slip systems,... A simple approach has been proposed by Schmid who assumes that the dislocation glide will occur if the shear stress acting on a slip system computed according to equation (4) reaches a critical value.
This condition can be written:

$$-\tau^c_{-S} \le \tau_S \le \tau^c_{+S} \qquad \Rightarrow \qquad -\tau^c_{-S} \le \underline{\underline{A}}_S \circ \underline{\underline{\sigma}} \le \tau^c_{+S} \tag{5}$$

where $\tau^c_{\pm S}$ are the so-called critical resolved shear stresses that derive from Schmid's law. Equal signs hold for plastic deformation, while the inequalities delimit the elastic domain. Equation (5) is then the definition of the yield locus of a single crystal.

Several different combinations of slip rates may achieve the prescribed plastic strain rate according to the first part of equation (3). Indeed, mathematically, the plastic strain rate can be decomposed into 5 independent components (the tensor is symmetric and deviatoric) while 12 or 24 (depending on the crystal lattice type) available slip systems can be activated. **Taylor's model** (Taylor (1938)) states that only the combination which minimises the internal power dissipation P in the slip systems is chosen:

$$P = \tau^c_S \cdot \left|\dot{\gamma}_S\right| = \min \tag{6}$$

In order to solve equation (3) constraint to the condition (6), we use a linear programming algorithm which computes the slip rates $\dot{\gamma}_S$ and gives the microscopic stress tensor $\underline{\underline{\sigma}}$ (Van Houtte (1988)).

As proposed by **Bishop-Hill's model**, the plastic power dissipation per unit volume P can also be defined according to the maximum work principle:

$$P = \underline{\underline{\sigma}} \circ \underline{\underline{\dot{\varepsilon}}} \tag{7}$$

As previously noticed, equation (5) is the expression of the yield locus of a single crystal. The matrix $\underline{\underline{A}}_S$ being constant, equation (5) defines, for one slip system, a set of 2 hyperplanes, i.e. planes in the 5-dimensionnal deviatoric stress space (the hydrostatic stress is not involved in plastic deformation). The stress state must remain between those 2 hyperplanes (elastic state) or on one of the 2 hyperplanes if plastic deformation occurs; this slip system is then activated. Combining the conditions of equation (5) for all the possible slip systems leads to the yield locus of the single crystal. It is a set of hyperplanes between which the stress state must remain. A 2-dimensionnal representation of such a yield locus is shown in Figure 1.

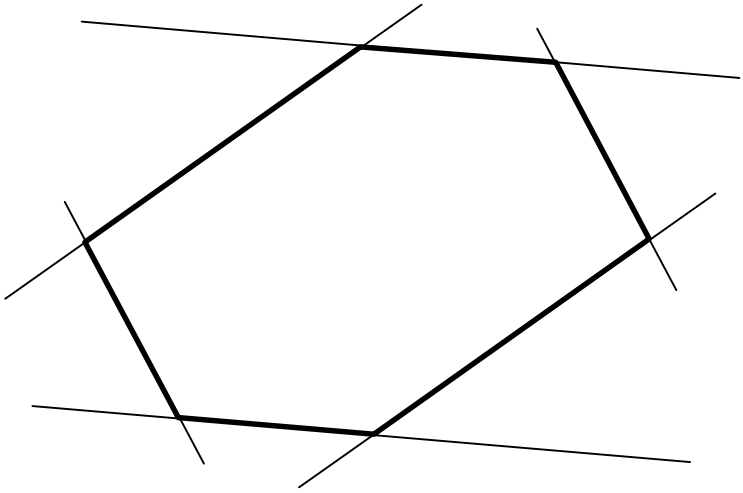

Figure 1: Schematic 2-dimensionnal representation of the yield locus of a single crystal

If the stress state lies on only one hyperplane, just one slip system is activated. The intersections of 2, 3 or 4 hyperplanes form edges where 2, 3 or 4 slip systems are active. A vertex is the point of intersection of 5 hyperplanes. 5 slip systems are then active. In the particular case of fcc metals having the same critical resolved shear stresses for all slip systems, vertices corresponding to the intersection of more than 5 hyperplanes have been noticed (up to 8).

From these considerations, it clearly appears that the yield locus of a single crystal is quite anisotropic and can hardly be modelled by a classical phenomenological yield locus.

Introducing the first part of equation (3) into equation (5) yields, for one slip system:

$$-\tau^c_{-S} \leq \frac{\dot{\underline{\underline{\varepsilon}}} \circ \underline{\underline{\sigma}}}{\dot{\gamma}_S} \leq \tau^c_{+S} \tag{8}$$

Equation (8), considering the equal signs, is the equation of two hyperplanes in the stress space. With the inequality signs, equation (8) means that the stress state must remain between these two hyperplanes. Furthermore, just like the vector with components *a, b* and *c* (in the 3-dimensionnal space *x,y,z*) is normal to the plane defined by equation (9), equation (8) shows that the plastic strain rate, when only one slip system is activated, is normal to the hyperplane.

$$a \cdot x + b \cdot y + c \cdot z = d \tag{9}$$

It can be proved furthermore that it is pointing outwards. The normality rule, generally applied in macroscopic yield locus formulations, is verified for the single crystal plasticity according to Taylor's model. If two or more slip systems are active, the normality rule states that the plastic strain rate is a positive linear combination of the normals corresponding to the active hyperplanes. In the 2-dimensionnal graph of Figure 2, this condition imposes that the plastic strain rate must remain between the 2 normals $\underline{\underline{n}}_1$ and $\underline{\underline{n}}_2$.

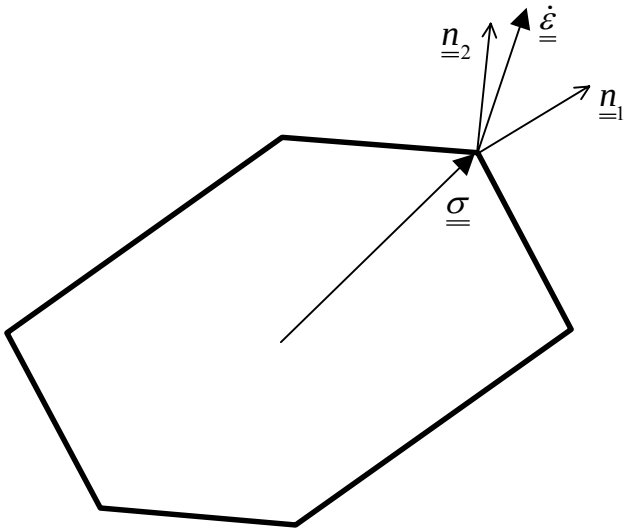

Figure 2: Schematic 2-dimensionnal representation of the normality rule

The maximum dissipation principle is directly derived from the normality rule. For a prescribed plastic strain rate, the associated stress state, belonging to the yield locus, that is really achieved gives more power dissipation (computed from equation (7)) than any other stress state inside or somewhere else on the yield locus. This can easily be checked on the case of Figure 2.
The maximum dissipation principle is the basis of Bishop-Hill's method for the computation of the microscopic stress corresponding to a prescribed plastic strain rate. The probability that the prescribed plastic strain rate is exactly normal to one hyperplane of the yield locus is zero. The same reasoning can be done for 2, 3 and 4 hyperplanes: the probability that the prescribed plastic strain rate is the positive linear combination of 2, 3 or 4 normals to hyperplanes is zero. So, the prescribed plastic strain rate must be the positive linear combination of 5 (or eventually more) normals to hyperplanes. The corresponding stress state is then the vertex intersection of the 5 hyperplanes. According to the maximum dissipation principle, it is the vertex for which the power dissipation is maximum. Bishop-Hill's method tests all the vertices of the yield locus and retains the one with the maximum power dissipation. This technique can be achieved easily when the stress states corresponding to all the vertices of the yield locus are known. In the case of fcc metals with the same critical resolved shear stress for all the slip systems: only 56 vertices have been listed by the authors of the technique (Bishop and Hill).

Finally, it is important to remark that the previously described Taylor's model for the computation of the microscopic stress and Bishop-Hill's method result from a primal-dual approach of the crystallographic slip resolution. For the mechanical state (stress, active slip systems) which is really achieved in the crystal, the internal power dissipation (which is minimised in strain rate space) and the plastic power dissipation (which is maximised in stress space) are the same.

3 *Polycrystal behaviour*

A polycrystal is constituted of numerous crystals linked together by boundaries. To characterise the polycrystal, several parameters are involved such as the size and the shape of each grain or crystal, its position inside the sample and the orientation of the crystal with respect to the sample coordinates.

3.1 Crystallographic orientation

At this stage, we will focus on the definition of the orientation of one crystal. It corresponds to the rotation from the sample coordinate system to the crystal coordinate system. The sample coordinate system is a fixed reference for the sample which can be chosen arbitrarily; for a metal sheet, it is convenient to use the Rolling Direction (RD), the Transverse Direction (TD) and the Normal Direction (ND) as sample coordinate system. For the crystal, any crystallographic direction can define arbitrarily the axes of the reference system. They must be defined the same way for each grain anyway. It is however interesting to take advantage of the crystal symmetry; for a cubic crystal symmetry, the most obvious choice for the reference axes is the cube edge directions, but it means 24 equivalent choices. Indeed, for the first axis, 6 choices are possible, which correspond to the 6 arrows in Figure 3. For the second axis, which must be orthogonal to the first one, only 4 choices remain. The third axis is determined by the two first ones.

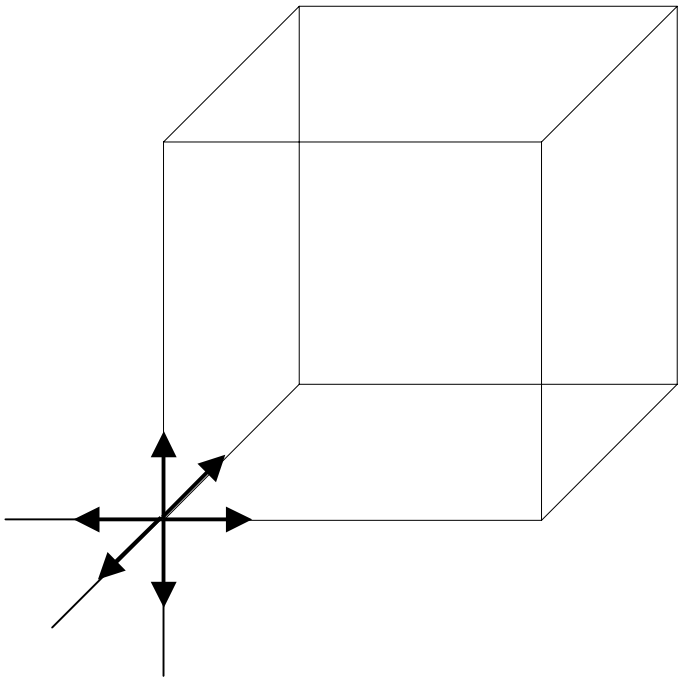

Figure 3: 24 equivalent choices for the reference system of a cubic crystal symmetry

Now, different choices are possible for the definition of the rotation from the sample coordinate system to the crystal coordinates (see Bunge (1982)):

- Matrix representation: it is a 3 by 3 matrix which transforms the coordinates of one point in the sample reference to the coordinates of the same point in the crystal reference.

- The Euler angles $(\varphi_1, \phi, \varphi_2)$: the crystal coordinate system is obtained by 3 successive rotations. Starting from the sample coordinate system, a first rotation about the Z-axis through the angle φ_1, then a rotation about the new X-axis trough the angle ϕ and finally a rotation about the new Z-axis (trough the angle φ_2) are achieved to obtain the crystal coordinate system (see Figure 4). As it is often used in the analysis of polycrystalline materials, this representation will be generally adopted in the present work. However, for the computation, the matrix representation is preferred due to its simplicity of application. The matrix rotation written in terms of Euler angles is obtained by multiplication of the elementary matrices defining the 3 successive Euler rotations:

$$\begin{pmatrix} \cos\varphi_1\cos\varphi_2 - \sin\varphi_1\sin\varphi_2\cos\phi & \sin\varphi_1\cos\varphi_2 + \cos\varphi_1\sin\varphi_2\cos\phi & \sin\varphi_2\sin\phi \\ -\cos\varphi_1\sin\varphi_2 - \sin\varphi_1\cos\varphi_2\cos\phi & -\sin\varphi_1\sin\varphi_2 + \cos\varphi_1\cos\varphi_2\cos\phi & \cos\varphi_2\sin\phi \\ \sin\varphi_1\sin\phi & -\cos\varphi_1\sin\phi & \cos\phi \end{pmatrix} \quad (10)$$

- A variant of the Euler angles (see Bunge (1982)) exists where the second rotation is carried about the Y-axis instead of the X-axis. To avoid confusion, in that case, the 3 angles are defined as: Ψ, Θ, Φ.
- The Rodrigues choice: the rotation is defined by a rotation axis (one direction) and a rotation angle around this axis. The Rodrigues vector ($\underline{r}$) is such an angle-axis parameterisation. It is defined by (see Dawson & Boyce (2002)):

$$\underline{r} = \underline{n} \cdot \tan\frac{\phi}{2} \quad (11)$$

where $\underline{n}$ is the rotation axis (unit vector) connecting both coordinate reference systems and ϕ is the angle of the rotation about this axis.

- Crystal direction and angle (see Bunge (1982)): a particular direction of the crystals is chosen arbitrary (but the same for all the crystals). The orientation of this direction is specified in the sample reference system by two angles. By giving, in addition, the angle of rotation of the crystal coordinates around the chosen direction, the rotation between the sample and the crystal reference systems is completely defined. As previously, 3 angles (which are 3 independent parameters) are used to define the rotation between both reference systems.
- The same reasoning can be used for an arbitrary direction in the sample coordinate system. The orientation of that direction in the crystal reference system and the rotation around that direction are the parameters defining the rotation between both coordinate systems.
- Pole figure and inverse pole figure: the directions defined in the two previous representations are plotted in stereographic projection. One direction of the crystal reference system plotted in the stereographic projection relative to the sample coordinate system defines one pole figure. While one direction of the sample reference system plotted in the crystal reference system defines the inverse pole figure. As one pole or inverse pole figure is not enough to define completely the rotation between both reference systems, some pole figures (relative to different chosen directions) are generally provided.
- A last way to specify a particular sample direction in the crystal reference system is the use of the Miller indices (see ref. Magnée). The Miller indices have already been used to define the slip systems in paragraph 2.

It is important to note that all these representations of a rotation from one reference system to another are always defined by only 3 independent parameters. They are furthermore equivalent to each other and it is always possible to obtain one representation knowing another as it is shown in equation (10) for the transformation of the Euler angles into a matrix representation.

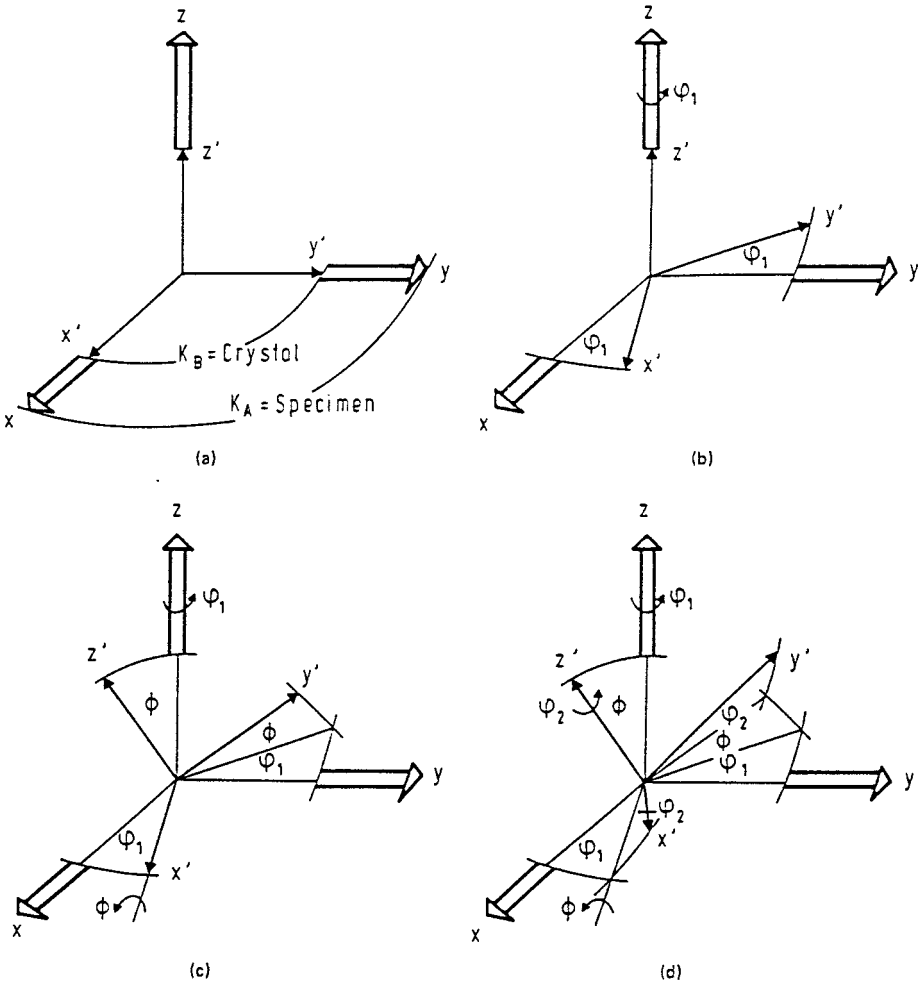

Figure 4: Definition of Euler angles (from Van Houtte (1995))

3.2 The Orientation Distribution Function (ODF)

Starting from any property of the material which is known inside each crystal, it is interesting to obtain the corresponding property for the polycrystal. This must be achieved in terms of amplitude and direction. Indeed, the properties of a polycrystalline material are generally anisotropic.

A convenient way to obtain the polycrystalline behaviour is to assume that the property of the polycrystal is the average of the corresponding property over all the constitutive crystals. This average can be achieved through the Orientation Distribution Function (ODF).

The definition of the ODF : *f(g)* is (see Bunge (1982))

$$\frac{dV}{V} = f(g)\,dg \tag{12}$$

where g specifies the orientation of a crystal with respect to the sample coordinates and represents one of the rotation definitions presented above.
dV is the volume of all the crystals the orientation of which lies in the domain $[g\text{-}dg;g+dg]$.
V is the total volume of the sample

By definition, one must verify that

$$\int f(g)\,dg = 1 \tag{13}$$

This integration must be achieved over all the possible orientations g of the crystals. The ODF is a quantitative representation of the texture of the material.

The averaging of any property of the crystals $a(g)$ depending on the orientation of the each grain is obtained by:

$$A = \int a(g)\,f(g)\,dg \tag{14}$$

giving the value A of the corresponding property for the polycrystal. This procedure requires that the ODF ($f(g)$) and the property of all the crystals depending on their orientation ($a(g)$) are known.

Equation (14) takes care of the crystal orientations in terms of volume fraction having a particular orientation but some important features such as the shape and the size of each grain are completely ignored. It is evident that a lot of small grains and the same volume fraction with a few large grains will not behave the same way. Furthermore, during the rolling process of metal sheets, the grains are generally aligned and flattened. The ODF can take alignment into account but is absolutely not an indicator of the flattening. The position of each crystal into the sample is neglected while it is well known that the neighbouring between grains has an important influence on the behaviour of the polycrystal. Some other features such as multiple phase materials or lattice defect are also neglected when equation (14) is used.

The ODF can be computed from X-ray diffraction pole figures obtained from measurements of a material sample using a texture goniometer.

3.3 Representative set of crystallographic orientations

In order to carry out computations on polycrystalline materials, a discrete set of crystallographic orientations representing the ODF is often required. The integral of equation (14) can then be advantageously be replaced by a summation:

$$A = \sum_{i=1}^{n} a_i w_i \tag{15}$$

The sum being achieved on the n grains of the representative set. a_i is the value of the selected property for the i^{th} grain orientation and w_i is a weighting factor corresponding to the volume fraction of the i^{th} grain orientation. From a computational point of view, this technique is very interesting but 3 important questions arise: which crystallographic

orientations should be selected to represent the ODF ? Which weighting factor must be attributed to each grain ? And how many crystals should be used ? (Or in other words, which value for *n* ?)
For the 2 former questions, several techniques have been developed to extract a discrete set of crystals that are expected to represent as much as possible the physical properties of the corresponding continuous ODF. Some of them are cited in the historical order of publication (see Toth & Van Houtte (1992)). New approaches have been recently developed (e.g. ODFLAM from the team of professor Van Houtte). Let us try to summarize the basic ideas of different methods:

- The Cutting Technique: a feature common to several methods is the discretisation of the Euler space. In the case of cubic-orthorhombic crystal symmetry, the range for the 3 Euler angles is $[0° - 90°] \times [0° - 90°] \times [0° - 90°]$; if a 5° discretisation is used, the Euler space is reduced to $19^3 = 6859$ points constituting a 5°-grid. These 6859 orientations can be used as representative set and the values of the ODF at these points are taken as the corresponding weighting factors. For the computation, a lower number of crystals is generally desired for the representative set (to reduce the computation cost as explained below). The cutting technique simply eliminates the points having a weighting factor (linked to the volume fraction) below a minimum value.
- The Statistical Method: the main drawback of the previous method is that it totally ignores the regions of the Euler space where low values of the ODF are found, which correspond to low volume fractions of particular crystallographic orientations. First, instead of just looking at the values of the ODF at the 19^3 grid points, 18^3 boxes (for cubic-orthorhombic symmetry) delimited by the grid points are constructed and the integral of the ODF in each box is calculated:

$$f_i = \int_{box\ i} f(g)\mathrm{d}g \tag{16}$$

The orientation of the centre of the box g_i is attributed the value f_i representing the discretised ODF. The $18^3 = 5832$ boxes must be considered in an arbitrary order. Then, a cumulative distribution function can be constructed:

$$F(j) = \sum_{i=1}^{j} f_i \tag{17}$$

This function is equal to 0 for j=0 and is equal to 1 for j equal to the total number of boxes. This indeed becomes equivalent to equation (13) when all the boxes are included into the summation.
The representative set of orientations is obtained trough the cumulative distribution function *F* using *n* (*n* being the number of desired crystals to be included in the set) numbers s_k (called "selectors" in Toth & Van Houtte (1992)) which are uniformly distributed (or randomly distributed but with a uniform probability) between 0 and 1. By inverting $F(j)$, one can obtain the *n* boxes having their cumulative distribution function equal to one selector. The representative orientation set comprises these *n* selected boxes or, more precisely is composed of the orientations of their centres g_i. It can be shown that the probability to select one particular box is equal to the associated f_i value, what proves the good selection of the representative set obtained with this method. The weighting factors w_i are the number of times one orientation is selected (it is generally 1

but this is not compulsory and values larger than 1 are frequent in case of sharp textures) divided by the total number of selected orientations (=n).

- The Limited Orientation Distance (LOD) method: the box discretisation presented above is used. The value of f_i in each box is however converted into a volume fraction w_i. The selection procedure starts at the box having the maximum w_i value. This box and the neighbouring ones (within a minimum orientation distance) are taken into consideration. A Gaussian distribution is used to evaluate the importance of the neighbouring boxes according to their misorientation from the initially selected box. Once the contribution of the central and the neighbouring boxes is added to the selected orientations trough its volume fraction, they are removed from the initial distribution. The same procedure can be repeated focussing on the maximum of the remaining distribution (until the maximum w_i is sufficiently low).

  Further details about the Statistical Method and the LOD method can be found in Toth & Van Houtte 1992.

The question about the number of crystal orientations that should be included into the representative set is very important and has already been investigated by several authors. In the finite element computation, each orientation must be treated; the computation time is then proportional to the number of crystals included in the representative set. On the other hand, the accuracy of the computation is increased if the representative set reproduces correctly the continuous ODF; which is improved if a large number of crystals is used. The number of grains to take into consideration must then result from a compromise between accuracy and computation time. Some authors propose:

- Kalidindi & Anand (1994): 180 or 200 crystals for compression tests;
- Anand et al. (1997): 32 crystals for cup-drawing simulations;
- Beaudoin et al. (1994): 256 for hydroforming process;
- Dawson & Kumar (1997): 200 for titanium rolling;
- Frénois (2001): 233 orientations for tantalum forming or 1144 if texture updating is investigated.

We have also investigated this question with our model (which is described in chapter 3). The influence of the number of crystals on the accuracy can be analysed from different point of views (see also Duchêne et al. (2000)).

In order to have a qualitative representation of this influence on the resulting texture, we have first compared sections of the original ODF of a high tensile steel (obtained from experimental measurements) with the corresponding sections of the discretised ODF (see Figure 5). These discretised ODF are calculated from the discrete set of crystals by assuming a Gaussian distribution around each orientation and computing the resulting distribution. The standard deviation of the Gaussian distribution has a significant influence on the discretised ODF. Values below 7° are not recommended (the representative set of crystals being computed on a 5°-grid in Euler space). On the other hand, large values of the standard deviation tend to smooth the ODF. The same standard deviation (7°) is then used in each case for comparison purpose.
On one hand, for the best case (2000 crystals), the shape of the sections of the discretised ODF and the locations of the maximum values are quite good. On the other hand, with only 200 crystals, there is still a similitude between the graphs but large differences appear. From this analysis, it is clear that a low number of orientations can significantly reduce the accuracy on the represented texture.

The second method that we have investigated is the comparison of stresses computed by the polycrystal Taylor's model (details are given in section 3.5) with different numbers of crystals (Figure 6). The stresses correspond to three prescribed velocity gradients (tensile test along X-axis, tensile test along Y-axis and a complex loading). Two steels, i.e. two initial textures are tested. The errors on stress values are obtained by using a case with a very high number of crystals as reference (40000 orientations). This way of comparison is supposed to be more significant because it is closer to our field of interest: FEM computation. Here again, the number of orientations has a large influence on the accuracy. According to these computations, a mean error smaller than 1% is obtained with at least 2000 orientations.
Then, we have compared the π-sections of the yield locus computed with our micro-macro model (details are given in chapter 3) for different discretised textures (Figure 7). This third method is directly linked to FEM simulations because the yield locus represents the material behaviour. The differences observed between the 3 sections of Figure 7 seem small. Nevertheless, they can considerably affect the results of a FEM simulation. Indeed, not only the scale of the yield stress is important but also the normal to the yield locus which is the direction of the plastic strain rate vector. Consequently, the comparison of the π-sections is not an appropriate criterion to decide the number of crystals of the representative set.
In order to emphasize the influence of the normal of the yield locus, we have computed the Lankford coefficients (noted 'r') corresponding to the yield loci obtained from the 3 different discretised textures of Figure 7. The Lankford coefficient is defined as the ratio of the transverse strain to the thickness strain during a tensile test achieved up to plastic deformation occurs. According to its definition, the Lankford coefficient is directly linked to the plastic strains and consequently, to the normal of the yield locus. Figure 8 shows the large influence of the number of crystals on the computed Lankford coefficients. The Lankford coefficient directly computed from the texture before the dicretisation is achieved is also presented for comparison. All the curves exhibit the same tendency except the curve corresponding to the case with only 200 crystals which is quite different from the other ones.

These considerations show that a particular attention must be paid to the choice of the number of crystallographic orientations. In the FEM simulations that have been achieved in the present work, a representative orientation set containing 2000 crystals is generally used.

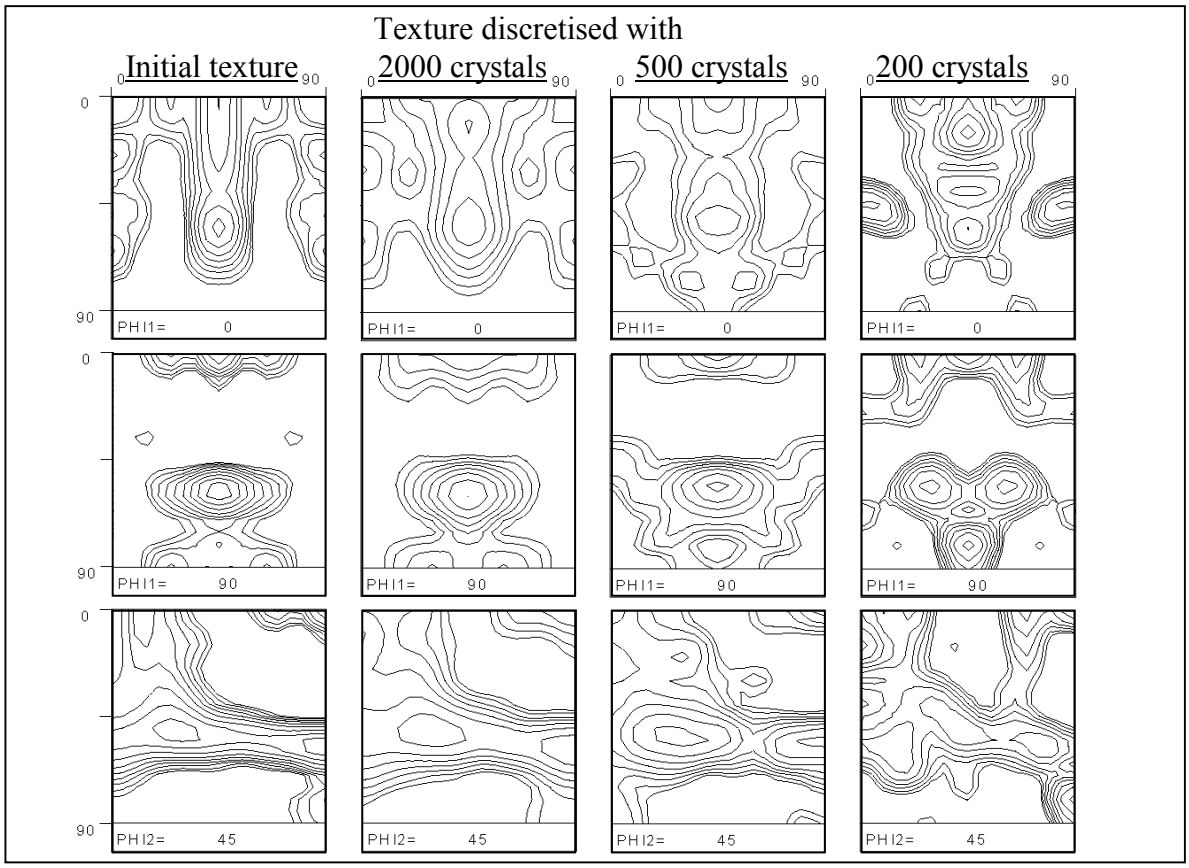

Figure 5: Sections of the ODF before and after discretisation

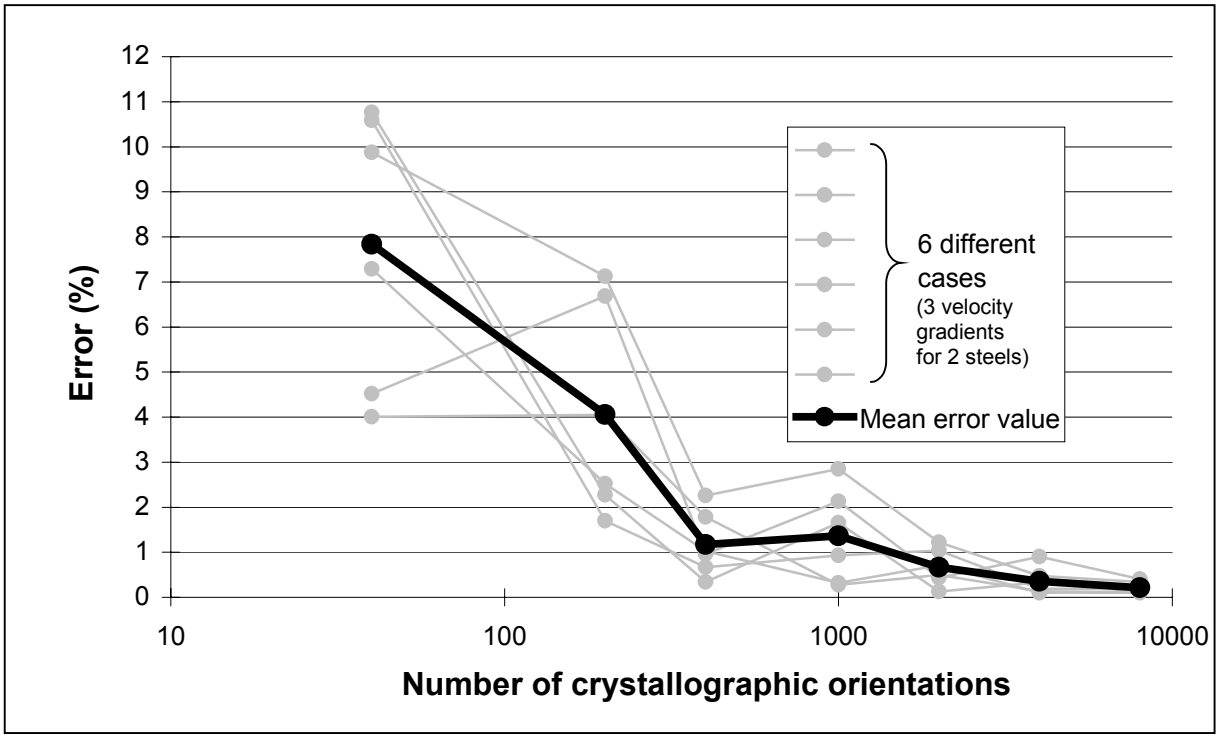

Figure 6: Influence of the number of crystal orientations on the accuracy (the reference result is taken as the one computed with 40000 orientations).

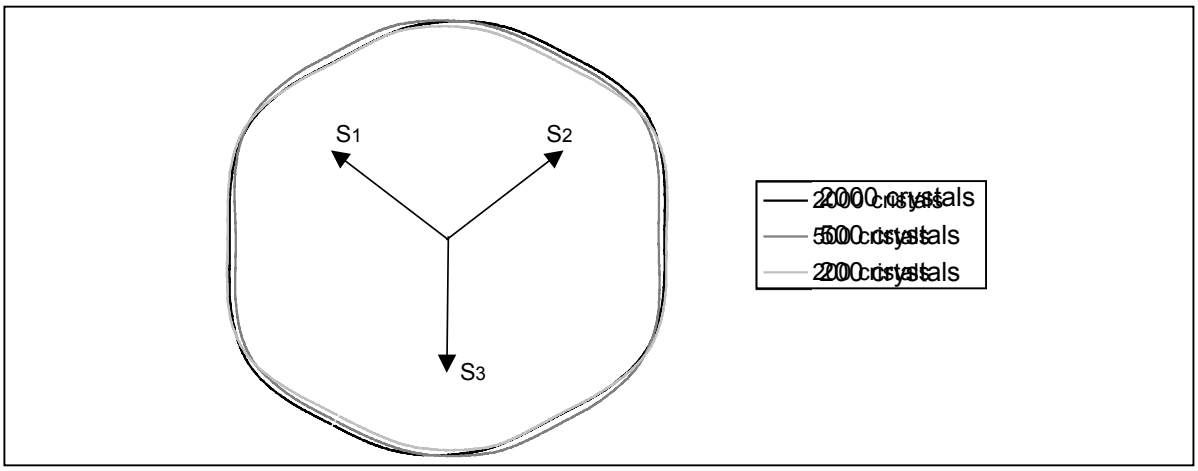

Figure 7: π-sections of the yield locus (S_1, S_2, S_3 are the 3 principal deviatoric stresses)

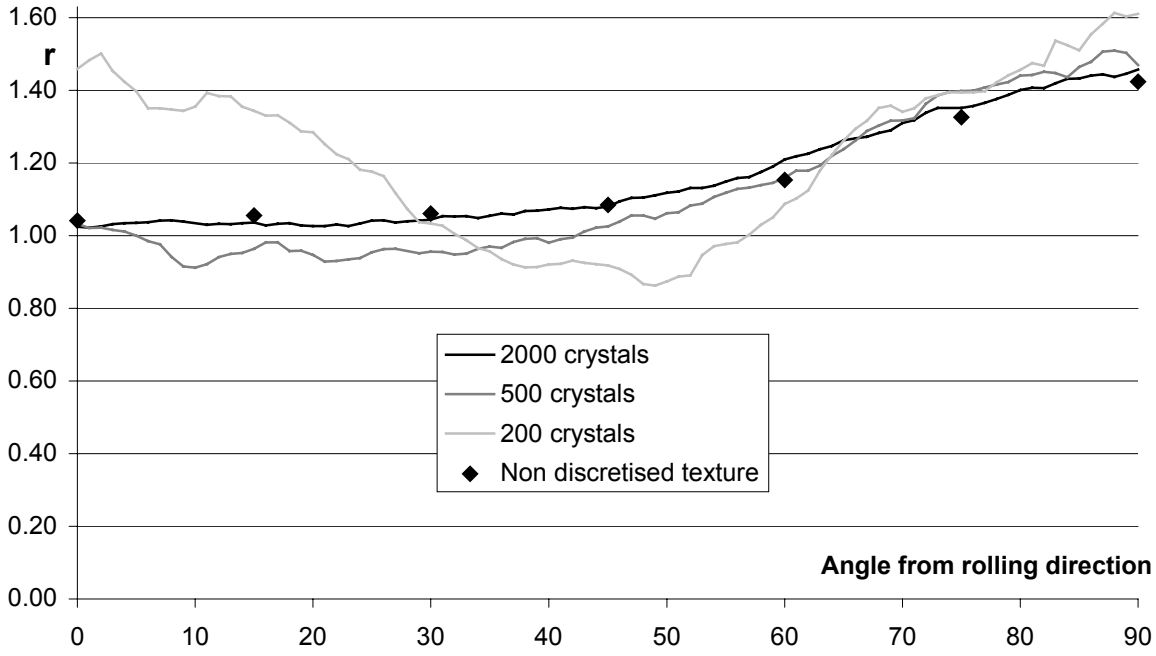

Figure 8: Lankford coefficients associated to the 3 yield loci computed with 200, 500 and 2000 crystals compared to the non discretised texture

3.4 Elasticity of the polycrystal

As we are interested in the mechanical behaviour of the studied material, the elastic properties are examined. From a phenomenological point of view, for small deformations, Hooke's law applies:

$$\underline{\sigma} = \underline{\underline{C}} \cdot \underline{\varepsilon} \tag{18}$$

where $\underline{\sigma}$ is the macroscopic stress

$\underline{\varepsilon}$ is the macroscopic strain

$\underline{\underline{C}}$ is the macroscopic stiffness tensor

To be rigorous, the stress and the strain are second order tensors and the stiffness is a fourth order tensor. But, due to the symmetry of the stress and strain tensors and thanks to the formulation of the deformation energy, they can be written as 6 components vectors. The stiffness tensor becomes, in a convenient way, a 6x6 symmetric second order tensor. However, one must always bear in mind that, in a theoretical point of view, the second and fourth order tensors apply. The stiffness tensor contains 21 independent parameters which reduce to 2 in the isotropic case (Young's modulus and Poisson's ratio).
By inverting equation (18), the compliance matrix $\underline{\underline{S}}$ is obtained:

$$\underline{\varepsilon} = \underline{\underline{S}} \cdot \underline{\sigma} \tag{19}$$

The same remark as above stands for the compliance tensor.

For a polycrystalline material, elasticity is the result of the behaviour of each crystal. In general, the elasticity of one crystal is highly anisotropic and is known for most elementary components of common materials (see Van Houtte (1995)). For instance, an isotropic material is, in most cases, the result of a random orientation distribution of anisotropic crystals.
The stress and the strain distributions are therefore heterogeneous in the polycrystal if the observation scale is of the order of the grain size or a little bit larger. Even inside each crystal, the stress and the strain are not homogeneous.
It seems then very difficult to obtain the macroscopic elastic behaviour from the microscopic one. Some assumptions must be done in order to be able to formulate a micro-macro transition for the elastic behaviour.
Voigt's model (see Voigt (1928)) assumes that the strain is homogeneous inside the polycrystal (from one crystal to another and inside each crystal) and is equal to the macroscopic prescribed strain. The stiffness matrix of each crystal is known. It depends of the material and of the orientation of the crystal reference system with respect to the sample reference system. As a result, the stress in each crystal is uniform but different from one crystal to another. The macroscopic stress is set to be the average of the microscopic stresses weighted by the ODF as previously shown in equation (14). From this, the macroscopic stiffness matrix is also obtained from the stiffness in each crystal trough equation (20).

$$\begin{aligned} \underline{\sigma}^{macro} &= \int \underline{\sigma}^{micro}(g) f(g) dg = \int \underline{\underline{C}}^{micro}(g) \cdot \underbrace{\underline{\varepsilon}^{micro}}_{=\underline{\varepsilon}^{macro}} f(g) dg \\ &= \underbrace{\int \underline{\underline{C}}^{micro}(g) f(g) dg}_{=\underline{\underline{C}}^{macro}} \cdot \underline{\varepsilon}^{macro} \end{aligned} \tag{20}$$

This model satisfies the strain compatibility between grains (the strain is uniform !) but nothing ensures that the stress equilibrium between grains is fulfilled. In fact, it will be generally violated with this model.

On the other hand, Reuss (see Reuss (1929)) assumes that the stress is homogeneous inside the polycrystal. A similar reasoning as above leads to the macroscopic strain and macroscopic compliance matrix given by equation (21).

$$\begin{aligned} \underline{\varepsilon}^{macro} &= \int \underline{\varepsilon}^{micro}(g) f(g) dg = \int \underline{\underline{S}}^{micro}(g) \cdot \underbrace{\underline{\sigma}^{micro}}_{=\underline{\sigma}^{macro}} f(g) dg \\ &= \underbrace{\int \underline{\underline{S}}^{micro}(g) f(g) dg}_{=\underline{\underline{S}}^{macro}} \cdot \underline{\sigma}^{macro} \end{aligned} \tag{21}$$

The stress equilibrium is satisfied between crystals and inside each crystal. However, the strain compatibility is not fulfilled: the strain is uniform inside each grain but different from one grain to its neighbours and nothing guarantees compatibility.
By inverting the macroscopic stiffness matrix computed by Voigt, the compliance matrix is found:

$$\underline{\underline{S}}^{macro}_{\text{Voigt}} = \left(\underline{\underline{C}}^{macro}_{\text{Voigt}} \right)^{-1} \tag{22}$$

As the hypotheses are not the same for both models, we generally obtain:

$$\underline{\underline{S}}^{macro}_{\text{Voigt}} \neq \underline{\underline{S}}^{macro}_{\text{Reuss}} \tag{23}$$

Voigt's and Reuss' models are primal-dual approximations of the elastic behaviour of the polycrystal. Voigt's model is a upper bound for the stress and the stiffness components for an energy formulation while Reuss' model is a lower bound.

According to these results, Hill proposed to use a mean compliance matrix:

$$\underline{\underline{S}}^{macro}_{\text{Hill}} = \frac{1}{2} \left(\underline{\underline{S}}^{macro}_{\text{Voigt}} + \underline{\underline{S}}^{macro}_{\text{Reuss}} \right) \tag{24}$$

More sophisticated models were further studied:
Eshelby's work permitted to find a solution to the problem of estimating the average stress and strain in a particular crystal under some assumptions: the crystal is treated as a spherical or ellipsoidal inclusion in a homogeneous and isotropic matrix (representing the rest of the polycrystal).
This is the basis of the self-consistent method: each crystal is successively computed as an inclusion in a matrix. At iteration *i*, the matrix approximately models the polycrystal. The computation of this matrix with one crystal being the inclusion yields to a better approximation of the polycrystal behaviour. This better approximation is then used as the matrix for iteration *i+1*. Each crystal being successively the inclusion, the behaviour of the matrix progressively approximates the elastic behaviour of the polycrystal.

In the present work, these complicated and computation time consuming elastic models are not used. Indeed, as we focus on the behaviour of metal sheet during forming processes involving large strains, elasticity is not predominant with respect to the plasticity at least

during the deformation process. This is no more the case during the unloading phase for the calculation of springback. A simple phenomenological isotropic Hooke's law is used.

3.5 Plasticity of the polycrystal

We are now interested in the micro-macro transition of the yield locus, from each particular crystal studied in paragraph 2 to the yield locus of the polycrystal. This must be achieved with care because it is a very important point when large strains are involved.

The stress field $\underline{\sigma}(\underline{x})$ and the plastic strain rate field $\underline{\dot{\varepsilon}^p}(\underline{x})$ are the variables used in the plasticity analysis. As in previous section, they are written as 6 components vectors. The elastic part of the strain rate is treated separately.

At this stage, different scales for the analysis of the problem must be used:

- The scale of the sample: only the macroscopic stress field and strain rate field are important at that scale. They are computed by the finite element code on the basis of the lower scale analysis
- The scale where the macroscopic fields are assumed to be constant in order to be able to achieve the micro-macro transition which is the topic of this paragraph. From a finite element point of view, this scale is the scale of one integration point of one finite element. From a physical point of view, this scale should be the smallest volume representative of the polycrystal behaviour. A sufficient number of crystals must be included in this volume to represent correctly the texture of the material.
- The scale of the crystal: the yield locus at that level in known according to paragraph 2. It is the starting data for the micro-macro transition.
- The mesoscopic scale: this scale is larger than a single dislocation but smaller than the crystal scale. The interaction between dislocations, the presence of obstacles or substructures inside one grain are analysed at this scale. In the present work, it is assumed that the stress and the strain rate are homogeneous inside each crystal. This allows us not to further analyse this scale.

Consequently, the smallest scale considered in this work is the scale of the crystal. In the sequel, it will be called the microscopic scale.

The micro-macro transition results from the averaging of the microscopic values over the representative volume element.

$$\underline{\sigma^{macro}} = \frac{1}{V}\int \underline{\sigma^{micro}} dV \tag{25}$$

$$\underline{\dot{\varepsilon}^{p,macro}} = \frac{1}{V}\int \underline{\dot{\varepsilon}^{p,micro}} dV \tag{26}$$

With the use of the definition of the ODF and relation (14), one has:

$$\underline{\sigma^{macro}} = \int \underline{\sigma^{micro}(g)} f(g) dg \tag{27}$$

$$\underline{\dot{\varepsilon}^{p,macro}} = \int \underline{\dot{\varepsilon}^{p,micro}(g)} f(g) dg \tag{28}$$

the integration being done over all the possible orientations of the crystals.

Thanks to the yield locus in each crystal, the relation between microscopic stress and plastic strain rate is known but the corresponding relation at the macroscopic level is not

straightforward. The averaging over all the crystallographic orientations seems a very simple concept but the averaging must be done simultaneously on the stress and the plastic strain rate because of their interaction in the single crystal. A solution to this problem is then very hard to find.

As for the elastic behaviour, several methods have been proposed in order to be able to solve the micro-macro transition. The main ones are:

- Sachs' model. From Sachs (1928), It can be derived the assumption of a homogeneous stress distribution throughout the whole polycrystal. The stress in each crystal is then chosen equal to the macroscopic stress. This assumption is equivalent to Reuss' model but applied here for the plastic behaviour. The averaging must then only be achieved on the plastic strain rate. This model is not very satisfactory and gives rise, in the general case, to a contradiction. Indeed, each crystal having its own orientation, imposing a common stress expressed in the sample coordinate system to all the crystals consists in imposing a different stress to each crystal in its reference system. The yield locus of each crystal being quite anisotropic (see Figure 2), the imposed stress cannot fall on the yield locus for each crystal. Similarly, the yield locus of each crystal is the same if expressed in its own reference system but the yield loci of all the crystals expressed in the sample reference system do not generally superimpose. Only the crystal with the smallest yield stress in the imposed stress direction will undergo plastic strain. This model can then give a lower bound for the yield stress but it is not interesting for the implementation in a finite element code since only one crystal yields.
- The full constraints (FC) Taylor's model (Taylor (1938)). According to literature, Taylor type models are the most widely used for the computation of the constitutive response of polycrystal aggregates. In a manner similar to Voigt's model, Taylor's model assumes a homogeneous distribution of the plastic strain rate trough the polycrystal. This is expressed for each crystal by:

$$\underline{\dot{\varepsilon}^{p,micro}} = \underline{\dot{\varepsilon}^{p,macro}} \tag{29}$$

Within a finite element code when elasticity is neglected, the plastic strain rate is the symmetric part of the velocity gradient $\underline{\underline{L}}$:

$$\begin{aligned} &\underline{\underline{\dot{\varepsilon}^{p,macro}}}(\text{tensorial form}) = \frac{1}{2}\left(\underline{\underline{L}} + \underline{\underline{L}}^{T}\right) \\ &\text{with } \underline{\underline{L}} = \frac{\partial \underline{v}}{\partial \underline{x}} \end{aligned} \tag{30}$$

$\underline{v}$ is the velocity field and $\underline{x}$ is the spatial coordinate.

Note that imposing the plastic strain rate is less restrictive than imposing the velocity gradient. The rigid body rotation is indeed not prescribed by Taylor's model while it would be if the velocity gradient were imposed.

Thanks to Taylor's assumption, the micro-macro transition can be implemented into a finite element code. The velocity gradient is given by the finite element code at each integration point and the corresponding stress is sought for. The plastic strain rate is deduced from equation (30) in a macroscopic point of view; the microscopic one is the same for all the crystals of the representative set of the integration point (see equation (29)) but it must be rotated to the crystal lattice reference system. Each crystal in its own reference system sustains a different plastic strain rate. The microscopic stress is computed for each crystal from its yield locus. The macroscopic stress of the polycrystal

is obtained by a weighted averaging of the microscopic ones with the use of the ODF as shown by equation (27).

This procedure can be computation time consuming if a large number of crystals is considered. Anyway, it offers the advantage that each crystal is treated successively and independently of the other crystals. So, multiprocessor can be easily applied. As Voigt's model is a upper bound for the elastic stiffness matrix, Taylor's model is a upper bound for the yield stress. The stress equilibrium between individual grains is often violated with Taylor's model.

According to literature (see e.g. Bachu and Kalidindi (1998)), in spite of its limitations, this model appears to be quite successful in the prediction of the stress-strain response of the polycrystal and of the texture during plastic deformations. It is however widely recognized that the textures predicted by Taylor type models are much stronger than the actual measurements. This point is one of the main goal of this work and is further investigated in chapter 4.

- The relaxed constraints (RC) models. Taylor's assumption of a homogeneous plastic strain rate is, in some applications, too restrictive. From a physical point of view, nothing ensures that the plastic strain rate is the same in all the crystals; it is not even sure that the plastic strain rate is close from one crystal to another. According to the considered forming process, it is interesting to modify the assumption of a homogeneous plastic strain rate. In the case of rolling, the X-axis being the rolling direction, the Y-axis being the transverse direction and the Z-axis being the normal direction, Lath's model relaxes the XZ component of the plastic strain rate. This means that that component is no more the same for all the crystals but is free. The Pancake model relaxes in addition the YZ component. The Lath's and the Pancake methods seem to be more satisfactory for the modelling of the rolling process than the FC Taylor's model (particularly for the prediction of deformation texture).

  So as to be able to solve the problem, the compatibility conditions that disappear on the relaxed plastic strain rate components must be replaced by equilibrium conditions on the corresponding stress components.

  The main disadvantage of these relaxed models is that they are dedicated to a particular forming process; they cannot be used for an arbitrary strain history. The generalised relaxed constraints method (see Van Houtte & Rabet (1997)) overcomes this drawback by choosing automatically the plastic strains that should be relaxed.
- The multiple points models: as it has been explained, due to their assumptions, the previous models treat each crystal in turn. This is interesting from a computational point of view but it increases the difficulty to take into account the effect of the interaction between adjacent crystals. That is the reason why multiple points models have been investigated. The Lamel model (Van Houtte et al. (1999), Van houtte et al. (2002), Liu et al. (2002)) is such a model where the interaction between 2 grains is examined. As the pancake model, the Lamel model is adapted for rolling simulation. The flattening and the elongation of the crystals observed during rolling led to the idea of considering 2 grains having the same size and shape and which lie exactly on top of each other. The boundary between these 2 grains being parallel to the plane of the steel sheet. The FC Taylor's condition of uniform plastic strain rate is here applied to the set of the 2 grains and not to both grains. Under such conditions, the crystals have 2 relaxations: the XZ and the YZ components of the velocity gradient are relaxed (using the same coordinates as above). But, and this is the difference from the RC model, the relaxation of the top grain must be the opposite of the relaxation of the bottom grain. The stress equilibrium between the 2 grains must be verified. Table 1 of Liu et al. (2002) shows that the Lamel model predicts more accurately the deformation texture than the RC or the FC Taylor's models. A more

recent Lamel version with, in addition, the relaxation of the XY component has also been investigated (Van houtte et al (2002)). A stack of 3 grains instead of 2 is also proposed by Liu et al. (2002).
Figure 9 schematically compares the FC Taylor's, the Lamel and the Pancake models. Opposite shear appears with the Lamel model (computed by minimization of the total plastic work rate in the two grains) ; No shear appears with the FC Taylor's model because it is prescribed in a macroscopic point of view while the Pancake model violates the compatibility between both grains.

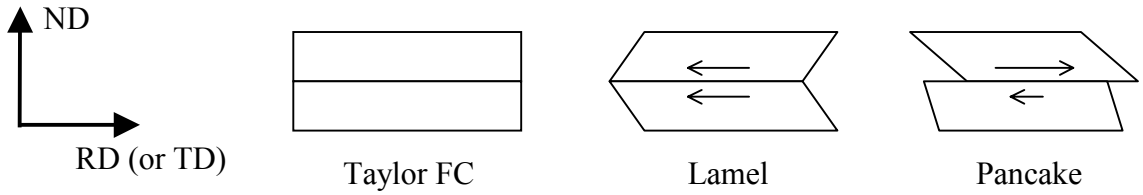

Figure 9: Comparison of the FC Taylor's, the Lamel and the Pancake models (adapted from Fig. 1 of Liu et al. (2002))

- The self-consistent model (see Berveiller & Zaoui (1984)). It is a generalisation of the multiple points models in the sense that all the crystals are treated as if they would act simultaneously. The self-consistent model considers each grain in turn as an inclusion embedded in an ideal homogeneous plastic matrix. As this plastic matrix is expected to represent the polycrystal behaviour, it is obtained by an averaging of the single crystal behaviour. An iterative procedure must be used. From a computational point of view, Taylor's model, for instance, is used to obtain a first approximation for the matrix behaviour. Each grain is then computed as the inclusion into that matrix. The new matrix behaviour is obtained by averaging on all the grains. The computation is repeated until convergence is obtained on the matrix behaviour. With this model, the stress and the plastic strain rate are allowed to be different from one grain to another (the assumption of uniform stress and plastic strain rate inside each crystal is however kept). This model should conceptually be more accurate than the previous ones but requires larger computation time.
  A first trial of a self-consistent approach was Kröner's model. On the basis of Eshelby's work, Kröner treats the problem of a spherical plastic inclusion representing one crystal embedded in an elastic matrix. The polycrystal behaviour is the average on all the crystals. The plastic incompatibility between the crystals is accommodated elastically. As a consequence, this model overestimates the yield stress just like Taylor's model. Moreover, as the matrix is assumed to be purely elastic, it cannot correctly represent the polycrystal behaviour. In that sense, Kröner's model is not literally a self-consistent model.
- Pilvin's model (see Frénois (2001)): in order to be able to simulate complex path loading, starting from Kröner's model, Pilvin added accommodation variables (β-law). A 2 stage complex mathematical formulation is used for the micro-macro transition. The physical meaning of this model is not clear; nevertheless, it compares favourably to other models.
- The finite element model (Bachu & Kalidindi (1998)): the micro-macro transition is here achieved trough a numerical averaging procedure utilizing the finite element technique. For this method, each finite element represents one grain of the polycrystal. The constitutive law for one particular element is then the microscopic law governing the

crystal behaviour (as presented in paragraph 2). In order to model the polycrystal behaviour, each finite element corresponds to a particular crystal orientation so that the ODF of the material is correctly represented by the entire element mesh. A particular procedure must be used to assign one specific orientation to each finite element of the mesh.

Note that some variants of this model are proposed: one finite element can represent more than one grain (for instance, each integration point is assigned a different lattice orientation; if each element contains 8 integration points, it has 8 different lattice orientations, i.e. each element is assumed to be made of 8 grains). On the other hand, each element of the finite element mesh can represent a region smaller than a grain; one grain is then modelled by several finite elements. Other variants have also been investigated (by e.g. Bachu & Kalidindi (1998)).

The main advantage of this model is that it simultaneously ensures stress equilibrium and deformation compatibility between grains. It is basically the goal of the finite element technique. This point has been proved to be a significant improvement of Taylor's model. Large deformation heterogeneities have indeed been observed with the finite element technique (as shown by Figure 10).

Figure 10: Deformed finite element mesh from the simulation of plane strain compression on model 3D-400E-400g2 to a 70% reduction level (ε=-1.2). From Bachu & Kalidindi (1998)

Unfortunately, this method requires larger computation time than Taylor's model. For the finite element simulation of a complex forming process, this technique can hardly be used such as it is. Indeed, for this method, one finite element has a size of the order of the size of one crystal. While the global mesh has the size of the sample. A very large number of elements should be used in most cases of real forming processes.

Nevertheless, a multi-scale approach or FEM^2 method would allow us to avoid (or reduce) the problem from previous approach. Two distinct finite element meshes must be used. The first one is a macroscopic mesh (at the scale of the sample) representing the forming process. The second finite element mesh is microscopic and is used to achieve the micro-macro transition. The size of that mesh is of the order of the representative volume element, i.e. the number of elements of this second mesh must be such that the ODF is correctly represented. Such a microscopic finite element mesh is then supposed to be placed at each integration point of the macroscopic mesh. One complete computation at the micro level must then be achieved each time an integration point of the macro level is treated.

The finite element technique has also been investigated by Sarma et al. (1998) to study the texture evolution during deformation of aluminium alloys at different temperatures. They focused on plane strain compression. The influence of temperature was taken into account in the number of allowed slip systems. It has indeed been noticed that, at elevated temperature, slip occurs on the 6 equivalent $\{1\ 1\ 0\}\langle 1\ 1\ 0\rangle$ systems in addition to the 12 usual $\{1\ 1\ 1\}\langle 1\ 1\ 0\rangle$ systems active at lower temperatures (see also Radhakrishnan et al. (1998) and Stout et al. (1998)). As they want to model crystal

plasticity more accurately, the restricting assumption of uniform stress and plastic strain rate inside each crystal is abandoned. A larger number of finite elements for each crystallographic orientation must then be used. At a first stage, a monocrystal was modelled using a regular mesh of 4096 finite elements (16x16x16) representing all the same crystallographic orientation. Then a polycrystal was modelled with 27000 elements (15x30x60) having 53 different crystallographic orientations representative of the material texture.

3.6 Hardening of the polycrystal

An isotropic work hardening is chosen (see Habraken and Munhoven (1996) and Winters (1996)) for implementation in our model. The yield locus of the polycrystal grows uniformly while its shape remains constant. The work hardening law can be expressed in a macroscopic point of view by a scalar formulation:

$$\sigma = K \cdot \left(\varepsilon^0 + \varepsilon^{plastic}\right)^n \tag{31}$$

where σ and $\varepsilon^{plastic}$ are scalars describing respectively the evolution of the yield stress amplitude and of the plastic strain amplitude. The strength coefficient K, the offset ε^0 and the hardening exponent n are material parameters fitted on experimental data. For convenience, tensile tests are generally used. In that case, σ and $\varepsilon^{plastic}$ are the stress and the plastic strain along the tensile direction.

According to Taylor's model, a macroscopic isotropic hardening behaviour can be taken into account at the crystallographic level trough an identical critical resolved shear stress $\tau^c_{\pm S}$ for all the slip systems and the grains. The size of the yield locus of the single crystal is indeed directly linked to this parameter.
In reality, $\tau^c_{\pm S}$ evolves differently for each particular slip system and for each grain as a function of the crystallographic slip γ_s accumulated on that particular slip, and associated with the dislocation density. The plastic strain rate also has an influence. However, to be able to describe this behaviour analytically, some assumptions have been done:

1. The critical resolved shear stress remains equal to a common value for all the slip systems for a particular grain.
2. The effect of work hardening is assumed to be the same for all the slip systems.
3. Furthermore, the $\tau^c_{\pm S}$ are the same for all the crystallographic grains at a particular material point. In the finite element analysis, a particular point will be one integration point of a finite element. In fact, constant critical resolved shear stress ratios $\alpha_{\pm S}=\tau^c_{\pm S}/\tau^c$ are used. τ^c describes the common evolution that is assumed for all the $\tau^c_{\pm S}$ but with different ratios $\alpha_{\pm S}$ depending on the slip systems. Values of 0.95 or 1 are generally used for $\alpha_{\pm S}$ (see Van Bael (1994)).

In other words, a common work hardening described by the evolution of τ^c occurs for all the slip systems of all the grains included in the representative set of crystal orientations associated with an integration point. However, a different value of τ^c is computed for each integration point. A spatially non-uniform work hardening occurs.
Taylor's model proposes the evolution of the critical resolved shear stress τ^c to be expressed as a function of the accumulated polycrystal induced slip Γ:

$$\Gamma(g) = \int_0^t \dot{\Gamma}(g) dt \tag{32}$$

where g represents a particular grain orientation. The total induced slip starts from zero in the initial annealed state and grows as plastic deformations occur.

The so-called Taylor's factor M is conventionally derived from the plastic power dissipation per unit volume P (see equation (6)) for a given strain rate mode $\underline{\underline{U_{\dot{\varepsilon}}}}$ as:

$$M\left(\underline{\underline{U_{\dot{\varepsilon}}}}\right) = \frac{P}{\tau^c \cdot \dot{\varepsilon}_{EQ}} = \frac{\underline{\underline{\sigma}} \circ \underline{\underline{\dot{\varepsilon}}}}{\tau^c \cdot \dot{\varepsilon}_{EQ}} = \frac{\underline{\underline{\sigma}} \circ \underline{\underline{U_{\dot{\varepsilon}}}}}{\tau^c} \tag{33}$$

where the prescribed strain rate $\underline{\underline{\dot{\varepsilon}}}$ has been split up into a scalar magnitude $\dot{\varepsilon}_{EQ}$ and a mode $\underline{\underline{U_{\dot{\varepsilon}}}}$ with the definition:

$$\dot{\varepsilon}_{EQ} = \sqrt{\dot{\varepsilon}_{ij} \cdot \dot{\varepsilon}_{ij}} \qquad \textit{and} \qquad \underline{\underline{U_{\dot{\varepsilon}}}} = \frac{\underline{\underline{\dot{\varepsilon}}}}{\dot{\varepsilon}_{EQ}} \tag{34}$$

and τ^c is the reference critical resolved shear stress. Equation (33) assumes that all τ^c_S are identical to τ^c.

The first assumption presented above allows us to express the total slip rate as a function of Taylor's factor M and of the plastic strain rate magnitude $\dot{\varepsilon}_{EQ}$:

$$\dot{\Gamma}(g) = \dot{\varepsilon}_{EQ} \cdot M(g) \tag{35}$$

The third assumption states that the work hardening is the same for all the grains. Then, the crystallographic orientation g can be eliminated by averaging:

$$\dot{\overline{\Gamma}} = \int \dot{\Gamma}(g) \mathrm{d}g \tag{36}$$

The averaged form of equation (35) must then be used:

$$\dot{\overline{\Gamma}} = \dot{\overline{\varepsilon}}_{EQ} \cdot \overline{M} \tag{37}$$

where the average of Taylor's factor $\overline{M}$ is only a function of the plastic strain rate direction (the length being taken into account in the plastic strain rate magnitude).
The integration on a time step can be done, assuming that Taylor's factor remains constant during this time interval:

$$\Delta\overline{\Gamma} = \Delta\overline{\varepsilon}_{EQ} \cdot \overline{M} \tag{38}$$

Due to this equation, the plastic equivalent strain describing the macroscopic evolution of the material behaviour in equation (31) can be replaced by the microscopic total induced slip. On the other hand, according to equation (33), the equivalent stress σ of equation (31) can be replaced by the critical resolved shear stress trough the use of Taylor's factor (see also Habraken (2000)). So, the macroscopic hardening stress-strain curve $(\sigma\text{-}\varepsilon^{plastic})$ can be converted into a microscopic critical resolved shear stress-induced slip curve $(\tau^c\text{-}\overline{\Gamma})$. The formulation is then:

$$\tau^c = K^* \cdot \left(\Gamma^0 + \overline{\Gamma}\right)^n \tag{39}$$

K^*, Γ^0 and n are the new material parameters to be fitted on tensile test data. By comparing equations (31) and (39) with the use of relations (33) and (38), one can find the link between these new material parameters and the ones of the macroscopic stress-strain curve:

$$\begin{cases} K^* = \dfrac{K}{\overline{M}^{n+1}} \\ \Gamma^0 = \varepsilon^0 \cdot \overline{M} \\ n \text{ is the same} \end{cases} \tag{40}$$

Some more elaborated evolution rules for the critical resolved shear stress have been proposed by different authors. The assumption of a common critical resolved shear stress on all the grains can be eliminated. Each orientation of the representative set must have its own critical resolved shear stress. The average used in equation (36) is done and the computation of the accumulated induced slip Γ is achieved separately for each crystal.
The assumption of a common evolution of the critical resolved shear stress for all the slip systems of one particular grain is more complicated to remove. A model closer from microscopic phenomena is the one where the critical resolved shear stress of each slip system is a function of all the slip rates. Such methods are presented by Lorrain et al. (2002) and Franciosi (1988). A hardening matrix formulation is used:

$$\dot{\tau}_g^c = H^{gh}\dot{\gamma}_h \tag{41}$$

The diagonal components of the hardening matrix H^{gh} express the self-hardening while the other components correspond to the latent hardening (or cross-hardening), i.e. the effect of one slip system activity on the hardening of other slip systems. Different formulations for the hardening matrix have been proposed. Khan and Cheng (1996) and Teodosiu (1997) review the different proposals. The self and the latent hardening are generally chosen to be different; furthermore, for latent hardening, the interaction between coplanar slip systems is different than for non-coplanar slip systems (Lorrain et al. (2002), Bachu & Kalidindi (1998)).

Chapter 3: Interpolated yield locus and stress integration

1 *Introduction*

Taylor-Bishop-Hill's model described in chapter 2, paragraph 2.1 is used for the computation of the microscopic behaviour of each crystal of the polycrystal. For the micro-macro transition from each grain to the global behaviour of the material, the full constraints Taylor's model described in chapter 2, paragraph 3.5 is used. For one particular plastic strain rate, Taylor's model gives the corresponding stress state. One point of the yield locus is then computed by one call to Taylor's model. The implementation of Taylor's model in a finite element code is not straightforward: contrarily to classical phenomenological yield loci (e.g. the well-known Hill (1948) yield locus or more recently: Banabic et al. (2002)), no mathematical formulation of the yield locus can be obtained directly; this yield locus is computed point by point.
The direct implementation of Taylor's model into a finite element code is however possible. Each time one point of the yield locus is required in the FE code, Taylor's model can be called. However, Taylor's model involves large computation time due to the large number of crystals and it would be called for each integration point of the finite element mesh, for each iteration of each time step. So, such a texture based micro-macro approach would consume prohibitive computation time and seems practically not useful.
Different approaches have been developed to overcome the computation time problem. A commonly used method is the fitting of an analytical yield locus formulation on several points computed by Taylor's model in a pre-processor. The fitting and the numerous calls to Taylor's model are then done once, outside the FEM code. Maudlin et al. (1996) have investigated such an approach with a yield locus approximated by a set of hyperplanes (plane in 5 dimensional deviatoric stress space). They called the fitting procedure "tessellation", highlighting the fact that the continuity between the hyperplanes must be fulfilled, i.e. the yield locus must be a continuous surface. The tessellation is achieved on 647 stress points that are calculated on the basis of the texture of the material. 1226 linear functions defining the hyperplanes are then obtained. The yield locus is described with a continuous mathematical formulation with sufficient detail to be integrated in a finite element code.
The first implementation of a texture based model in our non-linear finite element code Lagamine was also managed trough a fitting procedure. A 6^{th} order series yield locus was defined by a least square fitting on a large number (typically 70300) of Taylor's points (see Munhoven et al. (1996) and Winters (1996)). Contrarily to the set of hyperplanes of Maudlin et al. (1996), the continuity is directly fulfilled thanks to the mathematical formulation of the 6^{th} order series. The least square fitting is performed in a pre-processor using Taylor's model on the basis of the material texture,. It provides the 210 coefficients of the 6^{th} order series which are used during the whole finite element simulation to characterize the anisotropy of the material trough its yield locus.
The main advantage of these approaches is to reduce computation time by putting the time consuming calls to Taylor's model in the pre-processor; a fast constitutive law can then be used in the finite element code.
On the other hand, the fitting is performed on the basis of the initial texture of the material. The texture evolution due to plastic deformation is completely ignored with a pre-processor fitting. Taking texture evolution effects into account would imply the computation of the 210 coefficients of the 6^{th} order series or the 1226 hyperplanes of Maudlin et al. (1996) for each integration point of the finite element mesh, each time a texture updating is necessary (when

plastic deformations significantly alter the material behaviour). This would require an impressive amount of computation time (perhaps even more than direct calls to Taylor's model, depending on the texture updating criterion) and memory storage (the plastic deformation being different for each integration point, the updated texture and subsequently the updated yield locus will be different for each integration point; the 210 coefficients of the 6^{th} order series or the 1226 functions defining the hyperplanes have to be stored for each integration point).
These approaches are qualified of global yield locus approaches as the whole yield locus is described by a mathematical formulation. As the stress state generally remains in the same part of the yield locus or evolves slowly during forming processes, two "local yield locus" descriptions have been developed and implemented in the finite element code Lagamine. Only the interesting small part of the yield locus is explored and used for the fitting of an analytical formulation; only 5 or 6 (depending on the used approach) points of the yield locus are computed with Taylor's model. Texture evolution can then be taken into account more easily; only this small part of the yield locus must be updated.
The first investigated approach uses a set of 5 hyperplanes fitted on 6 Taylor's points to describe a small part of the yield locus. The 6 points must be advisedly chosen so that the zone of the yield locus under interest for the finite element computation is included in one of the 5 hyperplanes. It will be called "hyperplanes method".
For the second approach, 5 points are computed with Taylor's model around the interesting zone of the yield locus. No mathematical yield locus formulation is fitted on these 5 points but a direct stress-strain interpolation is achieved between these points. Its name is "stress-strain interpolation method".
Both methods (hyperplanes or stress-strain interpolation) allow us an important computation time and memory storage reduction with respect to the direct use of Taylor's model. Taylor's model is only called to compute some points in order to achieve the interpolation. These points must be computed in two cases:

- When the current part of the yield locus does not anymore contain the stress state that is required for the finite element simulation. A new local zone of the yield locus is computed.
- When the plastic strains significantly affect the material behaviour and induce changes in the crystallographic orientations representing the texture. A texture updating must take place and the old part of the yield locus is no more representative of the material behaviour; it must be computed with the new texture.

Our approaches with a local yield locus were first published in 1998 (hyperplane interpolation: Duchêne et al. (1998)) and in 1999 (stress-strain interpolation: Duchêne et al. (1999)).

Dawson and Boyce (2002) have developed a yield locus interpolation method similar to our stress-strain interpolation method. The interpolation formulation (equation (5) in Dawson and Boyce (2002)) is reported here:

$$D'(\xi) = \left[N^D(\xi) \right] \{D\}_{np} \tag{42}$$

$$\sigma'(\xi) = \left[N^D(\xi) \right] \{S\}_{np} \tag{43}$$

D' and σ' are the strain rate and the stress as functions of local coordinate ξ defined inside the interpolation domain. Common interpolation functions $N^D(\xi)$ are used in both spaces. Values between brackets are nodal values between which interpolation takes place. The main

difference with the stress-strain interpolation method developed in this thesis is that the whole yield locus is represented by interpolation over a set of domains covering all the possible directions of strain rate.
Dawson and Boyce (2002) use a similar interpolation technique for the representation of the crystallographic texture and the pole density distribution.

This chapter first describes the common features of the hyperplanes method and the stress-strain interpolation method that we have both developed. Next, some particularities of each method (especially their implementation in the finite element code) are treated successively in paragraphs 6 and 7. The hyperplanes method is presented first as it is the first method that has been investigated.

2 *N-dimensional space geometry*

2.1 2-D and 3-D illustrations

The yield locus is located in the 5-dimensional deviatoric stress space. In order to have a more physical view, 2-D and 3-D representations of the yield locus are now presented.
In 2-dimensional space, the yield locus would be a plane curve, i.e. a 1-dimensional domain. The most simple representation is a segment of a straight line limited by 2 points.
In 3-D space, the yield locus would be a surface (a 2-D domain). The most simple representation would be a triangular facet limited by the 3 lines (1-D domains) joining the 3 vertices of the facet.
In the same way, for *N*-dimensional space, the yield locus is a *(N-1)* dimensional domain. The most simple representation is an hyperplane (dimension: *N-1*) limited by *N* boundaries (dimension: *N-2*) and defined by *N* points.

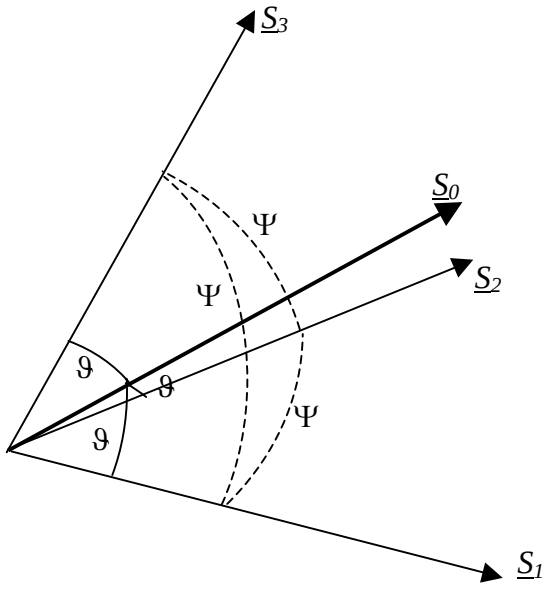

Figure 11: 3-D schematic representation of the domain limit vectors

2.2 Domain limit vectors

Around a reference direction called $\underline{S_0}$ (unit vector), a local domain is defined. To do so, one must find some vectors $\underline{S_i}$ uniformly located around $\underline{S_0}$ (see Figure 11). These vectors must fulfil the following prerequisites:

- In a *N*-dimensional space, *N* vectors $\underline{S_i}$ are required
- They are unit vectors:

$$\underline{S_i}^T \bullet \underline{S_i} = 1 \tag{44}$$

- There is a common angle between each of these vectors:

$$\underline{S_j}^T \bullet \underline{S_i} = \cos(\Psi) = 1 - \beta^2 \qquad ,i \neq j \tag{45}$$

Equations (44) and (45) give:

$$\underline{S_j}^T \bullet \underline{S_i} = 1 + \beta^2 \cdot \left(\delta_{ij} - 1\right) \qquad ,\forall i, j \tag{46}$$

(δ_{ij} is the Kronecker symbol)

- There is a common angle ϑ between $\underline{S_0}$ and each $\underline{S_i}$:

$$\underline{S_0}^T \bullet \underline{S_i} = \cos(\vartheta) \tag{47}$$

The angle ϑ is a user parameter and directly defines the size of the interpolation domain.
With these definitions, the reference vector $\underline{S_0}$ is the mean value of the domain limit vectors $\underline{S_i}$ (the length of $\underline{S_0}$ vector not taken into account):

$$\underline{S_0} = k \cdot \sum_{i=1}^{N} \underline{S_i} \tag{48}$$

Combining equation (47) and the fact that $\underline{S_0}$ is a unit vector, one can deduce the following relations:

$$k = \frac{1}{N \cdot \cos(\vartheta)} \qquad \Rightarrow \qquad \underline{S_0} = \frac{1}{N \cdot \cos(\vartheta)} \cdot \sum_{i=1}^{N} \underline{S_i} \tag{49}$$

$$\text{and} \quad \beta^2 = \frac{N}{N-1} \cdot \sin^2(\vartheta) \tag{50}$$

2.3 Definition of a vector basis in the domain

As the *N* $\underline{S_i}$ vectors are linearly independent, they can be used as a covariant vector basis in the *N*-dimensional stress space. They are not orthogonal to each other. It is useful to define *N* new vectors $\underline{SS_i}$ normal to the $\underline{S_i}$; forming a contravariant basis.

$$\underline{SS_i}^T \bullet \underline{S_j} = \delta_{ij} \tag{51}$$

Due to this definition, they are not unit vectors. They can be obtained by linear combination of $\underline{S_i}$ and $\underline{S_0}$:

$$\underline{SS_i} = a \cdot \underline{S_i} + b \cdot \underline{S_0} \tag{52}$$

Where *a* and *b* can be deduced from equation (51); the final form of the $\underline{SS_i}$ vectors is:

$$\underline{SS_i} = \frac{1}{\beta^2} \cdot \left[\underline{S_i} - \frac{1-\beta^2}{\cos(\vartheta)} \cdot \underline{S_0} \right] \tag{53}$$

Two useful relations can be deduced from the definition of the $\underline{SS_i}$ vectors:

$$\sum_{i=1}^{N} \underline{SS_i} = \frac{\underline{S_0}}{\cos(\vartheta)} \tag{54}$$

and

$$\underline{SS_j^T} \bullet \underline{SS_i} = \frac{\delta_{ij}}{\beta^2} - \frac{1-\beta^2}{\beta^2 \cdot N \cdot \cos^2(\vartheta)} \tag{55}$$

2.4 Curvilinear coordinates η

The vectors defined above will be used to decompose any (non unit) vector $\underline{V}$ in the following form:

$$\underline{V} = \sum_{i=1}^{N} \eta_i \cdot \underline{S_i} \tag{56}$$

The η_i coefficients can be obtained by projecting $\underline{V}$ on the $\underline{SS_i}$ vectors:

$$\underline{SS_j^T} \bullet \underline{V} = \sum_{i=1}^{N} \eta_i \cdot \underbrace{\underline{SS_j^T} \bullet \underline{S_i}}_{=\delta_{ij}} = \eta_j \tag{57}$$

These N η-coordinates are independent to each other; their knowledge is equivalent to the knowledge of vector $\underline{V}$, with its direction and its length. It can be easily found that:

$$\sum_{i=1}^{N} \eta_i = \frac{\underline{V}^T \bullet \underline{S_0}}{\cos(\vartheta)} \tag{58}$$

2.5 Intrinsic coordinates ξ

These coordinates are defined:

$$\xi_i = \frac{\cos(\vartheta)}{\underline{V}^T \bullet \underline{S_0}} \cdot \underline{V}^T \bullet \underline{SS_i} = \frac{\eta_i}{\sum_{j=1}^{N} \eta_j} \tag{59}$$

such that $\Sigma \xi_i = 1$, which is an interesting property.

Unlike the η-coordinates, these intrinsic coordinates are not independent. The N^{th} coordinate can be deduced from the $N-1$ others. The $\underline{V}$ vector is then no more completely represented by these ξ-coordinates; only its direction is known, its length must be defined separately.

It can be noticed that the direction and the length are completely uncoupled with this representation. This is an important property but, on the other hand, the $\underline{V}$ vector cannot be completely recovered knowing the intrinsic coordinates.

2.6 Properties of those coordinates

Some important properties of the η and ξ-coordinates are listed below:

- For a unit vector $\underline{V}$ corresponding to a domain limit vector $\underline{S_i}$, the η and ξ-coordinates are all equal to 0 or 1 ($\eta_j = \xi_j = \delta_{ij}$).
- Inside the interpolation domain all the η and ξ-coordinates are positive. From this property, it can be deduced that ξ_i *(1=1,N)* is smaller than 1 inside the interpolation domain.
- The *N* limit curves (or boundaries) of the domain correspond to $\eta_i = \xi_i = 0$, *i=1,N*.
- The *N* vertices are defined by $\eta_i = \xi_i = 1$ and the other coordinates equal to zero. They correspond to the domain limit vectors.
- The knowledge of the *N* η or ξ-coordinates is equivalent to the knowledge of the direction of any vector (corresponding to *N-1* independent variables); in addition, the η_i include the length of the vector.
- On a boundary, one intrinsic coordinate is equal to zero; so, this boundary, which is a *N-2* dimensional domain, is defined by *N-1* points and can be described by *N-1* intrinsic coordinates (the non-zero ones).

2.7 Computation of the $\underline{S_i}$ vectors

The way we compute the $\underline{S_i}$ vectors is described hereafter. One particular reference direction $\underline{S_0}^*$ is chosen such that its N components are equal. Temporary limit vectors are computed by successively adding each vector of the cartesian basis to the reference $\underline{S_0}^*$:

$$\underline{S_i}^* = \alpha' \cdot \underline{S_0}^* + \beta \cdot \underline{t_i} = \underbrace{\alpha' \cdot \frac{1}{\sqrt{N}}}_{=\alpha} \cdot \begin{pmatrix} 1 \\ 1 \\ 1 \\ 1 \\ 1 \\ 1 \end{pmatrix} + \beta \cdot \begin{pmatrix} 0 \\ 0 \\ \vdots \\ 1 \\ \vdots \\ 0 \end{pmatrix} \leftarrow i^{\text{th}} \text{ position} \tag{60}$$

According to equation (49), we have:

$$\underline{S_0}^* = \frac{1}{N \cdot \cos(\vartheta)} \cdot \sum_{i=1}^{N} \underline{S_i}^* = \frac{N \cdot \alpha + \beta}{N \cdot \cos(\vartheta)} \cdot \begin{pmatrix} 1 \\ 1 \\ \vdots \\ 1 \end{pmatrix} \tag{61}$$

where α and β are such that the unit conditions $\left\| \underline{S_0}^* \right\| = 1$ and $\left\| \underline{S_i}^* \right\| = 1$ are fulfilled. One can easily check that β is the same as the one defined by equation (50) and:

$$\alpha = \frac{\cos(\vartheta)}{\sqrt{N}} - \frac{\sin(\vartheta)}{\sqrt{N \cdot (N-1)}} \tag{62}$$

To obtain the actual $\underline{S_0}$ and $\underline{S_i}$ vectors (reference and domain limit directions), all these temporary vectors are rotated in order to have $\underline{S_0}^*$ and $\underline{S_0}$ pointing the same direction (see Figure 12).

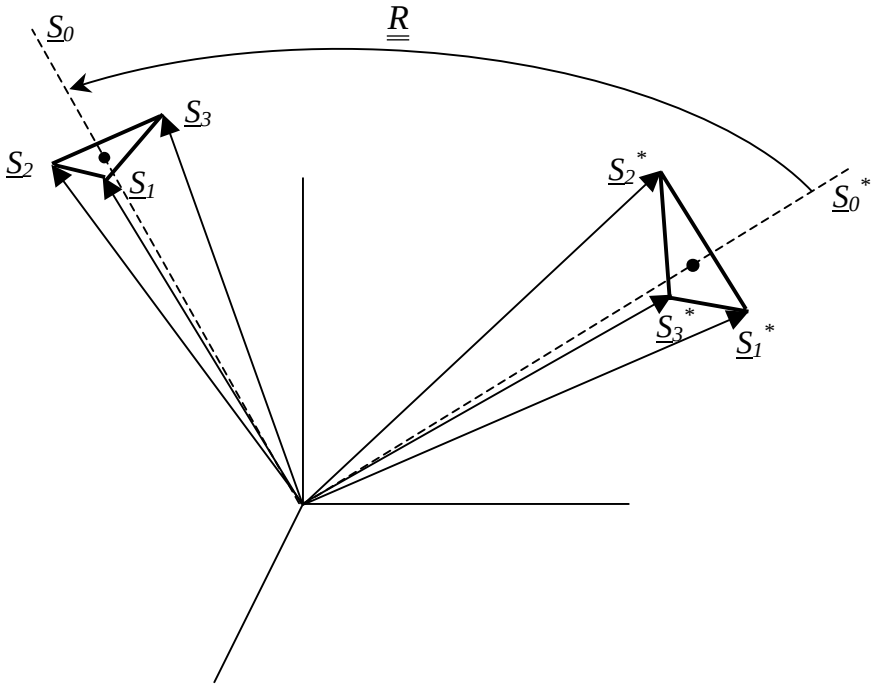

Figure 12: 3-D schematic representation of the computation of the limit vectors

The rotation matrix is computed according to equation (63):

$$\underline{\underline{R}} = \underline{\underline{1}} + 2 \cdot \underline{S_0} \cdot \underline{S_0^{*T}} - \frac{\left(\underline{S_0} + \underline{S_0^*}\right) \cdot \left(\underline{S_0} + \underline{S_0^*}\right)^T}{1 + \underline{S_0^T} \bullet \underline{S_0^*}} \tag{63}$$

Some remarks concerning $\underline{\underline{R}}$ are listed:

- This definition fulfils the rotation condition:

$$\underline{\underline{R}} \bullet \underline{\underline{R}}^T = \underline{\underline{1}} \tag{64}$$

- This rotation applies $\underline{S_0}^*$ on $\underline{S_0}$:

$$\underline{\underline{R}} \bullet \underline{S_0^*} = \underline{S_0} \tag{65}$$

- It is then used to compute the actual domain limit vectors:

$$\underline{\underline{R}} \bullet \underline{S_i^*} = \underline{S_i} \tag{66}$$

- If $\underline{S_0}^*$ and $\underline{S_0}$ are opposite vectors, equation (63) is not valid; then, the domain limit vectors $\underline{S_i}$ can be computed as the opposite of the $\underline{S_i}^*$.

It can be noticed that when the $\underline{S_i}$ vectors are computed, the $\underline{SS_i}$ vectors can be obtained through equation (53).

2.8 Entering the adjacent domain

During a finite element simulation, the domain where the yield locus is defined must be frequently updated. A new domain (identified hereafter by ') is computed when the old one is not anymore valid.

The classical way for such updating is based on the previous paragraph, where the reference direction $\underline{S_0}$, which is in the middle of the interpolated domain, is chosen as close as possible to the direction in which the yield locus must be explored.

However, it can be interesting to take advantage of the neighbouring of the domains. The 3-dimensional representation of Figure 13 compares two methods (A and B).

Next to a particular boundary, defined by *N-1* domain limit vectors (2 for the 3-D case), there exists only 2 adjacent domains. Those 2 domains are defined by their common boundary and only one additional domain limit vector. So, to go from one domain to the adjacent one, the required additional information is only one limit vector; the boundary of the initial domain being known.

As the computation of a vector according to Taylor's model is time consuming, method B is very interesting. Only one vector instead of *N* is computed.

If the initial domain is left along the boundary $\xi_i = 0$ (see paragraph 2.6), the domain limit vector $\underline{S_i}$ must be replaced by the new $\underline{S_i}'$ which is computed according to equation (67).

$$\underline{S_i'} = a \cdot \underline{S_i} + b \cdot \underline{S_0} \tag{67}$$

The constants *a* and *b* must be such that $\underline{S_i}'$ fulfils the following conditions:

$$\underline{S_i'}^T \bullet \underline{S'_i} = 1 \tag{68}$$

$$\underline{S_i'}^T \bullet \underline{S_j} = 1 - \beta^2 \qquad ,i \neq j \tag{69}$$

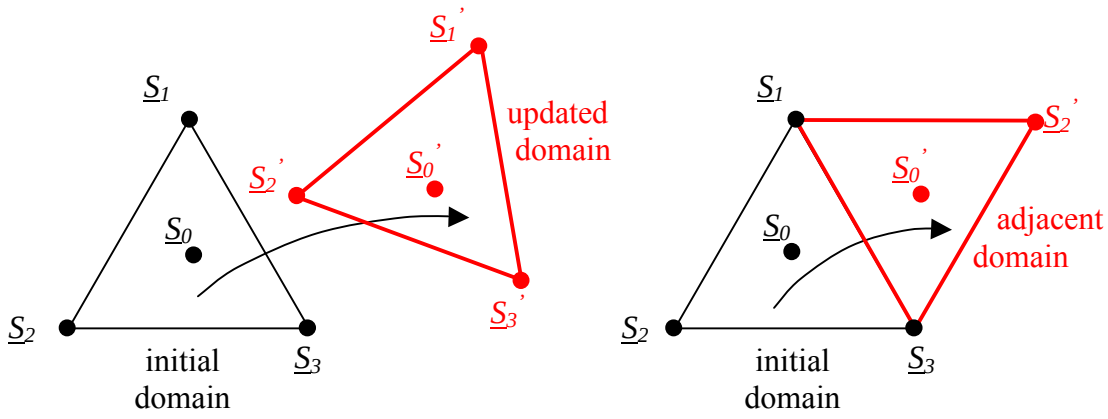

Figure 13: Classical and improved domain updating methods

Finally, as a new domain is explored, a new $\underline{S_0}'$ vector must be computed either according to its definition (equation (49)) or from the old domain values:

$$\left.\begin{aligned}\underline{S_0'} &= \frac{\sum_{j=1}^{N}\underline{S_j'}}{N\cdot\cos(\vartheta)}\\ \underline{S_0} &= \frac{\sum_{j=1}^{N}\underline{S_j}}{N\cdot\cos(\vartheta)}\end{aligned}\right\} \Rightarrow \underline{S_0'} = \underline{S_0} + \frac{\underline{S_i'} - \underline{S_i}}{N\cdot\cos(\vartheta)} \tag{70}$$

When the limit vectors of the new domain are computed, it is interesting to look at the new curvilinear coordinates. The boundary opposite to vertex $\underline{S_i}$ is defined by:

$$\eta_i = \underline{V}^T \bullet \underline{SS_i} = 0 \tag{71}$$

where $\underline{V}$ is a particular vector on the boundary.
Replacing $\underline{SS_i}$ by its definition (53), relation (71) becomes:

$$\underline{V}^T \bullet \underline{S_i} = \underline{V}^T \bullet \underline{S_0}\cdot\frac{1-\beta^2}{\cos(\vartheta)} \tag{72}$$

The other η-coordinates, which are not equal to zero, are:

$$\eta_k = \underline{V}^T \bullet \underline{SS_k} = \underline{V}^T \bullet \left(\underline{S_k} - \underline{S_0}\cdot\frac{1-\beta^2}{\cos(\vartheta)}\right)\cdot\frac{1}{\beta^2} \tag{73}$$

In the adjacent domain, the η-coordinates can also be computed. First, the η_i' coordinate corresponding to the new domain limit vector $\underline{S_i}$' is:

$$\begin{aligned}\eta_i' &= \underline{V}^T \bullet \underline{SS_i'}\\ &= \underline{V}^T \bullet \left(\underline{S_i'} - \underline{S_0'}\cdot\frac{1-\beta^2}{\cos(\vartheta)}\right)\cdot\frac{1}{\beta^2}\end{aligned} \tag{74}$$

Using equation (70) to express $\underline{S_0}'$:

$$\eta_i' = \underline{V}^T \bullet \left(\underline{S_i'} - \left(\underline{S_0} + \frac{\underline{S_i'} - \underline{S_i}}{N\cdot\cos(\vartheta)}\right)\cdot\frac{1-\beta^2}{\cos(\vartheta)}\right)\cdot\frac{1}{\beta^2} \tag{75}$$

$\underline{S_0}$ can be eliminated with the use of equation (53):

$$\begin{aligned}\eta_i' &= \underline{V}^T \bullet \left(\underline{S_i'} + \underline{SS_i}\cdot\beta^2 - \underline{S_i} - \frac{\underline{S_i'} - \underline{S_i}}{N\cdot\cos(\vartheta)}\cdot\frac{1-\beta^2}{\cos(\vartheta)}\right)\cdot\frac{1}{\beta^2}\\ &= \underbrace{\underline{V}^T \bullet \underline{SS_i}}_{=\eta_i} + \underline{V}^T \bullet \left(\underline{S_i'} - \underline{S_i}\right)\cdot\left(1 - \frac{1-\beta^2}{N\cdot\cos^2(\vartheta)}\right)\cdot\frac{1}{\beta^2}\end{aligned} \tag{76}$$

On the boundary between the two adjacent domains, as η_i is equal to zero, η_i' is equal to zero too if:

$$\underline{V}^T \bullet \underline{S_i'} = \underline{V}^T \bullet \underline{S_i} \tag{77}$$

Due to the definition of the new domain limit vector $\underline{S_i}$', equation (77) is fulfilled. Indeed, $\underline{V}$ is a vector on the boundary and this boundary is a symmetry plane between $\underline{S_i}$ and $\underline{S_i}$'. The projections of these two vectors on $\underline{V}$ are necessarily equal.
The boundary is then defined by $\eta_i' = \eta_i = 0$.
The other coordinates of the new domain can also be computed:

$$\begin{aligned} \eta_k' &= \underline{V}^T \bullet \underline{SS_k'} \\ &= \underline{V}^T \bullet \left(\underline{S_k} - \underline{S_0'} \cdot \frac{1-\beta^2}{\cos(\vartheta)} \right) \cdot \frac{1}{\beta^2} \end{aligned} \tag{78}$$

Note that $\underline{S_k}' = \underline{S_k}$ $(k \neq i)$ because they are kept from the old domain.
By the same way as previously, we get:

$$\eta_k' = \underline{V}^T \bullet \left(\underline{S_k} - \left(\underline{S_0} + \frac{\underline{S_i'} - \underline{S_i}}{N \cdot \cos(\vartheta)} \right) \cdot \frac{1-\beta^2}{\cos(\vartheta)} \right) \cdot \frac{1}{\beta^2} \tag{79}$$

Eliminating $\underline{S_0}$ with equation (53) applied to $\underline{SS_k}$:

$$\begin{aligned} \eta_k' &= \underline{V}^T \bullet \left(\underline{S_k} + \underline{SS_k} \cdot \beta^2 - \underline{S_k} - \frac{\underline{S_i'} - \underline{S_i}}{N \cdot \cos(\vartheta)} \cdot \frac{1-\beta^2}{\cos(\vartheta)} \right) \cdot \frac{1}{\beta^2} \\ &= \underbrace{\underline{V}^T \bullet \underline{SS_k}}_{=\eta_k} + \underline{V}^T \bullet \left(\underline{S_i'} - \underline{S_i} \right) \cdot \frac{-\left(1-\beta^2\right)}{N \cdot \cos^2(\vartheta) \cdot \beta^2} \end{aligned} \tag{80}$$

Finally equation (77) leads to:

$$\eta_k' = \eta_k \tag{81}$$

This equation implies that along a boundary between two adjacent domains, the η-coordinates computed from one or the other domain are equal. This is a very important and convenient property.

The main advantages of method B are that it requires only 1 (instead of 5) call to Taylor's model for an updating, it improves the continuity of the resulting yield locus and the continuity of its normal. A drawback is that it can only be used when the adjacent domain contains the current stress and then gives rise to positive new intrinsic co-ordinates. This condition is satisfied when the stress evolves smoothly which is often the case during a finite element simulation.

2.9 Non-regular domains

According to equation (45), the angles between the domain limit vectors are identical. This implies that only regular domains are used. For instance, in the 3-D illustration, the interpolated yield locus is represented by equilateral triangles.
However, it would be possible to define an interpolated domain based on non-uniformly located limit vectors. For the 3-D case, the triangular facets would not be equilateral anymore.
With a non-regular domain, the intrinsic coordinates are still available but some particularities should be noticed:

- The choice of the N domain limit vectors $\underline{S_i}$ is free; the angle between each of them is not fixed. However, as they constitute a basis in the N-dimensional space, they cannot be parallel to each other; they must be linearly independent.
- In order to compute the $\underline{SS_i}$ vectors, equation (53) is no more valid. The definition based on equation (51) ($\underline{S_i}^T.\underline{SS_j} = \delta_{ij}$) must be used. As the $\underline{S}$ vectors form a basis, it is always possible to compute the $\underline{SS_i}$ vectors. Equations (54) and (55) are no more fulfilled.
- The η-coordinates are still computed from equation (57) ($\eta_i = \underline{V}^T.\underline{SS_i}$). On the other hand, the $\underline{V}$ vector can be found knowing its coordinates according to equation (56) ($\underline{V} = \Sigma\ \eta_i\ \underline{S_i}$).
- The intrinsic coordinates are computed in the same way:

$$\xi_i = \frac{\eta_i}{\sum_{j=1}^{N} \eta_j} = \frac{\underline{V}^T \bullet \underline{SS_i}}{\underline{V}^T \bullet \sum_{j=1}^{N} SS_j} \tag{82}$$

  Note that this equation is slightly different from equation (59) (the original definition) in the sense that the sum on the $\underline{SS_i}$ vectors can no more be replaced by its value as a function of $\underline{S_0}$.
  The sum of the intrinsic coordinates is still equal to one.
- The $\underline{S_0}$ vector is no more a particular direction; it can however be defined:

$$\underline{S_0} = c \cdot \sum_{i=1}^{N} \underline{S_i} \tag{83}$$

  The c constant must be chosen such that $\underline{S_0}$ is a unit vector.
  For that direction, all the intrinsic coordinates are identical and their common value is $(1/N)$.
- Just like for regular domains, the N boundaries of the domain are defined by $\xi_i = \eta_i = 0$; the N vertices are defined by $\xi_i = 1$ and the other coordinates equal to zero.
- The property defined by equation (81) stating that the η-coordinates computed from two adjacent domains are equal on the common boundary is no more valid.

Aside those differences, the main properties of the ξ and η-coordinates are still fulfilled. So, non-regular domains can be used just like regular ones.

3 *Local yield locus approach – general features*

Contrarily to numerous phenomenological models, in the developments integrating the texture of materials, there does not exist a mathematical formulation describing the yield locus continuously. It is only possible to numerically compute, for a particular direction called $\underline{d}$, the length of the vector whose extremity lies on the yield locus. The length of this vector will be called s^*.
As the computation of one point of the yield locus with the texture model is time consuming, it is interesting to interpolate locally the yield locus between some computed points. Different methods can be used to define local domain of the yield locus; some are presented hereafter.
The problem to solve is to find a formulation in order to compute s^*, the length of a vector as a function of its direction $\underline{d}$ which can be described by the intrinsic coordinates defined in paragraph 2.5 (see also Godinas (1998 a) and Godinas (1998 b)).

In the finite element analysis, the stress space in generally chosen for the computation. Contrarily, Taylor's model allows to compute, for a given plastic strain rate direction, the stress direction and its length, i.e. one point of the yield locus. Nevertheless, if one wants to impose the stress direction, it is possible but it is necessary to iterate in order to find the corresponding plastic strain rate direction. The Taylor's model should preferably be used in strain rate space in order to avoid the computation time consuming iterative procedure.
The choice of the interpolation space is imposed by the texture model and the finite element code. Furthermore, both stress space and strain rate space are closely linked together.
Due to this fact, both spaces are used. For the plastic strain rate space, the domain limit vectors are computed according to the method presented in paragraph 2.7: a regular domain is obtained. Taylor's model is used to compute the N domain limit vectors in stress space corresponding to the ones in the plastic strain rate space. The vertices so obtained are not uniformly located. Their irregular spacing is function of the anisotropy of the material behaviour. The associated domain in stress space is non-regular.

Inside a domain, the intrinsic coordinates computed in stress space and in plastic strain rate space are not exactly equal, again due to the anisotropy of the material behaviour. However, the boundaries and the vertices respectively correspond in both spaces and the associated intrinsic coordinates are identical. Inside the domain, the stress space and its non-regular domains are chosen as reference for the computation of the intrinsic coordinates. One convenient approximation of the developed approaches is the use of these intrinsic coordinates in plastic strain rate space too.
The dimension of the space, i.e. the value of N, is the stress space dimension. As the yield locus is assumed to be independent of the hydrostatic stress, it is interesting to use the reduced deviatoric stress space $\hat{\sigma}_{ij}$ whose dimension is 5 instead of 6. The transformation used to compute 5 dimensional stress vectors from 3 dimensional second order stress tensors is:

$$\underline{s} = \begin{pmatrix} s_1 \\ s_2 \\ s_3 \\ s_4 \\ s_5 \end{pmatrix} = \begin{pmatrix} \frac{\sqrt{2}}{2} \cdot \left(\hat{\sigma}_{11}^{3D} - \hat{\sigma}_{22}^{3D} \right) \\ \frac{\sqrt{6}}{2} \cdot \left(\hat{\sigma}_{11}^{3D} + \hat{\sigma}_{22}^{3D} \right) \\ \sqrt{2} \cdot \hat{\sigma}_{23}^{3D} \\ \sqrt{2} \cdot \hat{\sigma}_{13}^{3D} \\ \sqrt{2} \cdot \hat{\sigma}_{12}^{3D} \end{pmatrix} \tag{84}$$

It fulfils the power conservation equation:

$$\underline{s}^{5D} \bullet \underline{t}^{5D} = \underline{\underline{S}}^{3D} \circ \underline{\underline{T}}^{3D} \tag{85}$$

if $\underline{s}^{5D}$ and $\underline{t}^{5D}$ respectively correspond to $\underline{\underline{S}}^{3D}$ and $\underline{\underline{T}}^{3D}$. In equation (85), a scalar product applies between 5D vectors and a double contracted tensor product applies between 3D tensors.

3.1 Hyperplanes method

This method is the most simple, it consists in a **linear interpolation in cartesian coordinates**. It only implies the computation of the lengths (s_i) of the yield stress vectors in the N directions defined by the domain limit vectors $\underline{S}_i$. These N yield stress vectors define the

stress nodes which are the vertices of the local interpolation domain. Any stress vector $\underline{\sigma}$ is defined as the weighted average of the yield stresses along the domain limit directions. The weight factors are the intrinsic coordinates of the selected direction $\underline{d}$:

$$\underline{\sigma} = s^* \cdot \underline{d} = \sum_{i=1}^{N} \xi_i \cdot s_i \cdot \underline{S_i} \qquad \text{with} \qquad \sum_{i=1}^{N} \xi_i = 1 \tag{86}$$

where the explored stress vector $\underline{\sigma}$ is decomposed in its length s^* and its direction $\underline{d}$.
Using the properties of the $\underline{SS_i}$ vectors, it is possible to compute the value of the interpolated length s^* as a function of the direction $\underline{d}$:

$$s^* \cdot \underline{SS_j^T} \bullet \underline{d} = \sum_{i=1}^{N} \xi_i \cdot s_i \cdot \underline{SS_j^T} \bullet \underline{S_i} = \xi_j \cdot s_j \tag{87}$$

$$\text{with} \qquad \sum_{i=1}^{N} \xi_i = \sum_{i=1}^{N} \frac{s^* \cdot \underline{SS_i^T} \bullet \underline{d}}{s_i} = 1 \tag{88}$$

$$\Rightarrow \qquad \frac{1}{s^*} = \sum_{i=1}^{N} \frac{\underline{SS_i^T} \bullet \underline{d}}{s_i} \tag{89}$$

An important remark should be mentioned here: when all the s_i for the N domain limit vectors are equal to s, the interpolated length s^* is not equal to this common value s:

$$\frac{1}{s^*} = \sum_{i=1}^{N} \frac{\underline{SS_i^T} \bullet \underline{d}}{s} \qquad \Rightarrow \qquad s^* = \frac{s}{\sum_{i=1}^{N} \underline{SS_i^T} \bullet \underline{d}} \neq s \tag{90}$$

Furthermore, for the case of a regular domain, equation (59) leads to:

$$\frac{1}{s^*} = \frac{\underline{S_0^T} \bullet \underline{d}}{\cos(\vartheta)} \cdot \sum_{i=1}^{N} \frac{\xi_i}{s_i} \tag{91}$$

For a regular domain, the inequality (90) still appears, according to equation (54):

$$s^* = s \cdot \frac{\cos(\vartheta)}{\underline{S_0^T} \bullet \underline{d}} \neq s \tag{92}$$

And e.g. for $\underline{d} = \underline{S_0}$:

$$s^* = s \cdot \cos(\vartheta) < s \tag{93}$$

This interpolation appears as a plane facet as shown in the 2-dimensional representation of Figure 14.

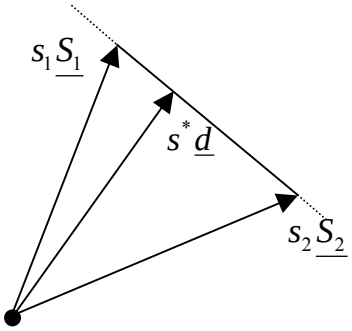

Figure 14: 2-D representation of the hyperplane interpolation

3.2 Stress-strain interpolation method

Instead of interpolating in cartesian coordinates, i.e. each component of the stress vector independently, it is possible to interpolate the stress direction and the stress vector length separately. One can see this method as a **linear interpolation in spherical coordinates.**
In a 3-dimensional space, the direction is represented by 2 scalars (which are often chosen to be 2 angles) and the length of any vector is 1 scalar. In the *N*-dimensional space, the direction is defined by *N-1* parameters and the length is 1 parameter. The *N* intrinsic coordinates ξ are used to represent the direction; indeed, they represent *N-1* independent parameters (see paragraph 2.5).
The interpolation is carried out the following way: the *N* intrinsic coordinates are deduced from the direction of the stress vector (the direction in which the yield locus is explored). The length s^* of the vector leading to the yield stress is linearly interpolated according to equation (94).

$$s^* = \sum_{i=1}^{N} \xi_i \cdot s_i \tag{94}$$

With this interpolation method, if the domain limit vector lengths s_i are identical, the interpolated value s^* will also be identical. So, a hypersphere (a sphere in the *N*-dimensional space) is exactly represented through this interpolation.

Both methods presented above (3.1 and 3.2 sections) are worth integrating in a finite element code. The first one is more adapted to represent a yield locus with facets (like Tresca's). The second one should be used for quadratic yield loci (like von Mises'). So, the superiority of one method depends on the material behaviour. Sections 3.3, 3.4 and 3.5 present alternative interpolations and section 3.6 studies continuity between adjacent domains.

3.3 Inverse interpolation

Instead of using equation (94), it is possible to interpolate the inverse of the vector length:

$$\frac{1}{s^*} = \sum_{i=1}^{N} \frac{\xi_i}{s_i} \tag{95}$$

This method is not very different from the direct interpolation; in particular, in the case of domain limit vectors having the same length, both interpolations lead to the same result. However, if the *N* vector lengths s_i are significantly different from each other, this

interpolation formulation is similar to the hyperplane method (compare equations (91) and (95)).
Another variant of equation (94) would be to use the η-coordinates:

$$s^* = \sum_{i=1}^{N} \eta_i \cdot s_i = \frac{\underline{d}^T \bullet \underline{S_0}}{\cos(\vartheta)} \cdot \sum_{i=1}^{N} \xi_i \cdot s_i \qquad (\text{for regular domains}) \tag{96}$$

3.4 'Bubble' mode

The cartesian and spherical linear interpolations presented above can be improved by the adjunction of one term:

$$aN \prod_{i=1}^{N} \xi_i \tag{97}$$

where a is a constant.
Due to the fact that on a boundary, at least one intrinsic coordinate is equal to zero, the added term only has an influence inside the interpolated domain. This is the reason why it is called 'bubble' mode.
The constant a must be such that a particular yield stress inside the domain fulfils the interpolation. So, this 'bubble' mode implies the computation of a new yield stress vector according to Taylor's model.
For convenience, if we choose the $\underline{S_0}$ direction (with all the ξ_i equal to $1/N$), the constant a can be easily found for the spherical interpolation:

$$s_0 = \sum_{i=1}^{N} \xi_i \cdot s_i + a \cdot \prod_{i=1}^{N} N \cdot \xi_i = \sum_{i=1}^{N} \frac{s_i}{N} + a \qquad \Rightarrow a = s_0 - \sum_{i=1}^{N} \frac{s_i}{N} \tag{98}$$

The formulation of the improved spherical interpolation is then:

$$s^* = \sum_{i=1}^{N} \xi_i \cdot s_i + \left(s_0 - \sum_{i=1}^{N} \frac{s_i}{N} \right) \cdot \prod_{i=1}^{N} N \cdot \xi_i \tag{99}$$

For the cartesian linear interpolation, the 'bubble' mode is a vector:

$$\underline{\sigma} = s^* \cdot \underline{d} = \sum_{i=1}^{N} \xi_i \cdot s_i \cdot \underline{S_i} + \underline{a} \cdot \prod_{i=1}^{N} N \cdot \xi_i \tag{100}$$

The $\underline{S_0}$ direction is also chosen for the determination of $\underline{a}$:

$$s_0 \cdot \underline{S_0} = \sum_{i=1}^{N} \frac{1}{N} \cdot s_i \cdot \underline{S_i} + \underline{a} \cdot \prod_{i=1}^{N} N \cdot \frac{1}{N} \qquad \Rightarrow \underline{a} = s_0 \cdot \underline{S_0} - \sum_{i=1}^{N} \frac{s_i \cdot \underline{S_i}}{N} \tag{101}$$

The 'bubble' mode improves the accuracy inside the domain for the cartesian and spherical interpolation but requires the computation of one additional particular yield stress.

3.5 Second order interpolation

Second order interpolation can be investigated. As for the 'bubble' mode, new yield stress vectors will have to be computed. We will choose points on the boundary between two vertices. In particular, the most interesting points have two intrinsic coordinates equal to ½

and the *(N-2)* other ones equal to zero. These new directions are called $\underline{S_{ij}}$ and the lengths corresponding to the yield stresses are s_{ij}.
As these new $\underline{S_{ij}}$ vectors are on a boundary just half-way between two vertices $\underline{S_i}$ and $\underline{S_j}$, they can be defined as:

$$\underline{S_{ij}} = \alpha \cdot \left(\frac{\underline{S_i}}{2} + \frac{\underline{S_j}}{2} \right) \tag{102}$$

The α-constant must be such that $\underline{S_{ij}}$ is a unit vector. One can easily find:

$$\underline{S_{ij}^T} \bullet \underline{S_{ij}} = 1 \qquad \Rightarrow S_{ij} = \frac{\left(\underline{S_i} + \underline{S_j} \right)}{\sqrt{4 - 2 \cdot \beta^2}} \tag{103}$$

The interpolation must combine a constant term, *(N-1)* linear terms (as the linear interpolations) and *N(N-1)/2* quadratic terms. With the use of the intrinsic coordinates, all these terms are contained in the *N(N+1)/2* quadratic terms of the *N* dependent ξ_i. Due to the fact that their sum is equal to one, the linear and constant terms are taken into account.

Indeed, for the spherical interpolation, the formulation is:

$$s^* = \sum_{i=1}^{N} \sum_{j=1}^{N} c_{ij} \cdot \xi_i \cdot \xi_j \qquad with \qquad c_{ij} = c_{ji} \tag{104}$$

If one wants to add linear terms having the form:

$$s_{lin}^* = \sum_{i=1}^{N} d_i \cdot \xi_i = \sum_{i=1}^{N} \left(d_i \cdot \xi_i \cdot \left(\sum_{j=1}^{N} \xi_j \right) \right) = \sum_{i=1}^{N} \sum_{j=1}^{N} d_i \cdot \xi_i \cdot \xi_j \tag{105}$$

they are included in the formulation of equation (104). For a constant term, the same conclusion appears:

$$s_{cons}^* = e = e \cdot \left(\sum_{i=1}^{N} \xi_i \right) \cdot \left(\sum_{j=1}^{N} \xi_j \right) = \sum_{i=1}^{N} \sum_{j=1}^{N} e \cdot \xi_i \cdot \xi_j \tag{106}$$

The *N(N+1)/2* constants c_{ij} are determined by identification with the *N* values along the vertices: s_i and the *N(N-1)/2* values on the boundaries between two vertices:

$$c_{ii} = s_i \tag{107}$$

$$c_{ij} = c_{ji} = 2 \cdot s_{ij} - \frac{s_i}{2} - \frac{s_j}{2} \qquad \text{with} \qquad i \neq j \tag{108}$$

Note that these two equations can be summarised in:

$$c_{ij} = c_{ji} = 2 \cdot s_{ij} - \frac{s_i}{2} - \frac{s_j}{2} \qquad \text{for any i and j} \tag{109}$$

if we define s_{ii} to be equal to s_i.

The second order interpolation can also be applied to the hyperplane method:

$$\underline{\sigma} = s^* \cdot \underline{d} = \sum_{i=1}^{N} \sum_{j=1}^{N} f_{ij} \cdot \xi_i \cdot \xi_j \cdot \underline{S_{ij}} \tag{110}$$

In this formulation, it is assumed that $\underline{S}_{ii}$ is defined to be $\underline{S}_i$ and $f_{ij} = f_{ji}$. The identification of these constants is done in a similar way as for the spherical interpolation.

The inverse interpolation can also be used:

$$\frac{1}{s^*} = \sum_{i=1}^{N} \sum_{j=1}^{N} g_{ij} \cdot \xi_i \cdot \xi_j \tag{111}$$

Higher order interpolation can also be investigated. Again, as the sum of the intrinsic coordinates is equal to one, only the higher order terms should be considered (see Munhoven et al. (1996) and Winters (1996)). Such methods improve the accuracy of the interpolations. On the other hand, more yield stresses have to be computed with Taylor's model. A compromise between accuracy and computation time must be done.

The size of the interpolation domain can also be linked to these two factors. Indeed, with higher order interpolations, it is possible to use larger domains with the same accuracy. Then, the compromise must be done between small domains with linear interpolation or large domains with a higher order interpolation. Both choices are valid. However, as the goal of our method is to integrate the texture updating, the interpolated domain will have to be updated regularly. Then, small domains with a linear interpolation have been chosen from the point of view of the computation time, no investigation of higher order interpolation has been achieved.

3.6 Continuity between adjacent domains

The *N* boundaries of the domains are defined by one intrinsic coordinate equal to zero. If the interpolations are formulated as polynomials of these coordinates, the values computed on a boundary will be only a function of the *(N-1)* non-zero coordinates. For the adjacent domain limited by the same boundary, the same conclusion will hold. Then, the continuity between the two adjacent domains is fulfilled.
It should be noticed that the continuity between the domains can only be fulfilled when the new domain is the neighbour of the old one (see paragraph 2.8 and Figure 13).

The continuity presented here is of the C_0 type; it ensures the continuity of the interpolated function, i.e. the length of the interpolated stress s^*. Unfortunately, a C_1 continuity is not fulfilled; the continuity of the yield locus normals cannot be obtained between two adjacent domains.

4 *Global yield locus identification*

Fitting the local yield locus parameters consists in its identification on some points of the actual yield locus, which have been computed with Taylor's model. Instead of interpolating only a part of the yield locus into a chosen domain, it can be interesting to fit a classical phenomenological yield locus that locally accurately describes the chosen domain.

The common form of phenomenological yield loci is:

$$f = F(\underline{\sigma}) - \sigma_s^2 = 0 \tag{112}$$

Based on classical formulation, the reliability of these yield models has already been proved. This is a first advantage. A second one concerns all the developments already investigated. For instance, the computation of yield locus normals and stiffness matrices are well known.
Note that equation (112) refers to a scaled yield locus. Only the shape of the yield locus representing the material anisotropy is taken into account. The scaling factor is based on the work hardening (see chapter 2 paragraph 3.6) and its introduction in the formulation is presented in paragraph 7.2.

4.1 Plane formulation

The most simple formulation for the local yield locus is:

$$f = \underline{C}^T \bullet \underline{\sigma} - \sigma_s^2 = 0 \tag{113}$$

It represents the equation of a plane in stress space. The N components of $\underline{C}$, which are the local yield locus parameters, can be determined by identification along the domain limit vectors $\underline{S_i}$:

$$f_i = s_i \cdot \underline{C}^T \bullet \underline{S_i} - \sigma_s^2 = 0 \tag{114}$$

Due to the property of the $\underline{SS_i}$-vectors (see equation (51)), it can be easily checked that the following form of $\underline{C}$ fulfils equation (114):

$$\underline{C} = \sigma_s^2 \cdot \sum_{j=1}^{N} \frac{\underline{\underline{SS_j}}}{s_j} \tag{115}$$

Replacing this value into the local yield locus formulation (equation (113)), one obtains:

$$\begin{aligned} f &= \left(s^* \cdot \underline{d}\right)^T \bullet \left(\sigma_s^2 \cdot \sum_{j=1}^{N} \frac{\underline{\underline{SS_j}}}{s_j} \right) - \sigma_s^2 = 0 \\ \Rightarrow \qquad \frac{1}{s^*} &= \sum_{j=1}^{N} \frac{\underline{d}^T \bullet \underline{\underline{SS_j}}}{s_j} \end{aligned} \tag{116}$$

which is exactly the form of equation (89) of the hyperplanes method. Indeed, these two formulations represent a part of a plane in the N-dimensional stress space.

4.2 Spherical local yield locus

The formulation is:

$$f = \underline{\sigma}^T \bullet \underline{\sigma} - \sigma_s^2 = 0 \tag{117}$$

which can be written:

$$f = \left(s^*\right)^2 \cdot \underline{d}^T \bullet \underline{d} - \sigma_s^2 = 0 \qquad \Rightarrow s^* = \sigma_s \tag{118}$$

This is the von Mises criterion which only requires one yield stress computation. As we expect a good representation of the anisotropy of the material behaviour, this too simple model is not kept.

4.3 Hill's yield locus

The local fitting of a Hill based yield locus for the modelling of a polycrystalline behaviour has already been investigated by Toth et al. (1996).
An anisotropic quadratic criterion is chosen:

$$f = \frac{1}{2} \cdot \underline{\sigma}^T \bullet \underline{\underline{A}} \bullet \underline{\sigma} - \sigma_s^2 = 0 \tag{119}$$

In this formulation, $\underline{\underline{A}}$ is a symmetric matrix containing *N(N+1)/2* components describing the material behaviour. Generally, the $\underline{\underline{A}}$ matrix has a dominant diagonal. A simplified orthotropic version is often used; in the 5-dimensional deviatoric stress space, only 6 (instead of 15) components are non-zero (see Li (1995-1996)).
For the sake of generality and accuracy, the complete version with 15 parameters will be used here.

For the identification of the parameters, the $\underline{\underline{A}}$ matrix will be written:

$$\underline{\underline{A}} = \sum_{i=1}^{N} \sum_{j=1}^{N} C_{kl} \cdot \underline{SS_k} \cdot \underline{SS_l^T} \tag{120}$$

using $\underline{SS_i}$ vectors defined in paragraph 2.3. The knowledge of the parameters C_{kl} is equivalent to the knowledge of the $\underline{\underline{A}}$ matrix. The identification will require *N(N+1)/2* known points to compute the *N(N+1)/2* components of the parameter matrix. The *N* domain limit vectors $\underline{S_i}$ (section 2.2) and the *N(N-1)/2* $\underline{S_{ij}}$ directions (defined in paragraph 3.5) will be used. For the first ones, we obtain:

$$f = \frac{1}{2} \cdot s_i^2 \cdot \underbrace{\underline{S_i}^T \bullet \left(\sum_{i=1}^{N} \sum_{j=1}^{N} C_{kl} \cdot \underline{SS_k} \cdot \underline{SS_l^T} \right) \bullet \underline{S_i}}_{=C_{ii}} - \sigma_s^2 = 0 \tag{121}$$

$$\Rightarrow \qquad C_{ii} = \frac{2 \cdot \sigma_s^2}{s_i^2} \tag{122}$$

For the $\underline{S_{ij}}$ vectors, the following formulation appears:

$$f = \frac{1}{2} \cdot s_{ij}^2 \cdot \underline{S_{ij}}^T \bullet \left(\sum_{i=1}^{N} \sum_{j=1}^{N} C_{kl} \cdot \underline{SS_k} \cdot \underline{SS_l^T} \right) \bullet \underline{S_{ij}} - \sigma_s^2 = 0 \tag{123}$$

with s_{ij} defined as the length of the vector belonging to the plastic yield locus in the direction $\underline{S_{ij}}$ (see section 3.5).
Due to the definition of the $\underline{S_{ij}}$ vectors of equation (103),

$$f = \frac{1}{2} \cdot \frac{s_{ij}^2}{\left(4 - 2 \cdot \beta^2\right)} \cdot \left(\sum_{i=1}^{N} \sum_{j=1}^{N} C_{kl} \cdot \underbrace{\left(\underline{S_i} + \underline{S_j} \right)^T \bullet \underline{SS_k} \cdot \underline{SS_l^T} \bullet \left(\underline{S_i} + \underline{S_j} \right)}_{=\delta_{ik} \cdot \delta_{li} + \delta_{ik} \cdot \delta_{lj} + \delta_{jk} \cdot \delta_{li} + \delta_{jk} \cdot \delta_{lj}} \right) - \sigma_s^2 = 0 \tag{124}$$

$$\Rightarrow \qquad f = \frac{s_{ij}^2}{2 \cdot \left(4 - 2 \cdot \beta^2\right)} \cdot \left(C_{ii} + C_{ij} + C_{ji} + C_{jj} \right) - \sigma_s^2 = 0 \tag{125}$$

$$\Rightarrow \qquad C_{ij} = C_{ji} = \frac{\sigma_s^2 \cdot \left(4 - 2 \cdot \beta^2\right)}{s_{ij}^2} - \frac{\left(C_{ii} + C_{jj}\right)}{2} \tag{126}$$

The formulation of the local yield locus (equation (119)) can be written in the form of an interpolation:

$$f = \frac{1}{2} \cdot \left(s^*\right)^2 \cdot \underline{d}^T \bullet \left(\sum_{i=1}^{N} \sum_{j=1}^{N} C_{kl} \cdot \underline{SS_k} \cdot \underline{SS_l}^T \right) \bullet \underline{d} - \sigma_s^2 = 0 \tag{127}$$

$$\Rightarrow \qquad \frac{1}{\left(s^*\right)^2} = \frac{1}{2 \cdot \sigma_s^2} \cdot \sum_{i=1}^{N} \sum_{j=1}^{N} C_{kl} \cdot \underline{d}^T \bullet \underline{SS_k} \cdot \underline{SS_l}^T \bullet \underline{d} \tag{128}$$

Using the definition of the η-coordinates, this can be written:

$$\frac{1}{\left(s^*\right)^2} = \frac{1}{2 \cdot \sigma_s^2} \cdot \sum_{i=1}^{N} \sum_{j=1}^{N} C_{kl} \cdot \eta_k \cdot \eta_l \tag{129}$$

For regular domains, according to equation (59), the interpolation can be expressed as a function of the intrinsic coordinates:

$$\frac{1}{\left(s^*\right)^2} = \frac{\left(\underline{d}^T \bullet \underline{S_0}\right)^2}{2 \cdot \sigma_s^2 \cdot \cos^2(\vartheta)} \cdot \sum_{i=1}^{N} \sum_{j=1}^{N} C_{kl} \cdot \xi_k \cdot \xi_l \tag{130}$$

This formulation can be compared to the one presented in sections 3.1 to 3.5; two particularities should be noticed:

- the interpolation is quadratic and inverse,
- the η-coordinates are used rather than the intrinsic coordinates. This is similar to the hyperplane interpolation. Note that the constant factor $(1/2\sigma_s^2)$ could be integrated in the constants C_{kl}.

4.4 Tsai's criterion

Hill's model can still be improved be the adjunction of a linear function:

$$f = \underline{C}^T \bullet \underline{\sigma} + \frac{1}{2} \cdot \underline{\sigma}^T \bullet \underline{\underline{A}} \bullet \underline{\sigma} - \sigma_s^2 = 0 \tag{131}$$

In comparison with Hill's model containing $N(N+1)/2$ parameters, this model requires N additional yield stresses computed with Taylor's model. So, in an interpolation domain, beside the N $\underline{S_i}$ and the $N(N-1)/2$ $\underline{S_{ij}}$ directions, N new other directions must be used.
Hill's and Tsai's models will not be further investigated due to the larger number of points on the yield locus to be explored for the identification of the parameters compared to the hyperplanes and the stress-strain interpolation methods. This would induce more calls to Taylor's model when an updating of the current domain occurs.

5 *Normal to the yield locus*

In order to be able to implement any method into a finite element code, the tangent stiffness matrix must be computed. This implies the computation of the normal to the yield locus. The stress integration also requires the computation of the normal to the yield locus. With a

classical analytical yield locus formulation, based on normality rule, the computation of this normal is well known. For the interpolation methods developed in the present work, the computation is presented here.
The normal to the yield locus is the derivative of the yield locus function with respect to the stress vector.
Different formulations of the yield locus can appear depending on the chosen variables, three cases are treated:

- The yield locus is a function of s, the length of the stress vector $\underline{\sigma}$ of direction $\underline{d}$:

$$\frac{\partial F}{\partial \underline{\sigma}} = \frac{\partial s}{\partial \underline{\sigma}} \cdot \frac{\partial F}{\partial s} + \frac{\partial \underline{d}}{\partial \underline{\sigma}} \bullet \frac{\partial F}{\partial \underline{d}} \tag{132}$$

With the use of the definition $\underline{\sigma}=s.\underline{d}$:

$$\begin{aligned} &\underline{\sigma}^T \bullet \underline{\sigma} = s^2 \qquad \Rightarrow \qquad s = \sqrt{\underline{\sigma}^T \bullet \underline{\sigma}} \\ &\Rightarrow \frac{\partial s}{\partial \underline{\sigma}} = \frac{1}{2} \cdot \left(\underline{\sigma}^T \bullet \underline{\sigma} \right)^{-½} \cdot 2 \cdot \underline{\sigma} = \frac{\underline{\sigma}}{s} = \underline{d} \end{aligned} \tag{133}$$

and:

$$\frac{\partial \underline{d}}{\partial \underline{\sigma}} = \frac{\partial \left(\frac{\underline{\sigma}}{s} \right)}{\partial \underline{\sigma}} = \frac{1}{s} \cdot \underline{\underline{I}} - \left(\frac{\underline{\sigma}}{s^2} \right) \cdot \frac{\partial s}{\partial \underline{\sigma}} = \frac{1}{s} \cdot \left(\underline{\underline{I}} - \underline{d} \cdot \underline{d}^T \right) \tag{134}$$

The normal is then:

$$\begin{aligned} \underline{n} &= \frac{\partial F}{\partial \underline{\sigma}} = \underline{d} \cdot \frac{\partial F}{\partial s} + \frac{1}{s} \cdot \left(\underline{\underline{I}} - \underline{d} \cdot \underline{d}^T \right) \bullet \frac{\partial F}{\partial \underline{d}} \\ &= \underline{d} \cdot \left(\frac{\partial F}{\partial s} - \frac{1}{s} \cdot \underline{d}^T \bullet \frac{\partial F}{\partial \underline{d}} \right) + \frac{1}{s} \cdot \frac{\partial F}{\partial \underline{d}} \end{aligned} \tag{135}$$

- If the yield locus is a function of the η-coordinates:

$$\frac{\partial F}{\partial \underline{\sigma}} = \sum_{i=1}^{N} \left(\frac{\partial \eta_i}{\partial \underline{\sigma}} \cdot \frac{\partial F}{\partial \eta_i} \right) \tag{136}$$

With the definition of the η-coordinates given by equation (57):

$$\begin{aligned} &\eta_i = \underline{d}^T \bullet \underline{\underline{SS_i}} \\ &\Rightarrow \frac{\partial \eta_i}{\partial \underline{\sigma}} = \frac{\partial \underline{d}^T}{\partial \underline{\sigma}} \bullet \underline{\underline{SS_i}} = \frac{1}{s} \cdot \left(\underline{\underline{I}} - \underline{d} \cdot \underline{d}^T \right) \bullet \underline{\underline{SS_i}} = \frac{1}{s} \cdot \left(\underline{\underline{SS_i}} - \eta_i \cdot \underline{d} \right) \end{aligned} \tag{137}$$

So,

$$\begin{aligned} \underline{n} &= \frac{\partial F}{\partial \underline{\sigma}} = \frac{1}{s} \cdot \left(\underline{\underline{I}} - \underline{d} \cdot \underline{d}^T \right) \bullet \sum_{i=1}^{N} \left(\underline{\underline{SS_i}} \cdot \frac{\partial F}{\partial \eta_i} \right) \\ &= \frac{1}{s} \cdot \sum_{i=1}^{N} \left(\underline{\underline{SS_i}} \cdot \frac{\partial F}{\partial \eta_i} \right) - \frac{\underline{\underline{d}}}{s} \cdot \sum_{i=1}^{N} \left(\eta_i \cdot \frac{\partial F}{\partial \eta_i} \right) \end{aligned} \tag{138}$$

- If the yield locus is a function of s, the length of the stress vector $\underline{\sigma}$, and of the intrinsic coordinates:

$$\frac{\partial F}{\partial \underline{\sigma}} = \frac{\partial s}{\partial \underline{\sigma}} \cdot \frac{\partial F}{\partial s} + \sum_{i=1}^{N} \left(\frac{\partial \xi_i}{\partial \underline{\sigma}} \cdot \frac{\partial F}{\partial \xi_i} \right) \tag{139}$$

With the use of equation (59) defining the ξ-coordinates:

$$\xi_i = \frac{\eta_i}{\sum_{j=1}^{N} \eta_j} \tag{140}$$

$$\begin{aligned} \Rightarrow \frac{\partial \xi_i}{\partial \underline{\sigma}} &= \frac{\frac{\partial \eta_i}{\partial \underline{\sigma}} - \xi_i \cdot \sum_{j=1}^{N} \frac{\partial \eta_j}{\partial \underline{\sigma}}}{\sum_{j=1}^{N} \eta_j} = \frac{\underline{SS_i} - \eta_i \cdot \underline{d} - \xi_i \cdot \sum_{j=1}^{N} \left(\underline{SS_j} - \eta_j \cdot \underline{d} \right)}{s \cdot \sum_{j=1}^{N} \eta_j} \\ &= \frac{\underline{SS_i} - \xi_i \cdot \sum_{j=1}^{N} \left(\underline{SS_j} \right)}{s \cdot \sum_{j=1}^{N} \eta_j} - \underline{d} \cdot \left(\frac{\xi_i}{s} - \frac{\xi_i \cdot \sum_{j=1}^{N} \eta_j}{s \cdot \sum_{j=1}^{N} \eta_j} \right) = \frac{\underline{SS_i} - \xi_i \cdot \sum_{j=1}^{N} \left(\underline{SS_j} \right)}{s \cdot \sum_{j=1}^{N} \left(\underline{SS_j^T} \bullet \underline{d} \right)} \end{aligned} \tag{141}$$

The yield locus normal can be computed:

$$\underline{n} = \frac{\partial F}{\partial \underline{\sigma}} = \underline{d} \cdot \frac{\partial F}{\partial s} + \frac{1}{s \cdot \sum_{j=1}^{N} \left(\underline{SS_j^T} \bullet \underline{d} \right)} \cdot \sum_{i=1}^{N} \left(\left(\underline{SS_i} - \xi_i \cdot \sum_{j=1}^{N} \left(\underline{SS_j} \right) \right) \cdot \frac{\partial F}{\partial \xi_i} \right) \tag{142}$$

For a regular domain, equation (54) can be used:

$$\begin{aligned} \sum_{j=1}^{N} \left(\underline{SS_j} \right) &= \frac{\underline{S_0}}{\cos(\vartheta)} \\ \Rightarrow \underline{n} &= \underline{d} \cdot \frac{\partial F}{\partial s} + \frac{1}{s \cdot \underline{S_0^T} \bullet \underline{d}} \cdot \sum_{i=1}^{N} \left(\left(\cos(\vartheta) \cdot \underline{SS_i} - \xi_i \cdot \underline{S_0} \right) \cdot \frac{\partial F}{\partial \xi_i} \right) \end{aligned} \tag{143}$$

The computation of the yield locus normal leads to an important problem. From plastic strain rate directions (the domain limit vectors in strain rate space), Taylor's model computes the corresponding stresses (the domain limit vectors in stress space). Then, a local yield locus formulation is used. From this yield locus, using equation (135), (138), (142) or (143), one yield locus normal is computed. The problem is that this direction does not always coincide with the actual plastic strain rate direction according to Taylor's model as the yield locus description is not perfect. Indeed, in associated plasticity, the normal to the yield locus is the direction of the plastic strain rate.
It could be possible to reduce this problem by increasing the number of parameters contained in the interpolation (higher order interpolation,…). However, from a numerical point of view, this solution can be worse than the initial problem: discontinuities between interpolated domains can appear.

Practically, when one stress direction is explored, slightly different ways can be followed for the computation of the corresponding normal:

- The first choice is the use the plastic strain rate associated to the explored stress direction according to Taylor's model. The normality of this plastic strain rate to the local yield locus is not fulfilled. Furthermore, the local yield locus approach has been investigated in order to reduced calls to Taylor's model; it is then not desired to use Taylor's model when the normal to the yield locus is required for the stress integration. Note that Taylor's model computes the stress from the plastic strain rate whereas it should do the opposite for the present problem.
- The second choice consists in using equation (135), (138), (142) or (143) for the computation of the normal to the local yield locus. This method does not require calls to Taylor's model; it fulfils the normality rule. Anyway, it suffers another problem. With a global yield locus approach, the continuity of the surface and the continuity of the normals are always fulfilled. With the local yield locus approach, as already mentioned in paragraph 3.6, the continuity of the yield locus between adjacent domains can be easily fulfilled due to a common interpolation on the boundary. However, the perfect continuity of the yield locus normals cannot be obtained. Consequently, on the boundary between two domains, two yield locus normals can be computed. The first one comes from equation (135), (138), (142) or (143) applied to the first domain; the second one is computed by the same equation but applied to the second domain. Note that these two different normals are only present on the boundary between adjacent domains.
  If the two normals on a boundary are divergent, the stress will tend to be localised on the boundary because all the plastic strain rate directions included between the two normals will correspond to a stress on the boundary. On the other hand, a locally non-convex yield locus corresponds to two convergent normals. This case is more inconvenient and leads to numerical instabilities and convergence problems (see the two-dimensional representation of Figure 15).
- In order to avoid the problems of the 2 previous methods, we finally decided to use a third way for the computation of the normal to the yield locus. The normal is computed by a weighted average of the plastic strain rate present at the domain limit points. The weight factors are the intrinsic coordinates of the explored stress direction. The plastic strain rate at each vertex of the domain is already known because it has been the input of Taylor's model during the construction of the interpolation domain. Our choice avoids the problem of different normals at the boundary between adjacent domains; it is in agreement with Taylor's model at the vertices of the domain. But it is not in agreement with Taylor's model inside the domain and it does not fulfil the normality rule. Paragraph 6.2 presents the application of this method for the hyperplane model.

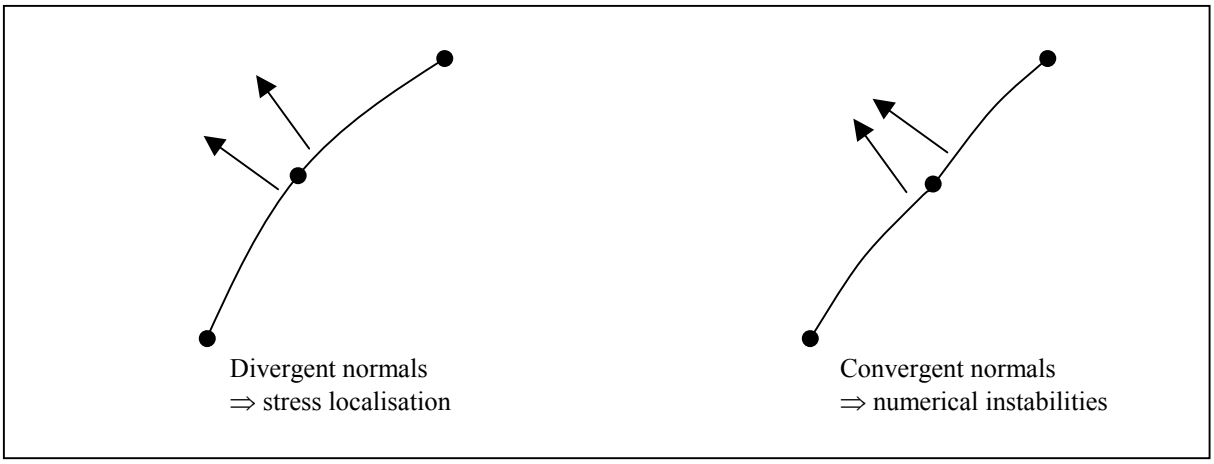

Figure 15: Yield locus normals at the boundary between adjacent domains

6 *Analysis of the hyperplanes method implemented in LAGAMINE code*

The method presented here is equivalent to direct calls to Taylor's model. Indeed, from a plastic strain rate direction, Taylor's model computes the corresponding stress. The interpolated local yield locus approaches also compute the stress from the plastic strain rate direction. The interest of the interpolation method is, in fact, to reduce computation time for plastic strain rate directions close to some already computed directions. We interpolate the results between some points that have been previously computed by Taylor's model.
The first investigated method to interpolate the yield locus between the points computed by Taylor's model is the fitting of an hyperplane on the domain limit yield stresses. This method has already been theoretically described in paragraphs 3.1 and 4.1.

6.1 Description of the interpolated yield locus

Taylor's model is called for 5 directions regularly located in the plastic strain rate space around one central direction according to the method presented in paragraph 2.7. The 5 yield stresses computed by this way can be used to fit an hyperplane.
The hyperplane model developed in practice is a little bit different in the sense that five hyperplanes are always computed simultaneously. In fact, in addition to the five domain limit vectors, the central point is also computed with Taylor's model. Six yield stresses are then available; the five hyperplanes are respectively fitted on the central point and on four of the five domain limit vectors.
This method requires one more point computed with Taylor's model but it is expected to be more accurate. Indeed, five small hyperplanes will better fit a convex surface than one large hyperplane. Figure 16 shows a 3 dimensional representation of the hyperplane model. 3 planes (instead of 5 hyperplanes) are fitted on one central and 3 (instead of 5) domain limit points or stress nodes (according to their definition in section3.1).

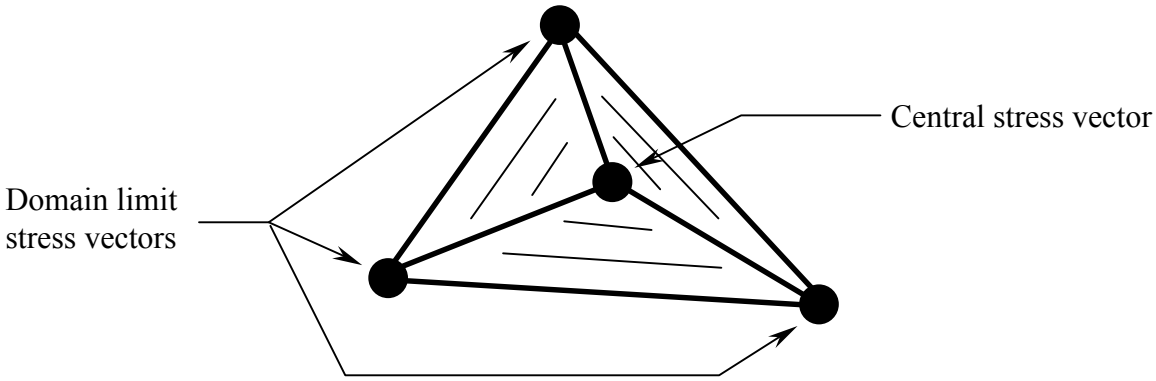

Figure 16: Schematic 3-D representation of the hyperplane model

This local yield locus composed by 5 hyperplanes is used in the finite element code to represent the material behaviour. If, during the finite element simulation, the yield locus needs to be explored along a direction not included in the hyperplanes (corresponding to at least one negative η or ξ-coordinate), a new set of 5 hyperplanes must be computed by Taylor's model. From this explanation, it clearly appears that the size of the local yield locus is an important feature. Small hyperplanes will yield to a more accurate local yield locus due to a reduced interpolation zone between Taylor's points. On the other hand, small hyperplanes will often need to be updated; more calls to Taylor's model will be required, yielding to larger computation time. As the interpolation technique has been introduced to reduce computation trough lower numbers of calls to Taylor's model, a compromise must be accepted on the size of the hyperplanes. The parameter defining the size of the interpolation domain is the angle ϑ described in paragraph 2.2 (equation (47)) and the value that should be used by the finite element code user has been largely investigated in Duchêne et al. (1998), Duchêne et al. (1999) and Duchêne (2000).

6.2 The normals with the hyperplane model

Since the normal to a hyperplane has a constant direction, the normality rule would imply that the plastic strain rate direction is fixed for a particular hyperplane. This assumption is not satisfactory and neglects the available information of the normals at the domain limit directions and the central direction. It also induces sudden plastic strain rate discontinuities when the stress direction perforates a new hyperplane or when an updating occurs. So, we chose to improve the model by using a non constant normal which is computed by interpolation between the normals corresponding to the five domain limit directions defining the current hyperplane (according to the methods presented in paragraph 5 and applied here to the hyperplanes local yield locus model). So, the normality rule is not anymore fulfilled in this model. The advantages of this method are very important for the hyperplane model because a constant normal on a hyperplane would imply several convergence problems in the finite element code. Only one plastic strain rate direction would then correspond to one hyperplane. As the plastic strain rate evolves continuously during a finite element simulation, the current point on the interpolated yield locus would, except particular case, always be on the boundary between two or more hyperplanes. A localisation of the stress at the boundaries would be noticed. Beside the convergence problems, this would lead to a large number of hyperplane updatings and, consequently of calls to Taylor's model. Figure 17 shows a 2 dimensional representation of the yield locus normals. The hyperplanes are straight lines between the

stress nodes. The normals at the stress nodes are the input of Taylor's model, the output being the yield stress. The normals to the hyperplanes are represented; they are constant on one hyperplane and large discontinuities are observed between 2 hyperplanes. At one particular point, the normal $\underline{n}^*$ that must be known for the finite element computation is approximated by the interpolated normal $\underline{n}^*_{inter}$ between the ones at the stress nodes defining the current hyperplane (the interpolation method has already been presented in paragraph 5). This method gives a non constant normal on one hyperplane and it improves the continuity between normals of different hyperplanes. The continuity is exactly fulfilled between the hyperplanes of the same set of 5 but it is not ensured when an updating of the local yield locus occurs.

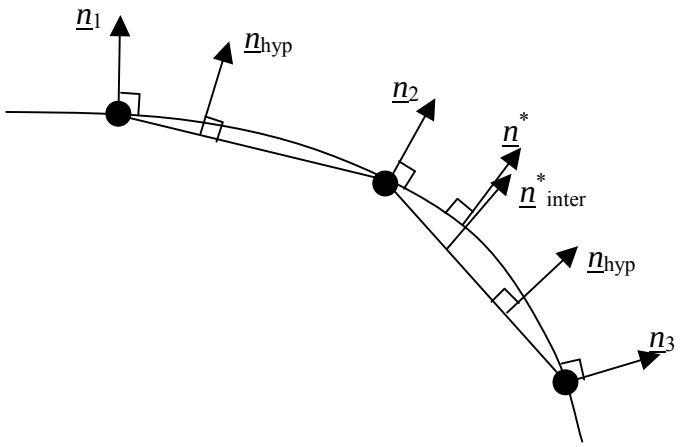

$\underline{n}_i$: Normal to the yield locus at the stress nodes (computed by Taylor's model)
$\underline{n}_{hyp}$: Normal to the hyperplanes
$\underline{n}^*$: Actual normal at one particular point (assuming actual yield locus shape is known)
$\underline{n}^*_{inter}$: Normal interpolated from $\underline{n}_2$ and $\underline{n}_3$ at the particular point

Figure 17: 2-D representation of the yield locus normals with the hyperplane model

6.3 Discontinuities of the interpolated yield locus

In spite of the interpolation of the normal, some convergence problems have been noticed with the use of the hyperplane method. As it has been presented in Duchêne 2000 and Duchêne et al. 1998, these convergence problems are mainly due to a lack of continuity of the interpolated yield locus. Large discontinuities can be observed between adjacent hyperplanes in the case of updating of the interpolation zone (method A in Figure 13). Figure 18 (from Duchêne 2000) shows the resulting interpolated yield locus through a section in the π plane (the plane perpendicular to the hydrostatic direction in the stress space). Exaggeratedly large interpolation domains have been used in order to emphasize the problems that are observed with the hyperplane interpolation method. The size of the domains is defined as ϑ=20° between the central direction and each of the domain limit vectors in the plastic strain rate space (a value of 5° generally gives a good compromise between accuracy and computation time).

The discontinuities between the hyperplanes appear clearly with such large interpolation domains. Between 2 hyperplanes of the same set of 5 hyperplanes defining one domain, the continuity is fulfilled; the hyperplanes are constructed in such a way that this continuity must be obtained (see Figure 16). The orientation of 2 adjacent hyperplanes is however very different and yields to a local yield locus with vertices (for smaller size of the interpolation domains, the resulting yield locus is of course smoother). On the other hand, between adjacent hyperplanes corresponding to different interpolation domains (an updating has occurred according to method A in Figure 13), large discontinuities are generally observed. This is of course at the origin of several convergence problems in the finite element code. In Figure 18, the normal to the yield locus is also presented. It corresponds to the interpolated normals as

computed in the finite element code according to the method presented in paragraph 6.2. In spite of some small discontinuities when an updating occurs, the interpolated normal method is clearly a good improvement with respect to the use of the hyperplane normal.

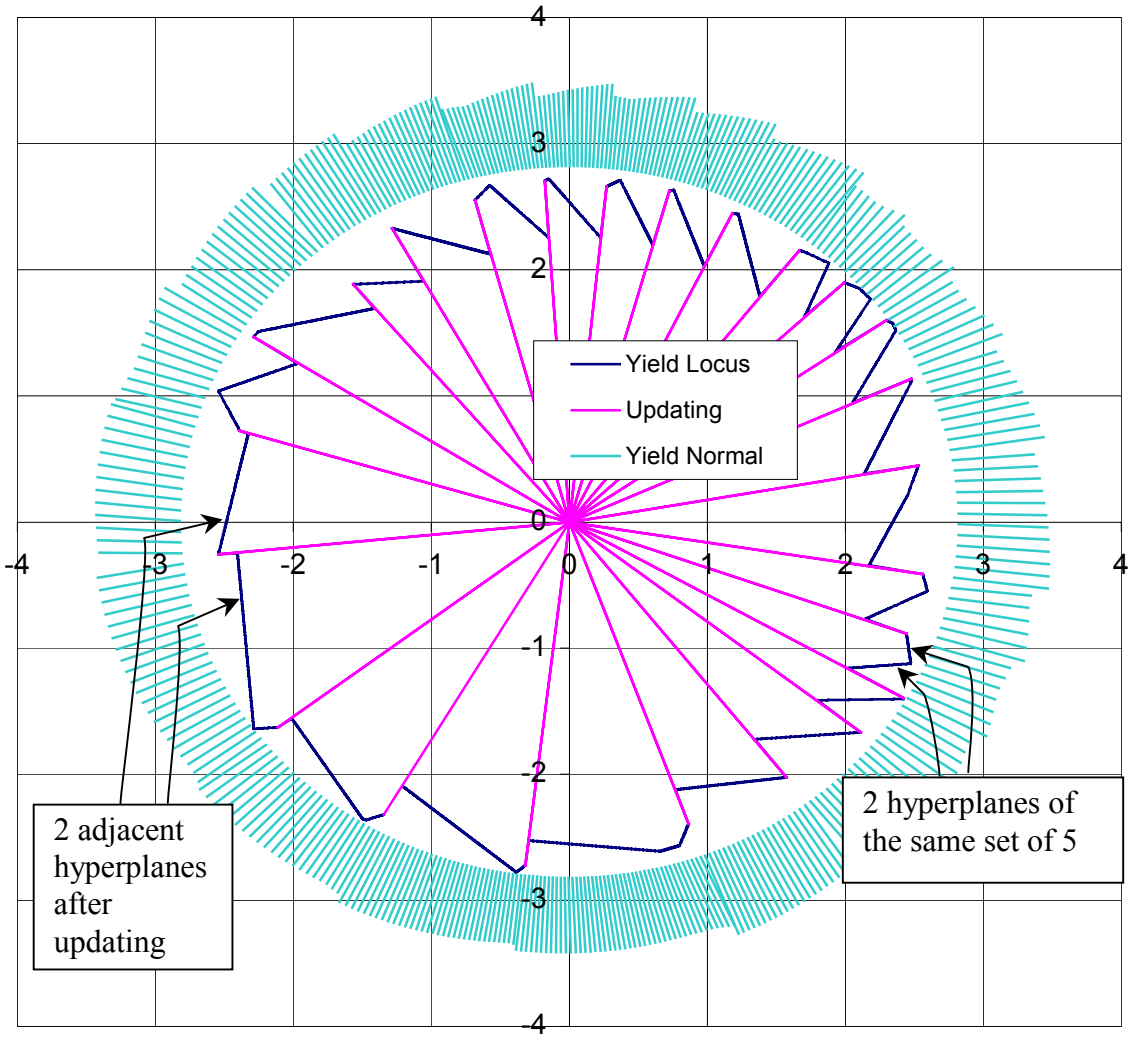

Figure 18: π-section of the interpolated yield locus with the hyperplane method (the size of the domain is fixed to 20°)

6.4 Stress integration

Beside the problems presented above, an excessively high number of calls to Taylor's model due to hyperplane updating has been noticed during finite element simulations. In order to reduce the number of hyperplane updatings as well as computation time, different stress integration schemes have been investigated (see Duchêne (1998)).

A Elastic predictor with 2 embedded loops

First, a stress integration scheme based on the elastic predictor and radial return method proposed by Li (1995-1996) was implemented. This method contains two embedded loops which are described by Figure 19. This stress integration scheme is not well adapted to a local yield locus formulation. The hyperplane yield locus is indeed called inside the first loop. This means that the yield locus is explored along several trial stress directions. A large number of

hyperplane updatings result from this method. The trial stress directions are in fact generally quite different from the initial or the final stress directions.

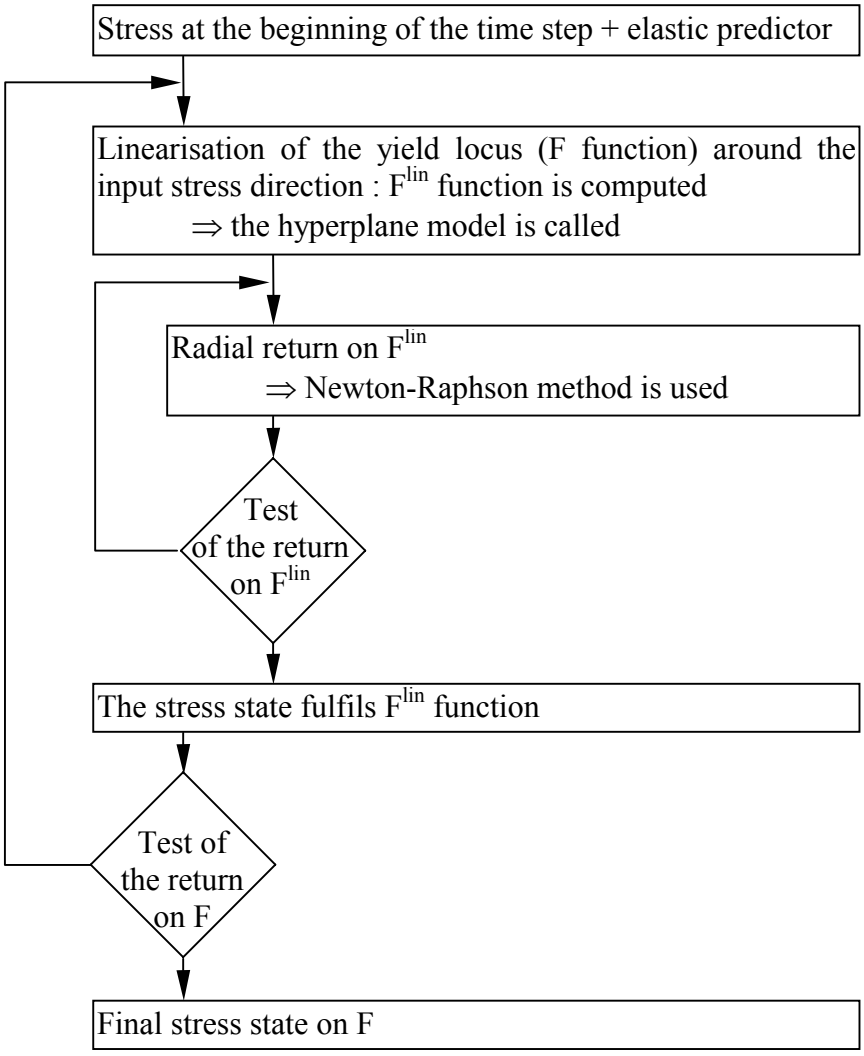

Figure 19: Flow chart of the elastic predictor stress integration method with 2 embedded loops

B ELASTIC PREDICTOR WITH A SINGLE LOOP

In order to reduce computation time, an improved stress integration method with only one loop has been developed. Its flow chart is described by Figure 20. Only one loop is used for the stress integration; an iterative Newton-Raphson procedure has to be used because of the non-linear hardening behaviour. Nevertheless, the hyperplane model is not called during this loop; it is only called at the beginning of the stress integration to compute the yield stress and the yield locus normal for the trial stress direction. It is also called at the end of the stress integration to adjust the length of the final stress state to be sure that it is exactly on the yield locus. A lower number of hyperplane updating is then expected; this yields to a lower number of calls to Taylor's model and then lower computation time. This fact has indeed been reported in Duchêne et al. (1998). Figure 21 graphically represents the same procedure. The

error on the final stress state (the distance between the real final stress state: $\underline{\sigma}_B$ and the computed one: $\underline{\tilde{\sigma}}_B$) can be visualized.

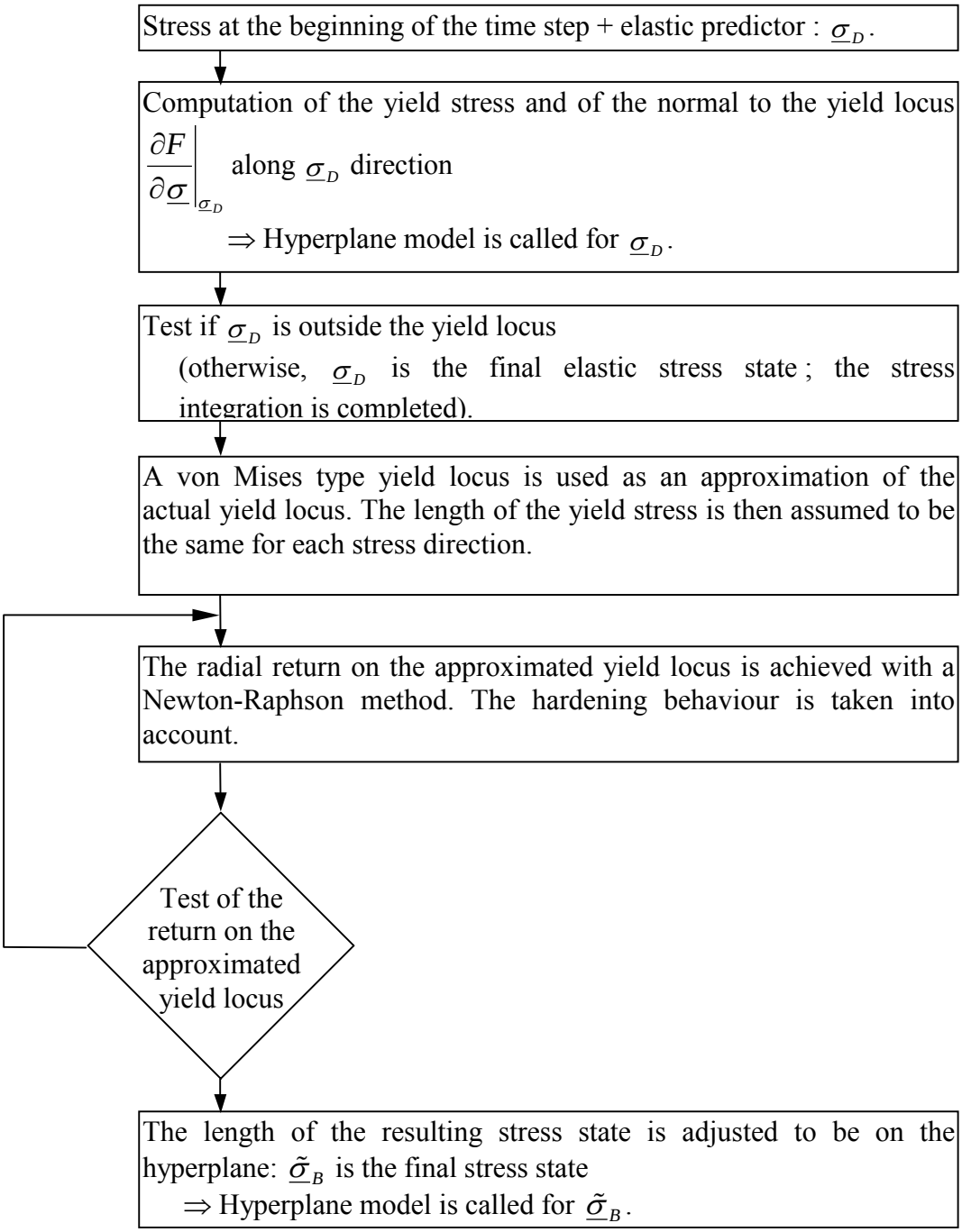

Figure 20: Flow chart of the elastic predictor stress integration scheme with a single loop

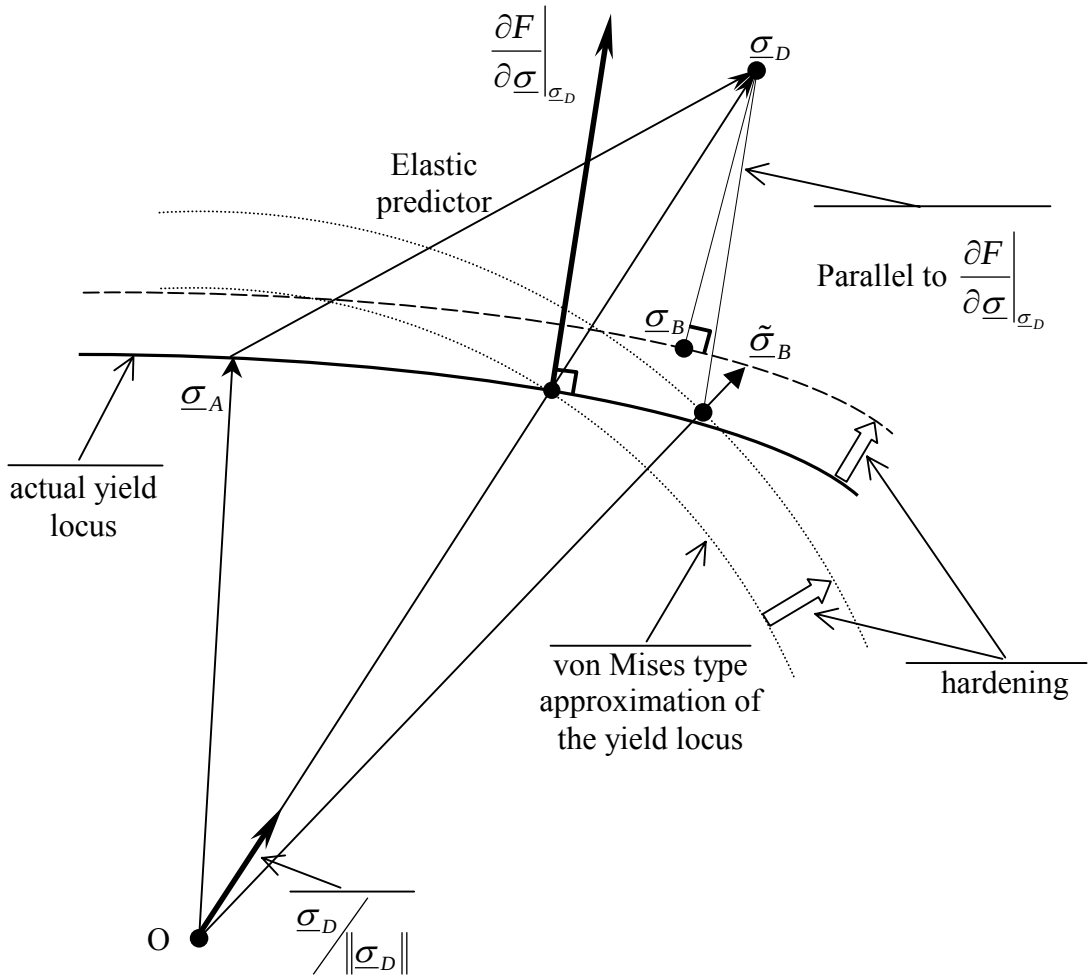

Figure 21: Schematic 2D representation of the elastic predictor stress integration method with a single loop

C PLASTIC PREDICTOR

Finally, as the second stress integration method was not yet completely satisfactory, a third one has been investigated. It was observed that the elastic predictor was supposed to be at the origin of the numerous calls to Taylor's model. Indeed, this predictor is a very bad assumption of the stress at the end of the step. So, during the stress integration scheme, a hyperplane containing the stress with the elastic predictor must be computed; after the radial return, this hyperplane is no more valid and another one must be computed. That is the reason why a new stress integration scheme without elastic predictor has been developed. In this new method, a plastic predictor is investigated. The plastic predictor is indeed expected to be very close to the stress at the end of the time step. The same hyperplane will then hopefully contain both vectors and no updating will be necessary.

The plastic predictor is so close to the final stress that the correction needed to exactly return on the yield locus is small and can be done by a proportional return instead of a radial return without any excessive reduction of accuracy. The computation of the plastic predictor is more complex than the computation of the elastic predictor because the elasto-plastic stiffness matrix is required instead of the elastic matrix. On the other hand, the iterative procedure used

for the radial return is eliminated thanks to the proportional return. Figure 22 presents this third method.

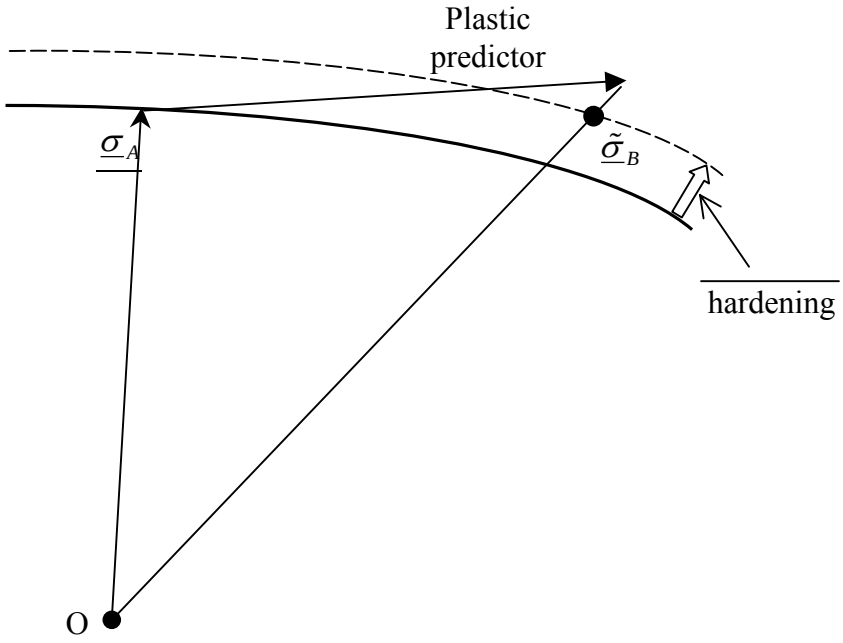

Figure 22: 2-D schematic representation of the plastic predictor stress integration method

The three methods have been compared in Duchêne et al. (1998). The comparison is based on the relative computation time needed to achieve the same tensile test simulation (see details in Duchêne et al. (1998)). Table 1 shows the results with the time unit arbitrarily set to 1 for the fastest case. It can be noticed that two simulations were stopped because they achieved less than a sixteenth of the tensile test simulation in more than three hundred time units. The differences in the simulation speed are mainly due to calls to Taylor's model. They are indeed more numerous when the size of the hyperplanes decreases. It can be seen that the second method of stress integration does not provide a noticeable improvement over the first one while the use of a plastic predictor instead of an elastic one allows us to achieve all tensile tests in more or less the same computation time. Moreover, further investigations showed that the plastic predictor provides a better convergence and is less sensitive to the time step during the tensile test simulations. It can be noticed that the stress integration scheme has a low influence on computation time for large hyperplane sizes (20° and 30°). The same (large) hyperplane can indeed contain the initial, the final and the trial stresses whatever the stress integration path is. On the other hand, the accuracy to represent correctly the actual yield locus is poor for large hyperplane sizes.

Table 1: Comparison of the computation time for a tensile test

Size of the hyperplanes (ϑ)	1°	5°	10°	20°	30°
2 embedded loops elastic predictor	-	98.9	1.40	1.27	1.15
Single loop elastic predictor	-	89.8	1.34	1.22	1.05
Plastic predictor	1.92	1.15	1.14	1.01	1

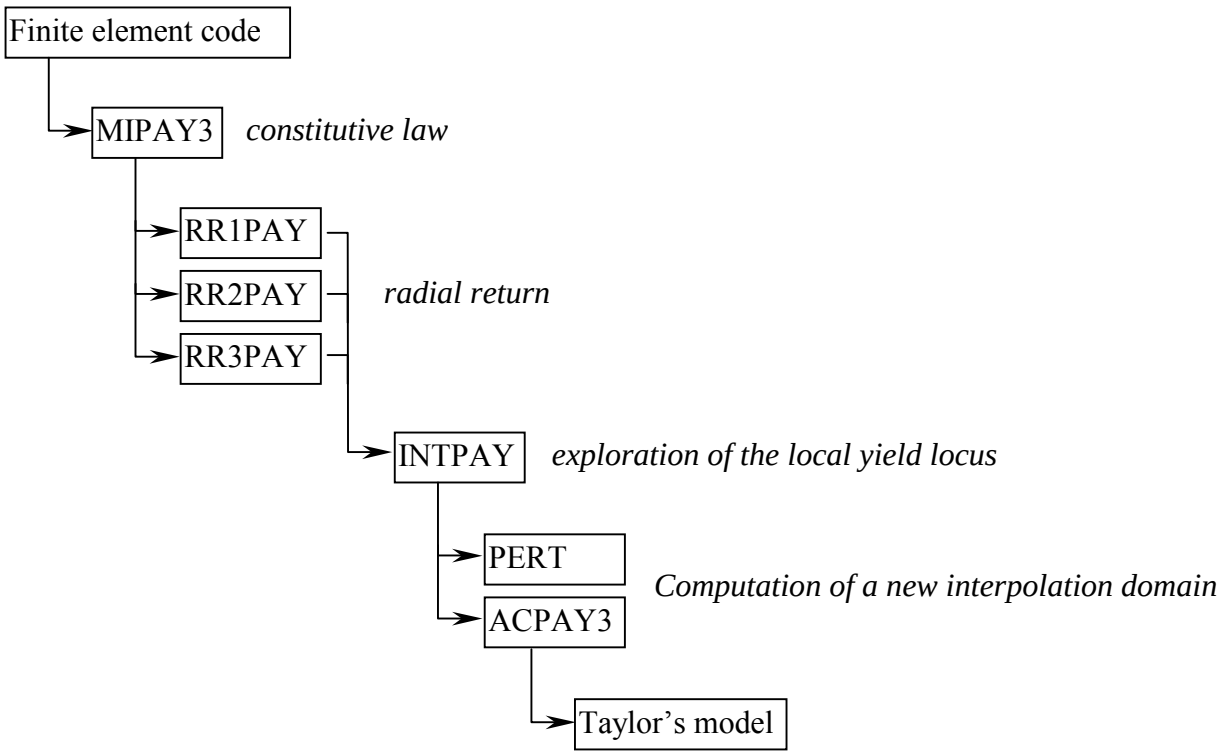

Figure 23: Flow chart of the subroutines for the hyperplane method

6.5 Implementation into the finite element code

Figure 23 presents the flow chart of the subroutines devoted to the hyperplane method which are described hereafter:

- The first one is called PERT. This subroutine computes the 5 domain limit directions in the plastic strain rate space according to the principle of paragraph 2.7. The size of the domain defined as the angle between each domain limit vector and the central vector (angle ϑ of equation (47)) is the most important parameter required by the subroutine and must be chosen by the user. A second important input of the subroutine is of course the central direction around which the domain limit vectors must be located. A regular domain is constructed by the PERT subroutine. This regular domain defines the interpolation domain in the plastic strain rate space (see Radu et al. (1997)).
- The second subroutine is ACPAY3 and is in charge of calls to Taylor's model along the plastic strain rate directions computed by PERT. The scaled yield stresses (the stress nodes) corresponding to particular plastic strain rate directions are determined. Because of the anisotropy of the material which is taken into account through Taylor's model, a non regular domain is constructed by ACPAY3 for the stress vectors.
- MIPAY3 is the main routine of the constitutive law based on the hyperplane interpolation. Its features are similar to any other constitutive law of the Lagamine code; it is in charge of calling all the subroutines linked to the hyperplane method and Taylor's model.
- RR1PAY is the subroutine devoted to the first radial return method (with two embedded loops and an elastic predictor).
- The second radial return method with only one loop and an elastic predictor is implemented in the subroutine RR2PAY.

- The third method with a plastic predictor is in RR3PAY.
  One of these three subroutines is called by MIPAY3 according to the choice of the user.
- The hyperplane interpolation is implemented in the subroutine INTPAY. This subroutine computes the length of the yield stress for any stress direction that is explored according to the current set of hyperplanes. If the stress direction falls outside the current set of hyperplanes, INTPAY calls the PERT and the ACPAY3 subroutines in order to update the set of 5 hyperplanes. It must be noted that the use of the adjacent domain to reduce computation time according to paragraph 2.8 has not been implemented for the hyperplane method. When a new set of 5 hyperplanes is needed, 6 points must be computed with Taylor's model. The INTPAY subroutine is called by MIPAY3 or one of the three radial return subroutines when one point of the yield locus must be found.
- The computation of the stress corresponding to one particular plastic strain rate according to Taylor's model is achieved trough some subroutines that are not further described here.

7 *Analysis of the stress-strain interpolation method implemented in Lagamine code*

In spite of the effort done for the stress integration with the hyperplane model, several numerical problems were not solved. The results of the tensile test presented in paragraph 6.4 are satisfactory with the third integration method. But, for more complex loadings, some convergence problems did not allow us to achieve some particular process simulations (Duchêne (1999 b)). The discontinuities of the interpolated yield locus between hyperplanes and the incompatibility of an hyperplane to correctly model a convex (by definition) yield locus were assumed to be at the origin of these problems. So, another interpolation method has been investigated.
The stress-strain interpolation method has already been presented in paragraph 3.2. It is further developed here for its implementation in the finite element code Lagamine.

7.1 Formulation of the stress-strain interpolation

The interpolation method presented in paragraph 3.2 can be applied on any variable:

$$\varphi = \sum_{i=1}^{N} \varphi_i \cdot \eta_i \tag{144}$$

where the φ_i are point values computed on the interpolation domain limits and η_i are the interpolation functions. φ can either be scalar, vector, tensor… When the domain of validity is updated by method B of Figure 13, the continuity of the interpolated variable is fulfilled; even the direction is continuous when φ is a vector.
The interpolation formulation will be particularised to the finite element application. The local yield locus presented here does not take work hardening into account. The stress vector $\underline{\sigma}$ and the plastic strain rate direction $\underline{u}$ (unit vector) are the two interesting variables. The formulation for $\underline{\sigma}$ and $\underline{u}$ are then:

$$\underline{\sigma} = \sum_{i=1}^{N} \underline{\sigma_i} \cdot \eta_i \tag{145}$$

and

$$\underline{u} = \sum_{i=1}^{N} \underline{u_i} \cdot \eta_i \tag{146}$$

where $\underline{\sigma_i}$ and $\underline{u_i}$ are the values computed at the domain limit points. Taylor's model computes the stress $\underline{\sigma_i}$ corresponding to the plastic strain rate direction $\underline{u_i}$ for the N vertices of the interpolation domain. The coordinates for the stress $\underline{\sigma}^*$ and the plastic strain rate direction $\underline{u}^*$ are computed with:

$$\eta_i = \underline{\sigma\sigma_i^T} \bullet \underline{\sigma}^* \tag{147}$$

$$\eta_i = \underline{uu_i^T} \bullet \underline{u}^* \tag{148}$$

for any stress $\underline{\sigma}^*$ or any plastic strain rate direction $\underline{u}^*$. The $\underline{\sigma\sigma_i}$ and the $\underline{uu_i}$ vectors are equivalent to the $\underline{SS_i}$ vectors defined previously and must fulfil following equations (see also equation (51)):

$$\underline{\sigma\sigma_i^T} \bullet \underline{\sigma_j} = \delta_{ij} \tag{149}$$

$$\underline{uu_i^T} \bullet \underline{u_j} = \delta_{ij} \tag{150}$$

In the finite element analysis, the 5-D deviatoric stress space and the 5-D plastic strain rate direction space correspond to each other. To one point on the yield locus corresponds one stress vector and one plastic strain rate direction. The link between the two spaces is Taylor's model.

Due to this close link between the two spaces, it is assumed that the coordinates computed with equation (147) or (148) are equal if the stress $\underline{\sigma}^*$ physically corresponds to the plastic strain rate direction $\underline{u}^*$. This property is exactly fulfilled on the domain limit directions: the stress $\underline{\sigma_i}$ corresponds to the plastic strain rate direction $\underline{u_i}$ and the coordinates are $\eta_i=1$ and $\eta_j=0$ $(i \neq j)$ in both spaces. Inside the domain, the property is assumed to be extended because it is the best approximation and the most convenient.

If we put together equations (145) and (148), we get:

$$\underline{\sigma} = \sum_{i=1}^{N} \underline{\sigma_i} \cdot \underline{uu_i^T} \bullet \underline{u} \tag{151}$$

or

$$\boxed{\underline{\sigma} = \underline{\underline{C}} \bullet \underline{u}} \tag{152}$$

This equation introducing the $\underline{\underline{C}}$ matrix is a very convenient way to present the interpolation formulation. Just like Taylor's model, equation (152) allows us to compute the yield stress corresponding to any plastic strain rate direction. Furthermore, this formulation is rather faster than Taylor's model as only a matrix multiplication is involved.

The definition of the $\underline{\underline{C}}$ matrix is based on the $\underline{\sigma_i}$ and the $\underline{uu_i}$ vectors which are computed on the interpolation domain vertices with Taylor's model. It should be borne in mind that this $\underline{\underline{C}}$ matrix is only valid inside the interpolation domain for which it has been computed. If a new domain is explored, a new matrix must be computed.

7.2 Work hardening

As presented in chapter 2 paragraph 3.6, an isotropic work hardening is chosen. The local yield locus described by equation (152) should then grow uniformly with its shape remaining constant. The power type hardening behaviour, described by equation (39) in terms of critical resolved shear stress as a function of the accumulated polycrystal induced slip, is introduced into equation (152) to integrate the work hardening into the interpolation formulation:

$$\underline{\sigma} = \tau \cdot \underline{\underline{C}} \bullet \underline{u} \tag{153}$$

Taylor's factor for the polycrystal can be expressed as a function of the interpolation variables. Starting from its definition (equation (33)):

$$\bar{M} = \frac{\underline{\sigma}^T \bullet \underline{u}}{\tau} = \frac{\left(\tau \cdot \underline{\underline{C}} \bullet \underline{u}\right)^T \bullet \underline{u}}{\tau} = \underline{u}^T \bullet \underline{\underline{C}}^T \bullet \underline{u} = \underline{u}^T \bullet \underline{\underline{C}} \bullet \underline{u} \tag{154}$$

Taylor's factor is linked to the microscopic total induced slip through equation (38).

7.3 Tangent stiffness matrix

As this interpolation model has a formulation rather different from classical approaches, the computation of the tangent stiffness matrix is also different. The developments presented hereafter are for the deviatoric part of the stresses and the strains. The hydrostatic part is computed separately and is assumed to have a perfect elastic behaviour.
During a finite element simulation, for a plastic loading, equation (153) representing the yield locus and equation (155) are fulfilled:

$$\frac{\partial \underline{\sigma}}{\partial t} = \underline{\underline{C}}^e \bullet \left(\frac{\partial \underline{\varepsilon}^{tot}}{\partial t} - \frac{\partial \underline{\varepsilon}^p}{\partial t} \right) \tag{155}$$

Equation (155) represents the stress rate and is based on Hooke's law which links the stress and the elastic strain through the elastic matrix $\underline{\underline{C}}^e$. The time derivative must be objective; Jaumann formulation is used.
The derivative of equation (153) yields:

$$\frac{\partial \underline{\sigma}}{\partial t} = \underline{\underline{C}} \bullet \left(\frac{\partial \tau}{\partial t} \cdot \underline{u} + \tau \cdot \frac{\partial \underline{u}}{\partial t} \right) \tag{156}$$

Using equations (155) and (156):

$$\underline{\underline{C}}^e \bullet \left(\frac{\partial \underline{\varepsilon}^{tot}}{\partial t} - \underline{u} \cdot \frac{\partial \varepsilon_{EQ}}{\partial t} \right) = \underline{\underline{C}} \bullet \left(\frac{\partial \tau}{\partial t} \cdot \underline{u} + \tau \cdot \frac{\partial \underline{u}}{\partial t} \right) \tag{157}$$

where the plastic strain rate has been decomposed into its direction $\underline{u}$ and its length, assuming a constant plastic strain rate direction during a time step. Furthermore, the fact that $\underline{u}$ is a unit vector implies that the following property is fulfilled:

$$\underline{u}^T \bullet \frac{\partial \underline{u}}{\partial t} = 0 \tag{158}$$

Equation (157) can then be written:

$$\underline{u}^T \bullet \underline{\underline{C}}^{-1} \bullet \underline{\underline{C}}^e \bullet \frac{\partial \underline{\varepsilon}^{tot}}{\partial t} - \underline{u}^T \bullet \underline{\underline{C}}^{-1} \bullet \underline{\underline{C}}^e \bullet \underline{u} \cdot \frac{\partial \varepsilon_{EQ}}{\partial t} = \frac{\partial \tau}{\partial t} \tag{159}$$

now, taking the derivative of equation (39), we get:

$$\frac{\partial \tau}{\partial t} = n \cdot K \cdot \left(\Gamma^0 + \Gamma\right)^{n-1} \cdot \frac{\partial \Gamma}{\partial t} = \frac{n \cdot \tau}{\left(\Gamma^0 + \Gamma\right)} \cdot \frac{\partial \Gamma}{\partial t} = \frac{n \cdot \tau}{\left(\Gamma^0 + \Gamma\right)} \cdot \bar{M} \cdot \frac{\partial \varepsilon_{EQ}}{\partial t} \tag{160}$$

Then, the equivalent plastic strain rate can be obtained:

$$\frac{\partial \varepsilon_{EQ}}{\partial t} = \frac{\underline{u}^T \bullet \underline{\underline{C}}^{-1} \bullet \underline{\underline{C}}^e \bullet \frac{\partial \underline{\varepsilon}^{tot}}{\partial t}}{\underline{u}^T \bullet \underline{\underline{C}}^{-1} \bullet \underline{\underline{C}}^e \bullet \underline{u} + \frac{n \cdot \tau}{\left(\Gamma^0 + \Gamma\right)} \cdot \bar{M}} \tag{161}$$

Replacing this value in equation (155), the stress evolution can be computed:

$$\frac{\partial \underline{\sigma}}{\partial t} = \underline{\underline{C}}^e \bullet \left(\underline{\underline{I}} - \frac{\underline{u} \cdot \underline{u}^T \bullet \underline{\underline{C}}^{-1} \bullet \underline{\underline{C}}^e}{\underline{u}^T \bullet \underline{\underline{C}}^{-1} \bullet \underline{\underline{C}}^e \bullet \underline{u} + \frac{n \cdot \tau}{\left(\Gamma^0 + \Gamma\right)} \cdot \bar{M}} \right) \bullet \frac{\partial \underline{\varepsilon}^{tot}}{\partial t} \tag{162}$$

The tangent stiffness matrix is then simply:

$$\underline{\underline{C}}^{\tan} = \underline{\underline{C}}^e - \frac{\underline{\underline{C}}^e \bullet \underline{u} \cdot \underline{u}^T \bullet \underline{\underline{C}}^{-1} \bullet \underline{\underline{C}}^e}{\underline{u}^T \bullet \underline{\underline{C}}^{-1} \bullet \underline{\underline{C}}^e \bullet \underline{u} + \frac{n \cdot \tau}{\left(\Gamma^0 + \Gamma\right)} \cdot \bar{M}} \tag{163}$$

This formulation can be simplified if two new vectors are defined:

$$\underline{a} = \underline{\underline{C}}^e \bullet \underline{u} \tag{164}$$

$$\underline{b} = \underline{\underline{C}}^{-T} \bullet \underline{u} \tag{165}$$

Then

$$\underline{\underline{C}}^{\tan} = \underline{\underline{C}}^e - \frac{\underline{a} \cdot \underline{b}^T \bullet \underline{\underline{C}}^e}{\underline{b}^T \bullet \underline{a} + \frac{n \cdot \tau}{\left(\Gamma^0 + \Gamma\right)} \cdot \bar{M}} \tag{166}$$

7.4 Stress integration

The stress at the end of a finite element time step cannot be obtained directly. Several methods with different accuracy levels are presented.

A EXPLICIT FORMULATION

The stress at the end of the time step $\underline{\sigma_B}$ is directly computed from the stress at the beginning of the time step $\underline{\sigma_A}$ with the use of the tangent stiffness matrix:

$$\underline{\sigma_B} = \left(\underline{\underline{I}} + \underline{\underline{\omega}} dt\right) \bullet \underline{\sigma_A} + \underline{\underline{C}}^{\tan} \bullet \Delta \underline{\varepsilon}^{tot} \tag{167}$$

where the first term represents the contribution of the Jaumann derivative. $\underline{\underline{\omega}}$ is the skew-symmetric part of the velocity gradient. Note that, as this formulation is explicit, the tangent stiffness matrix is computed at the beginning of the time step (state *A*).
This is a rather simple formulation, however its accuracy is not so good unless very small time steps are used. In order to reduce the error, this integration can be computed with sub-steps.

B EXPLICIT FORMULATION WITH RADIAL CORRECTION

An improvement of the previous method can easily be achieved. The problem with the previous explicit formulation is that the stress gradually deviates from the exact solution and, consequently, from the yield locus. The explicit method can then be used to compute the stress direction:

$$\underline{\sigma_{approx}} = \left(\underline{\underline{I}} + \underline{\underline{\omega}} dt\right) \bullet \underline{\sigma_A} + \underline{\underline{C}}^{\tan} \bullet \Delta \underline{\varepsilon}^{tot} \tag{168}$$

and a correction will be applied on the stress length:

$$\underline{\sigma_B} = k \cdot \underline{\sigma_{approx}} \tag{169}$$

where the factor k must be such that the stress at the end of the time step belongs to the yield locus. The interpolated yield locus formulation of equation (153) will be applied on the state corresponding to the end of the step:

$$\underline{\sigma_B} = \tau_B \cdot \underline{\underline{C}} \bullet \underline{u_B} \qquad \Rightarrow \underline{u_B} = \underline{\underline{C}}^{-1} \bullet \underline{\sigma_{approx}} \cdot \frac{k}{\tau_B} \tag{170}$$

The final stress lies on the yield locus if the final plastic strain rate direction $\underline{u_B}$ is effectively a unit vector:

$$\underline{u_B^T} \bullet \underline{u_B} = 1 \qquad \Rightarrow k = \frac{\tau_B}{\sqrt{\underline{\sigma_{approx}^T} \bullet \underline{\underline{C}}^{-T} \bullet \underline{\underline{C}}^{-1} \bullet \underline{\sigma_{approx}}}} \tag{171}$$

The influence of the work hardening is assumed to be small; the critical resolved shear stress at the end of the time step τ_B will then be computed explicitly:

$$\tau_B = \tau_A + \left[\frac{\frac{\partial \tau}{\partial t}}{\frac{\partial \varepsilon_{EQ}}{\partial t}}\right]_A \cdot \left[\Delta \varepsilon_{EQ}\right]_A \tag{172}$$

where $[\Delta\varepsilon_{EQ}]_A$ can be computed with a formulation similar to equation (161) applied at the beginning of the time step:

$$\left[\Delta \varepsilon_{EQ}\right]_A = \frac{\underline{u_A^T} \bullet \underline{\underline{C}}^{-1} \bullet \underline{\underline{C}}^{e} \bullet \Delta \underline{\varepsilon}^{tot}}{\underline{u_A^T} \bullet \underline{\underline{C}}^{-1} \bullet \underline{\underline{C}}^{e} \bullet \underline{u_A} + \left[\frac{n \cdot \tau}{\left(\Gamma^0 + \Gamma\right)} \cdot \bar{M}\right]_A} \tag{173}$$

C IMPLICIT FORMULATION

This method does not give a direct formulation for the stress at the end of the time step; an iterative procedure has to be used. However, more accurate results are expected.

The integration of the stress has a formulation close to the one of equation (167):

$$\underline{\sigma_B} = \left(\underline{\underline{I}} + \underline{\underline{\omega}}dt\right) \bullet \underline{\sigma_A} + \underline{\underline{C^e}} \bullet \left(\Delta\underline{\varepsilon^{tot}} - \Delta\underline{\varepsilon^{plastic}}\right) \tag{174}$$

However, the tangent stiffness matrix is no more used because it can only be computed on the basis of information known at the beginning of the time step. As this is not interesting, the elastic matrix is chosen.

The plastic strain increment $\Delta\underline{\varepsilon}^{plastic}$ can be decomposed into its length and its direction. Furthermore, its direction is assumed to be intermediate between the initial and the final plastic strain rate direction:

$$\Delta\underline{\varepsilon^{plastic}} = \Delta\varepsilon_{EQ} \cdot k \cdot \left(\left(1-\psi\right) \cdot \underline{u_A} + \psi \cdot \underline{u_B}\right) \tag{175}$$

The ψ-parameter must be chosen in the interval *[0;1]* and fixes the implicit/explicit ratio. If $\psi=0$, the method is explicit; if $\psi=1$, the method is fully implicit. An intermediate value is generally chosen.

The *k*-coefficient must be such that the intermediate direction computed between $\underline{u}_A$ and $\underline{u}_B$ is a unit vector:

$$k^2 \cdot \left(\left(1-\psi\right) \cdot \underline{u_A} + \psi \cdot \underline{u_B}\right)^T \bullet \left(\left(1-\psi\right) \cdot \underline{u_A} + \psi \cdot \underline{u_B}\right) = 1 \tag{176}$$

$$\Rightarrow \quad k = \frac{1}{\sqrt{1 + 2 \cdot \psi \cdot \left(1-\psi\right) \cdot \left(\underline{u_A^T} \bullet \underline{u_B} - 1\right)}} \tag{177}$$

The stress can be written:

$$\underline{\sigma_B} = \left(\underline{\underline{I}} + \underline{\underline{\omega}}dt\right) \bullet \underline{\sigma_A} + \underline{\underline{C}}^e \bullet \Delta\underline{\varepsilon}^{tot} - \Delta\varepsilon_{EQ} \cdot k \cdot \underline{\underline{C}}^e \bullet \left(\left(1-\psi\right) \cdot \underline{u_A} + \psi \cdot \underline{u_B}\right) \tag{178}$$

In this formulation, two unknowns are present: $\underline{u}_B$ and $\Delta\varepsilon_{EQ}$. Two additional equations are then required in order to be able to compute the stress at the end of the time step. The first one is the yield locus formulation applied on $\underline{\sigma}_B$-$\underline{u}_B$ (equation (153)). The second one expresses that $\underline{u}_B$ is a unit vector. The equation system obtained is not explicit and must be solved with an iterative method. Note that the hardening variable τ_B is computed explicitly according to equations (172) and (173).

7.5 Implementation into the finite element code

This paragraph briefly points out some particularities that have been encountered during the implementation of the constitutive law based on the stress-strain interpolation method.

As this method uses a refined representation of the plastic behaviour, it requires some particularities in its implementation into a finite element code.

A first remark is that it requires large computation time. Indeed, when a new interpolation domain must be computed or when texture updating takes place, Taylor's model is called for each crystallographic orientation of the representative set and this can occur at each integration point of the finite element mesh. As the number of the orientations should not be chosen smaller than 2000 and the number of integration points can also be very high depending on the structure to model, this constitutive law often leads to large computation time.

It should also be noticed that this model requires a lot of disk space and memory storage because it is compulsory to store the 3 Euler angles of each crystallographic orientation.

Furthermore, as the texture evolution can be different from one point to another, it is required to store those orientations for each integration point. In order to achieve the texture updating, as it is presented in chapter 4, the strain history of each integration point must also be stored.
For the interpolation method, the points computed by Taylor's model for each integration point must also be stored and updated each time a new local yield locus is computed.

The constitutive law has been divided into five main subroutines:

- The subroutines ACPAY3 and PERT already used by MIPAY3, are also called for the stress-strain interpolation method. Remember that PERT defines in the strain rate space the 5 domain limit vectors and that ACPAY3 via Taylor's model provides these 5 domain limit vectors in the stress space. The interpolation domain has the same boundaries for both interpolation methods since the domain limit vectors are imposed by PERT. The stress nodes are identical for the hyperplane model.
- The third subroutine is called INTERT. Knowing a stress direction, it achieves the stress interpolation on the basis of the 5 points computed by ACPAY3 according to the method presented in the previous paragraphs. If the actual domain is no more valid due to a stress direction evolution, a new domain must be determined. First, an adjacent domain is investigated according to the method presented in paragraph 2.8. If there is no valid adjacent domain, a completely new domain is computed with 5 new domain limit vectors computed with ACPAY3 along the directions proposed by PERT. INTERT tells if the trial stress is plastic or elastic.
- The fourth subroutine is SEARCHU; it computes the stress at the end of the time step in the elastoplastic case (stress integration).
- The last one is called MINTY3 (for Microscopic INTerpolated Yield locus 3 dimensions). This subroutine is the main part of the constitutive law and uses the 4 other ones to compute the stress at the end of the time step in the general case, the tangent stiffness matrix and the updated state variables. The "3-dimensions" characterise the geometric space associated to solid elements. This law is not available for axisymmetric state, plane strain or plane stress state.
- All the subroutines dedicated to Taylor's model computation are also identical to the ones for the hyperplane method.

The three subroutines INTERT, SEARCHU and MINTY3 are now more detailed as they are directly linked to the stress-strain interpolation method.

A **INTERT**

The input variable is the stress vector that must be compared to the interpolated yield locus. The output will be the ratio of the input stress to the yield stress along the same direction. It is then possible to know whether the input stress in inside, outside or on the yield locus. The corresponding plastic strain rate direction is also computed.
20 working vectors are necessary to achieve the interpolation; they are:

- 5 $\underline{\sigma_i}$ vectors which are the stresses computed by Taylor's model along the 5 domain limit directions,
- 5 $\underline{\sigma\sigma_i}$ vectors used to compute the η-coordinates and determined with equation (51),
- 5 $\underline{u_i}$ vectors which are the plastic strain rate directions corresponding to the 5 $\underline{\sigma_i}$, they define a regular domain in the plastic strain rate space,
- 5 $\underline{uu_i}$ vectors used to compute the η-coordinates for the plastic strain rate vectors.

Generally, and in particular when it is called by MINTY3, this subroutine computes the plastic strain rate direction from the input stress vector. However, the interpolation

formulation is not limited to this operation. The inverse operation can be performed: a stress can be obtained from a particular plastic strain rate direction. The subroutine has been implemented in both cases; the input and the output of the subroutine can be exchanged.

Figure 24 presents the flow chart of the subroutine INTERT. It should be noticed that two successive criteria are used for the updating of the interpolation domain:

- $\Sigma\, \eta_j \leq 0$
- $min\ \eta_j < 0$

Now, if the output plastic strain rate direction is projected on the $\underline{u_0}$ direction, that is the central direction of the domain limit vectors in plastic strain rate space, equations (47) and (56) applied to the plastic strain rates give:

$$\underline{u^{output}} \bullet \underline{u_0} = \left(\sum_j \eta_j \cdot \underline{u_j} \right) \bullet \underline{u_0} = \sum_j \eta_j \cdot \underbrace{\underline{u_j} \bullet \underline{u_0}}_{=\cos\vartheta} \tag{179}$$

$$\Rightarrow \sum_j \eta_j = \frac{\underline{u^{output}} \bullet \underline{u_0}}{\cos\vartheta} \tag{180}$$

The first criterion can be written $\underline{u}^{output} \bullet \underline{u_0} \leq 0$ (because ϑ will always be chosen much small, so $\cos\vartheta$ is positive). If this criterion is fulfilled it means that the output plastic strain rate direction $\underline{u}^{output}$ forms an angle larger than 90° with the direction $\underline{u_0}$, i.e. the direction pointing the middle of the interpolation domain. Obviously, the current part of the yield locus is not valid for the interpolation and must be completely updated. This usually happens if there is a sharp change in the strain path, e.g. unloading, of the considered integration point.

It should be noticed that at the beginning of the simulation, the working vectors $\underline{u_i}$, $\underline{uu_i}$, $\underline{\sigma_i}$, $\underline{\sigma\sigma_i}$ are not yet computed. During the first call to the subroutine INTERT, for any input stress vector, the computed η-coordinates are then all equal to zero. The first updating criterion is then fulfilled and a first interpolation domain is computed.

The second criterion is fulfilled when at least one η-coordinate is negative. This means that the input stress direction is outside the current interpolation domain. This criterion being less strict than the first one, the updating of only one point instead of five according to paragraph 2.8 is tried. It is verified whether an adjacent domain includes the input stress direction.
In order to check the validity of the adjacent domain, the new coordinates η' corresponding to the new domain must be computed. These η'-coordinates are computed without any call to Taylor's model. They are based on the old coordinates and on the properties of the interpolation model. The formulation presented in paragraph 2.8 is used knowing that regular interpolation domains are used in the plastic strain rate space. According to paragraph 2.8, the η and η'-coordinates are equal on the boundary between two adjacent domains. However, the explored point in not necessarily on that boundary; it is indeed expected to be inside the new domain. The property of equal coordinates is then not anymore fulfilled and the new coordinates must be computed.
Once the new coordinates are known, the validity of the adjacent domain can be checked; This means that all the new coordinates must be positive. If the new domain is valid, one new Taylor's point is computed; otherwise, the classical updating technique is used and five new points are computed.

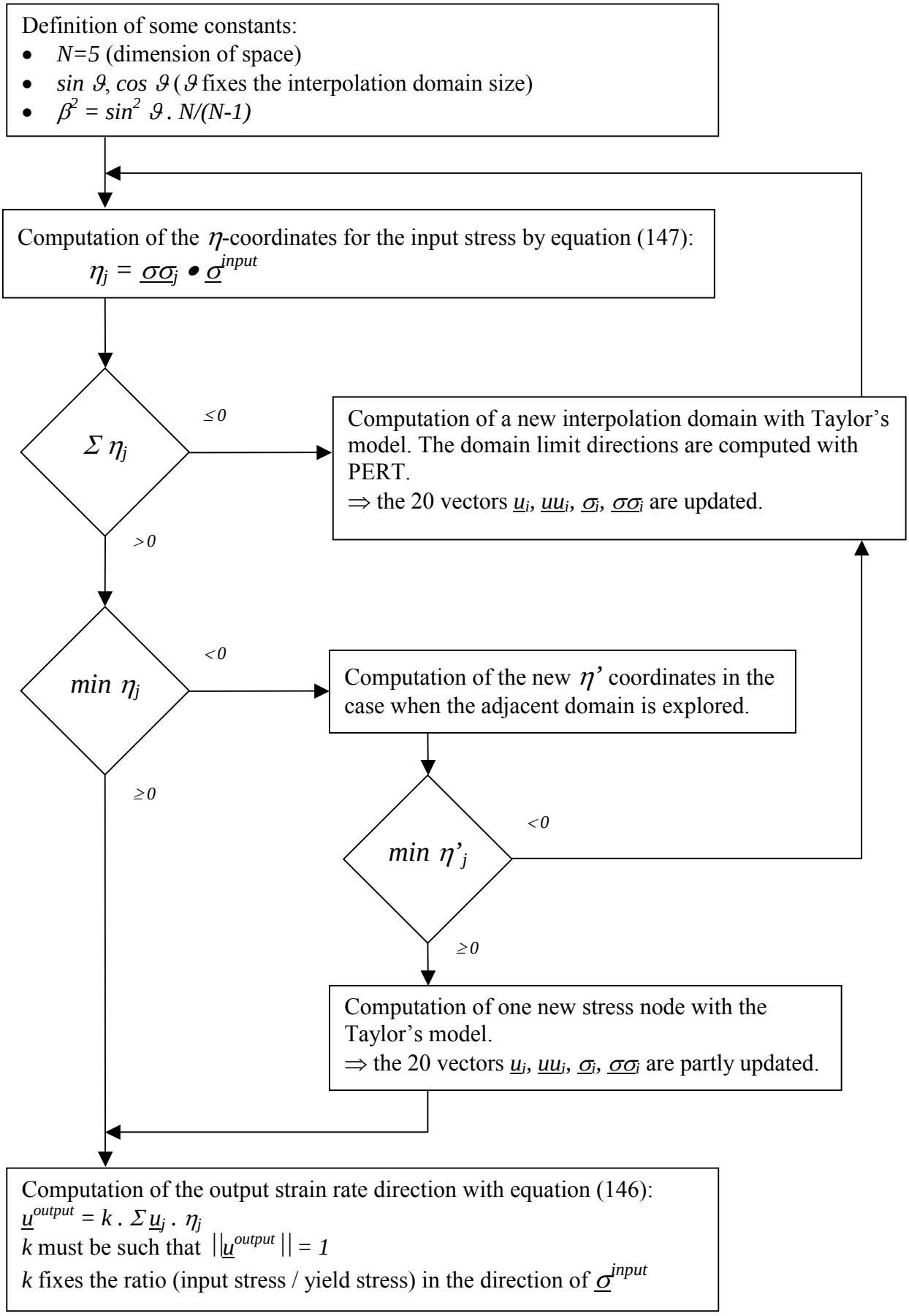

Figure 24: Flow chart of the subroutine INTERT

Whatever one or five new stress nodes are computed, the 20 working vectors must be updated or partly updated. The $\underline{u_i}$ and the $\underline{\sigma_i}$ are computed with subroutine PERT and Taylor's model (through subroutine ACPAY3). The $\underline{uu_i}$ vectors are computed with equation (53) because regular domains are used in the plastic strain rate space. For the $\underline{\sigma\sigma_i}$ vectors, the definition of equation (51) applied to the stresses must be used:

$$\underline{\sigma\sigma_i^T} \bullet \underline{\sigma_j} = \delta_{ij} \tag{181}$$

This equation means that the 5x5 matrix formed by the 5 $\underline{\sigma\sigma_i}$ vectors is the transpose of the inverse of the 5x5 matrix formed by the 5 $\underline{\sigma_i}$ vectors.

In the case of an updating of the 5 stress nodes, INTERT is in charge to call the PERT subroutine so as to form a regular domain in the plastic strain rate space around the explored part of the yield locus. This is not straightforward; indeed, the domain must be located around the input stress direction while PERT needs the central direction in the plastic strain rate space. The plastic strain rate direction corresponding to the input stress would be the best central direction for the construction of the regular domain in plastic strain rate space. The corresponding non regular domain in stress space computed with Taylor's model would of course contain the input stress.

Unfortunately, the plastic strain rate direction corresponding to the input stress is one of the outputs of INTERT and is not known at this stage. An approximation of it can be obtained relatively easily. The η-coordinates of the input stress in the current domain have been computed with equation (147) at the beginning of the subroutine. They have indeed proved that the current domain is not valid (at least one η-coordinate is negative). They can anyway be used to compute the plastic strain rate direction according to equation (146). This operation corresponds to an extrapolation outside the current domain. The accuracy of the extrapolation is in general poor but often sufficient to find an approximation of the central plastic strain rate direction such that the corresponding interpolation domain contains the input stress direction. The accuracy mainly depends on the anisotropy of the material whose yield locus is approximated. If the yield locus is perfectly isotropic (that case would however not require such a complicated yield locus approximation model !), the extrapolation would be perfectly correct. Note that for an isotropic yield locus, the input stress has the same direction as its corresponding plastic strain rate. The input stress direction can then advantageously be used as the central direction for the subroutine PERT. The input stress direction is only used for the computation of the first interpolation domain when the 20 working vectors are not yet defined and, in that case, the extrapolation cannot be achieved.
For most steels that have been modelled with the present yield locus interpolation method, which are not far from isotropic, the extrapolation is good enough to obtain a valid new interpolation domain.
Nevertheless, for the anisotropic steel used for the validation presented in chapter 4, paragraph 4, the extrapolation procedure is not accurate enough and did not allow us to find the updated interpolation domains required to achieve complex simulations. This steel is indeed highly anisotropic with Lankford coefficients ranging from 1.8 to 2.6. For this highly anisotropic steel, the information obtained from the current local yield locus cannot be extrapolated to the adjacent one with enough accuracy. Without the possibility to find new interpolation domains when it is required, the local yield locus method presented here could not be applied.
To avoid this encountered problem, two improvements of the extrapolation method were investigated. The first one consists in increasing the size of the interpolation domain in spite

of the value imposed by the finite element code user when difficulties are encountered in finding a new valid domain; the size being restored to the user's value when the problems are overcome. The probability that a larger domain, even if it is computed with a poor approximation of the central plastic strain rate direction, contains the input stress direction is larger than with a small domain. The second improvement is a numerical damping in the iterative procedure trying to find one valid interpolation domain. It has indeed been noticed that, when the material is strongly anisotropic, the extrapolation method is used iteratively, each iteration leading to an invalid interpolation domain. The oscillations that have been observed on the successive central plastic strain rate directions are eliminated with a numerical damping.
With these two improvements, valid interpolation domains have always been found even for complex simulations and with the anisotropic steel that caused problems.

The last step of INTERT's flow chart is the computation of the output values. It should be noticed that the k factor used to norm the plastic strain rate direction fixes the ratio of the input stress to the yield stress. Indeed, to a unit plastic strain rate direction corresponds a stress length lying on the yield locus. If the input stress is outside the yield locus, the length of the computed plastic strain rate direction is larger than one, and conversely if the input stress is inside the yield locus.

B **SEARCHU**

This subroutine computes the stress and the plastic strain rate direction at the end of the time step (state B) according to the stress integration scheme presented in paragraph 7.4C.
The input variables are the stress vector and the strain rate at the beginning of the time step (state A). The stress increment $\Delta\underline{\sigma}^{elastic}$ based on a purely elastic hypothesis and including Jaumann derivative is also an input to this subroutine.

The stress integration method presented in the flow chart of Figure 25 is based on the implicit method developed in paragraph 7.4C (see equation (178)). An iterative process must be used because the values at the end of the time step are required while their computation is in progress.
The equivalent plastic strain increment $\Delta\varepsilon^{plastic}$ is computed with equation (161) where the current plastic strain rate direction is chosen to be the approximation $\underline{u}_{plastic}$ in the absence of any better value.
The stress at the end of the step is computed according to equation (174) where the plastic strain rate has been decomposed into its length and its direction; this direction is computed with the method proposed by equations (175), (176) and (177).
The first convergence criterion compares the old value of $\underline{u}$ to the new one computed by INTERT according to the current approximation for stress at the end of the time step. The required accuracy is a parameter which is generally fixed to 10^{-5}. This value means that the scalar product of $\underline{u}_B$ and $\underline{u}_{new}$ must be close to 1, with an accuracy of 10^{-5}. This corresponds to an angle between these two directions of:

$$\begin{aligned} &\cos(\alpha) = \underline{u}_{new}^{T} \bullet \underline{u}_B > 1 - 10^{-5} \\ &\Rightarrow \alpha < \arccos(0.99999) = 0.26° \end{aligned} \qquad (182)$$

The second convergence criterion fixes the maximum number of iterations for the computation of the final plastic strain rate. This limit number is fixed by the user. If the limit value is reached, the subroutine is left with a flag indicating that the current step of the finite element simulation must be restarted with a reduced time increment.

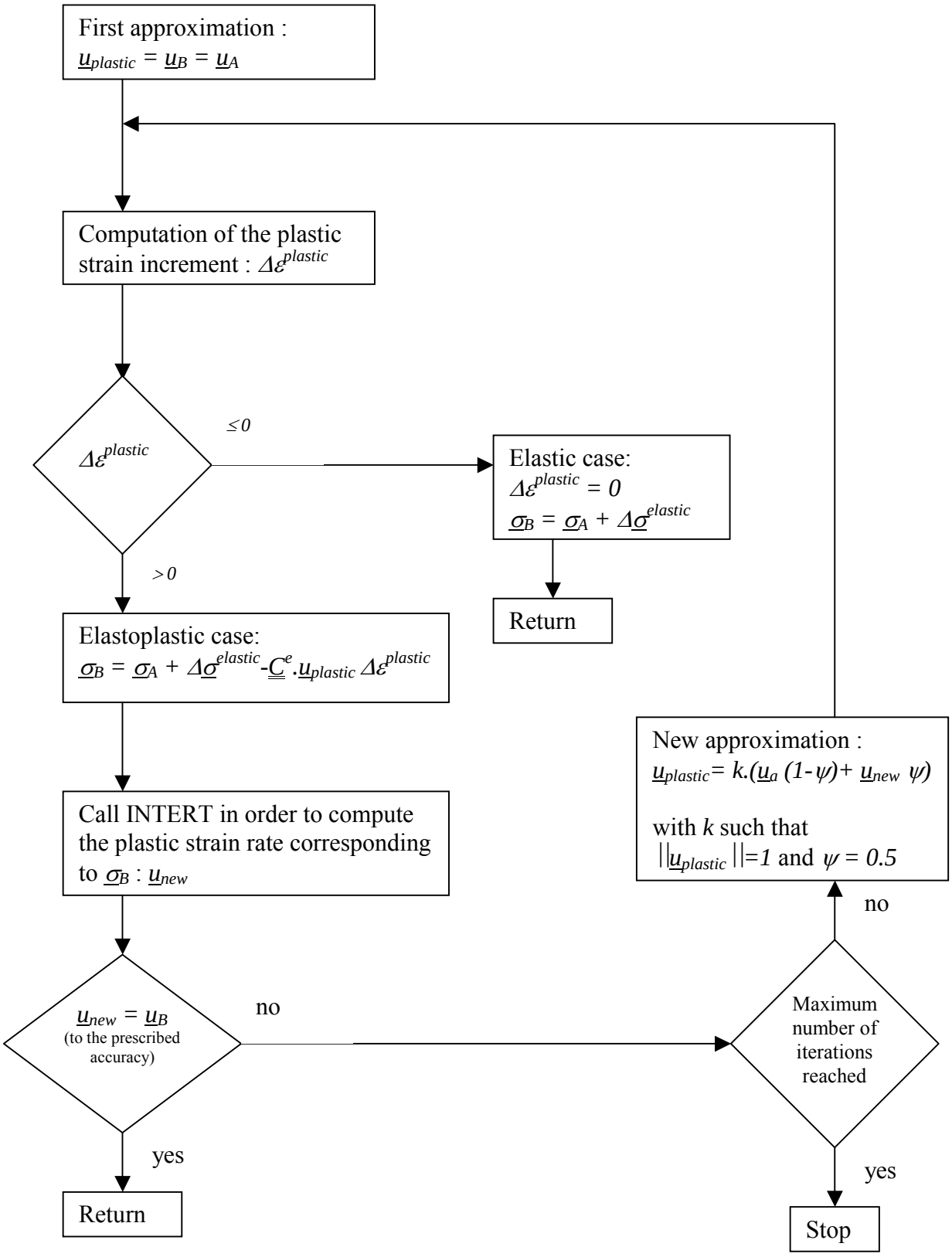

Figure 25: Flow chart of the subroutine SEARCHU

C MINTY3

The subroutine MINTY3 is the constitutive law routine. The input and output parameters are fixed by the finite element code. As any other constitutive law, MINTY3 mainly computes the stress at the end of the time step and the tangent stiffness matrix from the stress at the beginning of the time step and the prescribed velocity gradient. The input parameters are also the state variables at the beginning of the time step, the time increment, the material and the strategy parameters. MINTY3 also computes the state variables at the end of the time step. See also Duchêne (1999 a) for further details.

Figure 26 presents the flow chart of MINTY3. A first remark is that the separation of the hydrostatic and the deviatoric part is a well known method. The hydrostatic part is computed elastically due to the assumption of a constant material volume for the plastic deformations. The deviatoric part is extracted from the 3x3 general form of the stress tensor and transformed into a 5-dimensional vector. The constitutive law and the two subroutines INTERT and SEARCHU only use the vector form for stresses and strains. The conversion is achieved through equation (84).
The work hardening effect described by equation (39) is taken into account during the comparison of the final stress vector $\underline{\sigma}_B$ to the yield locus interpolated with INTERT. It is simply a scalar factor applied on the stress length.

Finally, the last remark is about the tangent stiffness matrix. It is possible to use a perturbation method to calculate it: a small perturbation is successively applied on each component of the velocity gradient. Each column of the tangent stiffness matrix corresponds to one perturbation. The constitutive law is then computed ten times (one without perturbation and nine for the nine perturbations corresponding to the nine components of the velocity gradient) for each integration point and at every time step.
In order to reduce computation time with the elimination of the loop on the perturbations, the analytical tangent matrix can be used. For the elastoplastic case, the formulation is presented in equation (166) where the $\underline{u}$-vector is the one computed by SEARCHU: $\underline{u}_{plastic}$. For the elastic case, SEARCHU is not called; so, $\underline{u}_{plastic}$ is not available. But, in that case, the tangent stiffness matrix is simply the elastic matrix $\underline{\underline{C}}^e$.
It should be noticed that this analytical tangent matrix is computed sub-step per sub-step. The contribution of each sub-step is computed separately. The final tangent stiffness matrix is the mean value of all these contributions. This method allows the tangent stiffness matrix to be almost consistent with the stress integration scheme. The resulting convergence of the finite element code is then improved.

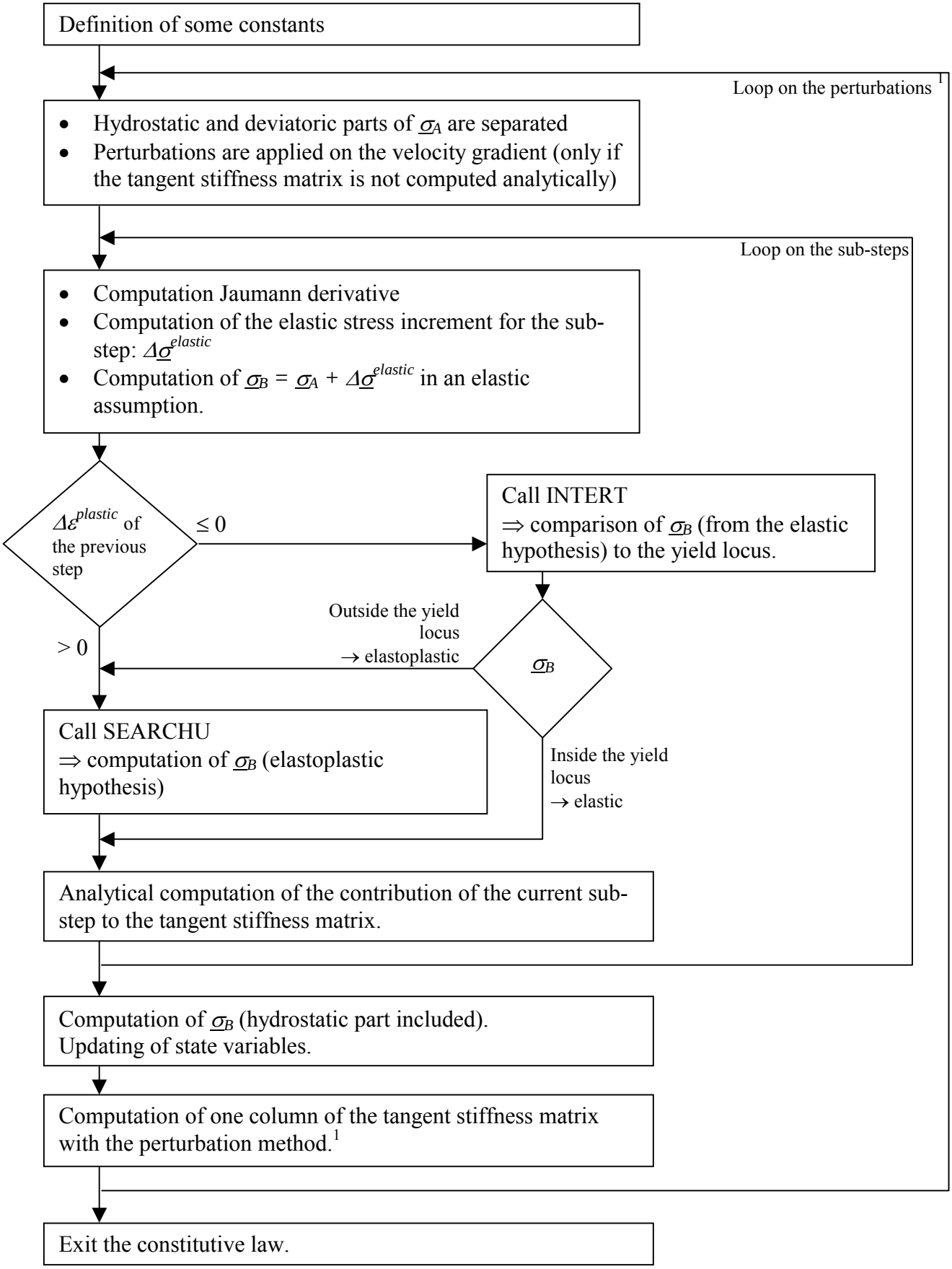

[1] only if the tangent stiffness matrix is not computed analytically

Figure 26: Flow chart of the subroutine MINTY3

8 *Implementation of the texture evolution*

The main goal of the local yield locus approach is to be able to integrate the prediction of the texture evolution during finite element simulations within sensible computation time. The evolution of the texture due to plastic deformation and the mechanical finite element analysis are computed simultaneously. The updating of the material behaviour caused by the evolution of its texture can then be taken into account during the finite element simulation.
Thanks to the local yield locus formulation, only 5 calls to Taylor's model (for one integration point) are required to update the interpolation domain used to represent the yield locus.

Global yield locus approaches have nevertheless been used for the prediction of texture evolution. A first method is to achieve the finite element simulation with a material behaviour based on the initial texture. During this computation, the strain history of some particular points under interest are stored. The texture evolution is computed in a post-processor for the selected points (see Van Bael (1994)). This method is relatively low computation time consuming but it cannot take into account the evolution of the yield locus due to texture updating during the finite element simulation.
This drawback can be partly avoided by achieving the computation of the texture evolution not only at the end of the finite element simulation but at regular time intervals during the computation (see Hoferlin (2001)). This method requires to regularly stop the finite element code in order to compute the evolution of the texture for each integration point according to its strain history. The global yield locus formulation is then fitted according to the new texture. A fitting must be achieved for each integration point as the texture evolves differently from one point to another. The finite element code is started again with the new yield loci. This method needs quite more computation time and memory storage than the previous one. The global yield locus parameters must indeed be stored separately for each integration point. The computation of the texture evolution and the fitting of the global yield locus for each integration point requires a lot of computation time. Generally, when this method is used, only a few texture evolutions are computed during the simulation of one process. Note that unfortunately, reducing computation time by increasing the time interval between successive texture evolution computation may lead to convergence problems in the finite element code due to too abrupt evolution of the material behaviour.

Kalidindi & Anand (1992) have investigated the post-processing technique for the computation of the predicted texture evolution during a closed die forging process of fcc metal. The strain history of some selected points is computed by the finite element code ABAQUS with a simple isotropic plasticity model. The evolution of the crystallographic texture is computed outside the FE code with a Taylor-type polycrystal model on the basis of the deformation gradient history. Comparison of the predicted texture with the experimentally measured ones shows qualitatively a good agreement.
Unfortunately, it has been noted in literature that, even if Taylor's model predicts correctly the texture evolution in a qualitative point of view, it generally overestimates the textures compared to measured ones. Bachu & Kalidindi (1998) have compared quantitatively the measured textures with the ones predicted by Taylor's model. They have also investigated a texture evolution method based on the finite element technique for the rolling process of fcc polycrystals. They observed that the finite element predictions captured well some particular densities of the ODF, which were poorly represented in Taylor's model predictions.
Nakamachi et al. (2002) have also developed an elastic/crystalline viscoplastic finite element model to evaluate the plastic strain induced crystal rotation. A new latent and self-hardening evolution is proposed, with a dislocation density tensor derived from the plastic strain

gradient (see Nakamachi et al. (2002) and Nakamachi & Dong (1997) for further details). They have achieved experimental tests and numerical simulations of aluminium single crystal tensile processes at different orientation from one crystal reference direction. They concluded that their FE analyses can predict the crystal rotations with good accuracy.

Stout et al. (1998) compared the measured texture and the predicted one for a compressive test of an aluminium alloy at elevated temperature. They used a classical Taylor's model with a texture represented by a discrete set of 768 orientations. The influence of the temperature was taken into account trough the use of the $\{1\ \ 1\ \ 0\}$ slip planes in addition to the usual $\{1\ \ 1\ \ 1\}$ planes and with the use of an increased strain-rate sensitivity.

A rather different approach is proposed by Dawson & Boyce (2002). They propose a conservation equation associated with the ODF (with their notation):

$$\frac{\partial A(\mathbf{r},t)}{\partial t} + \nabla A(\mathbf{r},t)\cdot\mathbf{v}(\mathbf{r}) + A(\mathbf{r},t)\nabla\cdot\mathbf{v}(\mathbf{r}) = 0 \tag{183}$$

where $A(\mathbf{r},t)$ is the ODF function of the Rodrigues vector ($\mathbf{r}$) defining the crystal orientation and function of time
$\mathbf{v}(\mathbf{r})$ is the reorientation velocity of crystal with orientation $\mathbf{r}$

The texture evolution is computed by integrating equation (183).

Beside the evolution of the texture, the grain size also evolves during plastic deformation. Takashima & Kopp (2002) focused on the evolution of the grain size during rolling simulations of H beams with a static and dynamic recrystallisation model.
Gahbiche et al. (2002) have also investigated the evolution of the ODF and the grain size during plastic deformation. Four loadings were performed on steel sheets: simple tensile tests, plane strain tensile tests, shearing and deep-drawing under pressure. They have noticed a large influence of the deformation process on the evolution of the texture. On the other hand, the grain size was not much influenced by the deformation process.

8.1 Rotation of the crystal lattice

As presented in chapter 2, Taylor's model allows us to express the velocity gradient as (see equation (1)):

$$\underline{\underline{L}} = \underline{\underline{K}}_S \cdot \dot{\gamma}_S + \underline{\underline{\omega}}^L \tag{184}$$

And the decomposition into the symmetric and skew-symmetric parts gives:

$$\begin{cases} \underline{\underline{\dot{\varepsilon}}} = sym(\underline{\underline{L}}) = \underline{\underline{A}}_S \cdot \dot{\gamma}_S \\ \underline{\underline{\omega}} = skw(\underline{\underline{L}}) = \underbrace{\underline{\underline{Z}}_S \cdot \dot{\gamma}_S}_{=\underline{\underline{\omega}}^P} + \underline{\underline{\omega}}^L \end{cases} \tag{185}$$

According to the first part of equation (185) and other developments of chapter 2, the slip rate of each slip system and the stress state can be computed for the prescribed strain rate. The second part of equation (185) is only useful if texture evolution is investigated.

Equations (184) and (185) are developed in details in a solid mechanics point of view in Van Houtte (1995).

At the level of one crystal, the rotation rates of equation (185) are defined as:

$\underline{\underline{\omega}}$ is the rate of rigid body rotation, it is the skew-symmetric part of the prescribed velocity gradient.

$\underline{\underline{\omega}}^P$ is the plastic spin or the slip induced spin. It represents the rotation due to the dislocation glide.

$\underline{\underline{\omega}}^L$ is the rate of crystal lattice rotation. This rotation is responsible of the evolution of the texture.

Figure 27 graphically represents these rotations.

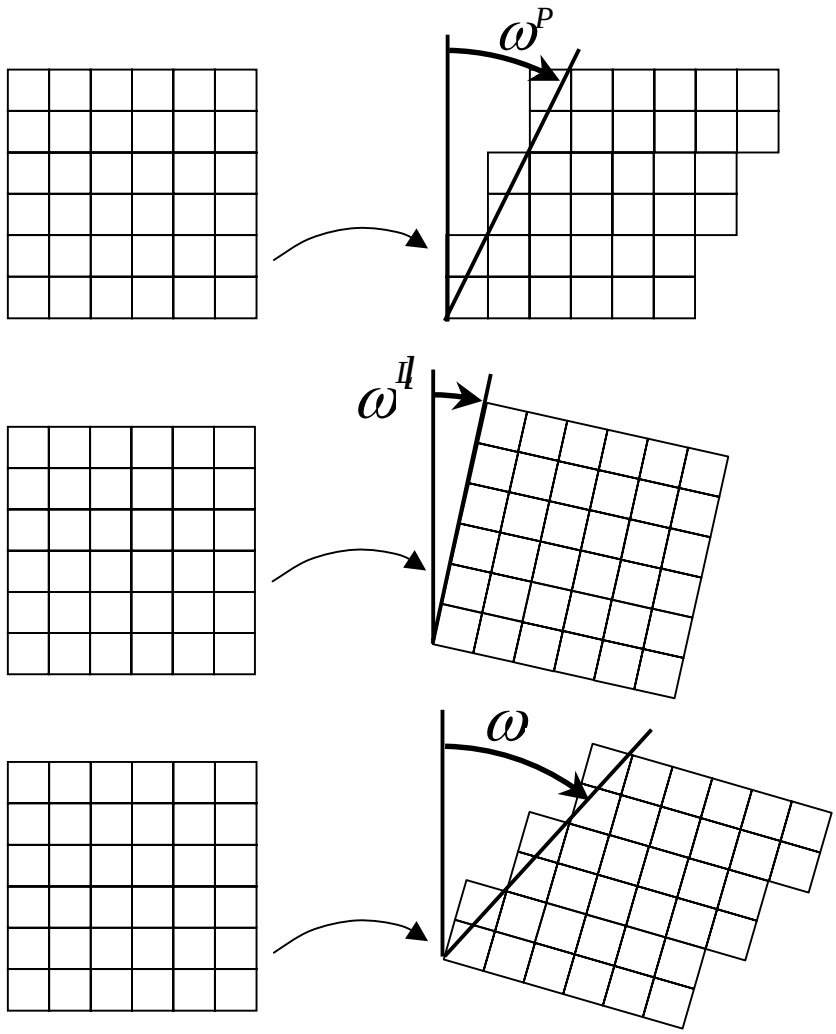

Figure 27: Schematic representation of the crystal rotations

Once the slip rates are computed with the use of Taylor's model, the rate of crystal lattice rotation of each grain (expressed in the crystal reference system) can be obtained by subtracting the slip induced spin from the prescribed rigid body rotation according to equation

(185). This computation must be achieved for each crystal in order to know the new orientation of all the grains. As the strain history (which corresponds to the prescribed velocity gradient) may be different for each integration point, the computation must also be achieved for each integration point of the finite element mesh.
So as to obtain the new Euler angles describing the new crystal orientations, equation (10) must be inverted to extract the three Euler angles when the matrix form of the rotation is known.

8.2 Integration into the FE code

As the strain history is required for the computation of the texture evolution, calls to Taylor's model related to the texture updating cannot be done during the classical finite element flowchart. The actual strain is indeed not known during the loop over the finite elements. Only an approximation of it is known; the iterative procedure of the FE code tends to compute the actual displacements and strains.
That is the reason why a second loop on the elements and on the integration points has been added in order to achieve texture updating only on converged time steps corresponding to a correct strain field.

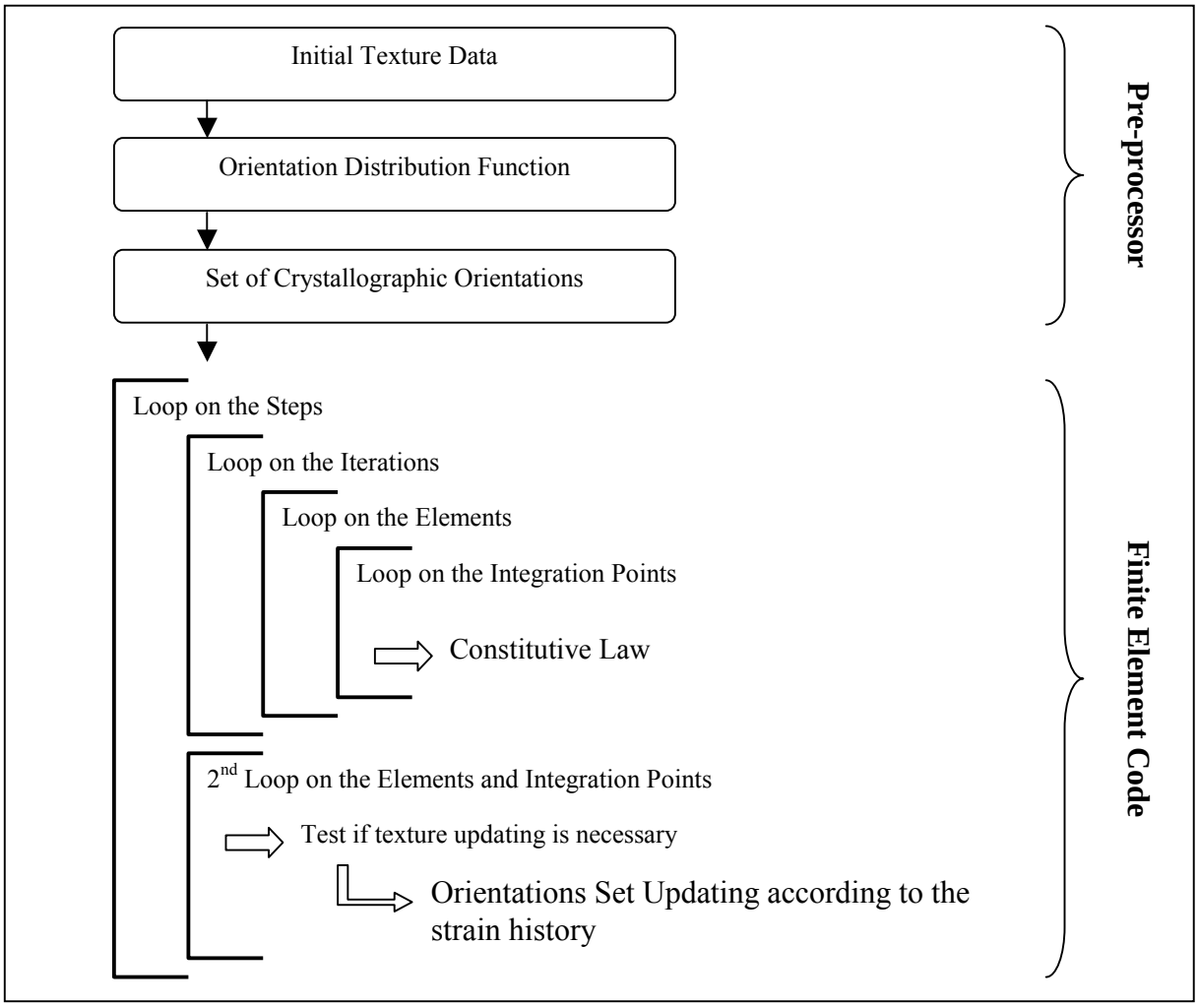

Figure 28: Flowchart of the FE code with texture updating

Figure 28 presents the general flowchart of the finite element code with the second loop on the finite elements and the integration points (the computation of the texture data in the pre-processor is also included). The first loop makes use of the constitutive law based on Taylor's model and the stress-strain interpolation method but without texture updating. Only the stress is computed by Taylor's model; the slip rates and the crystal rotations are not useful at this stage. The second loop on the finite elements calls Taylor's model for the computation of the updated texture with the actual strain history. The stress-strain interpolation is not used here.
A particular subroutine, called ACTUMI, has been added in the second loop on the finite elements. This subroutine achieves the following tasks:

- As it is shown in Figure 28, a test if texture updating is necessary is present. During a large finite element simulation, it is not reasonable to achieve a texture updating for each integration point and at the end of each time step. That is the reason why an updating criterion must be used to reduce computation time. This is still under investigation; at this stage, an updating occurs after a predefined number of time steps. A criterion based on a maximum cumulated plastic strain will also be examined.
- If a texture updating is not to be done at the current time step, ACTUMI stores the actual plastic strain rate (of each integration point) for the future texture updating computation.
- If a texture updating must be achieved, ACTUMI computes the plastic strain rate resulting from the previous time steps (since the last texture updating) and then calls Taylor's model. In the case of texture updating, ACTUMI also resets to zero the stress nodes in order to force the stress-strain interpolation (subroutine INTERT) to compute new interpolation domains, based on the new texture, the next time it is called.

9 *Accuracy and efficiency of the local yield locus approaches*

This paragraph presents three particular investigations of the local yield locus approaches in order to verify the accuracy and the efficiency of the method.
The first investigation tests the accuracy of both local yield locus approaches (the hyperplanes method and the stress-strain interpolation) at the level of one local domain. For the second study, only the stress-strain interpolation method is tested. The stress integration algorithm and the updating of local interpolation domains are checked for different complex strain paths. These two studies are achieved outside the finite element code.
The third investigation particularly tests the efficiency of the local yield locus approach compared to direct calls of the Taylor's model during a finite element simulation.

9.1 Accuracy of the local domain

For one particular domain, the computed yield stresses from both local yield locus approaches are compared to the yield stresses directly computed by Taylor's model. This particular domain is chosen to be centred around the deviatoric biaxial stress state where generally a strong curvature appears in the yield locus. Figure 29 presents a schematic representation of the local domain and explains the method used to perform these accuracy tests. The relative error on the yield stresses between the local approaches and Taylor's model is computed for 21 points: in addition to the central point of the domain (the biaxial state), 20 points are uniformly distributed in the domain. The mean error over these 21 points is also computed. The influence of the local approach: hyperplanes or stress-strain interpolation method is analysed; the influence of the domain size (the angle ϑ is defined by equation (47)) is also checked. The relative errors obtained are presented in Figure 30.

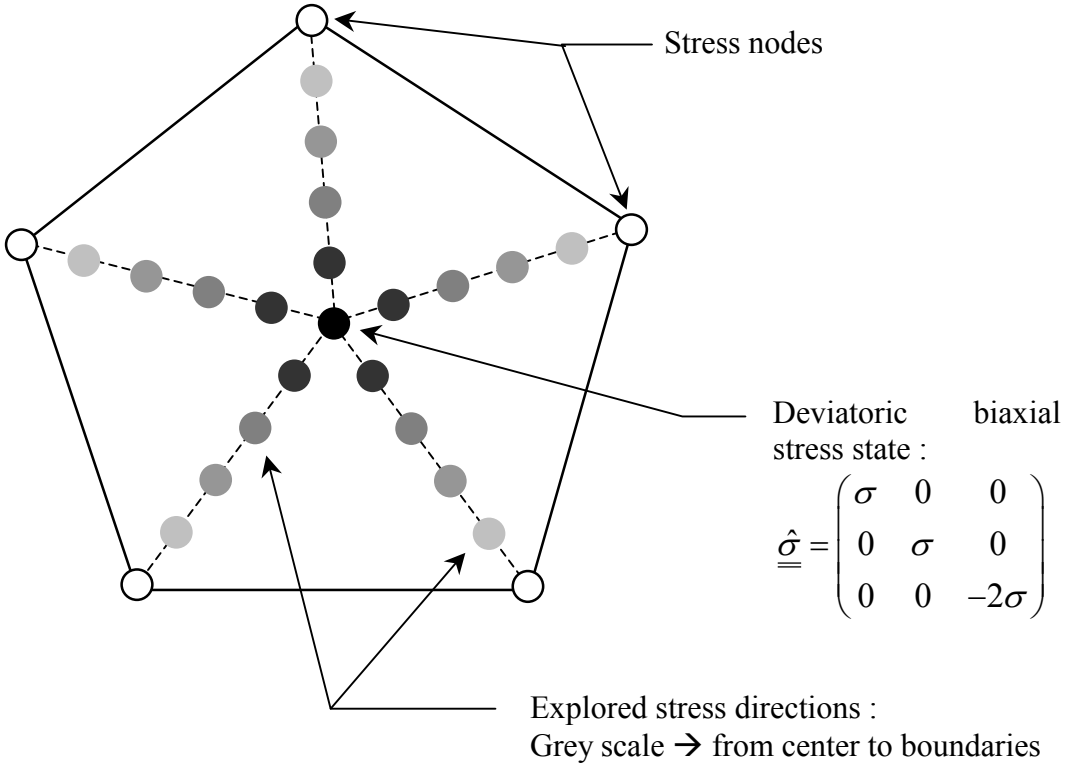

Figure 29: Distribution of the points where the relative error between Taylor's model and the local yield locus approaches is computed

A first remark concerning the computed errors from Taylor's model is, as expected, the large influence of the size of the domain: the mean relative error is almost multiplied by 100 if the size of the domain grows from 1° to 10°. Another important remark is the significant improvement of the accuracy of the stress-strain interpolation method compared to the hyperplanes method. A factor around 10 between the mean relative errors of the two methods is observed when the larger local domains are tested (ϑ=5° and 10°).
It can also be noticed that the relative error strongly varies from one point to another with the stress-strain interpolation method while it is more uniform and exhibits a particular shape with the hyperplanes method. Indeed, for the later method, the error is slightly lower at the centre of the domain (dark grey points) and the edges of the domain (light grey points) compared to other points in mid-grey. This can be explained by the fact that the error is smaller near the stress nodes (where the error is zero by definition) than far from them. Remember that one stress node is present at the centre of the domain with the hyperplanes method (see Figure 16). This point clearly appears in Figure 31.
Another remark not illustrated by Figure 30 where the absolute value of the relative errors are indeed presented, is the fact that the hyperplanes method always underestimates the yield stress. This point can also be clearly understood with Figure 31 and is due to the convexity of the actual yield locus.

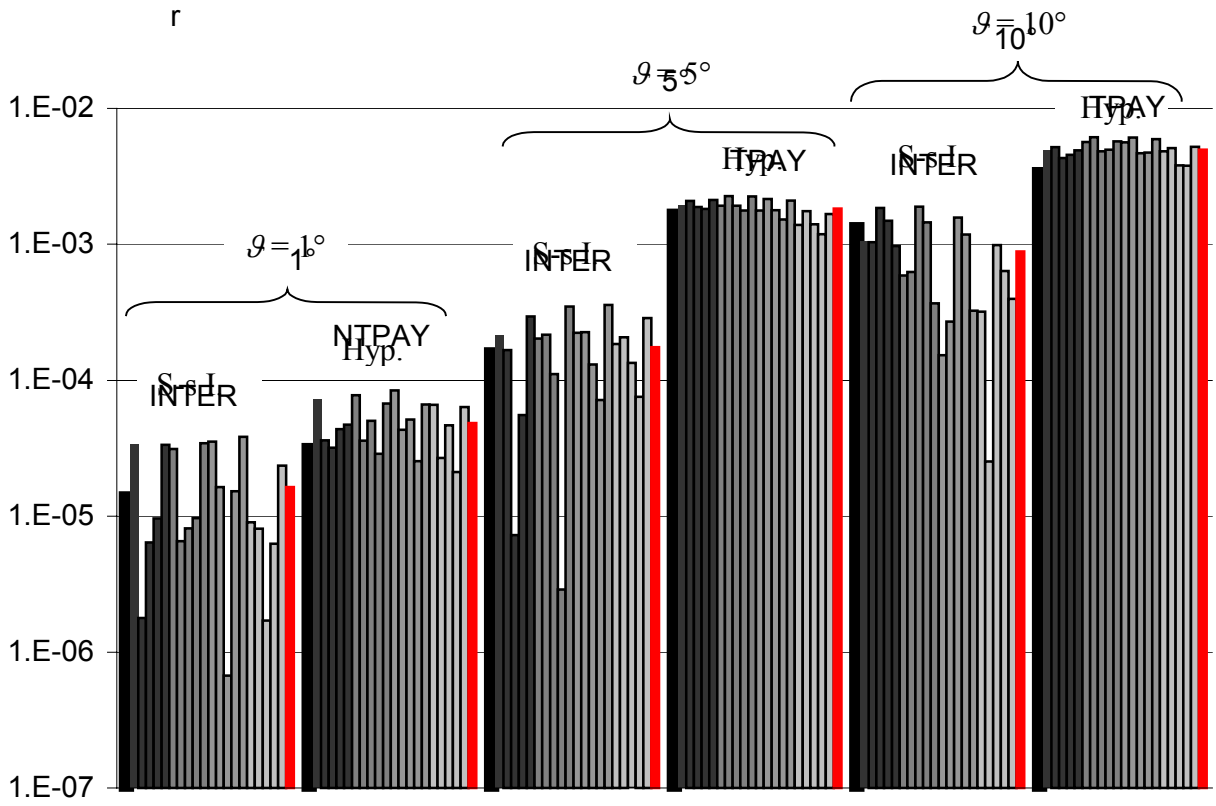

Figure 30: Relative error on the computed stress with respect to Taylor's model, 'S-s I.' stands for stress-strain interpolation and 'Hyp.' means hyperplanes method, grey scale is defined in Figure 29, red line provides mean relative error

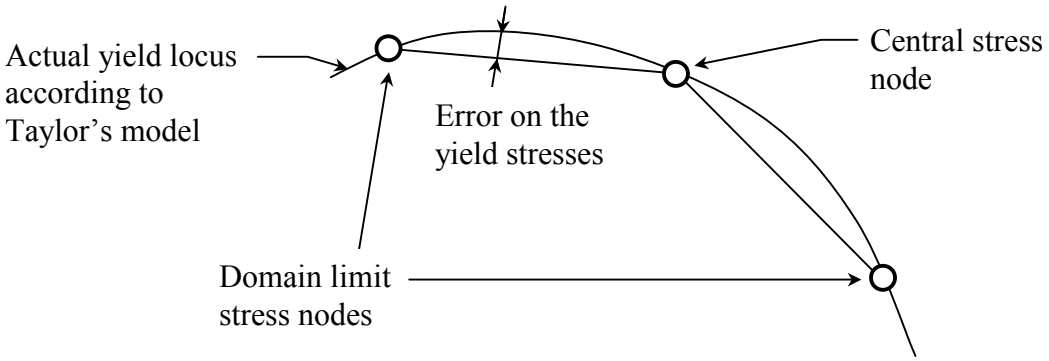

Figure 31: 2D representation of the hyperplanes method: analysis of the method accuracy

9.2 Complex loading paths

Complex loading paths are applied to the stress-strain interpolation method outside the finite element code to test the algorithm of local domain updating. The first complex path is a loading by tensile strain along the X-axis followed by a tensile strain along the Y-axis. The stress evolution computed by the constitutive law is plotted in Figure 32 (the black points linked by straight lines) where the π-section of the yield locus is examined (S_1 and S_2 are the

two first principal stresses). For the present computations, the hardening is eliminated; the size of the local domains is ϑ=8°.

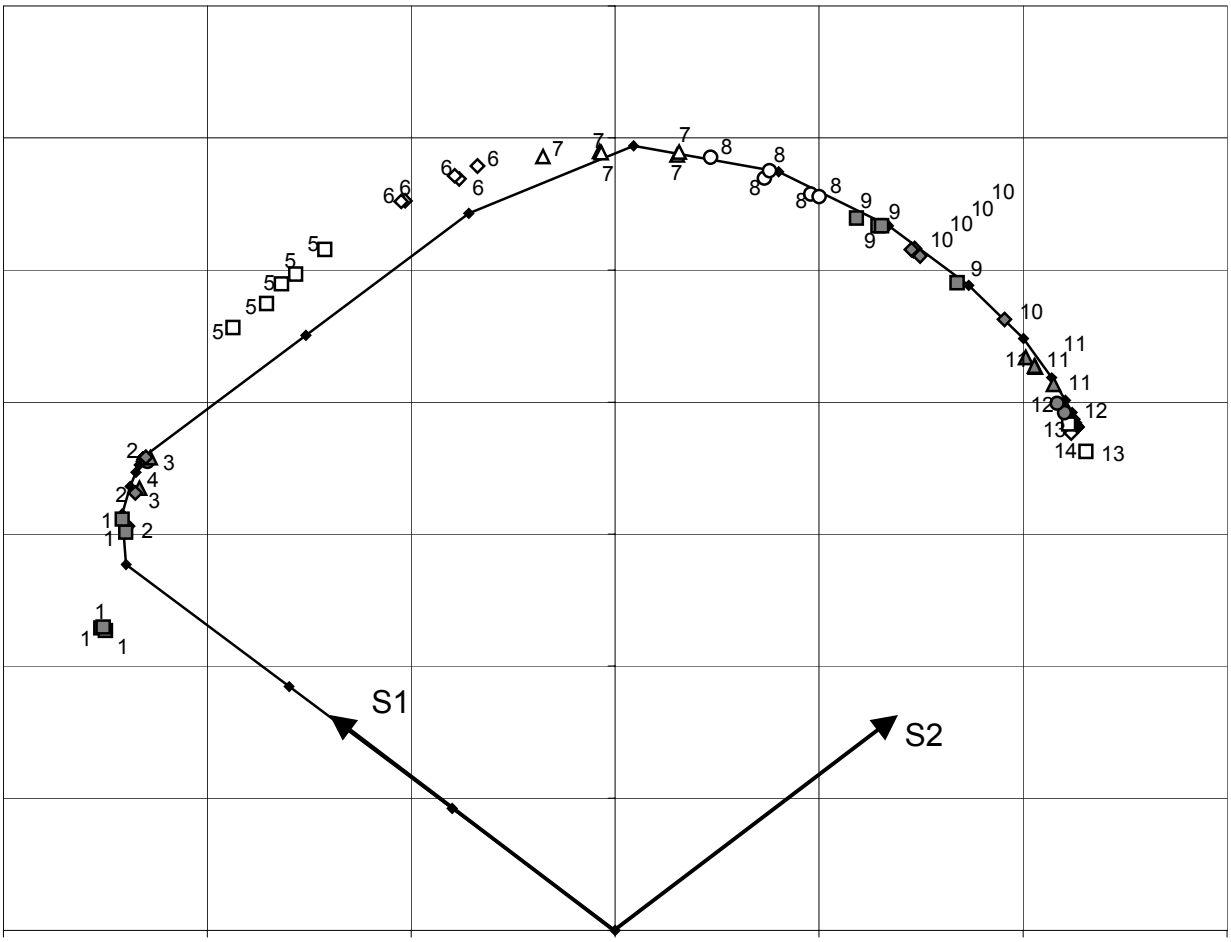

Figure 32: Analysis of the local yield locus approach during a complex loading path: X-axis tensile followed by Y-axis tensile (black line = stress state, symbols = stress nodes, number = local domain succession)

At the beginning of the X-axis tensile test, an increasing elastic stress state is observed. Then, when the yield stress is reached, the plasticity occurs. During the present computations, the total strain rate is imposed while the yield locus is plotted in stress space. As a consequence, due to the anisotropy of the yield locus, the stress state evolves on the yield locus during plastic deformations.

When the Y-axis tensile test is applied, an elastic unloading occurs followed by a reloading on another zone on the yield locus. Here again, the stress state evolves on the yield locus to accommodate the plastic deformations.

In Figure 32, the stress nodes corresponding to the successive local domains are also plotted (the symbols with a number). The numbers indicate the order into which the local domains defined by the corresponding stress nodes are computed. For instance, the 5 stress nodes constituting the 5th domain can clearly be visualised in Figure 32.

When it is possible, the updating of a local domain is achieved with the use of the adjacent domain as presented in paragraph 2.8. For instance, the number 4 only appears once in the graph. This means that the 4th domain explored is adjacent to the 3rd one. When one number appears twice, three or four times, it means that 2, 3 or 4 successive adjacent domains are explored before a satisfactory one is found.

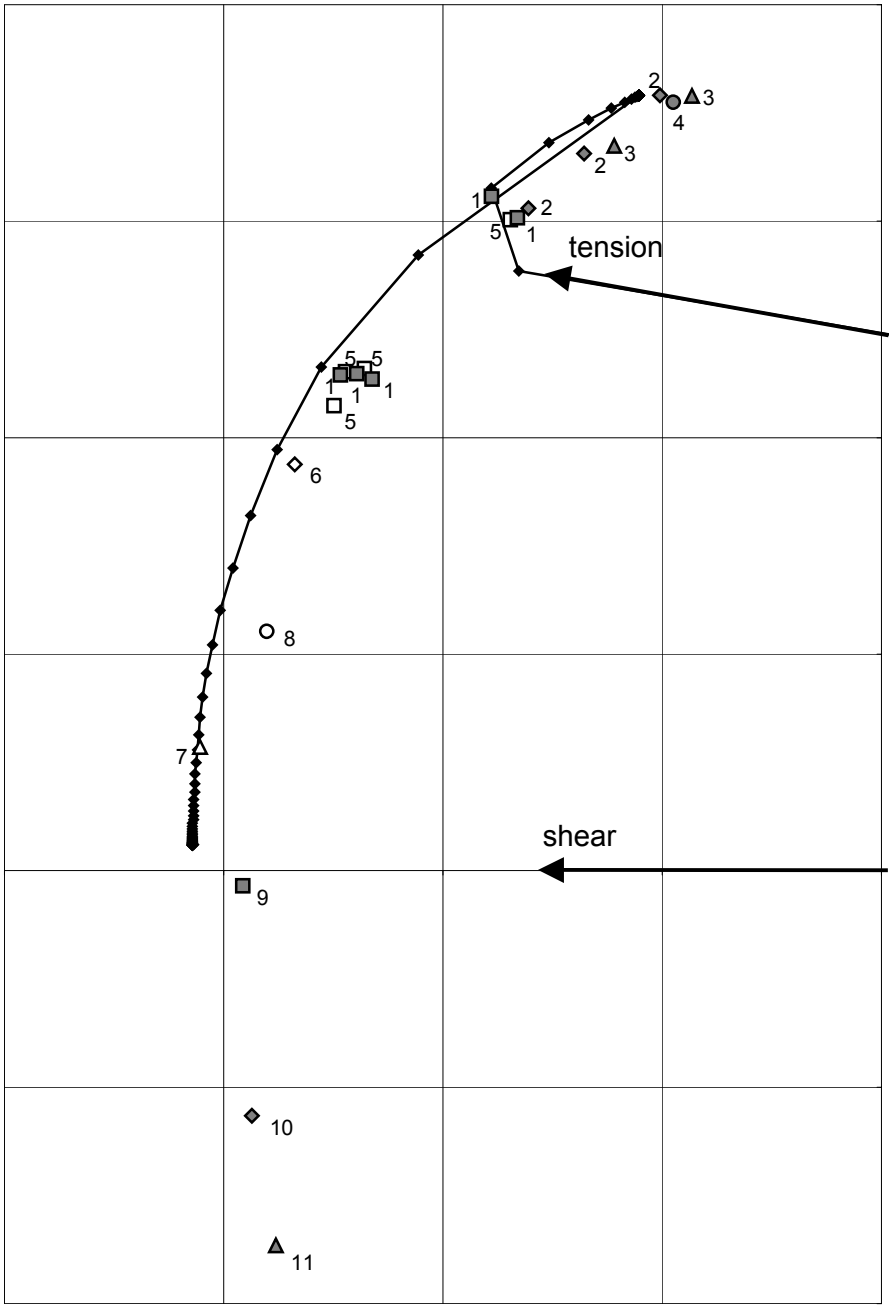

Figure 33: Analysis of the local yield locus approach during a complex loading path: X-axis tensile followed by shearing (black line = stress, identical symbols = one local domain, number = local domain succession)

Figure 33 presents another complex loading path: the X-axis tensile test is now followed by shearing. The π-section of the yield locus is also examined for the visualisation of the stress state evolution. Only a small part of the yield locus including tension and shear is plotted in Figure 33. An equivalent behaviour of the model is observed.
With the local yield locus approach, the representation of the yield locus is based on the stress nodes. In Figure 33, it seems however that the stress state evolves outside the limit defined by the stress nodes. This effect is due to the projection of the stress nodes in the π-section which

reduces their apparent amplitude. The computed stress is closer to the π-section; its amplitude is less influenced by the projection.

9.3 Efficiency of the local yield locus approach

The expected reduction of the computation time thanks to the local yield locus approach (the stress-strain interpolation method is examined) can be estimated by analysing the number of calls to the main subroutines linked to the implemented method. The deep drawing finite element simulations presented in chapter 4 paragraph 4 are tested. The size of the local domains is $\vartheta = 5°$.
The influence of the computation of the texture evolution on the computation time has also been analysed.
The computation time and the number of calls to texture related subroutines are presented in Table 2.

Table 2: Influence of the texture updating on computation time

	Calls to Taylor's model	Calls to ACTUMI	Calls to INTERT	Calls to MINTY3	Computation time
S-s I. Without texture updating	475 539	0	75 202 434	3 692 574	≈29 hours
S-s I. With texture updating	1 944 712	1 440 072	120 603 774	5 961 006	≈115 hours

For the case without texture updating, the number of calls to the constitutive law (subroutine MINTY3) is the total number of iterations during the finite element computation multiplied by the number of elements of the mesh (531 for this example). The number of calls to INTERT depends on the number of sub-steps imposed by the user and on the convergence of the stress integration scheme. Each time INTERT is called, the yield locus is explored. Note that Taylor's model is called only once for about **158** yield locus exploration. This factor constitutes the gain observed with the stress-strain interpolation method when the texture is not updated. The ACTUMI subroutine is not called if the texture is not to be updated.

For the case with texture updating, the ACTUMI subroutine is called for each element at each time step (531 elements multiplied by 2712 time step to perform the simulation). The updating criterion in ACTUMI states that the texture is updated every 10 time steps. 271 texture updatings are then performed during the finite element simulation. So, on the 1944712 calls to Taylor's model, 143901 (271 multiplied by 531 elements) are necessary for the computation of the updated texture. When a texture updating occurs, 5 new stress nodes are expected to be computed (143901 multiplied by 5 gives 719505 calls to Taylor's model). Finally, 863406 (143901 + 719505) calls to Taylor's model are directly linked to the texture updating. Globally, Taylor's model is called once for **62** (instead of the value of 158 obtained above) calls to INTERT. The gain of our method is lower if the texture evolution is desired. The increased number of calls to the subroutine MINTY3 is not directly linked to the texture updating but to an evolved behaviour of the material yielding to convergence problems (54% more iterations).
Finally, the computation time is multiplied by almost 4.

Chapter 4: Validation

1 *Introduction*

This chapter is dedicated to the validation of the local yield locus approach and more particularly the stress-strain interpolation method that we have developed. Three academic validations are presented: simulation of rolling with one finite element, investigations concerning the Swift effect and comparison of the compressive and torsional behaviour of isotropic material.
Two deep drawing processes with different steel grades are then investigated. The influence of the anisotropy of the steel sheets is largely focussed on.

2 *Academic validations*

2.1 Rolling simulation

The rolling process is simply modelled by one three-dimensional finite element in plane strain state as shown in Figure 34. The compressive force applied in direction *z* produces an expansion in direction *x* as the displacements in direction *y* are prevented.
The initial texture, represented by a discrete set of 2000 crystal orientations, is isotropic. The finite element is compressed until a height reduction factor of two is reached. It represents a 69% rolling reduction. Both bcc and fcc materials are simulated with an arbitrary but identical hardening law. For each material, two simulations are performed, one with texture updating at each time step and one with the initial texture.

The final texture computed by the simulations with texture updating exhibits a typical rolling texture. For the bcc material (see Figure 35), the ODF maximum is 11.9 times the random texture level and is located at $\varphi_1 = 25°, \Phi = 50°, \varphi_2 = 55°$. For the fcc material (see Figure 36), the ODF maximum is 14.7 at $\varphi_1 = 40°,\ \Phi = 70°,\ \varphi_2 = 20°$.

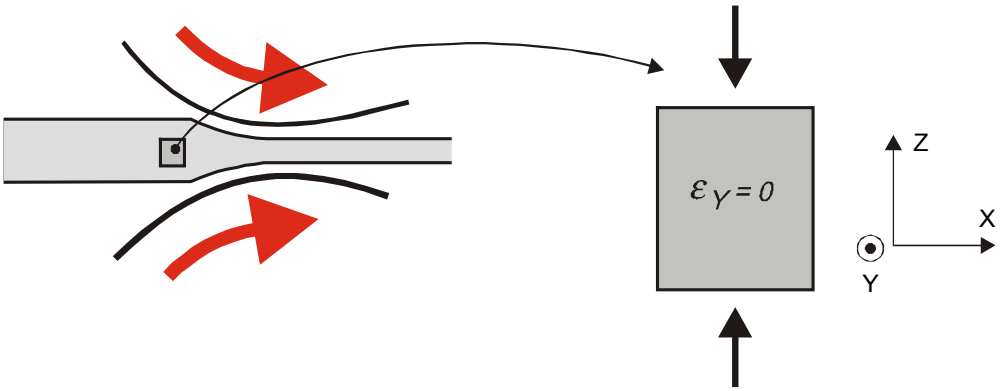

Figure 34: Rolling process represented by one finite element

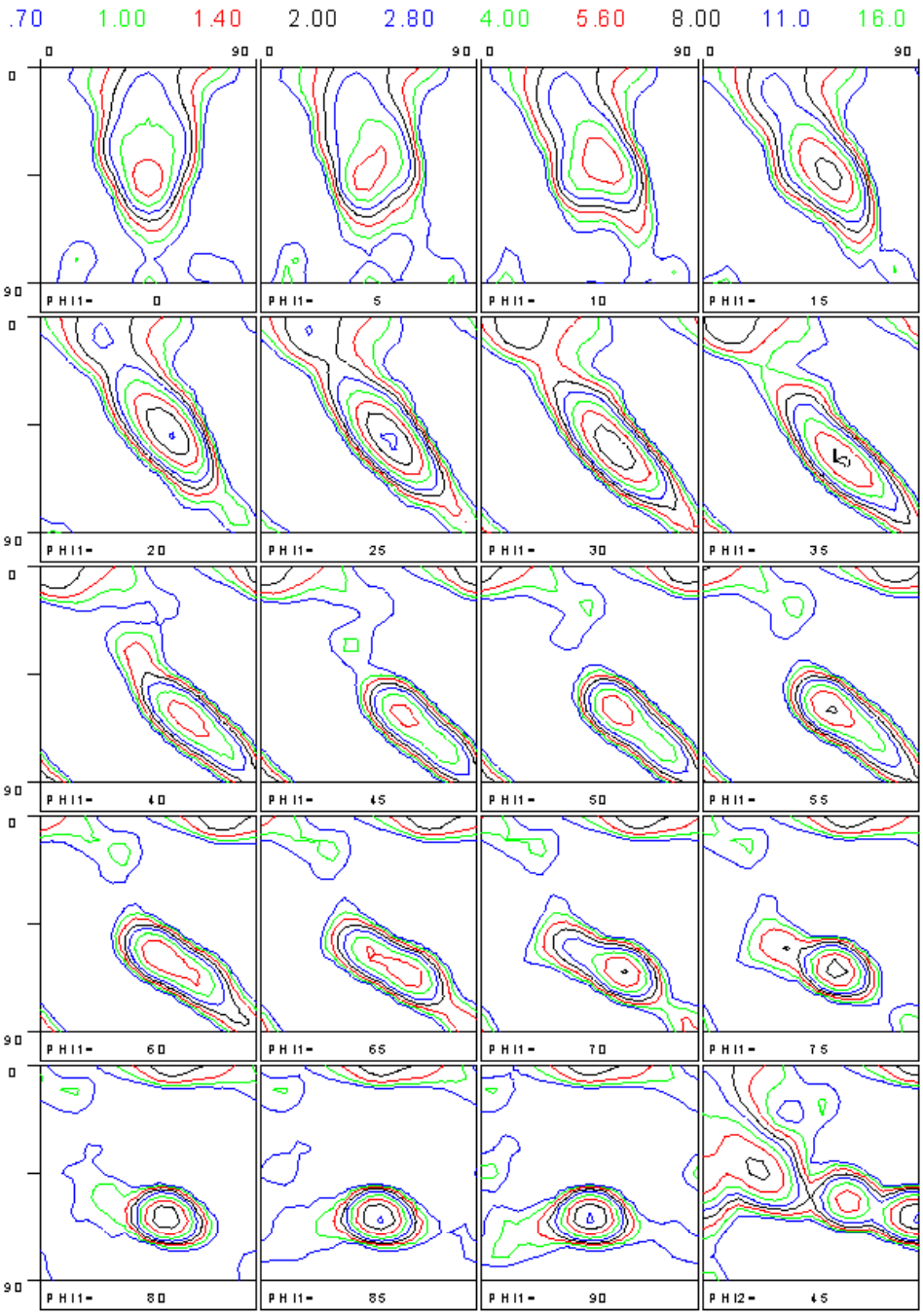

Figure 35: Sections φ_1=constants and φ_2=45° in the final ODF of the bcc material

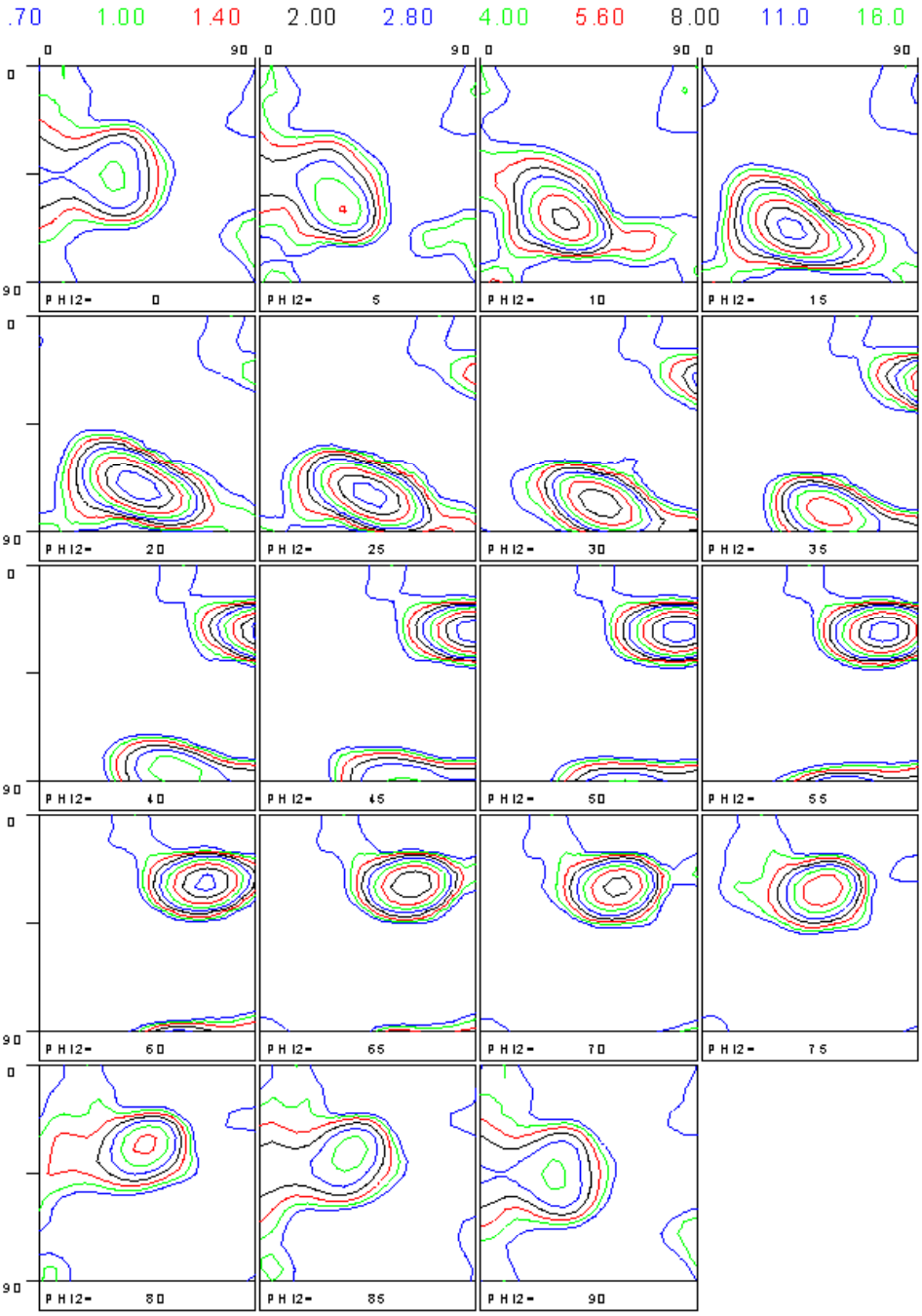

Figure 36: Sections φ_2 = constants in the final ODF of the fcc material

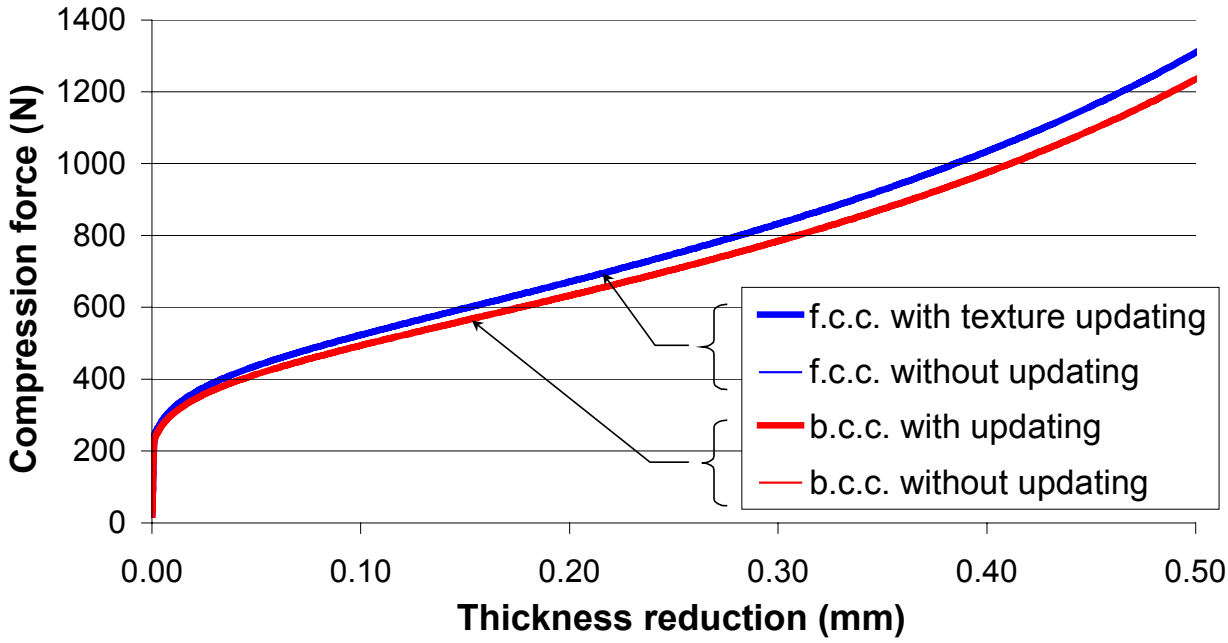

Figure 37: Rolling forces resulting of rolling simulations with or without texture updating for bcc or fcc materials

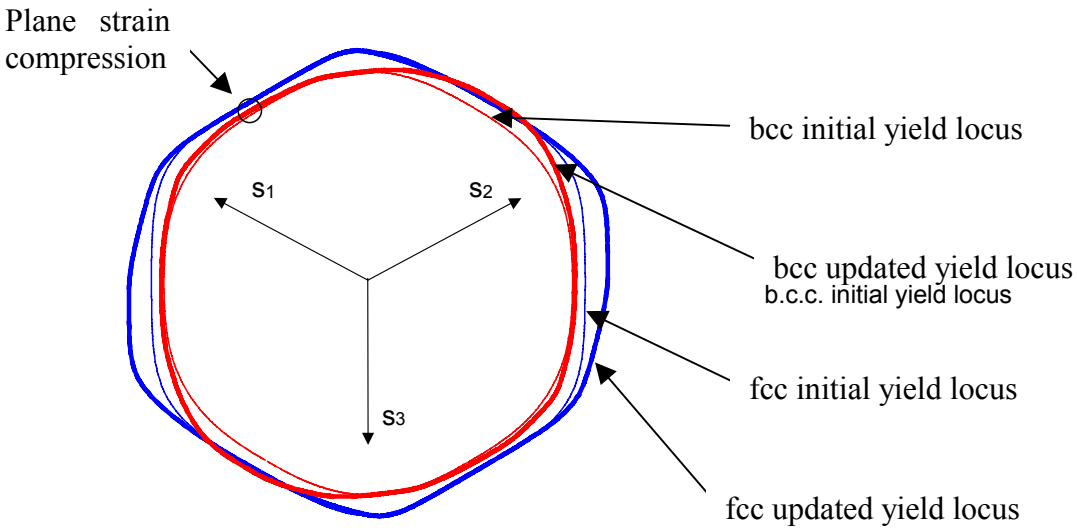

Figure 38: Initial and final π-sections in the yield locus computed from a random or a rolling texture for the bcc or the fcc materials

In spite of an assumed common hardening behaviour, a non-negligible influence of the crystal lattice is observed on the computed rolling forces as presented by Figure 37. The fcc compression force is about 6% higher then the bcc force at the end of the process. The larger stiffness observed for fcc metals can be related to a lower number of slip systems to accommodate the imposed deformation. Even if the texture evolution is important (see Figure 35 and Figure 36), no effect appears on the rolling force. As verified by Figure 38, which presents π-sections of the yield loci associated with the random or the rolling texture, it does not mean that these texture evolutions have no effect on the yield locus shape. It just happens that the point associated with the stress state in rolling is not affected by the shape evolution of the yield locus.

The yield locus associated with a random texture in the fcc material is larger than the one corresponding to the bcc material. This explains the larger rolling force required to perform rolling from a mechanical point of view. The texture evolution creates, in both materials, a strongly anisotropic yield locus.

2.2 Swift effect

The Swift effect has first been published in Swift (1947). It consists in an elongation of a cylinder when it is submitted to torsion.
The geometry of the sample can be a cylinder or a tube. The external loading is the torsion of the tube around its axisymmetry axis as shown by Figure 39. During the torsion of the tube, its height tends to increase. This deformation mode, i.e. the Swift effect, only occurs for large torsion strains, when large plastic strains are encountered.

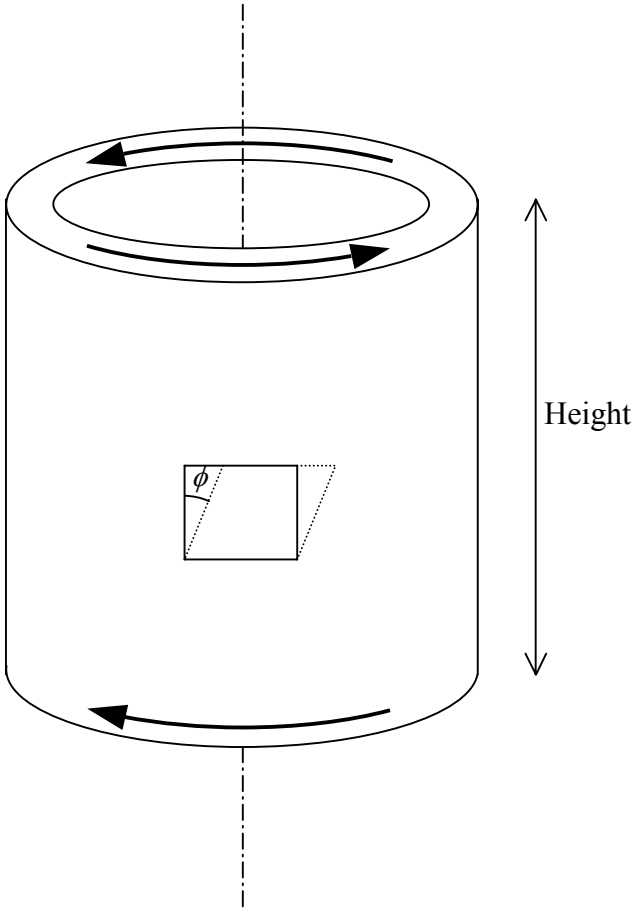

Figure 39: Torsion of a tube

This loading is called the free end torsion. The Swift effect can also be present in the case of a fixed end torsion. The increasing of the height of the tube is not permitted but, as a consequence, a compressive strain along the axisymmetry axis is measured.
The strain state on the small element of Figure 39 is shearing.

The elongation strains have been measured by several authors. First, in Figure 40 extracted from Swift (1947), seven metals are tested:

- a: 70-30 brass,
- b: stainless steel,
- c: aluminium,
- d: cupro-nickel,

- e: copper,
- f: mild-steel,
- g: 0.5 % carbon steel.

The axial elongation (in %) is plotted as a function of the shear strain (due to the torsion).

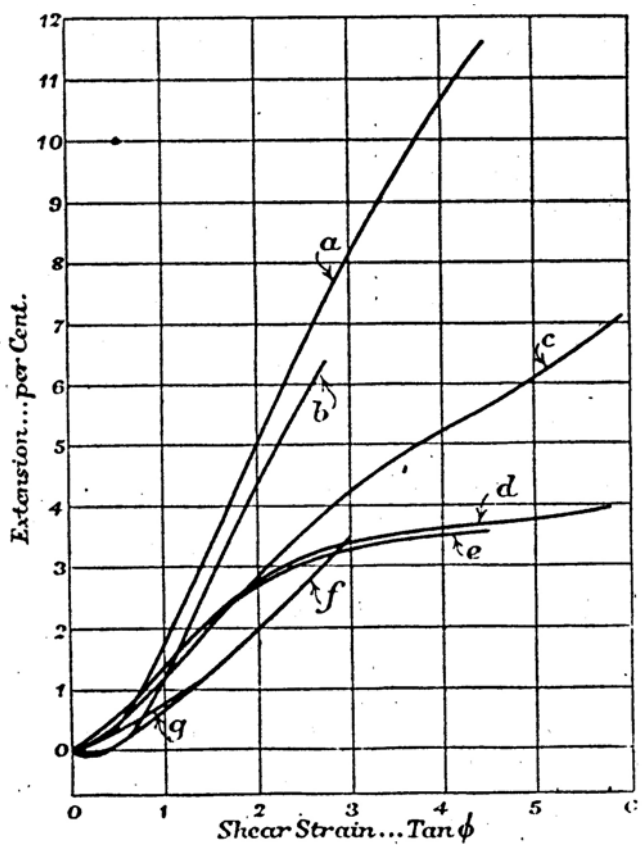

Figure 40: Extension as a function of the shear strain; experimental data for 7 metals (extracted from Swift (1947))

The observations of the author are: ”It will be seen that all seven metals show a general tendency to elongate under severe torsional strain. (…) The final elongation varies from about 1 per cent. for a carbon steel to over 11 per cent.”
Furthermore, he noticed that the Swift effect is more pronounced for fcc metals than for bcc ones.

For the torsion of a tube, the shear strain $\overline{\omega}$ is generally defined as:

$$\overline{\omega} = \frac{1}{2}\psi \overline{R} \tag{186}$$

where ψ is the twist angle per unit length of the tube and $\overline{R}$ is the initial mean radius of the tube. This definition of the shear strain $\overline{\omega}$ is at first approximation the half of the shear strain used by Swift (1947) : *Tan* ϕ, which is the abscissa of Figure 40.

Miller and McDowell (1996a) and Miller and McDowell (1996b) reported a 7% elongation strain during torsion of a 304L stainless steel. This elongation strain was obtained for a very high shear strain $\bar{\omega}$ of 130%.

According to Xiao et al. (2001), an elongation strain of approximately 6.8% (an axial elongation of 1.07) is observed experimentally: the full circle symbols in Figure 41. The corresponding shear strain $\bar{\omega}$ is larger than 120%.

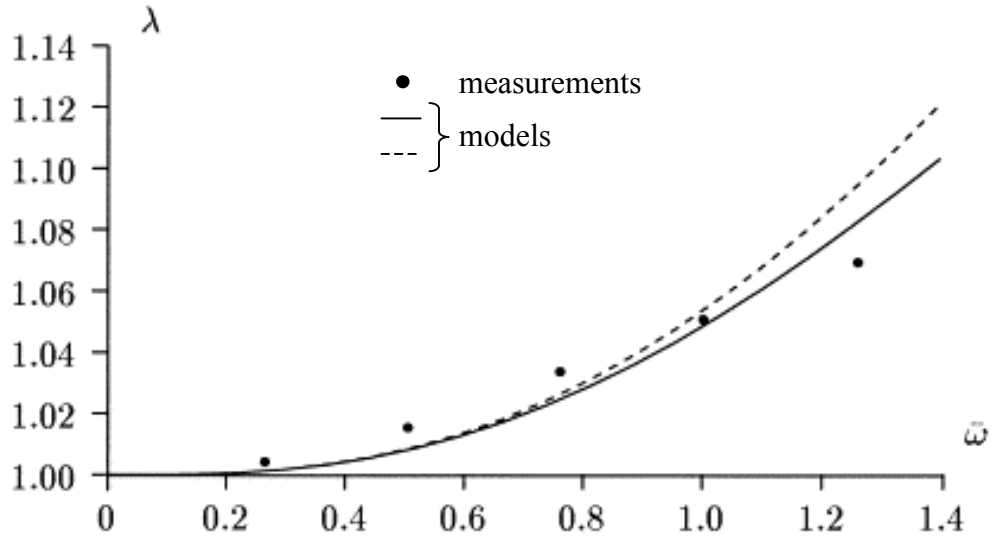

Figure 41: Swift effect: axial elongation versus the shear strain (extracted from Xiao et al. (2001))

Wu et al. (1996) and Rohatgi et al. (1995) also reported such elongation strains due to the Swift effect.

Several authors have developed numerical models able to predict the Swift effect during a torsion simulation. The results of Xiao et al. (2001) are plotted in Figure 41 (the dashed and the full lines correspond to 2 numerical methods to solve the equations they assumed to model the material behaviour).
Wu (2003) developed a model based on the Hill (1948) yield locus and predicted an elongation strain of 1.5% during the free end torsion of a thin-walled tube of aluminium.

As our model is largely based on microscopic physical events, we have also tried to predict the Swift effect. We have tried several cases but, unfortunately, no elongation strain could be observed.
First, the free end torsion of a cylinder was investigated. Thanks to the axisymmetry of the loading and the orthotropy of the material (the mechanical properties of the SPXI 250 steel largely detailed in paragraph 3.1 have been used), only a quarter of the cylinder was meshed. Then the free end torsion of a tube was also simulated.
A Hill (1948) constitutive law was also tried; with an isotropic and with a kinematic hardening.
Other materials were then tested: a mild steel, a fictive material with an isotropic texture (the crystallographic orientations are uniformly distributed in the Euler space) and with a bcc or a fcc crystal lattice. The results are presented in Figure 42.

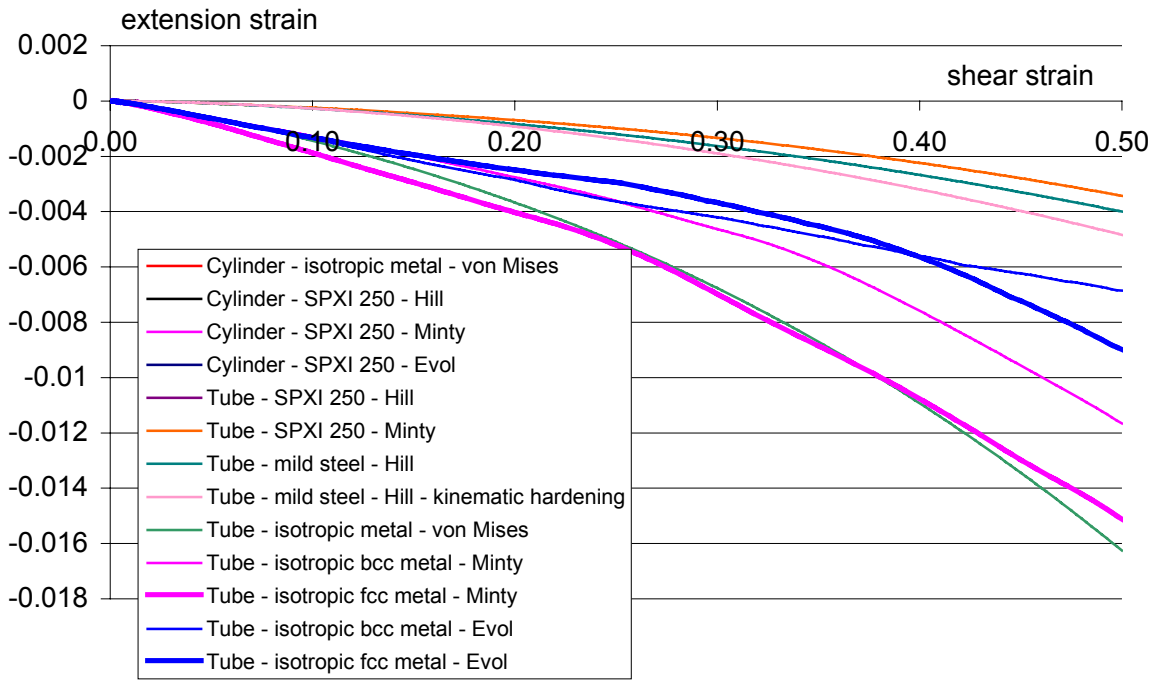

Figure 42: Extension strain versus the shear strain $\overline{\omega}$ for different geometries, metals and constitutive laws

Different sizes of the interpolation domain in Minty approach were tested as well as the influence of the number of crystals to represent the texture of the material. These results confirm that Swift effect is not predicted. They were not added to Figure 42 for its readability.
In the caption of Figure 42, the geometry (tube or cylinder) is first specified; the used metal is then cited and finally, the used constitutive law is mentioned.
A lot of curves are plotted and it is difficult to visualise each of them but it clearly appears that the extension strain is negative in every cases. This means that the height of the cylinder or the tube decreases as the torsion is applied, contrarily to experimental measurements.

The Hill (1948) and the von Mises constitutive laws were not expected to predict a Swift effect. But, to understand why our model is not able to predict the Swift effect, the microscopic physical phenomenon responsible of an elongation strain had to be identified.

Swift (1947) already proposed an explanation based on the slip system activity at the crystallographic level. Figure 43 shows how would deform the crystals if no rotation of the crystal lattice were possible. According to the initial orientation of the crystal lattice, 4 cases are presented. There exits a lot of slip systems in each crystal (generally, 12 for fcc metals and 24 for bcc metals are assumed); Figure 43 only indicates the one (or one of those) which is activated by the external load.
As a rotation of the crystal lattice frequently takes place, the deformation modes of Figure 43 must be modified. Figure 44 shows a 2D representation of the deformation modes of the microscopic grains according to the initial orientation of the crystal lattice. The global applied load is the shearing represented by the arrows in the figure. The 6 cases (‘a’ to ‘f’) are representative of all the orientations possible for a 2D analysis. The cases ‘a’, ‘e’ and ‘c’ have a crystal lattice orientation close to the axial direction of the cylinder or the tube; close means

that the angle between the two directions is lower than 45°. Whereas the cases ‘b’, ‘f’ and ‘d’ have an orientation close to the transverse plane (a plane normal to the axial direction). In Figure 44, the deformation modes presented in ‘a’, ‘e’ and ‘c’ are obtained by slip glide and rotation of the crystal lattice to accommodate the global deformation of the material. On the other hand, the cases close to the transverse plane are only submitted to slip glide and no rotation of the crystal lattice occurs according to the prescribed global deformation.
As the crystal lattice in the cases close to the axial direction rotates, the slip system which was activated (as shown by Figure 44) becomes not as well oriented with respect to the global loading as it was. As a consequence, this initial slip system is no more activated and the deformation is achieved with the use of another slip system.
For the cases with a slip system oriented close to the transverse plane, no rotation of the crystal lattice occurs and the same well oriented slip system always remains the one which is activated.
It appears that for the cases close to the axial direction, different slip systems are activated successively while only one slip system is activated for the cases close to the transverse plane.
For several metals, a hardening behaviour linked to the slip systems (as presented by equation (41) chapter 2) is often observed. With such a hardening, the 6 cases presented in Figure 44 will behave very differently. Indeed, the single slip system activated for the cases close to the transverse plane will be submitted to a large hardening while the cases close to the axial direction will harden less as the slip activity is distributed between several slip systems.
This point is the basis of Swift’s theory to explain the extension during torsion. The interaction between the axial oriented grains (noted ‘A’) and the transverse oriented grains (noted ‘T’) is presented in Figure 45. The initial shape of the grains is assumed to be circles. These grains deform in the shape of ellipses by slip glide according to the global shearing. For all the cases of Figure 45, except case ‘e’, the interaction between ‘A’ and ‘T’ grains always force the ‘A’ grains to rotate clockwise. While ‘T’ grains tend to rotate anticlockwise. The ‘T’ grains, which are highly hardened, tend to be aligned with the height of the tube (or cylinder). The low hardened ‘A’ grains tend to be aligned perpendicularly to the height of the tube. This phenomenon is assumed to be at the origin of the Swift effect.

This explanation of the Swift effect proposed by Swift (1947) is largely speculative but it is in agreement with the experimental observations.
First, it can explain why fcc metals are more subjected to the Swift effect than bcc metals. The explanation above being closely linked to the slip system activity, a lower number of slip systems in each crystal will emphasise the phenomenon.
As noted by Jonas et al. (1998) and Weber et al. (2000), the extension during torsion is only observed at low (room) temperatures. At higher temperatures, a shortening of the tube is observed experimentally. The explanation of Swift is based on the work hardening in each crystal; at high temperatures, dynamic recrystallization occurs and annihilates the work hardening based extension.
Furthermore, a non hardening material like lead is not subjected to the Swift effect even at room temperature. Whereas, room temperature is too low to permit dynamic recrystallization in steel, aluminium or copper for instance and thus only lengthening is observed.

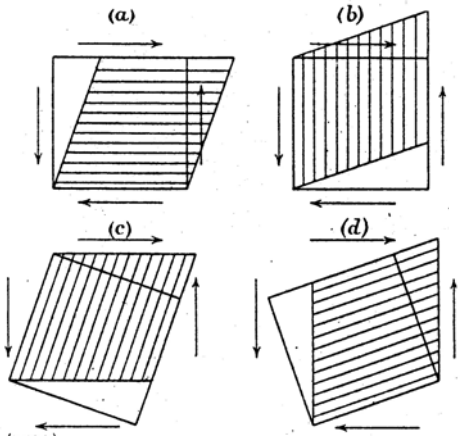

Figure 43: Deformation due to slip glide without rotation of the crystal lattice (extracted from Swift (1947))

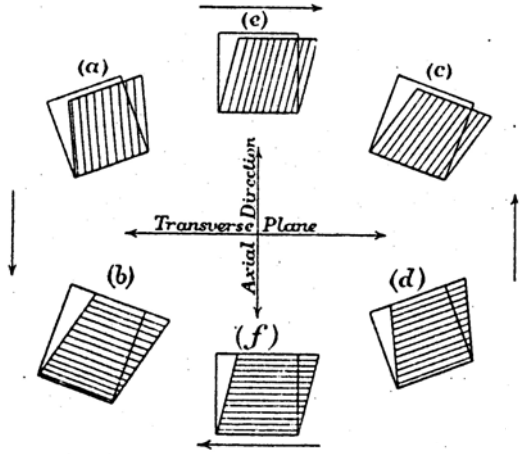

Figure 44: Rotations of the crystal lattices in accordance with the global deformation mode (extracted from Swift (1947))

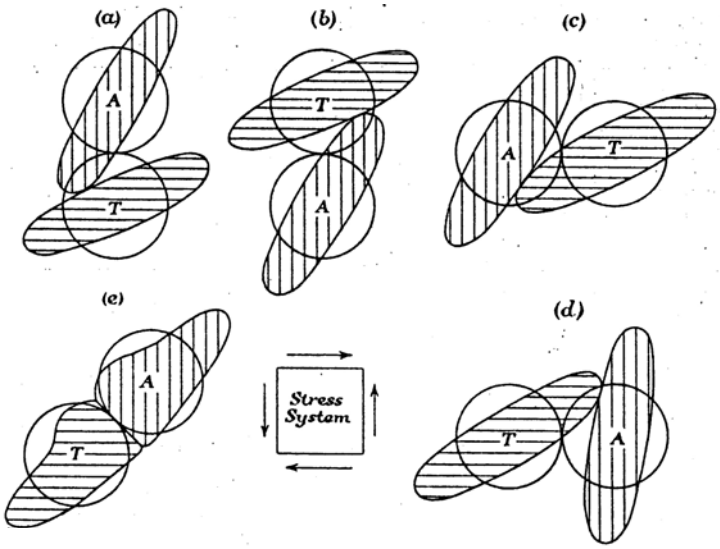

Figure 45: Interaction between transverse grains (T) and axial grains (A) (extracted from Swift (1947))

According to the explanation of Swift (1947), a numerical model is able to predict the Swift effect only if the following features are taken into account:

1. the plasticity of the material must be computed thanks to the slip system activity,
2. the activated slip systems must be identified,
3. the hardening behaviour must be of the type of equation (41). The possibility of a different hardening for each slip must be included in the model. And the hardening must be linked to the slip activity.
4. The rotation of the crystals according to the external load must be computed.

With our Taylor's model based constitutive law, only the third point concerning the hardening is not fulfilled. Indeed, an isotropic hardening has been implemented.
This explains why no Swift effect was observed in Figure 42.

In order to check the theory proposed by Swift with our model, a slip system activity based hardening has been implemented. The evolution rule of such a hardening is (see equation (41) from chapter 2):

$$\dot{\tau}_g^c = H^{gh}\dot{\gamma}_h \tag{187}$$

So, the evolution of each critical resolved shear stress is linked to the slip rate of each slip system. The H matrix must be chosen in order to correctly represent the physical microscopic events. The diagonal terms of H correspond to the self hardening and the off-diagonal terms correspond to the latent hardening.
Even if the H matrix should be based on the physic of the hardening behaviour, a non physic based hardening has been implemented just to check its effect on the prediction of the Swift effect.
In our model with the isotropic hardening, the evolution of the critical resolved shear stress is identical for each slip system and for each crystal representing the material behaviour at one integration point of the finite element mesh. However, as presented in chapter 2 paragraph 3.6, initial ratios between the critical resolved shear stress of each slip system are defined. Generally, the ratios are equal to unity but they can be chosen different than 1. These ratios are called $\alpha_{\pm i}$ where the i stands for the i^{th} slip system and + and – define the direction in which the slip system is activated.
In the initial isotropic hardening model, the $\alpha_{\pm i}$ are defined identical for all the crystals at the beginning of the finite element simulation and remain constant during the computation.
We have simply improved this hardening behaviour by allowing the $\alpha_{\pm i}$ to evolve as a function of the activity of the corresponding slip system for each crystal. The evolution rule for the $\alpha_{\pm i}$ is not based on the physic: each $\alpha_{\pm i}$ is simply multiplied by a factor (called p) each time its slip system is activated. Compared to equation (187), these modifications of our model correspond to a non physic self hardening and no latent hardening is introduced.
With this slip system activity based hardening, the $\alpha_{\pm i}$ will evolve differently from one slip system to another but the α_+ and the α_- for one slip system are always identical. The direction in which the slip system is activated is not taken into consideration in this hardening behaviour. So, $\alpha_{\pm i}$ is replaced by α_i hereafter. However, as the torsion loading required to show the Swift effect is monotonous, this limitation has no effect on the present investigations.

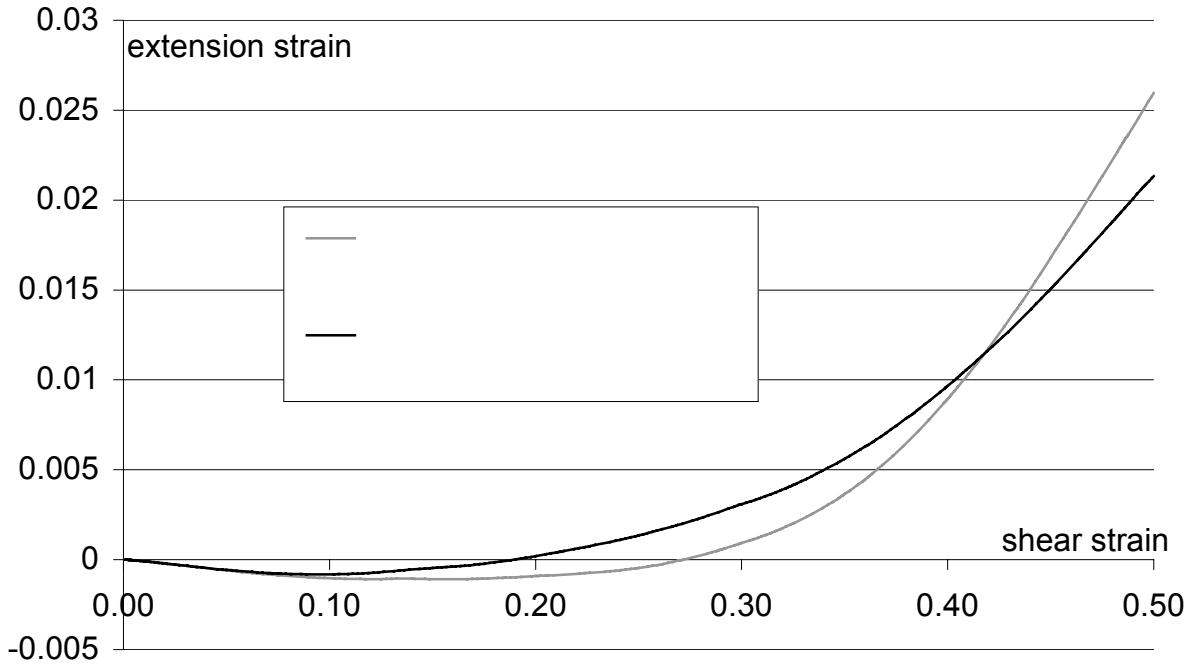

Figure 46: Swift effect predicted with our model and a slip system activity based hardening

In addition to the orientation (the 3 Euler angles) of the 2000 crystals, representative of the texture for each integration point, this slip system activity based hardening model requires to store the α_i ratios for each crystal. For a fcc metal with 12 slip systems, there are 24000 (12 ratios for 2000 crystals) additional real numbers to store and to compute for each integration point.
Figure 46 shows the extension strain versus the shear strain for the torsion of a tube computed with the slip system activity based hardening. The stress-strain interpolation model is used without ('Minty') and with ('Evol') computation of the evolution of the texture.
An initially isotropic fcc metal with a random texture represented by 2000 crystals is used.
An elongation of the tube, i.e. the Swift effect, is observed.
For these simulations, the initial value for the critical resolved shear stress ratios is 1 for each crystal and each slip system and each α_i is multiplied by p=1.04 each time its slip system is activated. At the end of the simulation, we have observed that the α_i are very different from each other: some are still equal to 1 (the corresponding slip systems have not been activated) and the maximum ratios obtained with this torsion simulation are equal to $(1.04)^{26}$=2.77 (the corresponding slip systems have been activated 26 times: the maximum value according to the number of time steps necessary to complete the simulation).

The assumption of Swift (1947) concerning the large influence of the hardening behaviour on the Swift effect appears to be founded.
The fourth assumption concerning the computation of the rotation of the crystals can also be checked. In Figure 46, the Swift effect is observed for both cases with and without computation of the evolved texture, i.e. the rotation of the crystals. However, for these simulations, the constitutive law is defined in local axes, which follow the material rotations. For the case 'Minty', the rotation of each crystal is not computed but the global behaviour of the material is rotated according to the deformation of the tube. And this global rotation of the local axes is enough to predict a Swift effect. If the non physical simulations are performed

without using local axes, the case 'Minty' using the initial texture throughout the computation cannot predict the Swift effect. The extension strains obtained at the end of the simulation (for a shear strain of 50%) are presented in Table 3. It can be noticed that the only case where no rotation of the crystals is computed (either by computing the texture evolution or by using local axes) does not predict a Swift effect (the extension strain is negative). Note that the values obtained with local axes can also be measured in Figure 46.

Table 3: Influence of the use of local axes on the extension strain during torsion

	Using local axes	Using global axes
Minty	2.60%	-1.55%
Evol	2.13%	1.46%

To analyse why the slip system activity based hardening can predict the Swift effect, the influence of the hardening on the yield locus describing the behaviour of the material is investigated. As the yield locus is defined in the 5 dimensional deviatoric stress space, a section of it must be computed. A section, showing the stress state actually computed during the simulation, should be chosen. Furthermore, the extension along the axial direction of the tube should also be visualised. Figure 47 shows the τ_{23} - σ_3 section of the yield locus at the end of the simulation. The section is computed in the local axes of the material (the chosen axes appear to be very sensitive for the current investigations). For the graph, the scale of the yield loci have been chosen so that the yield stress for a tensile test along the third local axis (σ_3) is identical. The slip system activity based hardening yield locus is compared to the yield locus with an isotropic hardening. The stress state computed during the simulation (with a scaling factor) is plotted in Figure 47 (the oblique line and the 2 black points).

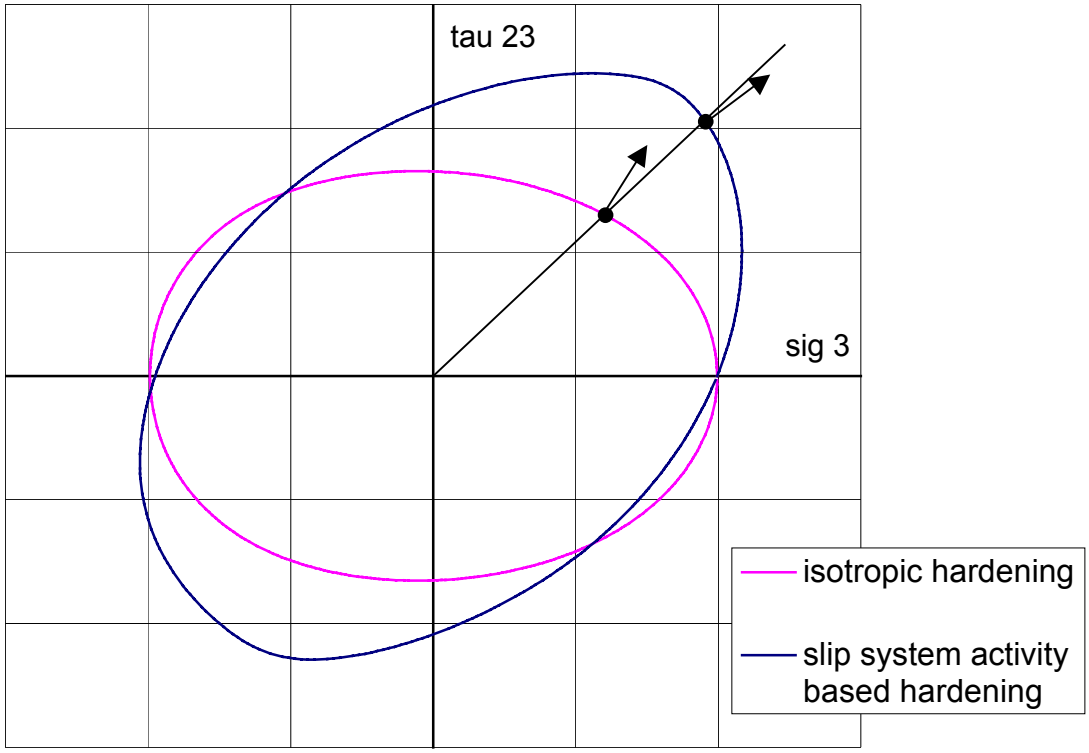

Figure 47: Section τ_{23} - σ_3 of the yield locus in the local axes

The Swift effect is linked to the strain state. However, thanks to the normality rule, the plastic strains can be visualised in Figure 47. The normals to the yield locus at the interesting stress point must be examined.
It clearly appears in Figure 47 that the normal to the yield locus corresponding to the slip system activity based hardening is much more oriented along the σ_3 axis than the normal obtained with the isotropic hardening. According to the analysis of the yield loci, the hardening law has a significant influence on the material behaviour.
To quantify the tendency of the material to extend along the tube axis during torsion, the plastic strains visualised in Figure 47 should be expressed in the global axes. Indeed, the local axes have been rotated during the simulation. The Z global axis corresponds to the axis of the tube along which the extension must be measured.
Table 4 shows the plastic strain rates expressed in the local axes and the same plastic strain rates rotated back in the global axes. The tensors of Table 4 are normalised.

Table 4: Unitary plastic strain rates depending on the hardening

	Expressed in local axes	Expressed in global axes
Isotropic hardening	$\begin{pmatrix} -0.033 & 0 & 0 \\ 0 & -0.422 & 0.554 \\ 0 & 0.554 & 0.455 \end{pmatrix}$	$\begin{pmatrix} -0.033 & 0 & 0 \\ 0 & 0.231 & 0.673 \\ 0 & 0.673 & \boxed{-0.198} \end{pmatrix}$
Slip system activity based hardening	$\begin{pmatrix} -0.171 & 0 & 0 \\ 0 & -0.530 & 0.314 \\ 0 & 0.314 & 0.702 \end{pmatrix}$	$\begin{pmatrix} -0.171 & 0 & 0 \\ 0 & 0 & 0.686 \\ 0 & 0.686 & \boxed{0.170} \end{pmatrix}$

The negative value of the global axes Z component obtained with the isotropic hardening proves the tendency to contract. While the positive value for the slip system activity based hardening is compatible with the Swift effect.

Remark: in following applications (sections 2.3 to 4), the basic assumption of isotropic hardening is applied; the slip system activity based hardening is a non standard option of our model.

2.3 Comparison of the torsional and compressive behaviour

Beside the Swift effect, another phenomenon linked to a slip system based plasticity is the fact that the von Mises criterion is not fulfilled even if a random (isotropic) texture is used.
For an isotropic fcc metal, Bishop and Hill (1951) showed that a 6.85% lower equivalent yield stress is expected in torsion compared to tension or compression based on the computation of the average Taylor's factors for torsion and tension.
Figure 48 (extracted from Miller and McDowell (1996b)) shows that such a different behaviour in torsion and compression is also measured experimentally. During experimental tests, the difference between torsion and compression is amplified by the evolution of the initial isotropic texture and by the hardening behaviour.

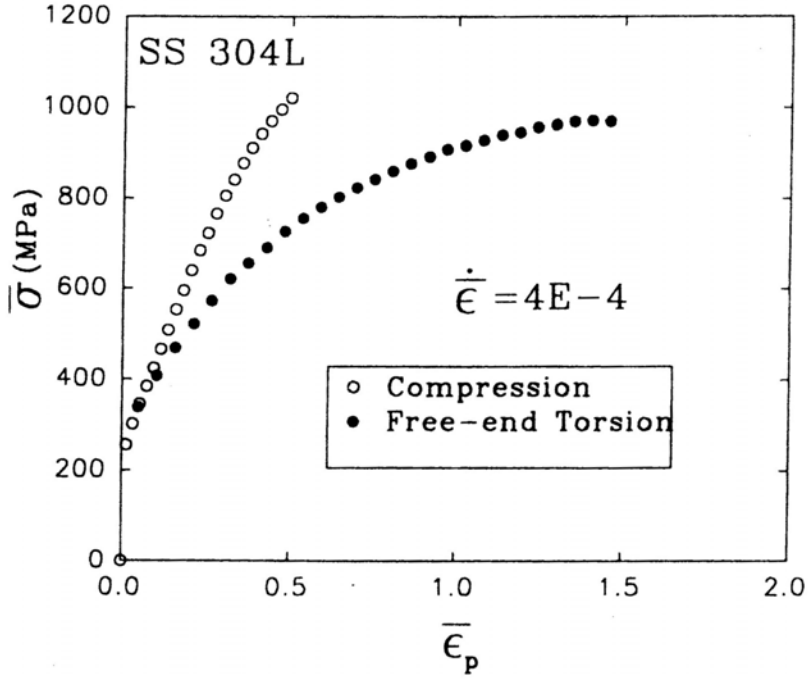

Figure 48: Equivalent stress-strain curves: comparison of the compression and the free-end torsion on experimental data (extracted from Miller and McDowell (1996b))

Torsional and compressive finite element simulations have been performed with our model to show the difference in the respective behaviour. Figure 49 shows the results obtained for an initially isotropic bcc metal. The initial texture is represented by 2000 crystals uniformly distributed in Euler space. A larger number of crystals has been investigated and led to similar results.
The von Mises equivalent stress strain curves are plotted. The influence of the computation of the texture evolution (case 'Minty' or 'Evol') is also investigated. For comparison purposes, a Hill (1948) law with isotropic Hill parameters is also used, that is to say a von Mises model.
It appears that all the curves obtained for the compression simulations are superimposed. This is due to the low influence of the texture evolution for that process and to the fact that the same isotropic hardening law is used.
The torsion computed with the Hill law is also superimposed to the compression curves. The Hill law with isotropic parameters is effectively isotropic (in the meaning of von Mises) leading to identical von Mises equivalent stress strain curves.

With the Taylor based models, the yield stress computed in torsion is lower compared to compression. So, the anisotropic yield locus (in a von Mises meaning) is able to capture this phenomenon. When the texture is evolving during the simulation, the difference between compression and torsion is increased. A textural softening is observed during torsion simulations.

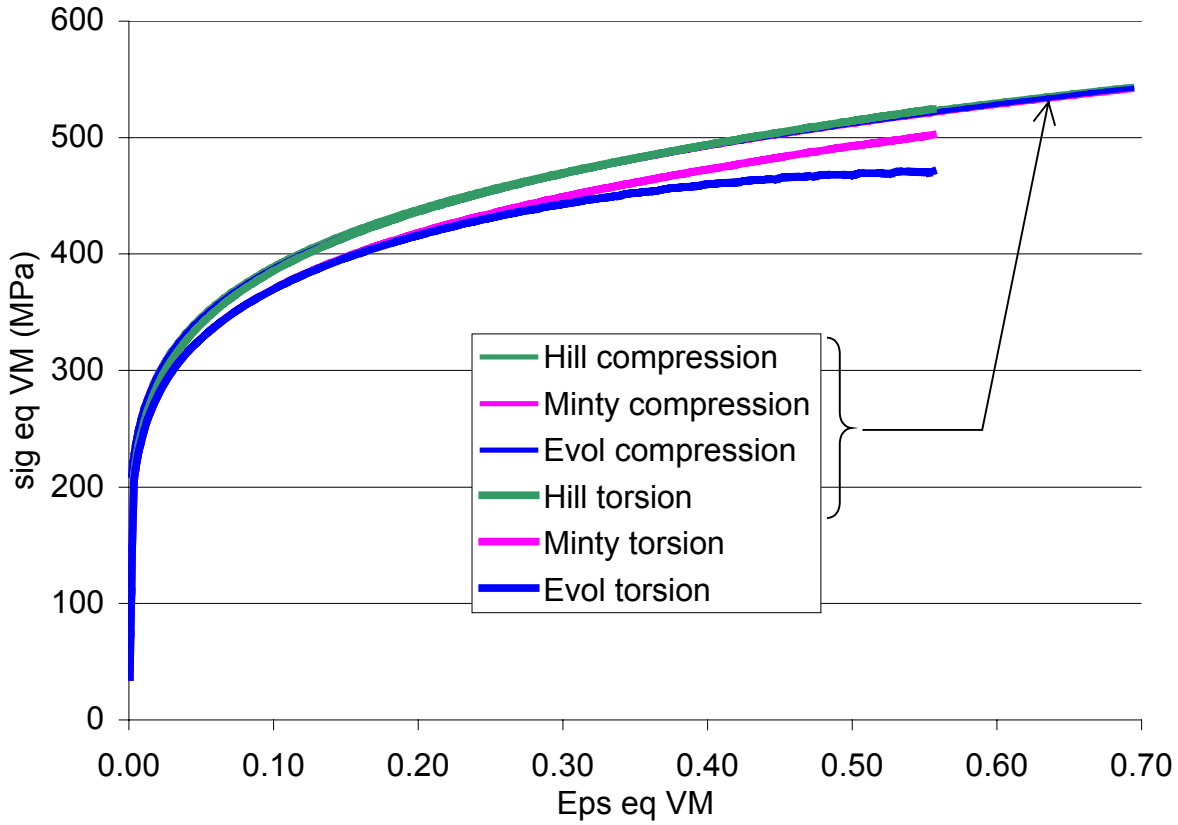

Figure 49: Equivalent stress-strain curves: comparison of the compression and the free-end torsion (computed results for an isotropic bcc metal)

Figure 50 presents the results obtained with an initially isotropic fcc metal. The same observations can be done. It should however be noticed that the difference in the yield stresses for torsion and compression is more pronounced for the fcc metal than for the bcc one; especially for the case computed with the initial texture ('Minty').
The different behaviour observed for torsion and compression has its origin in the slip systems based plasticity. The lower number of slip systems of the fcc metals are then expected to emphasize the phenomenon and is numerically predicted.

The different behaviour between torsion and compression (or tension) can also be analysed on the yield locus of the material. Figure 51 shows π-section of the yield locus (only 1/12 of the whole section is represented). The scale of the different models is adjusted to be identical for the tension state. Tresca's model is represented by a straight line and von Mises' model is an arc of a circle. These 2 classical models are upper and lower bounds for the other models.
The π-sections of the yield locus computed with our model on the basis of isotropic fcc and bcc metals are plotted. The results obtained by Bishop and Hill (1951) for a fcc metal (already discussed at the beginning of this paragraph) are also plotted.

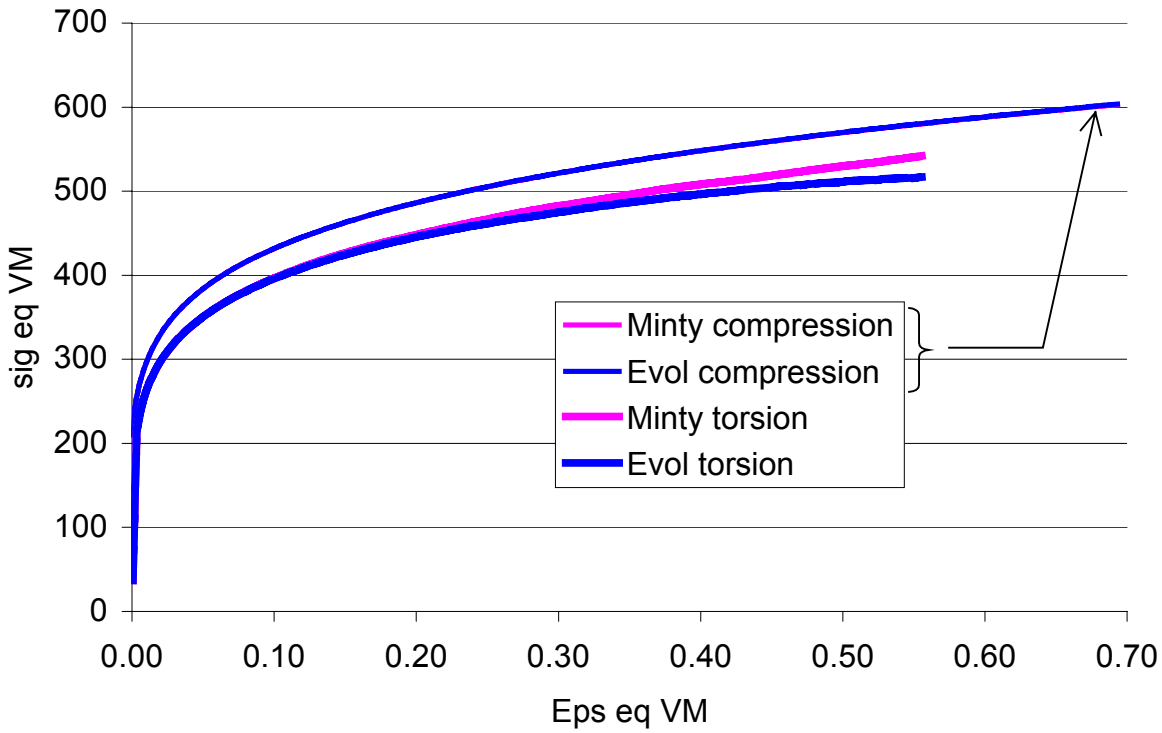

Figure 50: Equivalent stress-strain curves: comparison of the compression and the free-end torsion (computed results for an isotropic fcc metal)

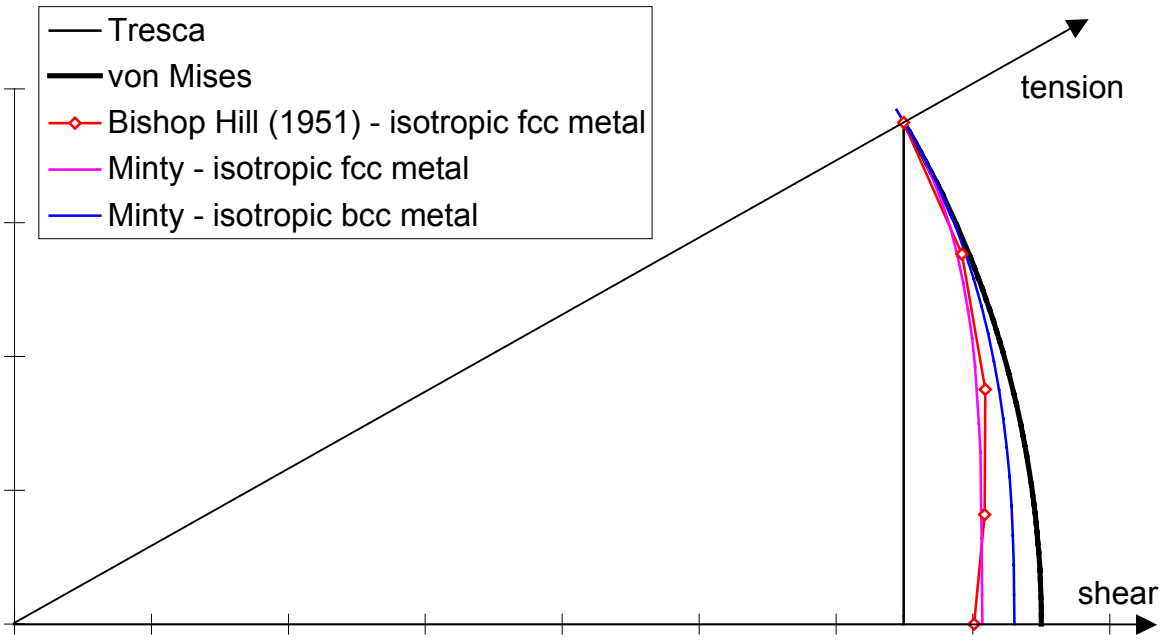

Figure 51: π-section of the yield locus for an isotropic metal

It appears in Figure 51 that the different behaviour between torsion and compression compared to von Mises is observed with our model even without texture evolution. As already mentioned, the difference is more pronounced for the fcc crystal lattice case.
The 5 points of the yield locus computed by Bishop and Hill (1951) using an isotropic texture and a fcc crystal lattice are in good agreement with our results. Indeed, the plasticity is assumed in both cases to be exactly represented by the Taylor's model.

The π-sections presented in Figure 51 have been computed with a random texture represented by 2000 crystals. Identical results have been obtained using 12995 crystals.
The lack of isotropy of the Taylor based models compared to von Mises criterion is not due to a too low number of crystals to represent the texture but to the fact that the plasticity is only possible by slip glides.
Indeed, major differences can be noticed between torsion and compression at the level of the crystals. The plastic strain rates for torsion and compression can be reduced with a scaling factor to:

$$\begin{array}{cc} \text{Torsion} & \text{Compression} \\ \underline{\underline{\dot{\varepsilon}}}^{p} = \begin{pmatrix} 1 & 0 & 0 \\ 0 & -1 & 0 \\ 0 & 0 & 0 \end{pmatrix} & \underline{\underline{\dot{\varepsilon}}}^{p} = \begin{pmatrix} -1 & 0 & 0 \\ 0 & 0.5 & 0 \\ 0 & 0 & 0.5 \end{pmatrix} \end{array} \qquad (188)$$

These plastic strain rates are expressed in their principal axes. Due to the Taylor's hypothesis, these global plastic strain rates are also acting on each individual crystal but expressed in the axes of the crystal. As the texture is isotropic, the crystal orientations are uniformly distributed and the plastic strain rate acting on each crystal can be deduced from the Mohr circles of Figure 52. Indeed, these Mohr circles are related to the plastic strain rates of equation (188); the plastic strain rate on one particular crystal must be in the hatched zone for the torsion case and on the half circle for the compression.
The plastic deformations of the material can only be achieved by shearing of the crystals; the γ/2 component of the plastic strain rate acting on each crystal is then predominant for the material behaviour. And it appears in Figure 52 that the torsion and the compression are clearly different from that point of view.

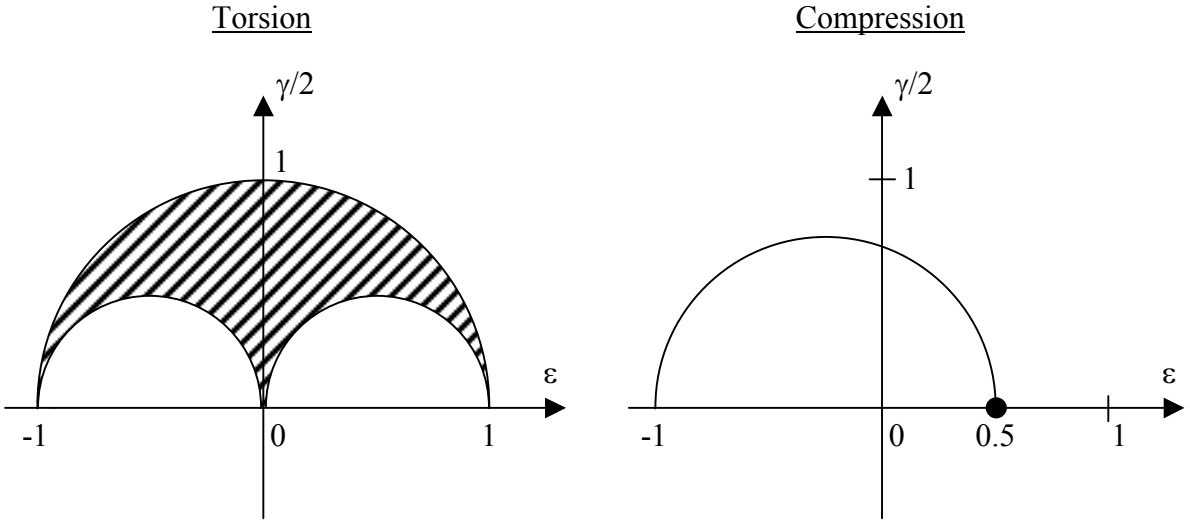

Figure 52: Comparison of the torsion and the compression with Mohr circles

3 *Deep drawing tests performed by RDCS*

Deep drawing tests have been performed in order to validate the texture based models that we have developed. The geometry investigated for the deep drawing process is rather simple (see sections 3.2 and 3.3) but the simulations are closer to industrial processes than for the academic validation of the previous paragraph. Furthermore, for comparison, experimental tests were performed by RDCS (Recherche et Développement Cockerill Sambre, groupe Arcelor) and are described in section 3.2.
Two steels are used for these deep drawing tests; they are described in section 3.1. Section 0 compares the experimental and the simulated results. The influence of some important numerical parameters on the results is investigated in section 3.5.

3.1 Material description

Two steels were provided by RDCS. The first one is a high tensile steel called SPXI 250. The second one is an interstitial free steel well adapted for deep drawing; its name is ULC Ti. Both steels are produced in the shape of steel sheets by rolling. The thickness of the sheets at the end of the rolling process is 0.8 mm for both steels.

A CHEMICAL COMPOSITION AND METALLURGICAL PROPERTIES

SPXI 250 and ULC Ti are both made of ferritic steel. It corresponds to a body centred cubic (bcc) crystal lattice. The mean grain size is 6 μm for the SPXI 250 steel and 19 μm for the ULC Ti steel.
The chemical composition is presented in Table 5 for SPXI 250 steel and Table 6 for ULC Ti steel.

Table 5: Chemical composition of SPXI 250 steel

element	C	Mn	Si	P	S	N	Al	Cr	Ni	Cu	Sn	Ti	Nb	B	As	V	Mo
ppm	470	2340	90	110	40	35	330	280	260	120	10	30	10	38	10	20	30

Table 6: Chemical composition of ULC Ti steel

element	C	Mn	Si	P	S	N	Al	Cr	Ni	Cu	Sn	Ti	Nb	B
ppm	30	1500-2500	200	200	100	550	200-600	500	700	700	250	400-800	50	70

B MECHANICAL PROPERTIES

The mechanical properties of both steels have been determined trough tensile tests along different directions with respect to the rolling direction. The results corresponding to 0°, 45° and 90° from the rolling direction are presented in Table 7. The stress-strain curve related parameters are defined according to the schematic representation of Figure 53. r is the Lankford's coefficient and n is the Hollomon's exponent parameter describing the hardening behaviour according to equation (189) fitted on the actual stress-strain curve.

$$\sigma = K \cdot \varepsilon^n \tag{189}$$

Table 7: Mechanical properties of steels SPXI 250 and ULC Ti

Steel	Angle from RD	Rp 0.2 % (MPa)	Rm (MPa)	Ag (%)	A80 (%)	r	n
SPXI 250	0°	276.0	392.8	18.3	32.8	0.89	0.175
	45°	284.6	392.7	17.0	32.9	1.02	0.172
	90°	295.3	398.6	17.8	32.8	1.13	0.172
ULC Ti	0°	126.9	300.6	23.1	47.8	2.08	0.244
	45°	132.5	306.3	21.9	42.9	1.85	0.230
	90°	128.8	297.7	22.8	44.5	2.59	0.236

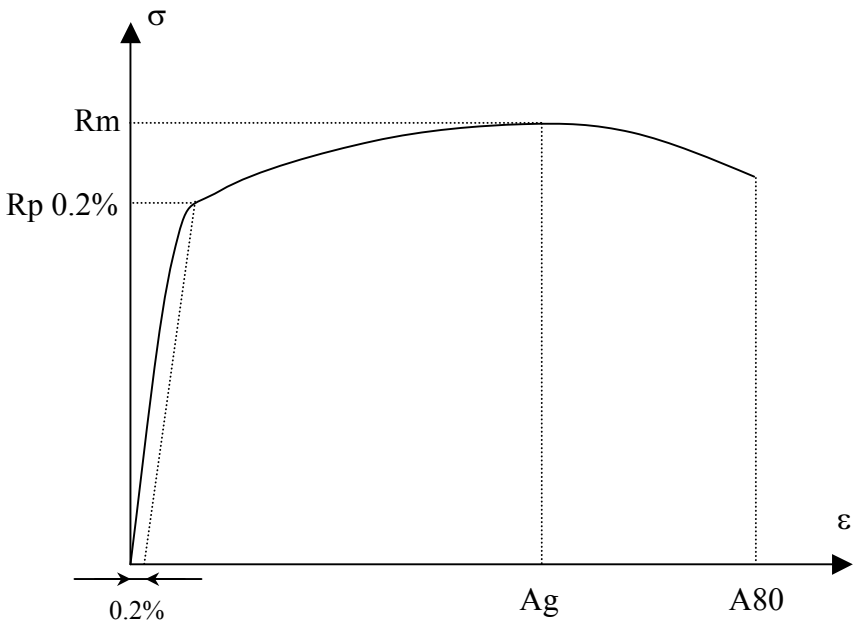

Figure 53: Schematic stress-strain curve

From Table 7, it can be noticed that SPXI 250 steel, which is a high tensile steel, has higher values of the stresses (Rp 0.2% and Rm) as compared to ULC TI steel. On the other hand, ULC Ti steel allows larger strain before failure; this steel is more ductile.
The high ability of ULC Ti steel for deep-drawing can also be proved by its high Lankford coefficients.
The Hollomon's exponent cannot be used with the hardening behaviour that is implemented in our model. The power-type law of equation (31) from chapter 2 contains an offset parameter not present in Hollomon's law.

$$\sigma = K \cdot \left(\varepsilon^0 + \varepsilon^{plastic}\right)^n \tag{31}$$

The parameters of our hardening model have then been fitted on the stress-strain curve of the tensile test along the rolling direction. The values are summarised in Table 8.

Table 8: Hardening parameters of SPXI 250 and ULC Ti steels

Steel	K	ε^0	n
SPXI 250	579.5	0.0028	0.1726
ULC Ti	559.58	0.004594	0.3054

From the tensile tests, the elastic properties have also been extracted. Young's modulus (E) and Poisson's ratio (ν) are presented in Table 9 for both steels. As justified in chapter 2 paragraph 3.4, an isotropic elasticity is implemented in our model.

Table 9: Elastic properties of SPXI 250 and ULC Ti steels

Steel	E (MPa)	ν
SPXI 250	209880	0.28
ULC Ti	157242	0.36

Since we focus on the formability of these steels, the Forming Limit Diagram (FLD) are also investigated. It is indeed a good measure of the maximum strain that can be sustained by the steel sheet before failure occurs (for a radial loading, i.e. $\varepsilon_2/\varepsilon_1$ = constant). The FLD of SPXI 250 and ULC Ti steels are presented in Figure 54. The experimental Marciniack method has been used for the measurements. The higher ability for deep drawing of ULC Ti steel is again proved.

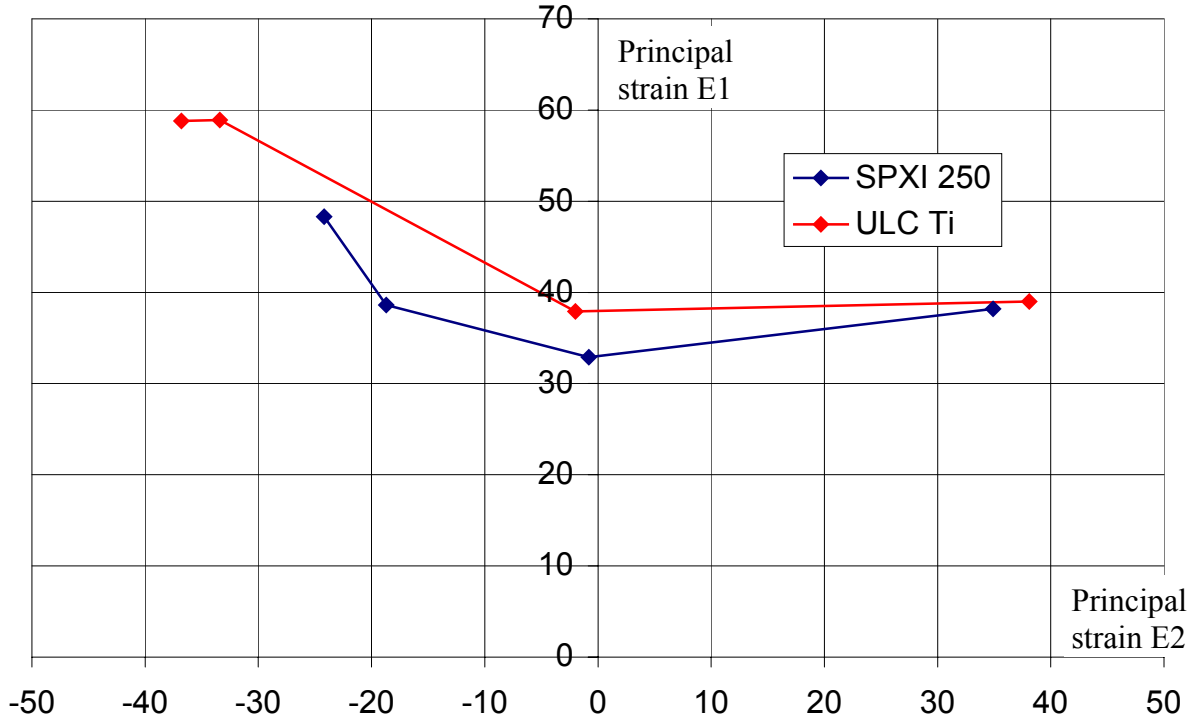

Figure 54: Forming Limit Diagram of SPXI 250 and ULC Ti steel (determined by Marciniack tests)

C INITIAL TEXTURE

To be used with our micro-macro model, the texture of these steels has been measured. The texture measurements of SPXI 250 and ULC Ti steels has been obtained by X-ray diffraction. Sections of the ODF are presented in Figure 55 for SPXI 250 steel and Figure 56 for ULC Ti steel. The Euler angles are used for the representation of the ODF; sections of the ODF with φ_1 constant are presented, the constant ranging from 0° to 90° by 5° steps. One section with φ_2 equal to 45° is also presented.

Both steels exhibit a γ fibre which is typical for rolled steels. The maximum value of the ODF (corresponding to the most represented orientation in the polycrystal) is 5.86 for the SPXI 250 and 10.91 for the ULC Ti steel. Note that a value of 1 would correspond to a uniform distribution of the crystal orientations.

The larger anisotropy of ULC Ti steel with respect to SPXI 250 steel can be illustrated by the higher value of the maximum of the ODF. The higher Lankford coefficients of ULC Ti (mean r value of 2.17 compared to 1.01 for SPXI 250) also prove its stronger anisotropy.

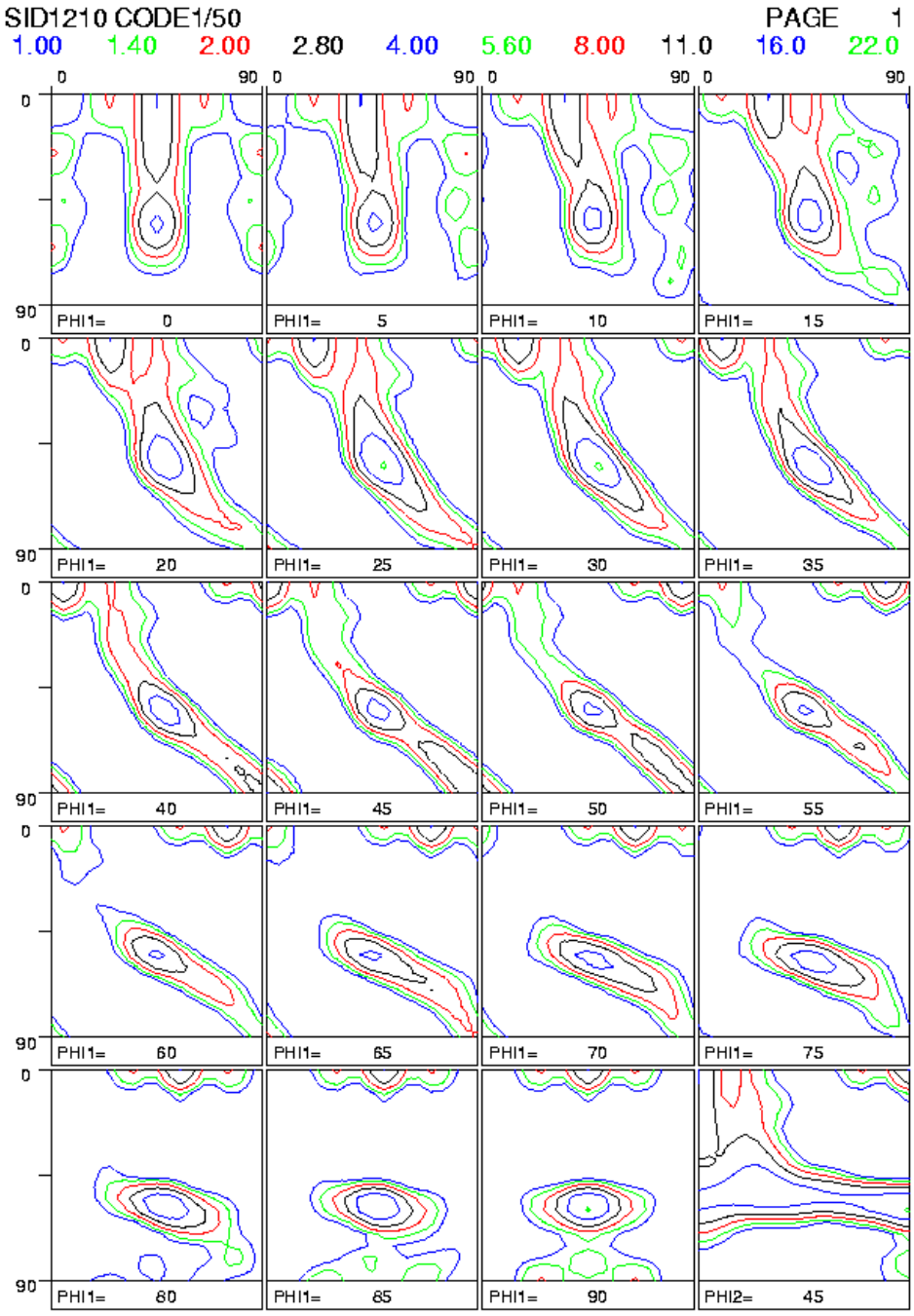

Figure 55: Sections of the ODF of SPXI 250 steel

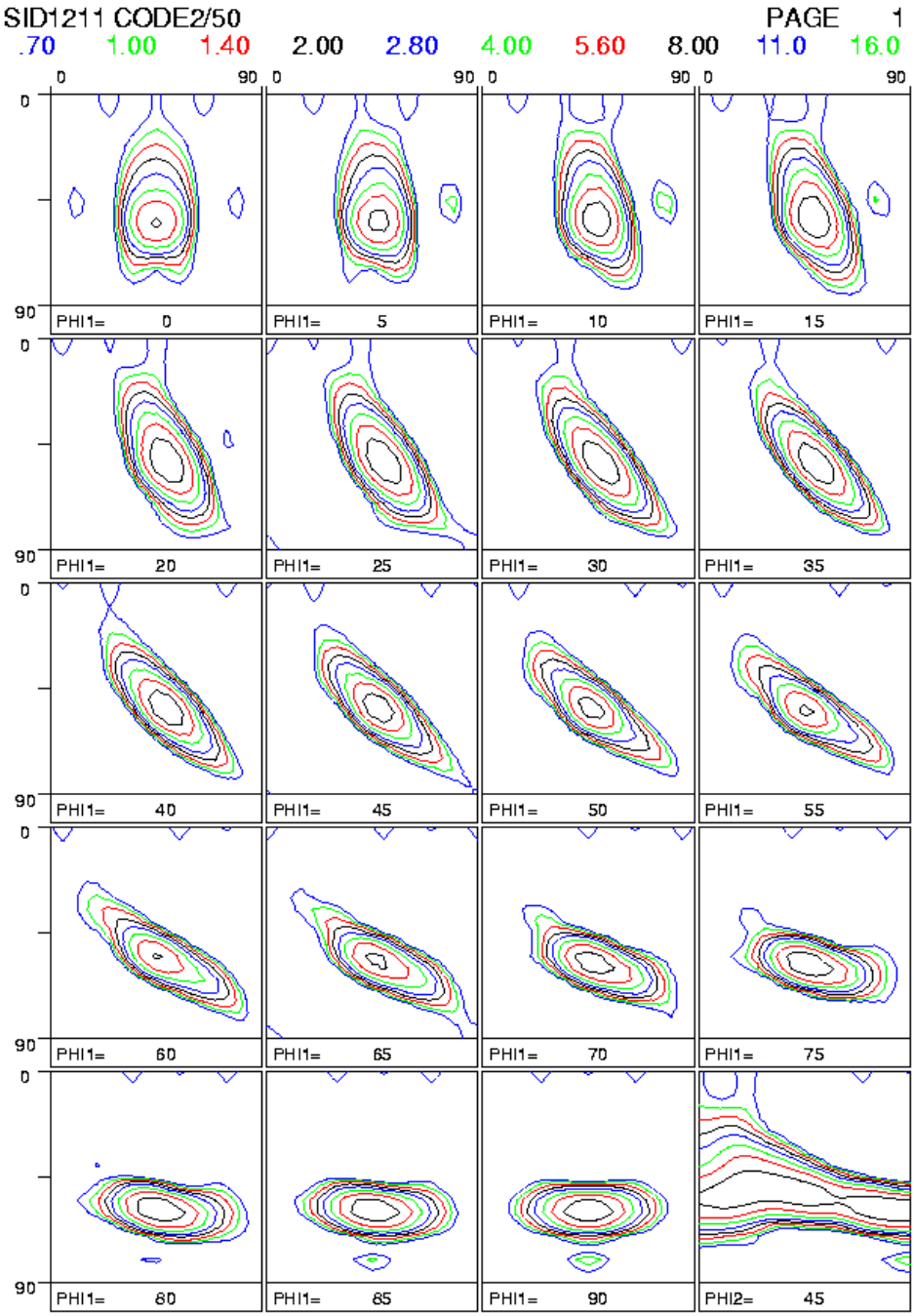

Figure 56: Sections of the ODF of ULC Ti steel

3.2 Experimental tests and procedures

Four experimental deep drawing tests have been conducted by RDCS. For both steels, 2 lubrication techniques were used. The first lubricant is an oil and the corresponding Coulomb friction coefficient (μ) is 0.13. The second lubrication technique makes use of a nylon film placed between the blank and the tools. For that case, the friction coefficient is smaller (μ=0.02).

A TOOLS AND BLANK GEOMETRY

A hydraulic press has been used for the deep drawing tests. The punch force is applied by a hydraulic jack. The blankholder force is also applied by hydraulic jacks acting on the corners of the blankholder. The blankholder maintains the steel sheet during the deep drawing process in order to avoid wrinkling. Without any blankholder or with a too low blankholder force, wrinkles would appear at the zone of the sheet near the edges. A too high blankholder force would lead to failure of the steel sheet during the deep drawing process. A range can be found for the blankholder force. This range depends on the steel used for the deep drawing but also on the geometry of the final cup and particularly on the ratio of the blank diameter to the punch diameter (defined as the drawing ratio). A blankholder force of 10 tons (98,1 kN) has been used for the 4 deep drawing tests and did not lead neither to wrinkling nor to failure.

The geometry of the tools and the blank is defined in Figure 57. The blank and the tools are axisymmetric. The blank is a disc cut out the rolled steel sheet. The drawing ratio is 2.0 (=150/75).
The exact position of the symmetry axis of the punch, the matrix and the blankholder with respect to each other must be checked when the tools are mounted on the hydraulic press. The exact position of the symmetry axis of the blank must be carefully checked before each deep drawing process.

The 4 deep drawing processes are performed up to a drawing depth of 80 mm. Considering the geometry of the blank and the tools, this drawing depth yields to a non completely drawn cup. A part of the blank remains under the blankholder even at the end of the process. This can be noticed on the photo of the deformed cup (Figure 58).

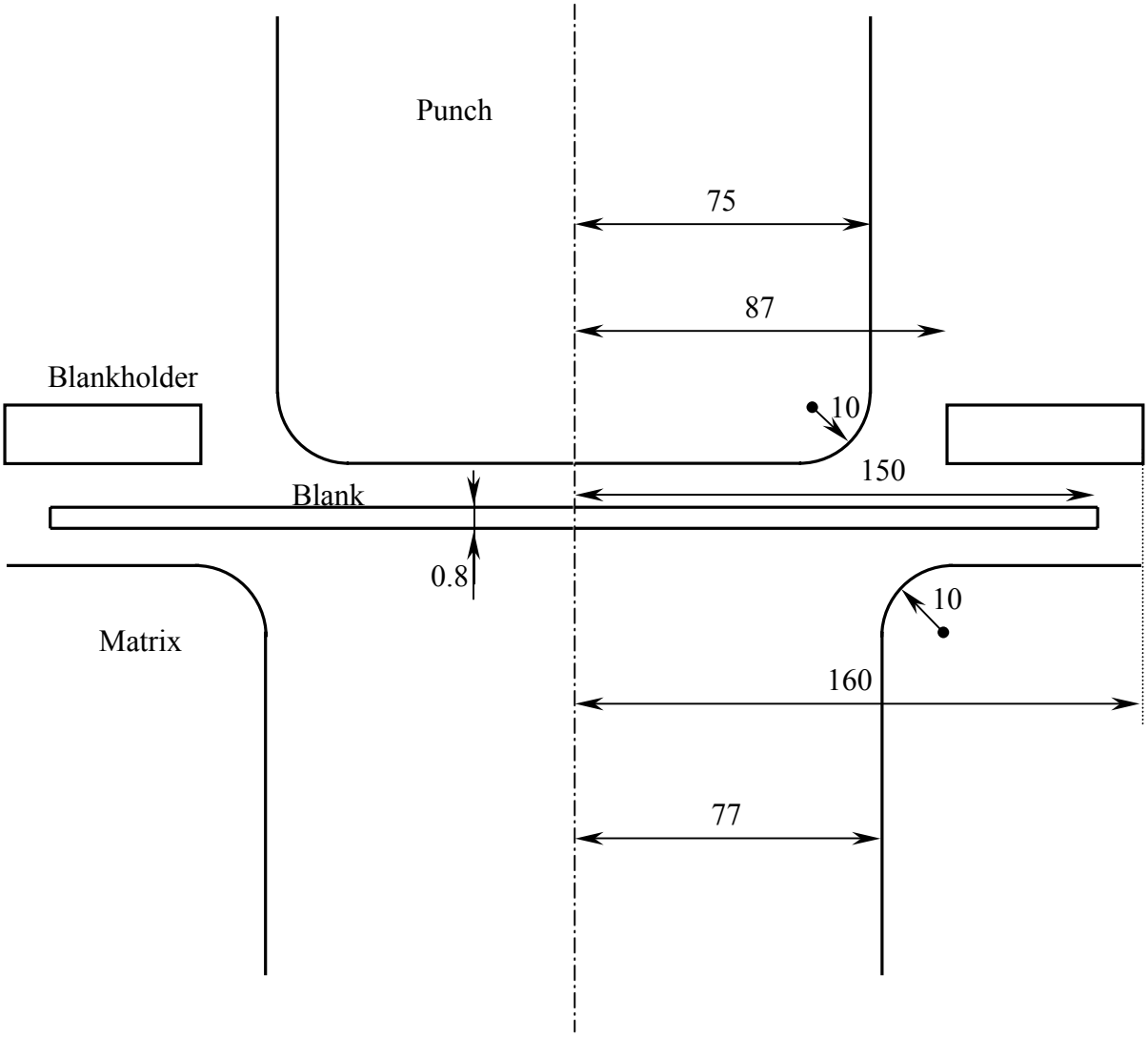

Figure 57: Geometry of the tools and the blank (dimensions in mm)

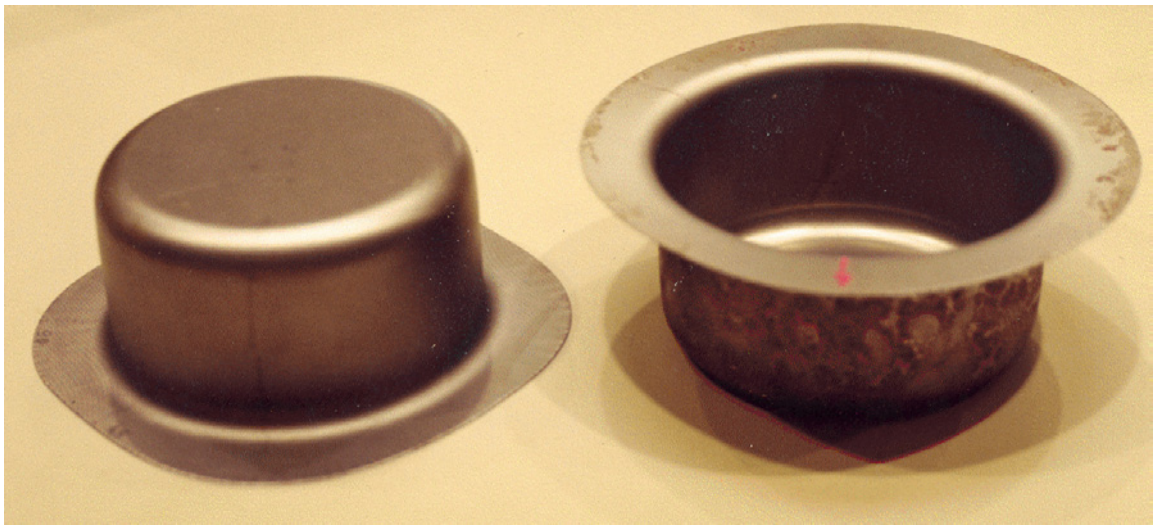

Figure 58: Photography of the deformed cup

B PUNCH FORCE MEASUREMENTS

During each deep drawing test, the punch force and the punch displacement are measured. The punch force as a function of the punch travel is presented in Figure 59 for the ULC Ti steel.

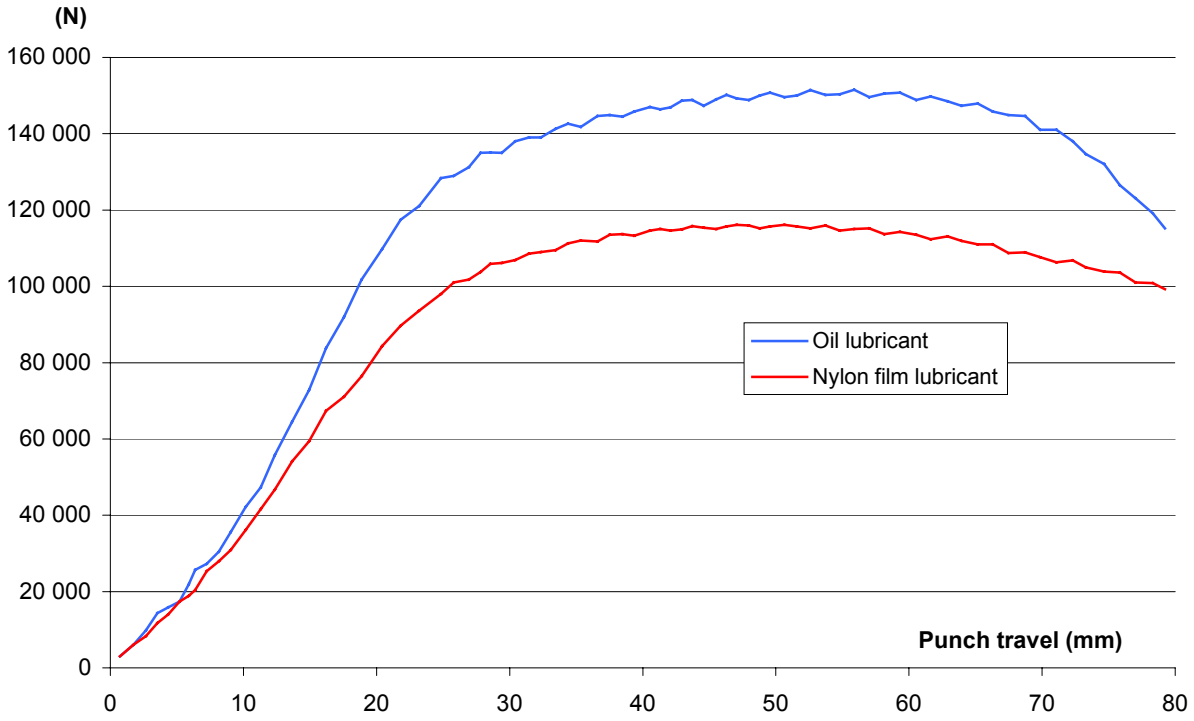

Figure 59: Punch force versus punch travel for the ULC Ti steel

The curves for the SPXI 250 steel are presented in paragraph 3.4.
At the beginning of the test, when the blankholder force is applied and the punch starts to move, the measurement cells are set to zero in order to avoid a shift of the measured curves.
In Figure 59, it can be noticed that the oil lubricant corresponding to a higher Coulomb friction coefficient yields to a higher punch force required to achieve the deep drawing process. The force needed to extract the blank clamped between the matrix and the blankholder is indeed higher if the friction is higher.
The oscillations of the 2 curves of Figure 59 are also present for the SPXI 250 steel. These oscillations, with approximately the same frequency have also been observed on other deep drawing processes achieved with the same hydraulic press. The hydraulic pomp generating the oil pressure is then suspected to be at the origin of these oscillations.

C THICKNESS STRAIN MEASUREMENTS

In order to analyse the deformed cups, their thickness is measured on several points. These points are aligned along the (deformed) rolling direction (RD), 45° from the rolling direction (45°) and along the transverse direction (TD) as presented by Figure 60.

For each of the 3 directions presented in Figure 60, around 30 measurements have been achieved, regularly placed along the 4 deformed cups.

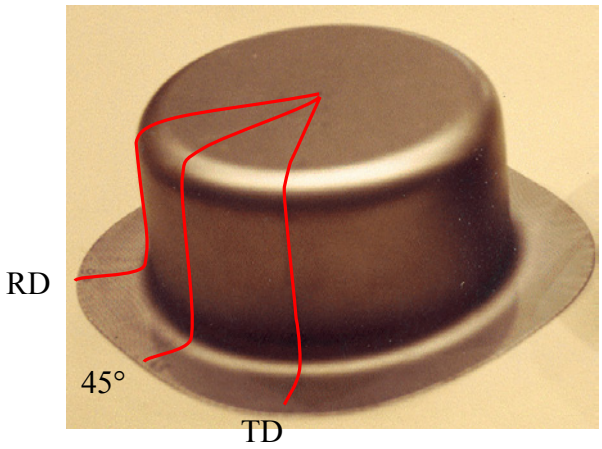

Figure 60: Rolling, transverse and 45° directions used for thickness and strain measurements

A Palmer micrometer is used for these thickness measurements. To make it possible, each cup was cut along directions at around -22.5°, 22.5°, 67.5° and 112.5° from the rolling direction. The measurement directions were not affected by these cuttings. Quarters of the deformed cups were obtained allowing us to place correctly the Palmer micrometer at each measurement point.
The precision of the thickness measurements is about 0.01 mm on the flat parts of the cup. At the level of the curved parts, even if the 2 parts of the Palmer micrometer in contact with the steel sheet are hemispherical, allowing a pointwise contact, the precision is worse.
The precision of 0.01 mm in the thickness measurements corresponds, for the steel sheets of 0.8 mm thick, to a precision of 0.0125 (or 1.25 %) in the true thickness strain measurements. They are presented in paragraph 3.4.

D STRAIN MEASUREMENTS IN THE PLANE OF THE SHEET

In addition to the thickness measurements, the strains in the plane of the deformed steel sheets are examined. To do so, a grid of circles is printed on the blank before the deep drawing process starts. The diameter of each circle is 2 mm. They are printed every 3 mm covering uniformly the whole surface of the blank.
These circles deform the same way as the sheet. Each circle becomes an ellipse whose dimensions are linked to the strains of the steel sheet.
Along the 3 strain measurement directions of Figure 60, an optical measure of the deformed circles has been achieved on the same points as the ones whose thickness was measured.
For each measurement, the picture of the ellipse is enlarged on the screen. As this ellipse is not perfect (thickness of the line, non uniform deformation, printing problems,…), a perfect ellipse is fitted on it (see Figure 61).

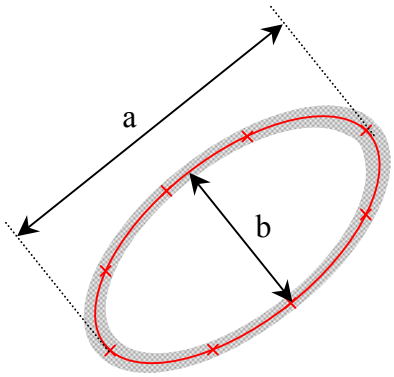

Figure 61: Fitting of an ellipse on the deformed printed circle

The fitting procedure can be automatic: a software computes an ellipse (in red in Figure 61) by picture recognition and prints it on the screen, superimposed to the visualised one (in grey). The fitting can also be interactive: the user picks several points on the picture of the deformed ellipse (the red crosses) and the software fits an ellipse on these points.
The first and the second principal strains of the steel sheet in the zone near the ellipse can be easily determined when the lengths of the axes (a and b) of the perfect ellipse are known:

$$\varepsilon_1 = \ln\frac{a}{d_0}$$
$$\varepsilon_2 = \ln\frac{b}{d_0} \qquad (190)$$

where ε_1 and ε_2 are the first and the second principal strains and d_0 is the diameter of the initial circle. To be accurate, the nominal diameter of the circles (2 mm) is not used as a value for d_0. A calibration procedure must be achieved: the diameter of some circles printed on a steel sheet not submitted to any deformation process is measured. The mean value of these measured diameters is used as an accurate value of d_0.

With this principal strain measurement technique, the orientation of the principal strain axes is not known. Indeed, the optical device is hold against the steel sheet by the hand; the orientation is not fixed.
For technical reasons, the grid of circles was printed at the upper surface of the cup (in contact with the punch and the blankholder) for the oil lubricated cases and at the lower surface (in contact with the matrix) for the nylon film lubricated cases.
The measured strains are presented in paragraph 3.4.

Just like the thickness strain measurement, the optical measurement of the principal strains is well adapted and accurate for the flat parts of the deformed cup. But, on the curved parts of the cup, the accuracy is lower. Indeed, the optical device must be located at a predefined distance of the measurement point to reproduce correctly the picture on the screen. Along the curves, this distance cannot be fulfilled as shown by Figure 62.

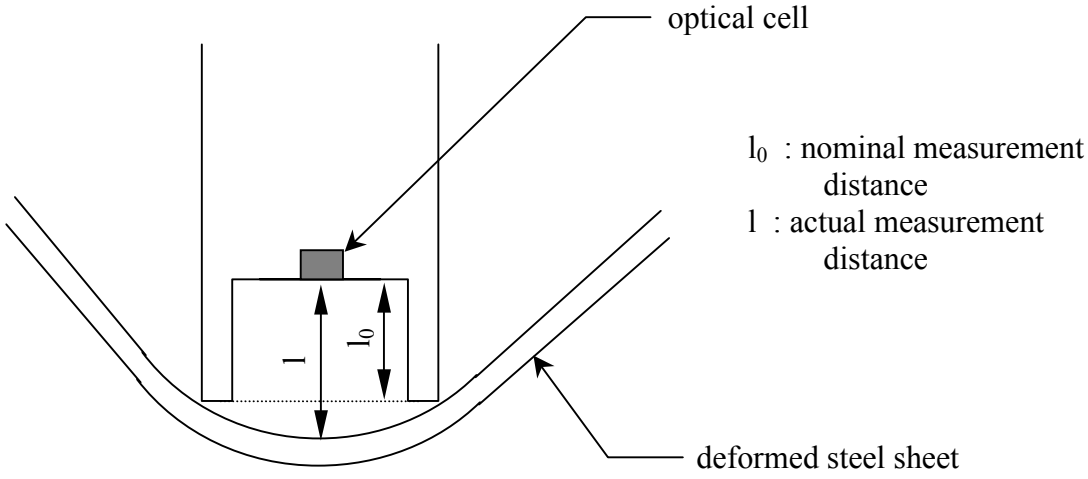

Figure 62: Optical strain measurement device

In the curve parts of the deformed cup, the error on strain measurements is difficult to estimate. However, the plastic incompressibility during plastic deformation can be advantageously taken into consideration. Indeed, at the end of the deep drawing process, the cup is unloaded. The stress state at each point of the deformed cup is relatively low compared to the stress state during the process; only residual stresses remain. Consequently, the strain state on the deformed cup is mainly due to plastic deformation. The plastic incompressibility then imposes that the sum of the 2 principal strains in the plane and of the thickness strain is equal to 0.

Figure 63 presents the sum of the 3 principal strains as a function of the curvilinear abscissa from the pole of the deformed cup (the pole is the intersection of the axisymmetry axes of the blank or of the tools; it is the centre of the cup) for the 3 measurement directions of Figure 60. These results correspond to the SPXI 250 steel with an oil lubricant. As shown in Figure 63, the plastic incompressibility is more or less respected on the measured points along the 3 measurement directions except for curvilinear abscissa from 60mm to 80mm and from 130mm to 160mm. These 2 zones correspond to the 2 shoulders of the deformed cup. The misfit of the plastic incompressibility is mainly due to errors on the measured strains in the shoulders of the cup.

The lack of accuracy of the measured strains on the curved parts of deformed cups has also been noticed by Frénois (2001).

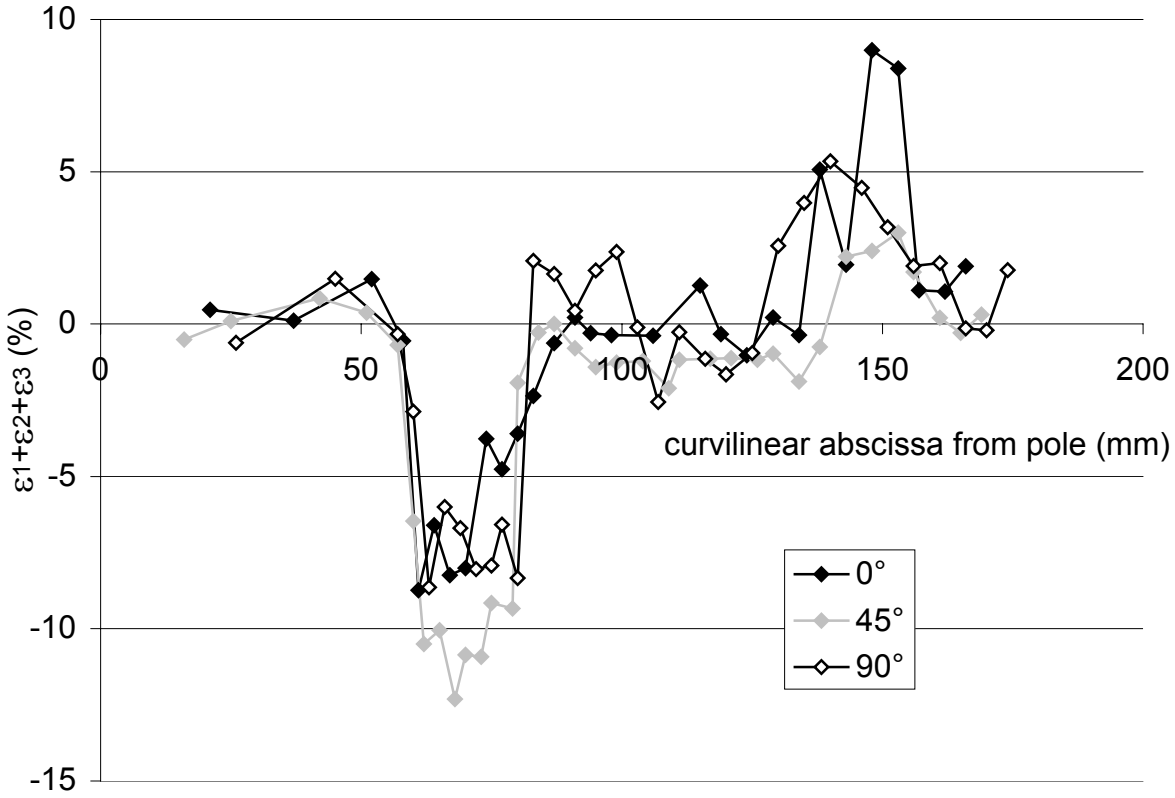

Figure 63 : Sum of the measured principal strains along the rolling direction, transverse direction and 45° direction (SPXI 250 with oil lubricant)

E EARING MEASUREMENTS

The anisotropy of the steel sheet can be taken into consideration by looking at the earing profile of the deformed cup. The geometry of the blank and the tools is axisymmetric; with an isotropic steel sheet, the deformed cup would also be axisymmetric (no earing).
As the deep drawing process described here is stopped after 80mm of punch travel, the steel sheet is not completely drawn. The earing profile does not correspond to the height of the deformed cup (which is fixed by the punch travel) but it corresponds to the diameter of the cup as a function of the orientation with respect to the rolling direction.
The diameter of the deformed cups has been measured manually every 5°. Considering the orthotropic symmetry of the rolled steel sheet, the diameters measured from 0° to 90° should be identical to those measured from 90° to 180°. However, due to experimental errors, this is not exactly the case and the mean value is used.

Large discrepancies have indeed been noticed between the 2 symmetric diameter measurement directions. A non correct location of the blank at the beginning of the deep drawing process can be at the origin of such errors. If the centre of the blank does not exactly correspond to the centre of the tools, the earing profile can be largely influenced. We have also noticed irregularities in the earing profile that could not be induced by the deep drawing process. These irregularities are angles that must have been done during the cutting of the blank.

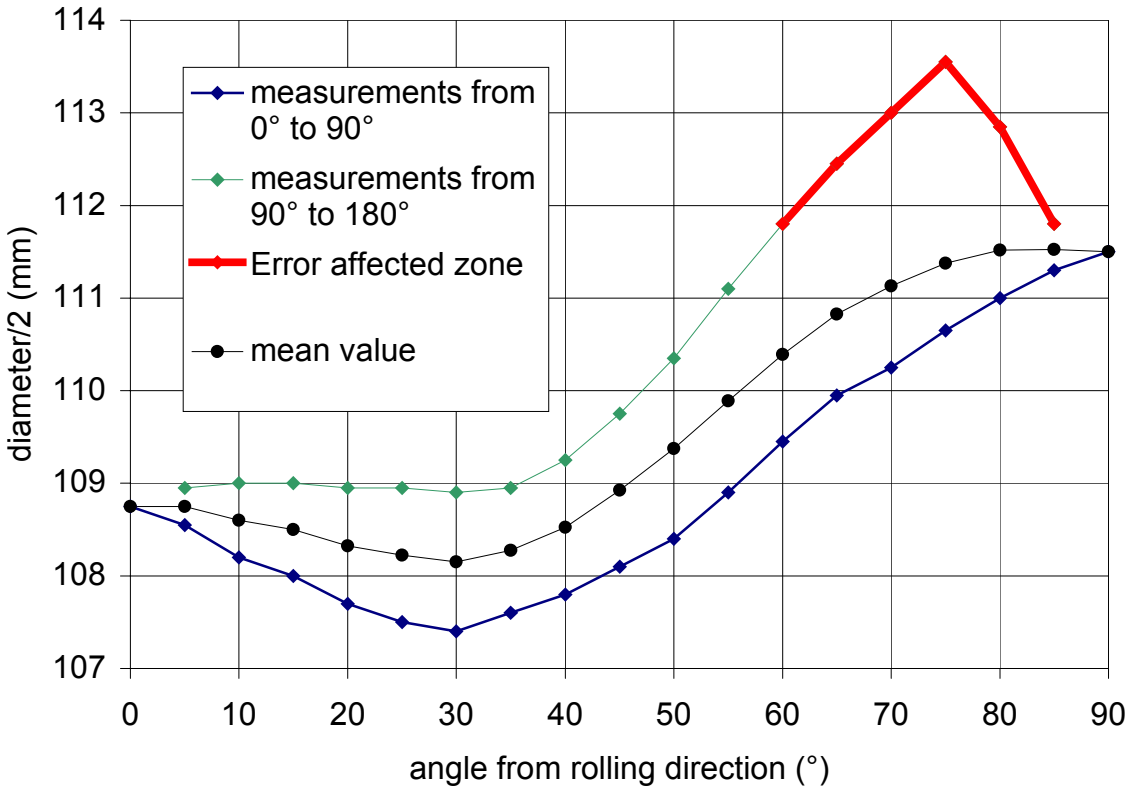

Figure 64: Earing profile measurement: error due to a wrong geometry of the blank

Figure 64 presents the measured diameters of the deformed cup for the SPXI 250 steel with oil lubricant. The diameters measured from 90° to 180° are reported in the graph in the range 0° to 90° thanks to the symmetry of the blank. As it can be seen, the symmetry is not perfect; the mean value is then used. Furthermore, an angle appears in the deformed cup (in red in Figure 64); the error affected zone is eliminated when the mean value is computed.
An error on the exact orientation of the rolling direction can also be at the origin of errors in the earing profile.

F TEXTURE MEASUREMENTS

The micro-macro model that we have developed takes texture into account to describe the anisotropy of the material. It is also able to compute the texture evolution during plastic deformation. That is the reason why it is interesting to compare the computed texture to the measured one at the end of the drawing process.
The texture evolution depends on the plastic deformation and is then supposed to be different from one point to another of the cup. We have selected points where the evolution is supposed to be the most important. Points at the mid-height of the flange of the cup are selected. The plastic deformation are indeed larger there than under the punch or between the blankholder and the matrix. Frénois (2001) had also noted that the texture evolution is the most significant at the flange of the cup but is low at the pole and under the blankholder (note that Frénois (2001) considers the hydroforming of a tantalum blank with a hemispherical punch).
Finally, points at mid-height of the flange along the rolling, the transverse and the 45° directions for the SPXI 250 steel with oil lubricant and along the rolling and 45° directions for the SPXI 250 with nylon film lubricant were selected for texture measurement.

For these 5 points, a square sample of 20mm long is cut out the deformed cup around each point. The samples were sent to the laboratory in charge of the texture measurements: the MTM department of the Katholieke Universiteit Leuven.
The samples were polished up to their mid-thickness in order to measure the evolved texture at that depth. Frénois (2001), for his deep drawing case, noted that the measured texture is little influenced by the depth at which it is measured. Dawson et al. (1998) studied more deeply the variation of the texture through the thickness of a sheet; a rolled aluminium plate was analysed.

For the samples cut out at 0° or 90° from the rolling direction, the sides of the samples are parallel to the rolling direction and the transverse direction of the non deformed blank. As the deep drawing process is symmetric about these axes, the orthotropy of the steel sheet is conserved for these samples. This fact has indeed been proved by the texture measurements.
On the other hand, for the samples at 45° from the rolling direction, the sides of the samples, which are symmetry axes for the deep drawing process are aligned at 45° from the initial orthotropy axes of the blank. The initial orthotropy of the blank is then not conserved during the deep drawing process. The measured textures confirm this point; this is consistent with Daniel et al. (1993) which achieved similar measurements.

The measured textures are presented in paragraph 3.4.

3.3 Finite element model

As already stated, the geometry of the blank and the tools is axisymmetric. However, due to the orthotropy of the material behaviour, an axisymmetric 2D analysis cannot be performed. A 3D analysis, modelling only a quarter of the deep drawing test is achieved. Adequate boundary conditions must be imposed at the symmetry axes. These symmetry axes are defined as the global X and Y axes in the finite element mesh; the global Z axis is parallel to the punch displacement direction.

A FINITE ELEMENT MESH

The geometry of the finite element model is that of the experimental process shown by Figure 57.
The tools are considered as perfectly rigid and are modelled by foundation elements. The mesh consists in triangular facets defined by 3 nodes. The volume of the tools is not modelled; only their external surface is meshed.
The mesh of the quarter of the punch is made of 456 triangular facets as presented by Figure 65. The matrix is meshed with 576 facets and the blankholder with only 48 facets because it is flat. A total of 626 nodes are required for the 3 tools.
In addition, for each tool, one pilot node is defined to determine the position of the tool during the deep drawing simulation. Each pilot node fixes the position of the whole tool to which it is linked. The pilot node of the punch can be seen in Figure 65 (the small circle on the symmetry axis).
At the beginning of the deep drawing simulation, the pilot node of the blankholder is used to apply the blankholder force on the blank (98.1 kN). Then, the pilot node of the punch drives the punch down to achieve the simulation up to a displacement of 80mm. The pilot node of the matrix remains fixed throughout the process.

Figure 65: Mesh of the punch with triangular facets

The blank is meshed with BLZ3D finite elements (see Zhu and Cescotto (1994)). BLZ3D is a solid finite element with 8 nodes using a mixed formulation (in stress and strain). These elements are adapted for large strains and large displacements. One integration point per element is defined.
A quarter of the circular blank is meshed with 2256 BLZ3D elements in the shape of 3 layers of 752 elements. The mesh is presented by Figure 66. 3192 nodes are defined for the mesh of the blank.

Contact elements are required to model the contact of the blank with the tools. CFI3D contact elements are used (see Habraken and Cescotto (1998)). They consist in plane elements defined by 4 nodes; 4 integration points per element are defined. These contact elements are meshed on the surface of the blank using the same nodes that the ones defined for the blank. For the contact between the blank and the matrix, 752 CFI3D elements are located on the lower layer of the blank. For the contact between the blank and the punch or the blankholder, 752 contact elements (for each tool) are located on the upper layer of the blank. As the nodes used for the meshes of the contact elements and the ones used for the mesh of the blank are the same, the contact elements will deform like the blank and follow its displacements.

A section of the finite element mesh is presented by Figure 67. The pilot nodes of the punch and the blankholder can be seen.

In order to reduce computation time, an efficient sub-tree algorithm is used for the contact searching. This algorithm can be summarised as follows: for each tool, at the beginning of the finite element simulation, all the foundation triangular facets are placed in one box; this box is a fictitious volume having its 6 faces parallel to one of the planes formed by the global X, Y and Z axes. This box is divided in 2 along the 3 global directions forming 8 sub-boxes. The

triangular facets are classified into these 8 sub-boxes according to their coordinates. This procedure is repeated until each sub-box contains only one triangular facet.
Then, during the finite element simulation, when the contact of one contact element with its corresponding tool is examined, the interesting triangular facet is rapidly found using a tree game algorithm on the basis of the successive sub-boxes.
As the tree of boxes is made at the beginning of the simulation on the basis of the initial coordinates of the triangular facets forming one tool, this technique can only be used with non deformable tools. A rigid displacement of a tool can be taken into account by shifting all the boxes.

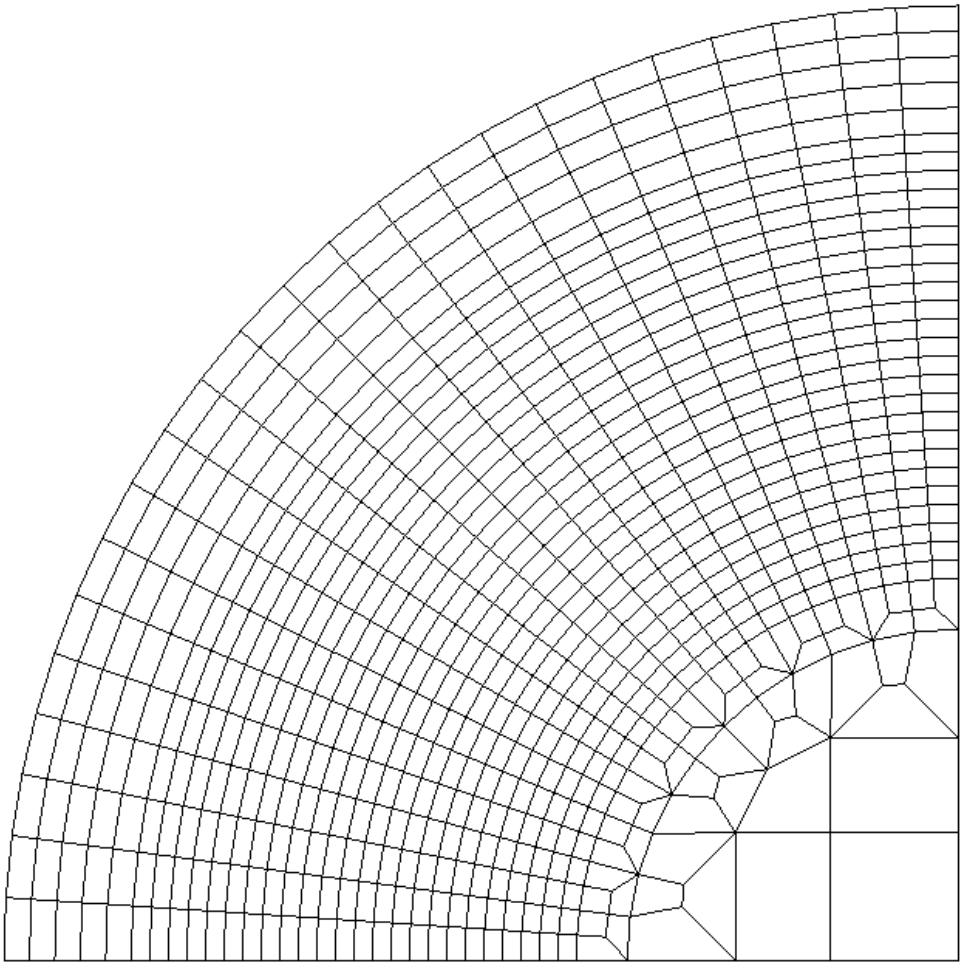

Figure 66: Mesh of the blank with 3 layers of 752 solid elements

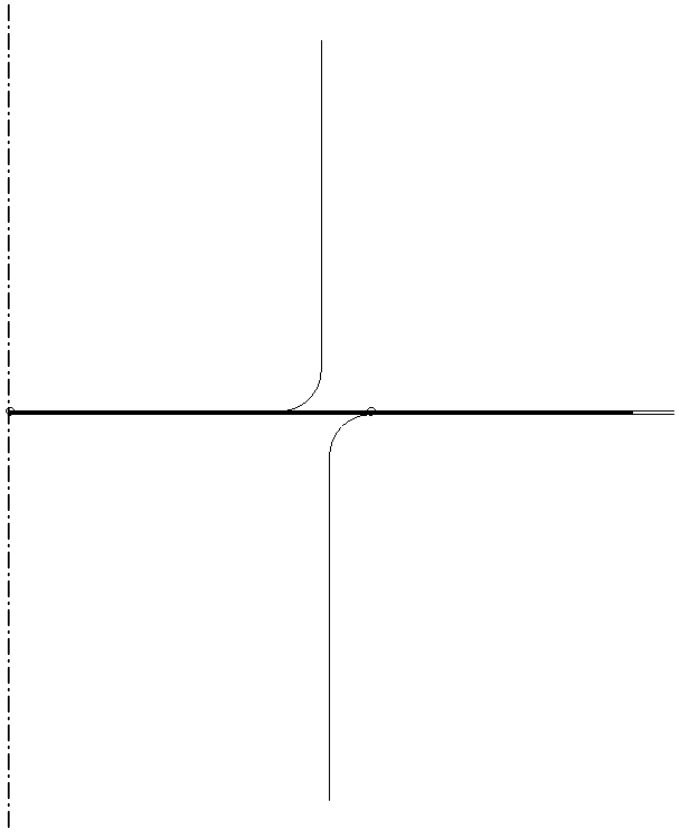

Figure 67: Section of the finite element mesh for the deep drawing simulation

During the deep drawing simulations, large displacements and large rotations occur. The behaviour of the steel sheet must follow these rotations to represent correctly the anisotropy of the material. Local axes, which are linked to the actual orientation of the steel sheet during the simulation, are used. Their position is computed according to an assumption of constant symmetric velocity gradient at each step. Details can be found in Munhoven (1995), Munhoven et al. (1995) and de Montleau (2003). The initial orientation of the local axes corresponds to the orthotropy axes of the steel sheet (the rolling, the transverse and the normal directions).

B CONSTITUTIVE LAWS

Several constitutive laws have been investigated to model the mechanical behaviour of the blank during the deep drawing simulation.

The first one is of course the micro-macro law using the stress-strain interpolation technique. As this constitutive law is largely presented in chapter 3, only the input data are described here. The input data can be separated in 2 groups: the data needed to characterise the behaviour of the material and the data required for computation related aspects.

The data linked to the material are:

- Both steels have a bcc crystal lattice. Their 24 slip systems are summarised by the 2 slip system families $\{1\ 1\ 0\}\langle 1\ 1\ 1\rangle$ and $\{1\ 1\ 2\}\langle 1\ 1\ 1\rangle$. These slip systems are required by Taylor's model to compute points of the yield locus.
- The elastic properties are required by the constitutive law. Young's modulus and Poisson's ratio given in Table 9 are used. Isotropic elastic properties are assumed.

- The work hardening parameters presented in Table 8 are also input for the law.
- To represent correctly the anisotropy of the material behaviour, the texture is required. From the texture measurements, the ODFLAM procedure (recent version developed by the team of professor Van Houtte) is used to compute a set of crystal orientations representative of the material behaviour. As it has proved to be a good compromise between accuracy and computation time, a set of 2000 crystals is used for these deep drawing simulations.

The data linked to numerical aspects are:
- The size of the interpolation domain (the angle ϑ of equation (47)) must be chosen by the user. This parameter has been largely investigated in Duchêne (2000). A size of 5° is chosen. This choice yields to reasonable number of local yield locus updatings with a good accuracy.
- 20 sub steps are used for the stress integration.
- The tangent stiffness matrix is computed analytically to reduce computation time.
- The user can choose to activate or not the texture evolution computation. If it is not activated, the initial texture of the material is used throughout the deep drawing simulation. This allows computation time reduction but the micro-macro model is not used with all its features. If the texture evolution computation is activated, the user must enter the frequency of the texture updatings. Up to now, the frequency is defined by a number of time steps separating 2 successive texture updatings. For the simulations presented here, a texture updating occurs every 10 time steps.

The stress-strain interpolation based constitutive law without texture evolution is referred to as **Minty** in paragraphs 3.4 and 3.5 (indeed, Minty is the name of the subroutine). If the texture evolution is activated, **Evol** is used to represent the corresponding results.

The second constitutive law used is the analytical 6th order series yield locus based on points of the yield locus computed by Taylor's model and linked to initial texture. This constitutive law is described in Munhoven et al. (1996) and Winters (1996) and is referred to as **ANI3VH**.

We have also performed the deep drawing simulations with a classical Hill (1948) constitutive law. Hill (1948)'s yield locus is largely implemented in several finite element codes and then allows the comparison of different FE codes eliminating the influence of the yield locus formulation.
Hill (1948)'s yield locus is defined by:

$$f = \frac{1}{2} \cdot \underline{\sigma}^T \underline{\underline{H}} \underline{\sigma} - \sigma_F^2 = 0 \tag{191}$$

where $\underline{\sigma}$ is the yield stress expressed as a 6 component vector; σ_F is a scalar describing the work hardening. The isotropic work hardening evolution of equation (31) is also used for the Hill constitutive law. $\underline{\underline{H}}$ is the matrix containing the Hill parameters describing the anisotropy of the material. It is written:

$$\underline{\underline{H}} = \begin{pmatrix} G+H & -H & -G & 0 & 0 & 0 \\ -H & H+F & -F & 0 & 0 & 0 \\ -G & -F & F+G & 0 & 0 & 0 \\ 0 & 0 & 0 & 2N & 0 & 0 \\ 0 & 0 & 0 & 0 & 2L & 0 \\ 0 & 0 & 0 & 0 & 0 & 2M \end{pmatrix} \tag{192}$$

The 6 parameters of this matrix must be adjusted to fit correctly the behaviour of the steel sheet. Three possibilities can be considered.

1. If the yield stresses for 3 tensile tests along the orthotropy axes and the yield stresses for 3 shear tests along the same axes are known, the 6 Hill parameters can be determined according to the following equations:

$$\sigma_{YY}^{yield} = \sqrt{\frac{2}{H+F}} \cdot \sigma_{XX}^{yield} \tag{193}$$

$$\sigma_{ZZ}^{yield} = \sqrt{\frac{2}{G+F}} \cdot \sigma_{XX}^{yield} \tag{194}$$

$$\sigma_{XY}^{yield} = \sqrt{\frac{1}{N}} \cdot \sigma_{XX}^{yield} \tag{195}$$

$$\sigma_{XZ}^{yield} = \sqrt{\frac{1}{L}} \cdot \sigma_{XX}^{yield} \tag{196}$$

$$\sigma_{YZ}^{yield} = \sqrt{\frac{1}{M}} \cdot \sigma_{XX}^{yield} \tag{197}$$

with the additional condition :

$$H + G = 2 \tag{198}$$

This condition states that the yield stress for a tensile test along X direction ($=\sigma_{XX}^{yield}$) is equal to the initial value of σ_F, i.e. the value before any plastic deformation or work hardening occurs.

As the yield stresses for shear tests are not easy to obtain experimentally for steel sheets, the 3 conditions (195), (196) and (197) to compute N, L and M can be advantageously replaced by the following one using the tensile test along the 45° direction:

$$\sigma_{45°}^{yield} = \sqrt{\frac{8}{G+F+2N}} \cdot \sigma_{XX}^{yield} \tag{199}$$

with the additional conditions:

$$N = L = M \tag{200}$$

2. In the present work, the tensile yield stresses along the X, Y, Z and 45° axes were not measured experimentally but computed by Taylor's model on the basis of the texture of the material. This method yields to a Hill formulation close to the texture measurements and avoids the problem of experimentally measuring the yield stress along the direction normal to the steel sheet. The corresponding Hill parameters are presented in Table 10.

3. Another fitting method perhaps more convenient in the case of metal sheets consists in performing 3 tensile tests and using the following fitting through the Lankford coefficients:

$$r_0 = \frac{H}{G}; \quad r_{90} = \frac{H}{F}; \quad r_{45} = \frac{2N - F - G}{2(F + G)} \tag{201}$$

with the additional conditions:

$$H + G = 2; \quad N = L = M \tag{202}$$

The fitting on the basis of the experimentally measured Lankford coefficients was also achieved for SPXI 250 and ULC Ti steels. The corresponding Hill parameters are also in Table 10.

Table 10: Hill parameters for SPXI 250 and ULC Ti steels

steel	Fitting on	*F*	*G*	*H*	*N*	*L*	*M*
SPXI 250	Yield stresses	1.001	1.047	0.953	2.938	2.938	2.938
	Lankford coefficients	0.814	0.974	1.026	2.892	2.892	2.892
ULC Ti	Yield stresses	0.965	0.970	1.030	2.899	2.899	2.899
	Lankford coefficients	0.557	0.683	1.317	2.761	2.761	2.761

It should be noticed that the 3 fitting procedures presented above do not provide the same shape of the yield locus. This clearly appears in Table 10. Indeed, each fitting procedure gives enough equations to compute the 6 Hill coefficients, but Hill's model is not close enough from the actual yield locus shape to reach an unique set of Hill's parameters.
However, for an isotropic material, the von Mises criterion can be recovered. The condition on the Lankford coefficients gives:

$$\left.\begin{aligned} r_0 &= 1 \\ r_{90} &= 1 \\ r_{45} &= 1 \end{aligned}\right\} H = G = F = 1; N = L = M = 3 \tag{203}$$

and the condition on the yield stresses gives:

$$\left.\begin{aligned} \sigma_{YY}^{yield} &= \sigma_{ZZ}^{yield} = \sigma_{XX}^{yield} \\ \sigma_{45°}^{yield} &= \sigma_{XX}^{yield} \end{aligned}\right\} H = G = F = 1; N = L = M = 3 \tag{204}$$

A mixed fitting procedure between the fitting on the yield stresses and the fitting on the Lankford coefficients can also be defined:

$$\mathcal{H}^{mixed} = \chi \cdot \mathcal{H}^{r} + (1 - \chi)\mathcal{H}^{sig} \tag{205}$$

where - $\mathcal{H}^{r}$ represents the Hill parameters fitted on the Lankford coefficients,
- $\mathcal{H}^{sig}$ represents the Hill parameters fitted on the yield stresses,

- $\mathcal{H}^{mixed}$ represents the mixed Hill parameters,
- χ is the fitting parameter.

For a fitting parameter χ equal to 0 or 1, the fittings presented in Table 10 are recovered. The results of the deep drawing simulations presented in paragraph 3.4 are obtained with a fitting based on the Lankford coefficients (χ=1); the influence of the fitting parameter is presented in paragraph 3.5 where a mixed fitting with χ=0.5 is presented.

The results with the Hill law are referred to as **Hill (r)** for χ=1 and **Hill (sig+r)** for χ=0.5

A constitutive law must also be used to model the contact between the contact elements and their associated tool. The contact law we used is called COU3DC (see Charlier and Cescotto (1988) and Habraken and Radu (1992)). It is a constitutive law for unilateral thermo-mechanical contact. A Coulomb dry friction law is used; the Coulomb friction coefficients are 0.02 for the nylon film case and 0.13 for the oil lubricated case.
The contact condition is enforced via a penalty method (an augmented Lagrangian method is also available with this contact law (Bille et al. (1994))). In case of contact between a contact element and a foundation, the repulsive stress (σ_C) is defined as:

$$\sigma_C = K_p \cdot \delta \tag{206}$$

where K_p is the penalty coefficient and δ is the penetration of the contact element inside the foundation.
To reduce the penetration, a high penalty coefficient should be used. On the other hand, a too large penalty coefficient yields to convergence problems. For the deep drawing simulations presented here, localisation of the strains on the flange of the cup have been noticed for too large penalty coefficients. These strain localisations correspond to deep drawn cups reaching failure, which does not correspond to the experimental observations.
In order to avoid these strain localisation problems without allowing a too high penetration, a penalty coefficient of 1000 N/mm^3 is used for the contact between the blank and the matrix and a coefficient of 500 N/mm^3 is used for the contact between the blank and the punch and the blankholder. A larger coefficient is used for the contact with the matrix because a large zone of the steel sheet is successively in contact with the matrix shoulder during the deep drawing simulation. The correct modelling of the curvature of the matrix shoulder is then expected to be an important point for the accuracy of the results.
With these penalty coefficients, no strain localisation occurred and the penetration is smaller than 15% of the thickness of the blank. The major penetration is observed for the contact of the blank with the shoulder of the punch.

The influence of the friction coefficient is analysed from an experimental point of view and a numerical point of view in paragraph 3.4. The influence of the penalty coefficient is examined in paragraph 3.5.

Finally, the local yield locus based on the hyperplanes method has not been used for the deep drawing simulations due to the convergence problem linked to this method.

C COMPUTATION

Most of these computation time consuming simulations have been achieved on the SGI Origin3800 computer present at the SEGI of the University of Liège. This computer is equipped of 60 processors allowing parallel computation.
Thanks to the work of Moto Mpong et al. (2002a), Moto Mpong et al. (2002b) and de Montleau et al. (2002), parallel processing is possible with the FE code Lagamine. This parallel approach is not an usual domain decomposition approach but a more local one using Open MP protocol. Also, the element loop is directly parallelised between the available processors and a direct solver adapted to multiprocessing has been implemented with the help of J.M. Cela of the University of Cataluna (Cela (2001)).

To have an idea of the computation time required for these deep drawing simulations depending on the constitutive law used, Table 11 presents the case of the SPXI 250 steel with oil lubricant and nylon film lubricant. The computation times reported in Table 11 are the sum of the computation times of each processor used in case of parallel computation. For instance, the case 'Evol' with nylon film lubricant required 299 hours of computation. Nevertheless, if this simulation is executed with 8 processors, the simulation can reasonably by achieved in 50 to 60 hours of real time depending on the acceleration factor (see Moto Mpong et al. (2002a) for more details).
A large influence of the constitutive law on the computation time can be noticed. Our model, especially when the texture is updated, requires large computation time. For instance, for the case 'Minty' with oil lubricant, it takes 113 hours of computation. Among these 113 hours, only 2% are used for the resolution of the equation system and 95% are spent in the constitutive law.
The higher computation observed for the Hill law compared to the ANI3VH law can be attributed to a larger number of sub-steps imposed (100 sub-steps for Hill and 4 sub-steps for ANI3VH)

Table 11: Computation times for the deep drawing simulations with SPXI 250 steel (hours)

Constitutive law used	Oil lubricated	Nylon film lubricated
'Minty'	113	123
'Evol'	297	299
'Hill (r)'	12	20
'ANI3VH'	6	9

3.4 Results

All the results available on the experimental cups have been computed with the numerical models for a validation purpose.
The experimentally drawn cups are treated successively. The case of SPXI 250 steel with oil lubricant is presented in paragraph A below; the same steel with a nylon film lubricant is treated in paragraph B while the oil lubricated ULC Ti steel appears in paragraph C. The cup with ULC Ti steel and nylon film lubricant is not further investigated.

A SPXI 250 WITH OIL LUBRICANT

(1) Strain measurements

For the numerical models described in paragraph 3.3 and for the experimental results, the principal strain distributions on a section along the rolling direction are reported in Figure 68. All these strains are measured on the upper layer of the cup due to technical reasons (see paragraph 3.2); the strains are computed numerically on the same layer.

On the deformed cup and on the strain distributions of Figure 68, 5 zones can clearly be distinguished on the cup:

- The first zone is the part of the steel sheet which is under the punch at the end of the deep drawing process. This zone is located near the pole and corresponds to a curvilinear abscissa *s* measured from the pole smaller than 60mm. The maximum principal strain in the plane of the sheet (E1 in Figure 68) is relatively small in this zone while large displacements take place. Indeed, in that part of the cup, the steel sheet follows the punch travel without large deformation.
  Figure 68 also shows the second (smallest) principal strain in the plane of the sheet along the rolling direction (E2 in the figure). Here again, a low constant value near the pole is reported. An equi-biaxial tension state or stretched zone is present (E1 ≈ E2).
  The thickness strain (E3) is negative, corresponding to a thickness reduction.
  The numerical curves are almost superimposed for all the constitutive laws. The low anisotropy of the SPXI 250 steel sheet is indeed well represented by all the numerical models. Furthermore, the freedom on the strain distributions is limited by the geometry of the deep drawing process.
  A significant difference from the experimental curves is observed. The differences can be explained by a poor modelling of the friction. The Coulomb friction law used with a constant coefficient of 0.13 is perhaps not adapted for all the zones of the cup (the friction of the steel sheet with the curved part of the punch is certainly different from the friction with the flat blankholder). A better agreement with experimental results is indeed reported for the nylon film lubricant presented in paragraph B.
- The second zone is the part of the steel sheet applied against the shoulder of the punch. It is for *s* between 60mm and 80mm. The strain state also corresponds to stretching in the second zone but with E1 larger than E2 (for the numerical curves). The difference between experimental curves and numerically computed ones can be explained in that zone by the errors in the measurements as explained in paragraph 3.2. Indeed, a maximum in E1 and E3 (in absolute value) is reported numerically but not in the experimental curves. This maximum is created at the beginning of the deep drawing simulation, for a punch travel of 20mm (80mm corresponds to the end of the deep drawing process). At that moment, the steel sheet in contact with the curved part of the punch is highly stretched due to the effect of the blankholder which retains the sheet. After that moment, the strains in this second zone remain constant.
- The third zone is the flange of the cup, corresponding to *s* between 80mm and 135mm. The maximum principal strain increases in this zone as *s* increases while the minimum principal strain decreases and is negative. The thickness strain is also negative but almost constant. This zone corresponds to a restrained zone typical of deep drawing processes (E1>0 and E2<0).
  The numerical results are in good agreement with experimental measurements in this third zone.

- The fourth zone corresponds to the steel sheet applied against the shoulder of the matrix (for *s* between 135mm and 155mm). In this zone, the restrained state is maximum and the thickness strain becomes positive (the thickness of the steel sheet increases).
- The last zone is the part of the steel sheet which remains under the blankholder at the end of the process (for *s* larger than 155mm). After the maximum of the previous zone, The restrained strain state decreases in this zone as the contact with the matrix and the blankholder reduces the tension of the sheet.
  The second principal strain (E2) is a compression strain and becomes larger than the tensile strain E1 (E1>0, E2< 0 and $\|E1\| < \|E2\|$). This strain state would give rise to instability and wrinkling without the action of the blankholder. But it yields to an increase of the sheet thickness.

The strains measured in the plane of the deformed cup (E1 and E2) can be compared to the Forming Limit Diagrams of the corresponding steel to check that they are all under the FLD curve. This must of course be the case because no failure occurred during the deep drawing processes presented here.
However, the FLD is only available for strain ratios (E2/E1) comprised between -0.5 and 1. A ratio of -0.5 corresponds to a simple tensile state and a ratio of 1 is for an equi-biaxial stretching state. Unfortunately, the most critical zone of the deformed cup is the curved part of the cup in contact with the matrix shoulder (zone 4) and is a restrained zone with a strain ratio of -1 (E2≈-E1). These strains cannot therefore be compared to the FLD.
Furthermore, the FLD are obtained for a radial loading of the steel sheet (a constant strain ratio) while the deep drawing process corresponds to complex loading paths which do not allow to use FLD for the prediction of failure (see Vacher et al. (1998)).

The strain distributions along a direction at 45° from the rolling direction are reported in Figure 69 and Figure 70 corresponds to the transverse direction. The differences between the curves at 0°, 45° and 90° from the rolling direction are due to the anisotropy of the steel sheet. However, the differences can hardly be noted on these curves. Therefore they do not constitute a convenient measure of the anisotropy of the material.

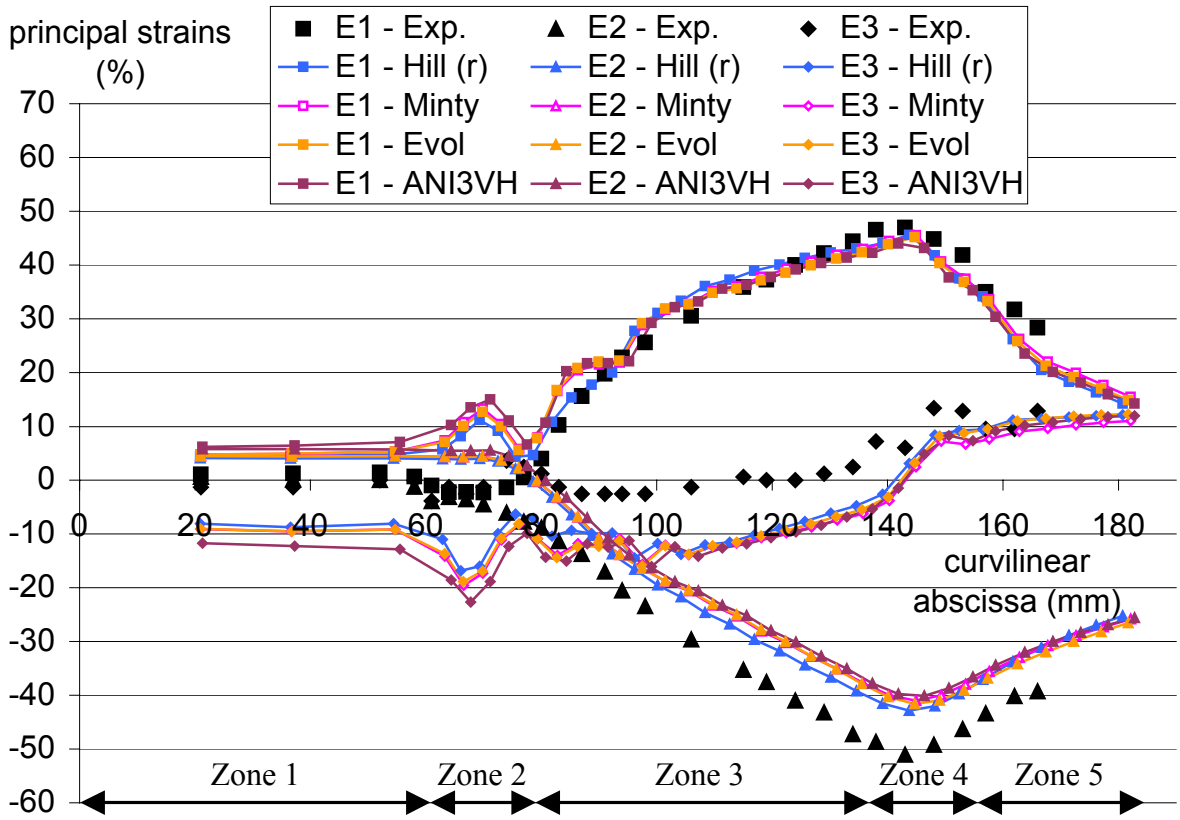

Figure 68: Principal strains along the rolling direction (SPXI 250 oil lubricated)

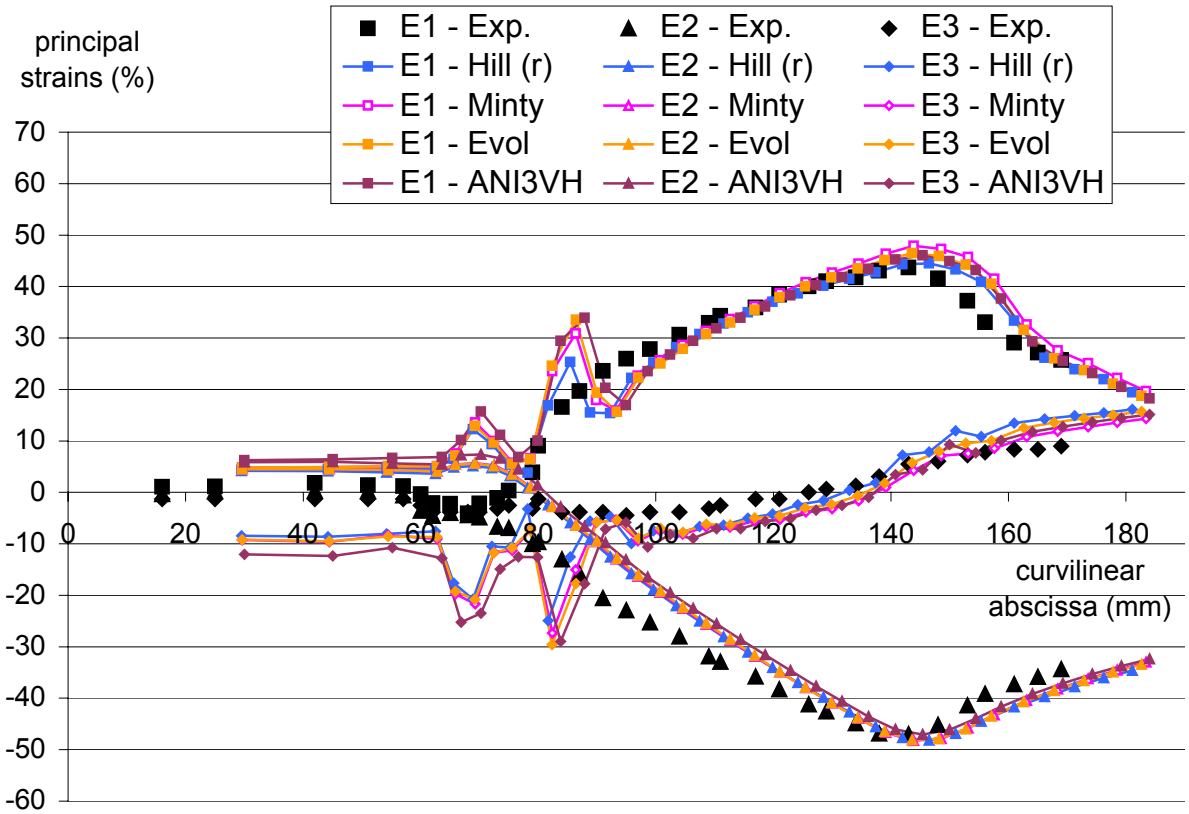

Figure 69: Principal strains along the 45° direction (SPXI 250 oil lubricated)

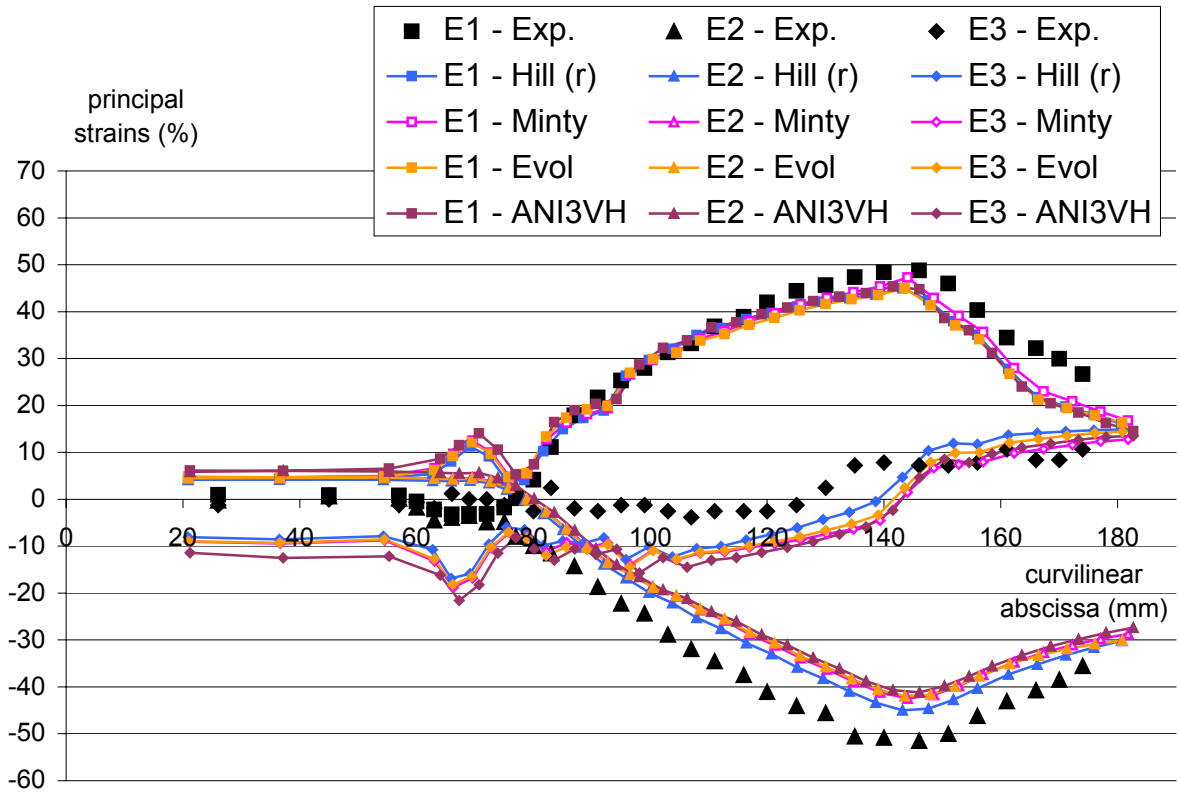

Figure 70: Principal strains along the transverse direction (SPXI 250 oil lubricated)

(2) Punch force

The punch force as a function of the punch travel is presented in Figure 71. These curves are not linked to the anisotropy of the steel sheet but to the global stiffness of the material and to the hardening behaviour.

The beginning of the deep drawing process is characterized by an increasing punch force linked to the increased force required to initiate the bending of the steel sheet. The maximum is reached when the steel sheet is completely applied against the shoulder of the punch and the matrix.

The end of the deep drawing process is characterized by a more or less constant punch force linked to the extraction of the steel sheet clamped between the matrix and the blankholder.

It can be noticed that all the numerical curves are almost superimposed except the one with the Hill constitutive law which is a little bit higher. These curves are in relatively good agreement with the experimental curve. The maximum is however too low and the slope at the beginning of the deep drawing simulation is too high. The error on the maximum of the curve is very sensitive to the Coulomb friction coefficient (see paragraph 3.5). The nominal coefficient (0.13 for this case) is perhaps not perfectly adapted to the deep drawing process.

The hardening parameters also have a large influence of the maximum of the punch force. These parameters have been fitted on a tensile test along the rolling direction which is certainly not a perfect representation of the hardening behaviour during a deep drawing process.

The error on the slope at the beginning of the simulation can be attributed to a poor modelling of the bending behaviour with the used finite element type. The influence of the finite element type is treated in paragraph 3.5 and a better agreement at the beginning of the simulation is indeed obtained with another finite element type.

The oscillations noticed on the numerical curves are due to the passing of the successive finite elements on the matrix shoulder. The elements are submitted to bending when they reach this zone. As the bending stiffness is different if one considers the bending of one finite element or the bending between two elements, oscillations are present on the punch force curves.

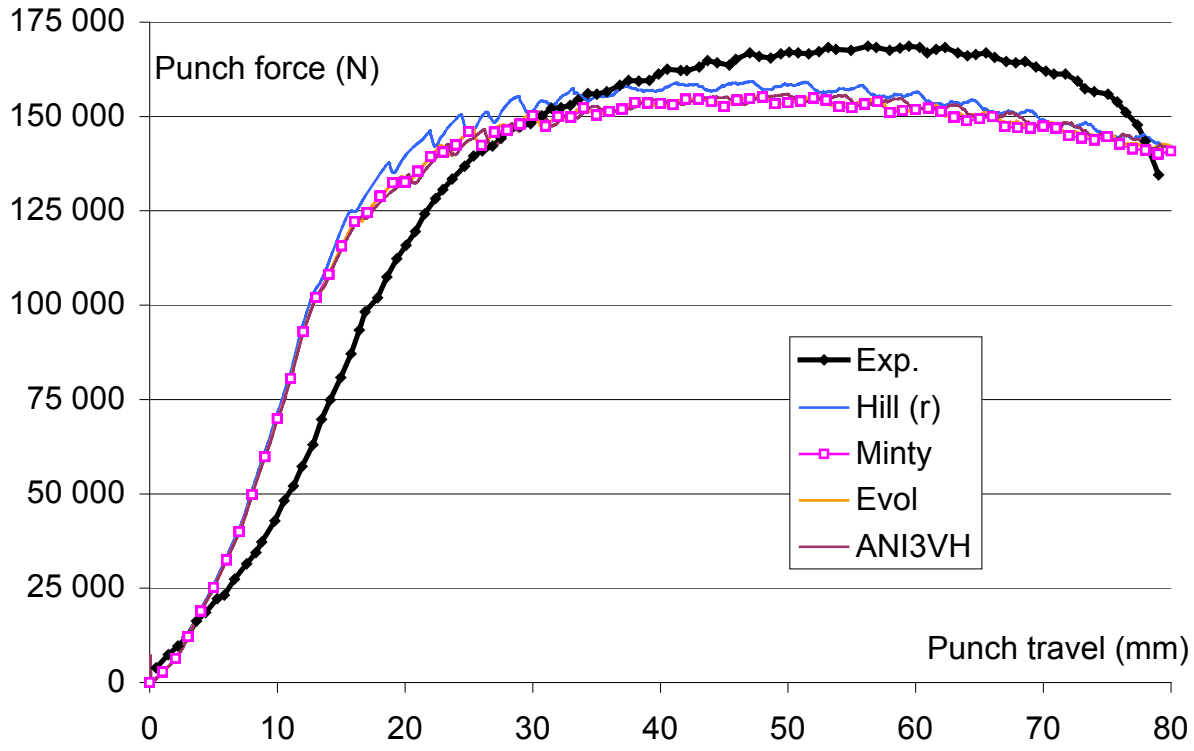

Figure 71: Punch force versus punch travel (SPXI 250 oil lubricated)

(3) Earing profile

Figure 72 presents the earing profile for the SPXI 250 steel with oil lubricant. The earing profile is the radius of the deformed cup as a function of the angle from the rolling direction.
This measure is directly linked to the anisotropy of the steel sheet. For finite element simulations, this anisotropy is introduced in the constitutive law (either the Hill coefficients or the texture data).
The shape of the curves is identical for all the numerical models: a maximum at 45° from the rolling direction and lower values at 0° and 90°. The anisotropy of the material is then modelled similarly with the different constitutive laws. A shift can however be noticed between these curves showing small differences on the ductility of the material according to the law.
Unfortunately, the shape of the numerical curves is very different from the experimental one. This difference is not yet completely explained. A lack of accuracy during the experimental process can be at the origin of the problem. This point has already been investigated in paragraph 3.2 E.
Furthermore, the SPXI 250 steel is weakly anisotropic. The earing profile obtained for this anisotropy can then largely be influenced by other parameters. Experimental parameters such as the homogeneity of the lubrication can be mentioned. A large influence on the earing

profile of some numerical parameters such as the number of element layers, the penalty coefficient or the fitting procedure for the Hill law has been noticed. This point is investigated in paragraph 3.5.

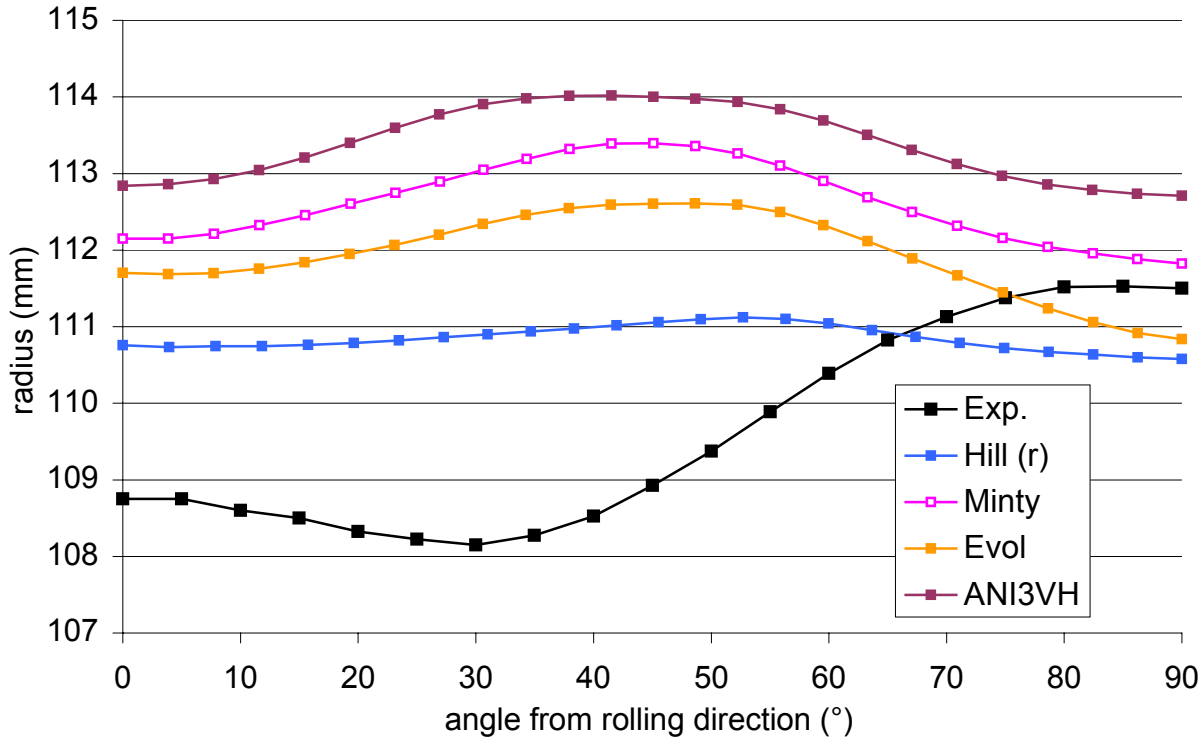

Figure 72: Earing profile for SPXI 250 steel with oil lubricant

(4) Texture analysis

The texture measurements are used to validate our model. The evolved texture computed at the end of the deep drawing simulation is compared to the experimentally measured one. For the cup with the SPXI 250 steel with oil lubricant, the textures are measured at the mid-height of the flange along the rolling, the 45° and the transverse directions. Finite elements located at these 3 points on the deformed cup are then selected. As the textures are measured at mid-thickness of the steel sheet, the elements on the middle layer are used (the mesh has 3 element layers).

To compare the experimental and the computed textures, a post-processing must be achieved. Indeed, during the simulation, the texture is represented by a set of discrete orientations (2000 in our case). The set of crystals must be extracted for the selected elements from the file containing the crystals of the whole finite element mesh. Then, a continuous texture representation must be computed from the discrete set of crystals. To do so, a program which fits a Gaussian distribution around each crystal orientation is used. This program then computes the continuous texture from all the Gaussian distributions. An important parameter at this stage is the spread of the Gaussian distribution. A value of 7° is generally recommended but we have noticed that the sharp textures are better represented with a lower value; a spread of 4° is then used.

The continuous textures so obtained are expressed in the local axes of the finite element under consideration. Indeed, the constitutive law (which is based on the texture) is initially expressed in the orthotropy axes of the steel sheet (the rolling and transverse directions). But, as local axes are used during the simulation, the texture is expressed in axes which are linked to the deformation of the sheet.
Contrarily, the measured textures are linked to global axes of the deformed cup.
The local axes in which the computed textures are expressed are in blue in Figure 73 and the texture measurement axes are in black. For the comparison, the computed texture along the 45° and the transverse directions are rotated.

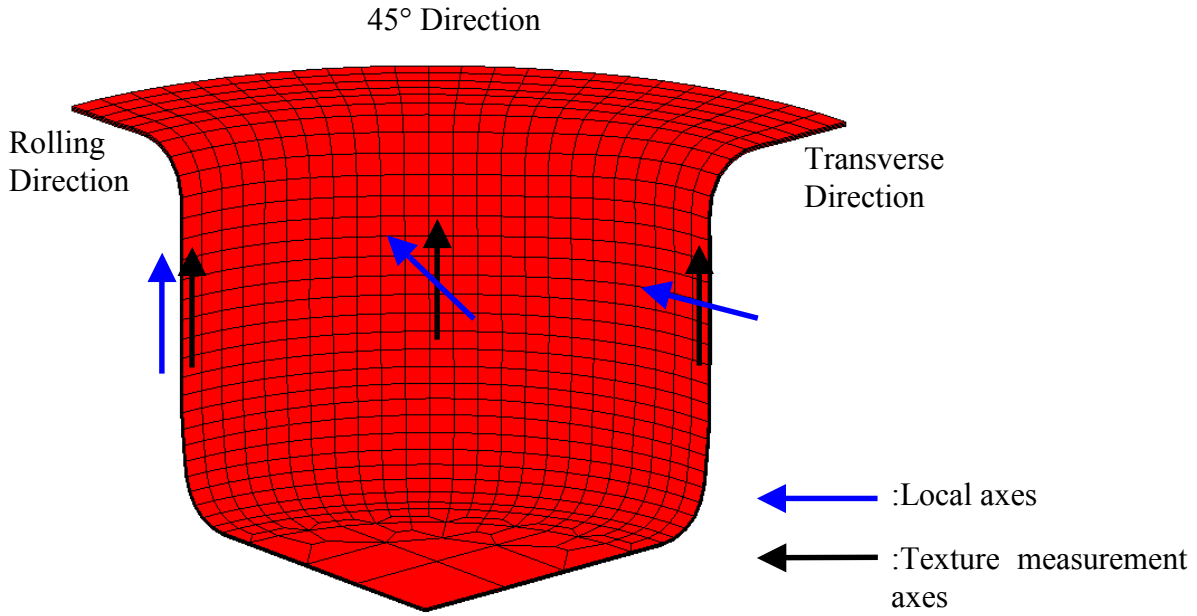

Figure 73: Axes of the textures on the deformed cup

As explained in paragraph 3.2 F, the orthotropy of the steel sheet is preserved for the cases along the rolling and the transverse directions. However, for the 45° direction, the steel sheet is no longer orthotropic. The ODF used to represent the continuous textures is represented in term of Euler angles. The range for the Euler angles $(\varphi_1, \phi, \varphi_2)$ is [0°;90°]×[0°;90°]×[0°;90°] for the orthotropic cases but it is [0°;180°]×[0°;90°]×[0°;90°] for the case along the 45° direction.
The treatment of the texture is achieved thanks to the software developed in the MTM department of the Katholieke Universiteit Leuven (see Van Houtte (1988) for the theoretical developments and Van Houtte (1994) and updated versions for the user's manual).

Figure 74 presents sections of the ODF of the measured texture along the rolling direction. Figure 75 presents the corresponding texture predicted by our model. φ_1 constant sections of the ODF are used; ϕ is the vertical axis and φ_2 the horizontal one. The $\varphi_2 = 45°$ section of the ODF is also plotted; in this case the horizontal axis stands for φ_1.

Comparing Figure 74 (the measured texture at the end of the deep drawing process) and Figure 55 (measured texture of the SPXI 250 steel), it appears that a strong texture evolution occurs during the deep drawing for the point of the cup that is considered.

Comparing Figure 74 and Figure 75, it appears that our model is a good qualitative model for the prediction of texture evolution. The location of the maximums of the ODF are indeed well predicted. However, the intensities of these maximums are underestimated with our model.

Figure 76 and Figure 77 compare the φ_2 = 45° section of the ODF associated to the experimental and the predicted textures along the 45° and the transverse directions respectively. Here again, the predicted textures are qualitatively in good agreement with the measured ones but the intensities of the maximums are underestimated.
The texture at the end of the deep drawing process along the rolling direction is quite similar to the one along the transverse direction although the initial axes of the material are rotated for the transverse case. The influence of the initial texture on the final one is then relatively small for this process. That is not surprising as the initial texture is weak.

The predicted textures on points where the experimental one has not been measured is presented in Figure 78. The textures under the punch and under the blankholder are analysed. The comparison of the texture under the punch to the initial one (the φ_2 = 45° section of Figure 55 is reported here) shows that the texture evolution is small in that zone. Small plastic strains have indeed been noticed under the punch. This fact justifies our choices for the points to submit to texture measurement.
The zone of the steel sheet under the blankholder is submitted to a larger texture evolution but the measurements in that zone would have been hard to achieve due to the proximity of the edge of the steel sheet and to the curved part of the cup. A square sample of 20mm is almost not possible to cut out that zone.

The effect of the texture evolution on the material behaviour can be analysed through the computation of the Lankford coefficients on the basis of the initial and the final texture. The Lankford coefficient is indeed directly linked to the shape of the yield locus and particularly to the normal of the yield locus. Figure 79 compares the Lankford coefficients computed from the initial texture of the SPXI 250 steel, the final texture measured on the deformed cup along the rolling direction (SPXI 250 steel with oil lubricant) and the corresponding predicted texture.
It appears that a large evolution of the Lankford coefficients is observed on the basis of the texture measurements. Unfortunately, the too low intensities of the predicted texture yield to a too low evolution of the Lankford coefficients compared to values obtained from the texture measurement.

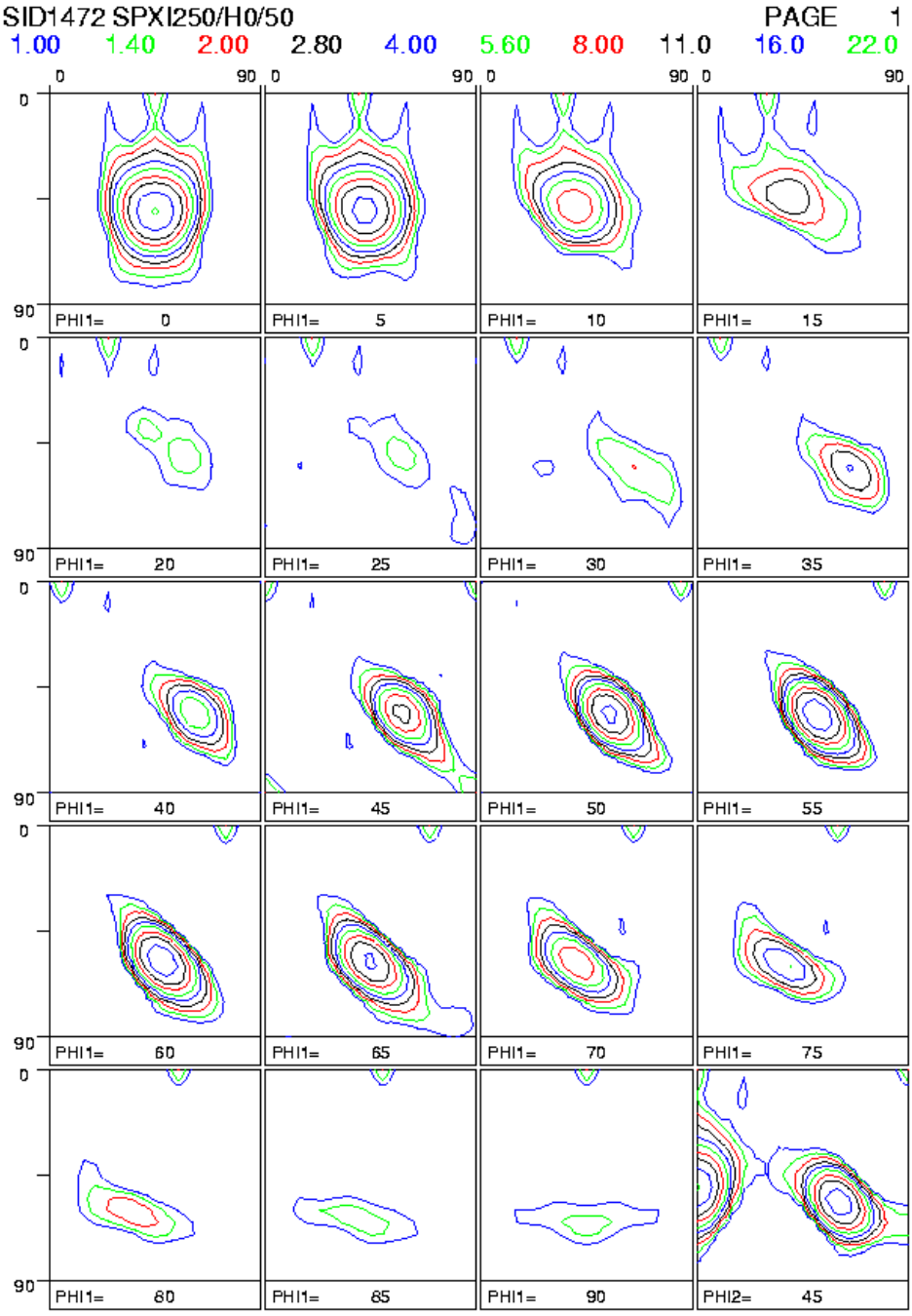

Figure 74: Texture measurement along the rolling direction (SPXI 250 with oil lubricant)

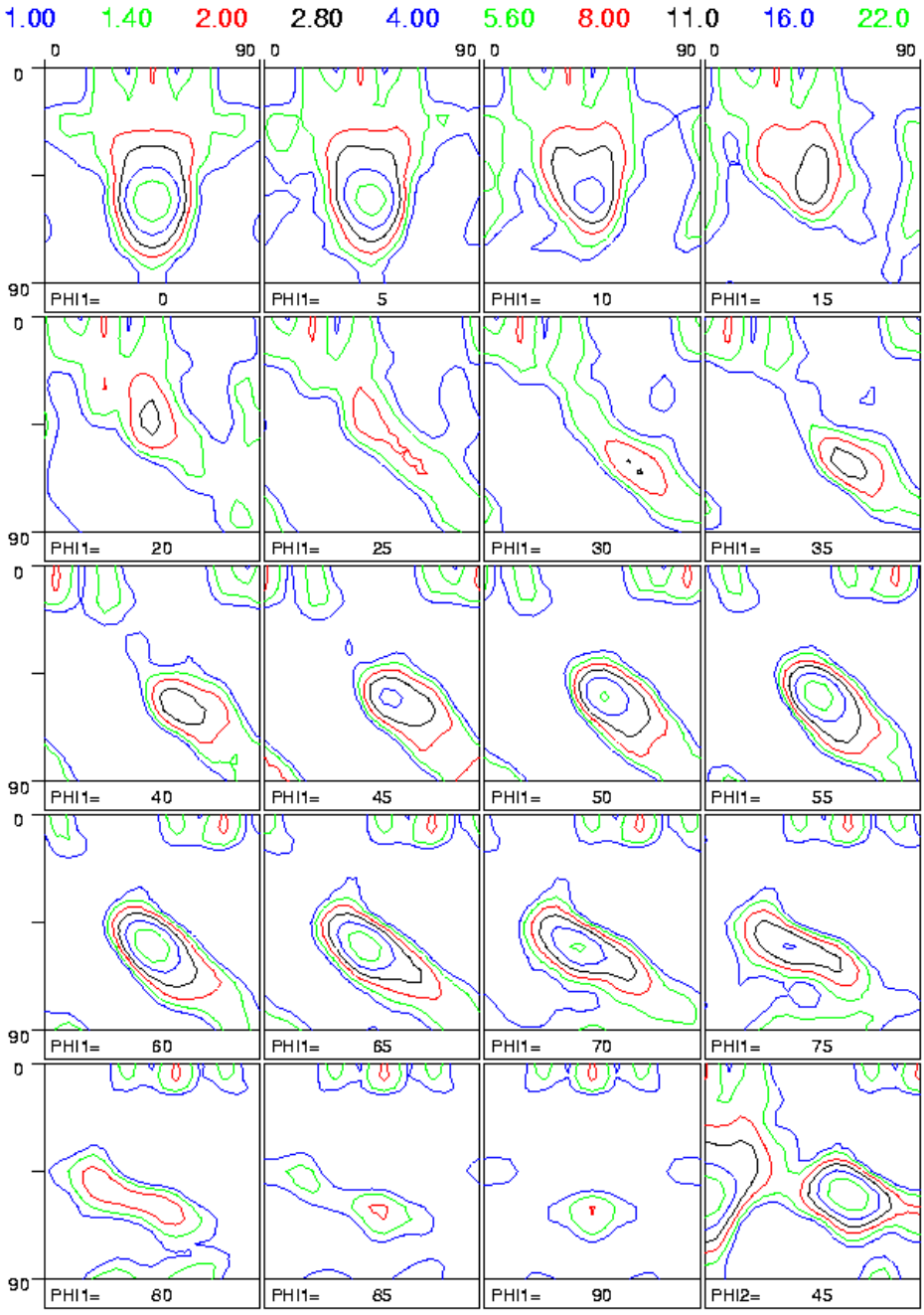

Figure 75: Computed texture along the rolling direction (SPXI 250 with oil lubricant)

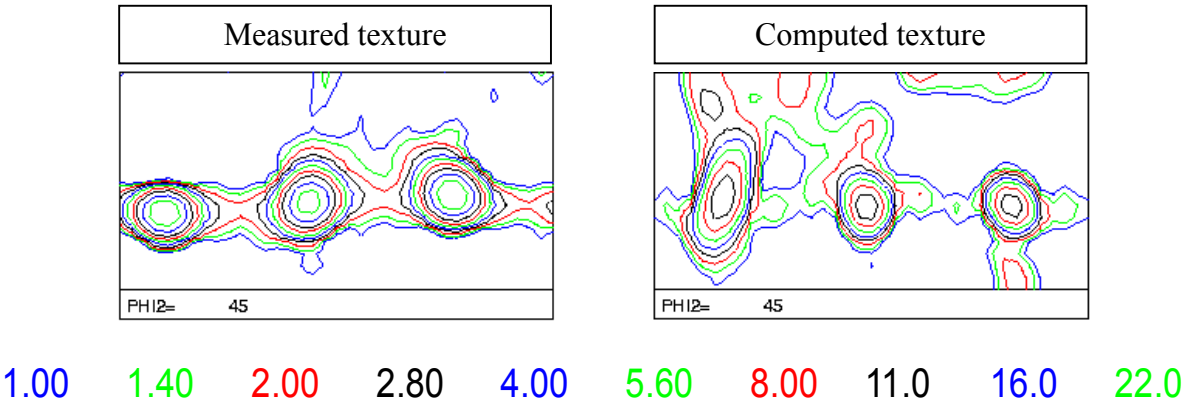

Figure 76: Comparison of the experimental and the computed textures for the 45° direction (SPXI 250 steel with oil lubricant)

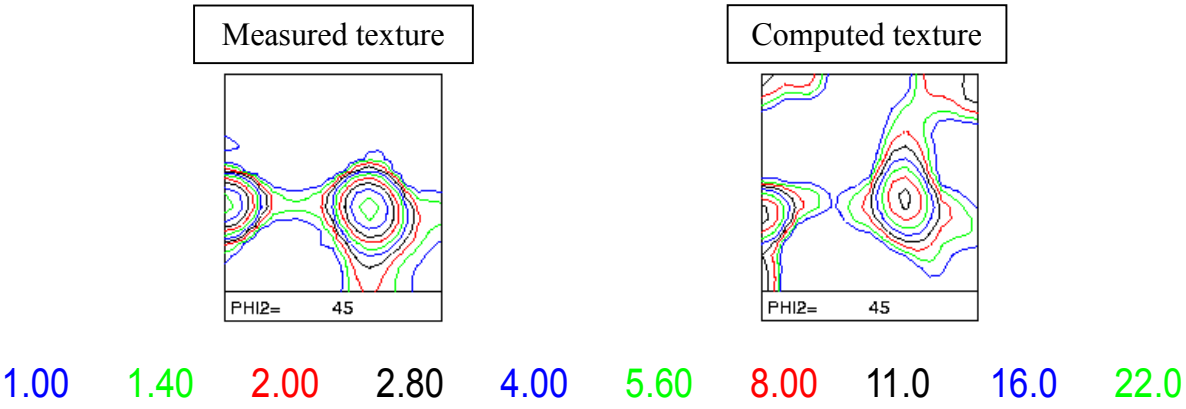

Figure 77: Comparison of the experimental and the computed textures along the transverse direction (SPXI 250 steel with oil lubricant)

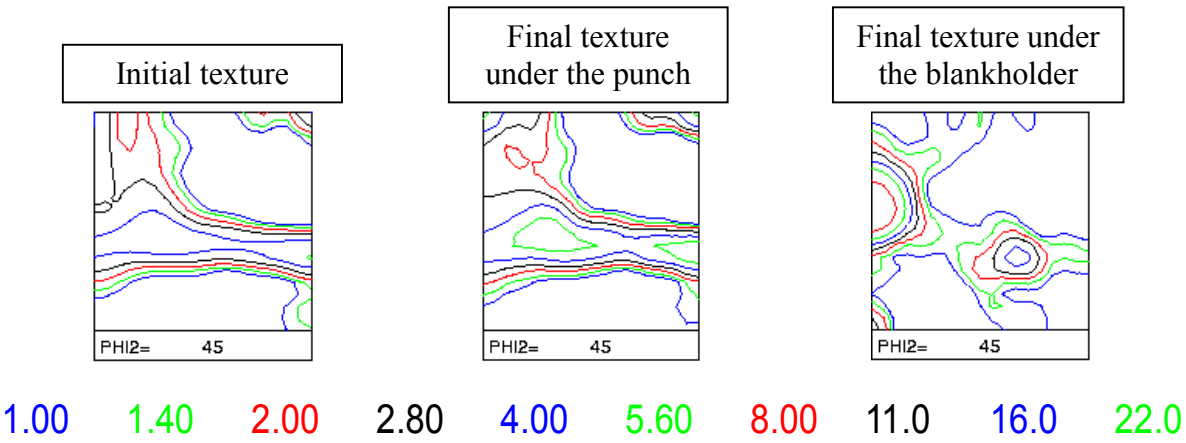

Figure 78: Predicted texture under the punch and under the blankholder compared to the initial texture (SPXI 250 steel with oil lubricant)

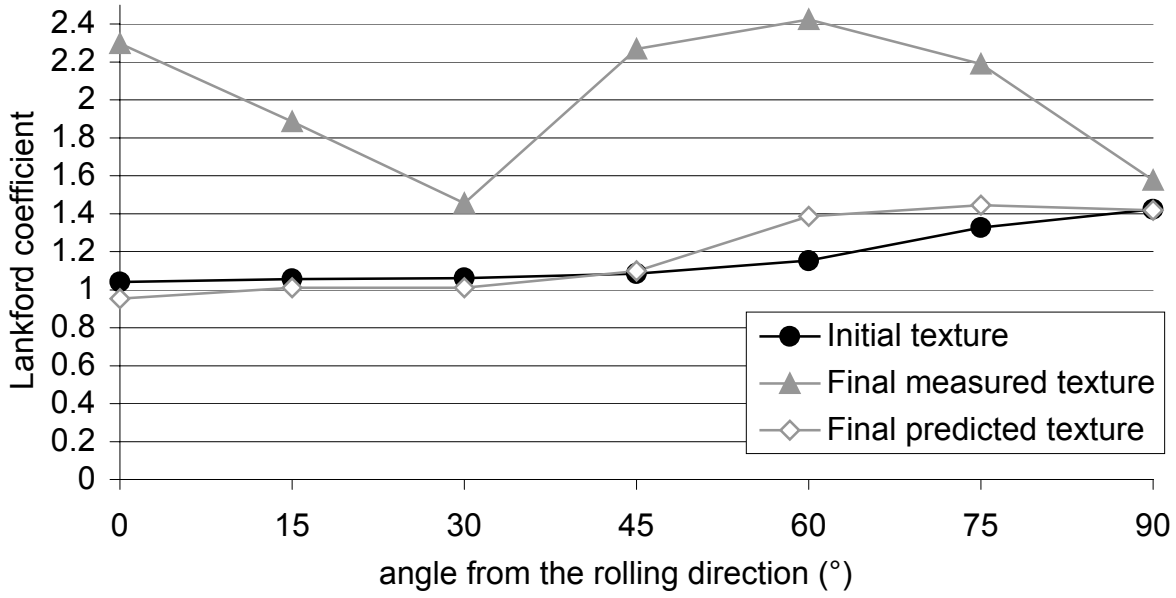

Figure 79: influence of the texture evolution on the Lankford coefficients (computed from texture measurements or predicted texture)

B SPXI 250 WITH NYLON FILM LUBRICANT

Compared to the previous paragraph, only the Coulomb friction coefficient is adapted: μ=0.02 with the nylon film lubricant.

Figure 80 presents the principal strains in the plane of the steel sheet (E1 and E2) and along the thickness direction (E3). As it was observed in the previous case of an oil lubricant, all the numerical curves are almost superimposed. However, the large differences noticed between experimental results and the computation for the zone under the punch are largely reduced with the nylon film lubricant. This can be explained by a better modelling of the friction behaviour when the Coulomb friction coefficient goes from 0.13 to 0.02.

Table 12 shows the maximum principal strain under the punch. The oil and the nylon film lubricants are compared. The experimental measurements and the strains computed with our model are also compared. The values are computed or measured for a curvilinear abscissa *s* around 20mm and along the rolling direction.

From the numerical results, it appears that the maximum principal strain under the punch increases when the friction coefficient increases. This can be explained by a larger punch force required to extract the steel sheet clamped between the matrix and the blankholder. The forces are studied in Figure 71 and Figure 82 and confirm this assumption.

Experimentally, the larger punch force obtained from a larger friction coefficient does not induce larger strains under the punch because the movement of the steel sheet is slowed along the curved part of the punch (due to the larger friction coefficient). As a consequence, the maximum principal strain increases faster at the beginning of the flange of the cup (for *s* around 80mm). But under the punch, the strain is smaller in high friction case than for low friction. These observations clearly appear in Figure 81.

The assumption of a constant Coulomb friction coefficient in the flat and the curved parts of the tools should be improved, especially for the oil lubricated case.

Table 12: Comparison of the maximum principal strain under the punch (%)

	Oil lubricant (μ=0.13)	Nylon film lubricant (μ=0.02)
Experimental measurements	1.08	3.09
Numerical results (Minty)	4.79	2.35

The principal strains along the rolling and the transverse directions are similar to the 45° direction.

The punch force as a function of the punch travel is presented in Figure 82. The shape of the curves is very similar to the oil lubricated case. The main difference is the value of the maximum which is largely influenced by the friction coefficient acting on the steel sheet clamped by the blankholder. The maximum of the experimental punch force is 169 kN for the oil lubricated case and decreases to 133 kN with the nylon film lubricant.

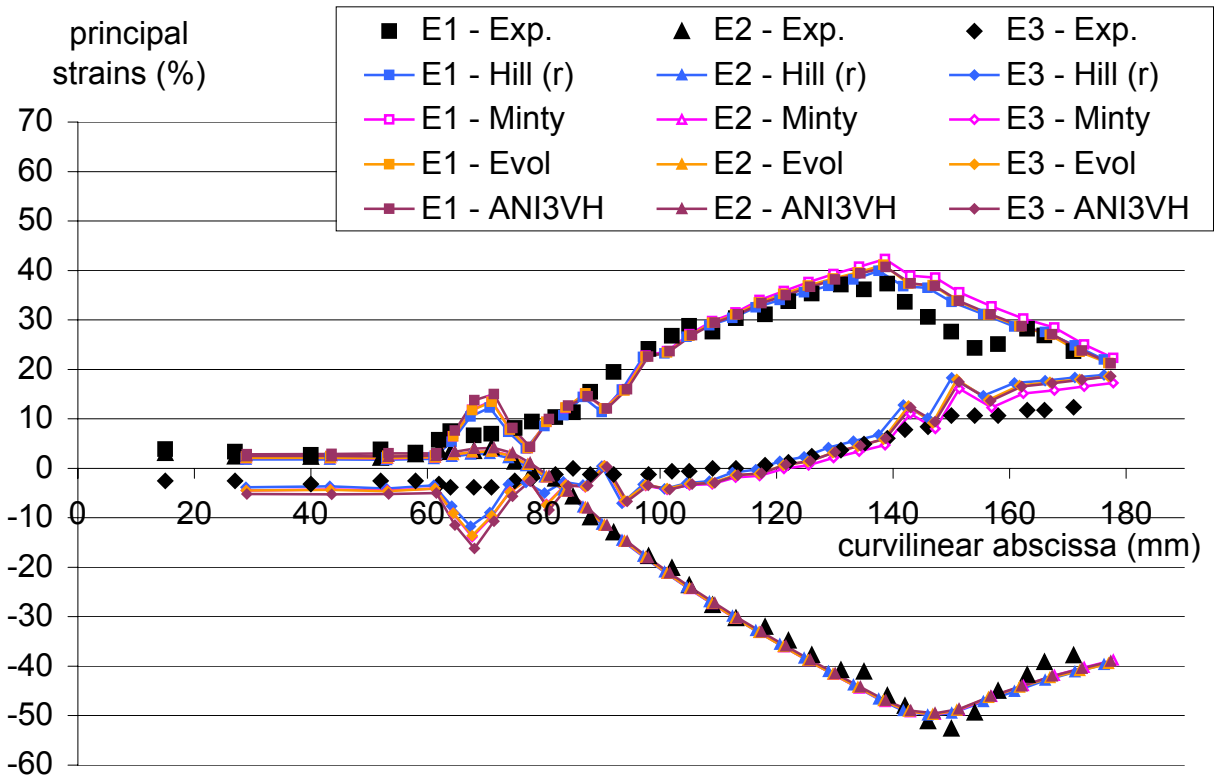

Figure 80: Principal strains along the 45° direction (SPXI 250 with nylon film lubricant)

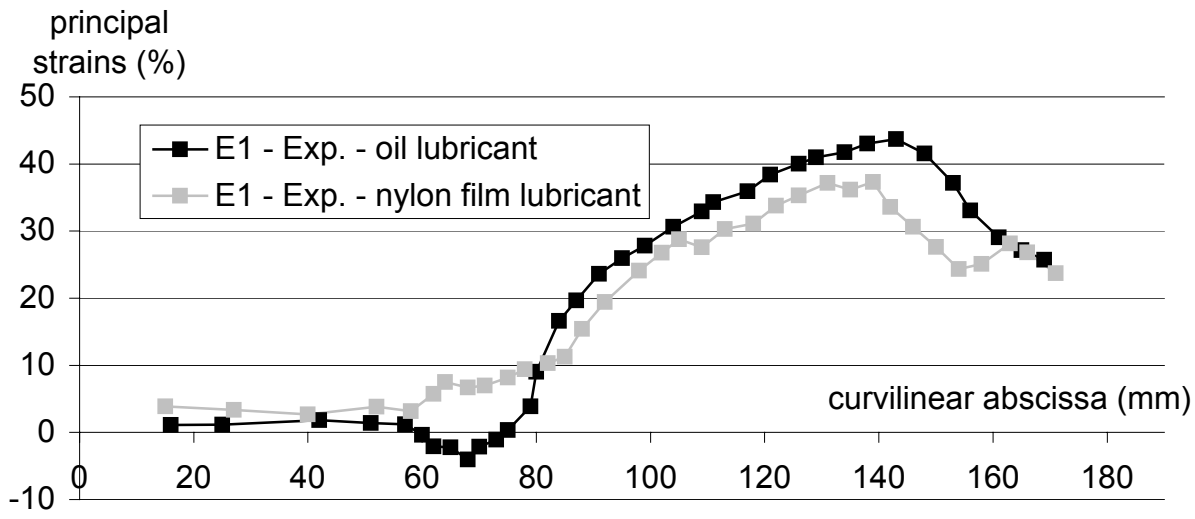

Figure 81: Influence of the friction coefficient on the experimental first principal strain (SPXI 250 steel)

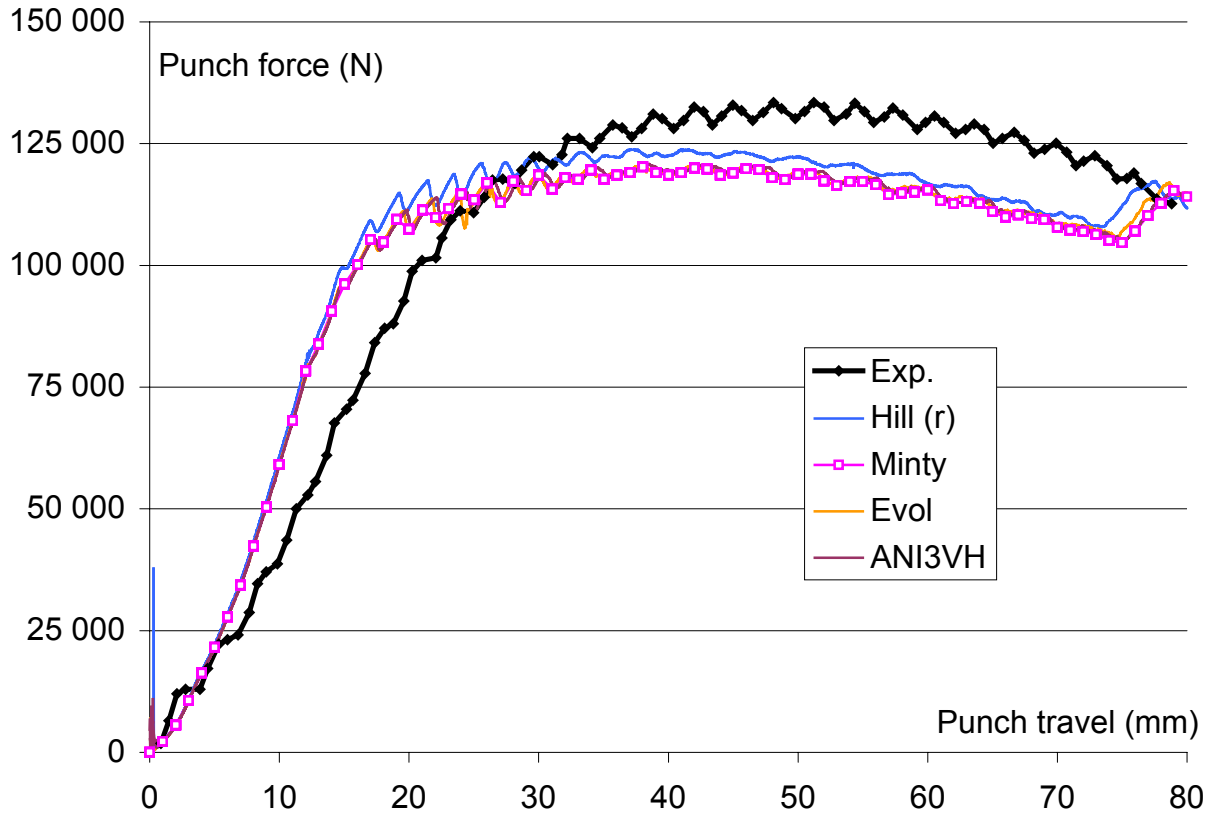

Figure 82: Punch force versus punch travel (SPXI 250 with nylon film lubricant)

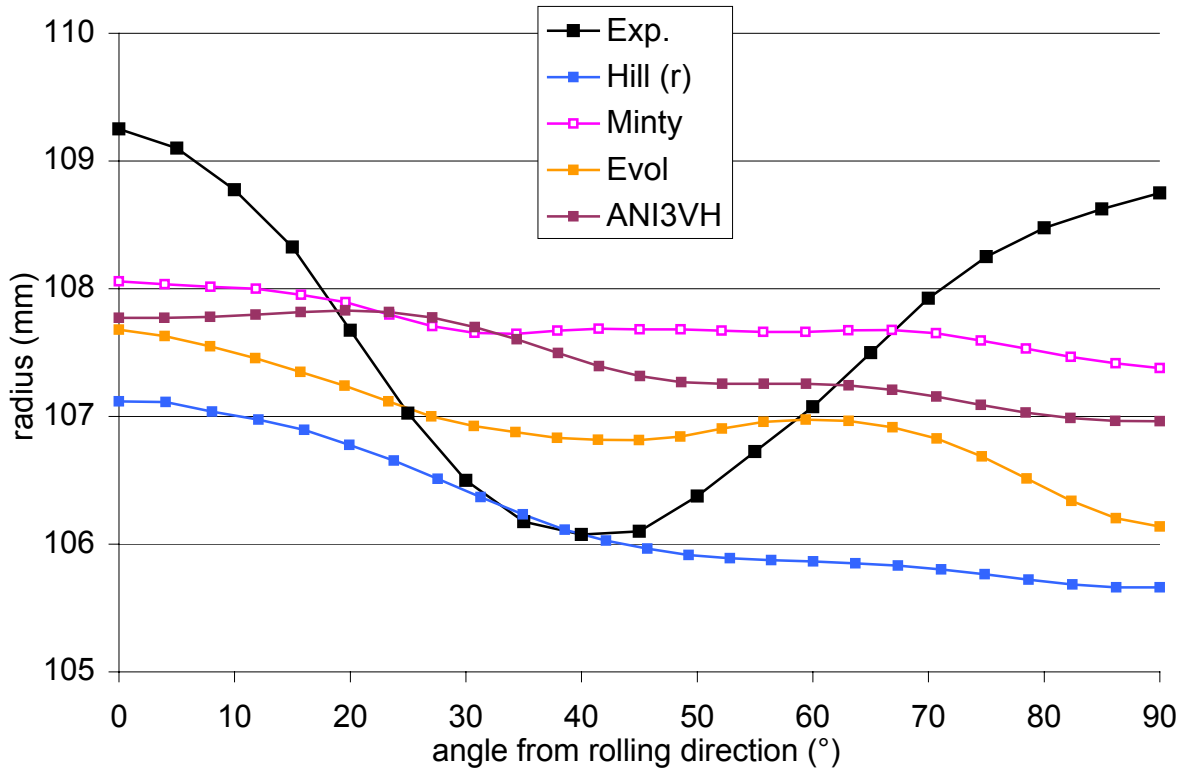

Figure 83: Earing profile for SPXI 250 steel with nylon film lubricant

Figure 83 presents the earing profile. As for the oil lubricated case, the agreement between the experimental curve and the numerical ones is not good.
The same trend is observed for all the computed curves; this trend of the earing profile can be predicted by the Lankford coefficient. Indeed, a high *r* value corresponds to a lower thickness deformation during a tensile test. Under the blankholder, the compression strain is predominant: E1>0 and E2<0 with $\|E_1\| < \|E_2\|$. This can be seen on the principal strain curves for the different studied cases (Figure 68, Figure 69, Figure 70 and Figure 80). So, the thickness tends to increase (E3>0 under the blankholder) and this effect is more pronounced where the *r* value is small. Due to the conservation of the volume during plastic deformations, where the thickness is the larger, the earing is minimum. Then, a smaller *r* corresponds to a lower earing.
Considering a point along the rolling direction, the compression strain is acting along a circumferential direction which coincides with the transverse direction for this point. Similarly, along the transverse direction, the compression direction is the rolling direction and for the 45° direction, it is the direction at 45° from the rolling direction. The strain states along the different directions are analysed in Figure 84. The consequences on the earing profile are presented in Figure 85.

The Lankford coefficient of the SPXI 250 steel as a function of the angle from the rolling direction is presented in Figure 86. The link between the Lankford coefficient and the earing profile applies in the case of this cup (compare Figure 83 to Figure 86). However, with the oil lubricant, this link was not verified as one can check by comparing Figure 72 and Figure 86. The small anisotropy of the steel was certainly hidden by the friction behaviour.

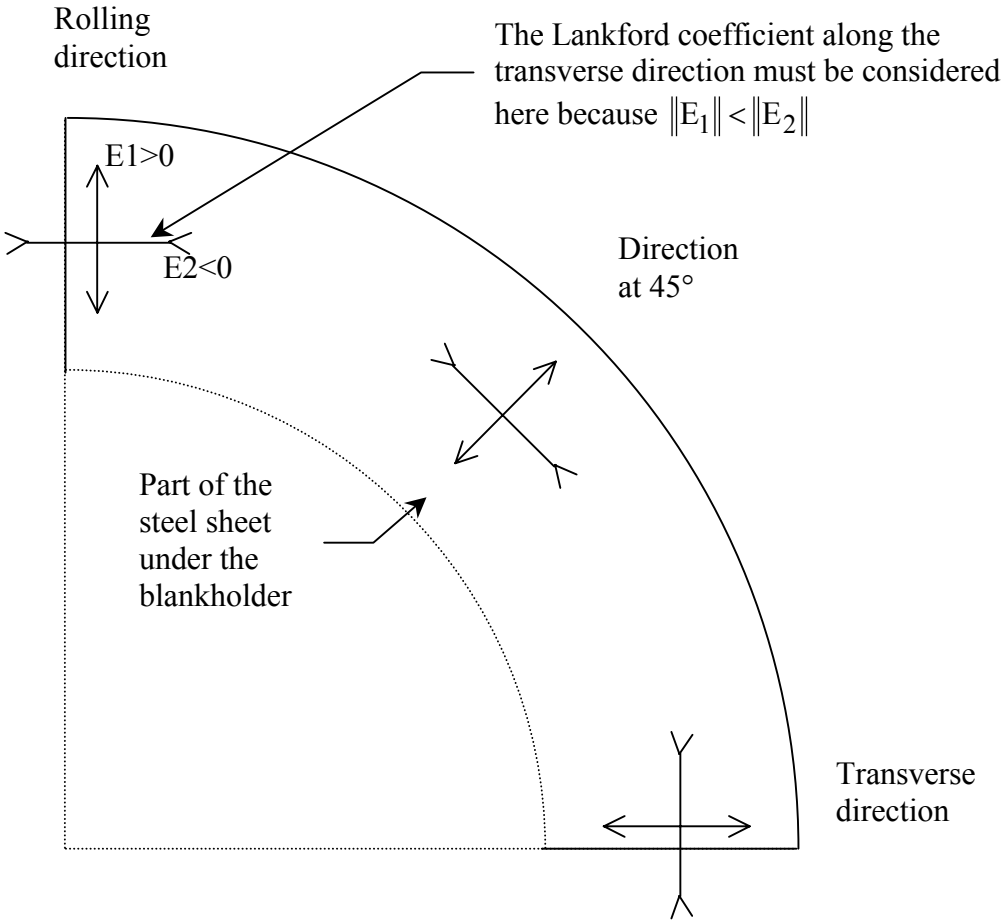

Figure 84: Strains observed under the blankholder

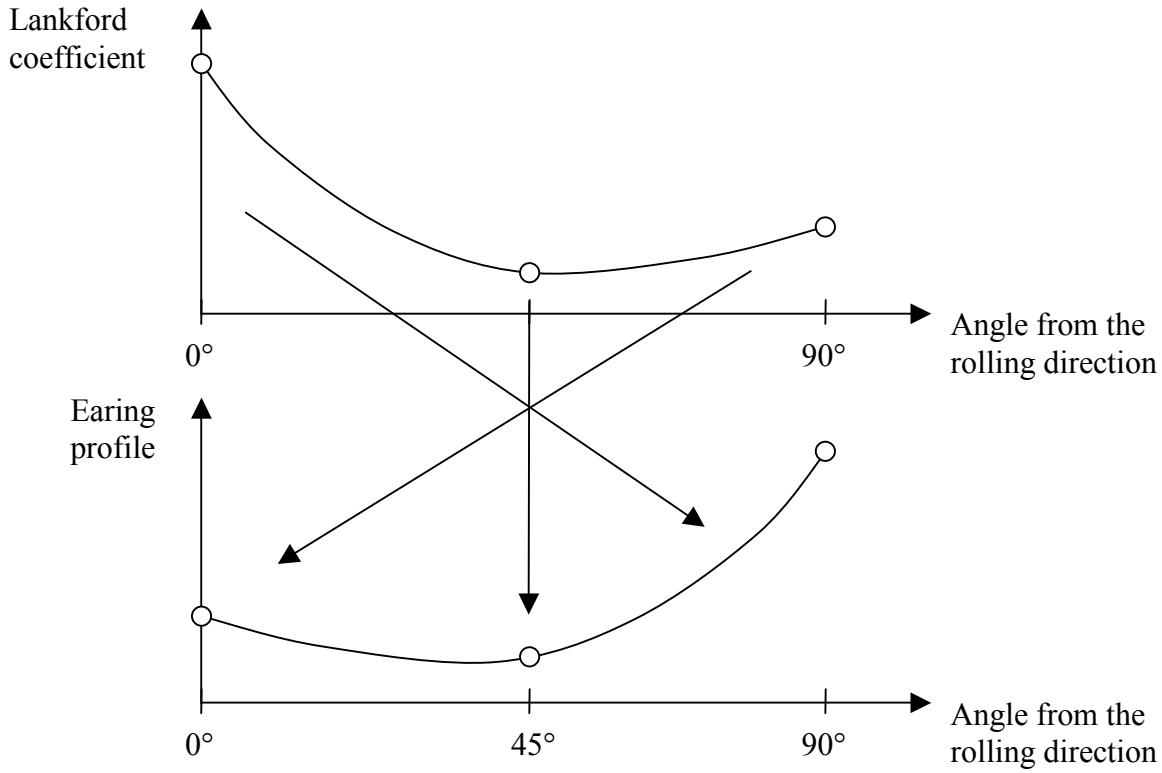

Figure 85: Link between the earing profile and the Lankford coefficient

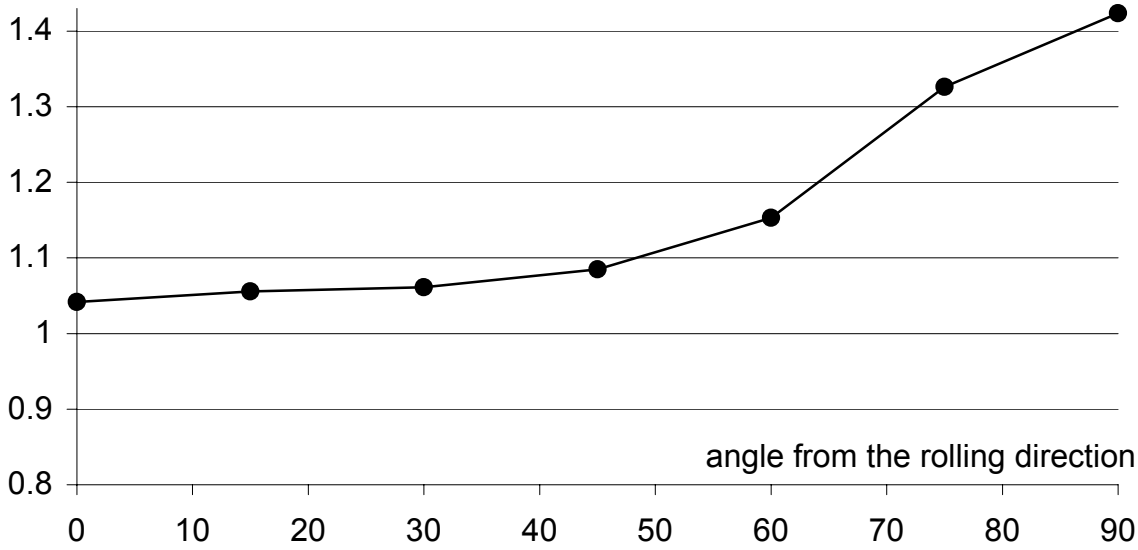

Figure 86: Lankford coefficient of the SPXI 250 steel (computed on the basis of the texture measurement)

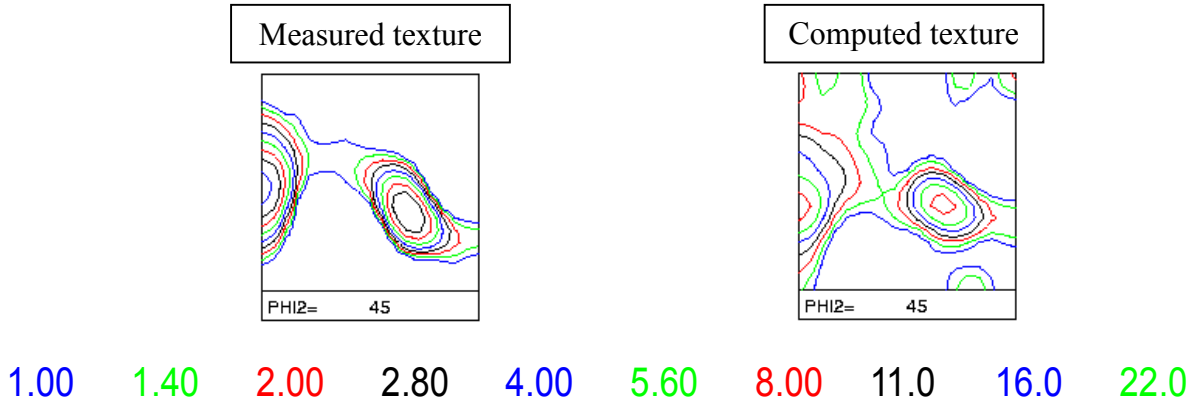

Figure 87: Comparison of the predicted texture to the measured one along the rolling direction (SPXI 250 steel with nylon film lubricant)

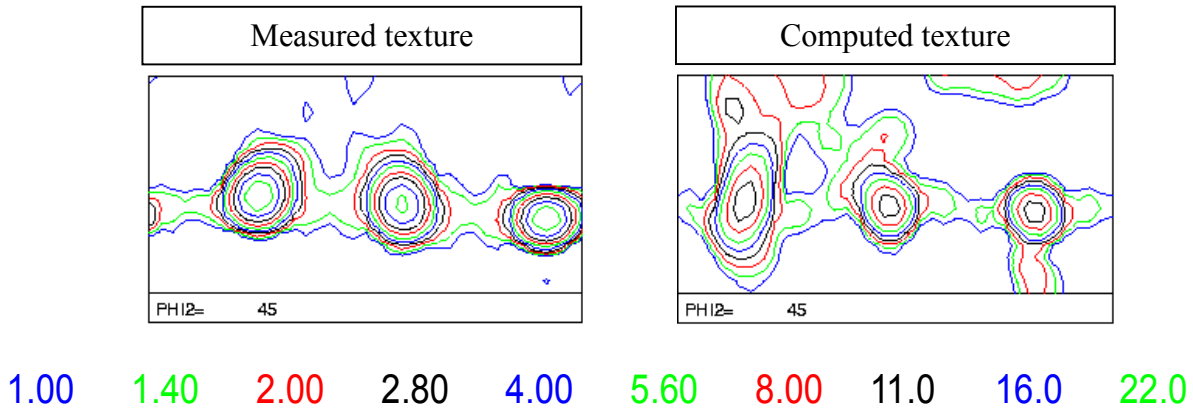

Figure 88: Comparison of the predicted and the experimental textures along the 45° direction (SPXI 250 steel with nylon film lubricant)

The comparison of the predicted texture to the measured one is presented by Figure 87 for the rolling direction and by Figure 88 for the 45° direction. The measurement along the transverse direction has not be done for this case.
As it was noticed for the previous case, the location of the maximums of the ODF is well predicted but the intensities are too low.

c ULC Ti with oil lubricant

For this steel, the numerical results with the ANI3VH constitutive law are not available.
The computation with the Hill law has only been achieved with a penalty coefficient of 100 N/mm^3 (for the 3 tools). The case corresponding to 1000 N/mm^3 for the contact with the matrix and 500 N/mm^3 for the punch and the blankholder is not available.

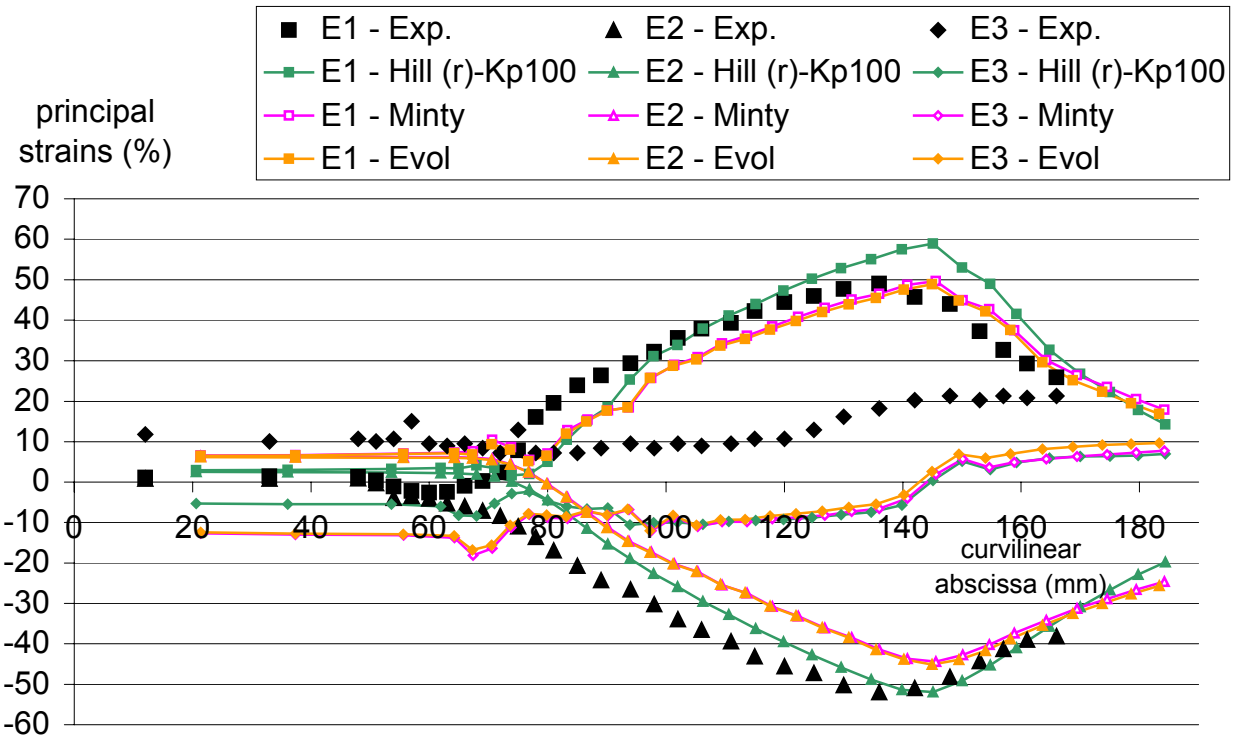

Figure 89: Principal strains along the rolling direction (ULC Ti with oil lubricant)

Figure 89 presents the evolution of the principal strains along the 3 measurement directions.
The shift between the experimental curve and the numerical ones for the thickness strain (E3) can be explained by a difference between the nominal steel sheet thickness (0.8mm) used for the numerical computations and the actual thickness of the sheet (larger than 0.8mm) used experimentally. Indeed, the experimental positive value for the thickness strain under the punch is not sensible; unfortunately, the actual steel sheet thickness is not available.

Figure 90 presents the punch force versus the punch travel. The maximum force computed numerically is too low compared to the experimental value.
The ULC Ti steel is more ductile than the SPXI 250. The punch force is then lower: 152 kN compared to 169 kN for the SPXI 250 with the same lubricant.

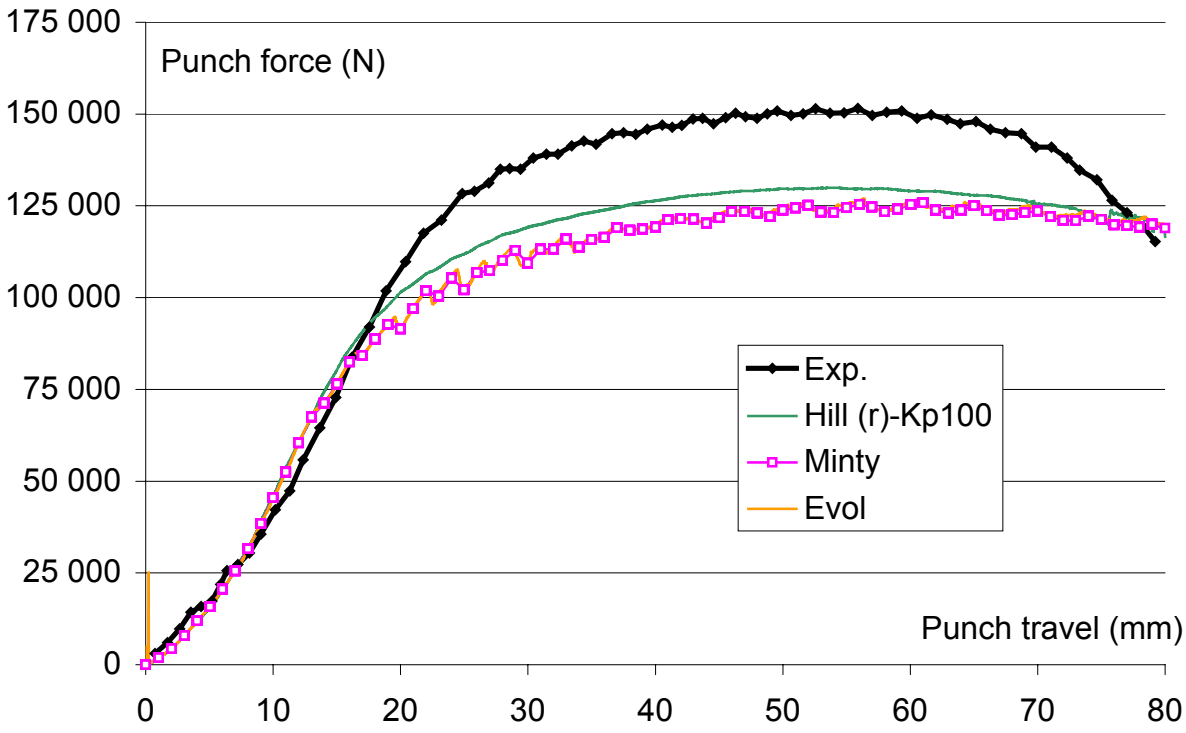

Figure 90: Punch force versus punch travel (ULC Ti with oil lubricant)

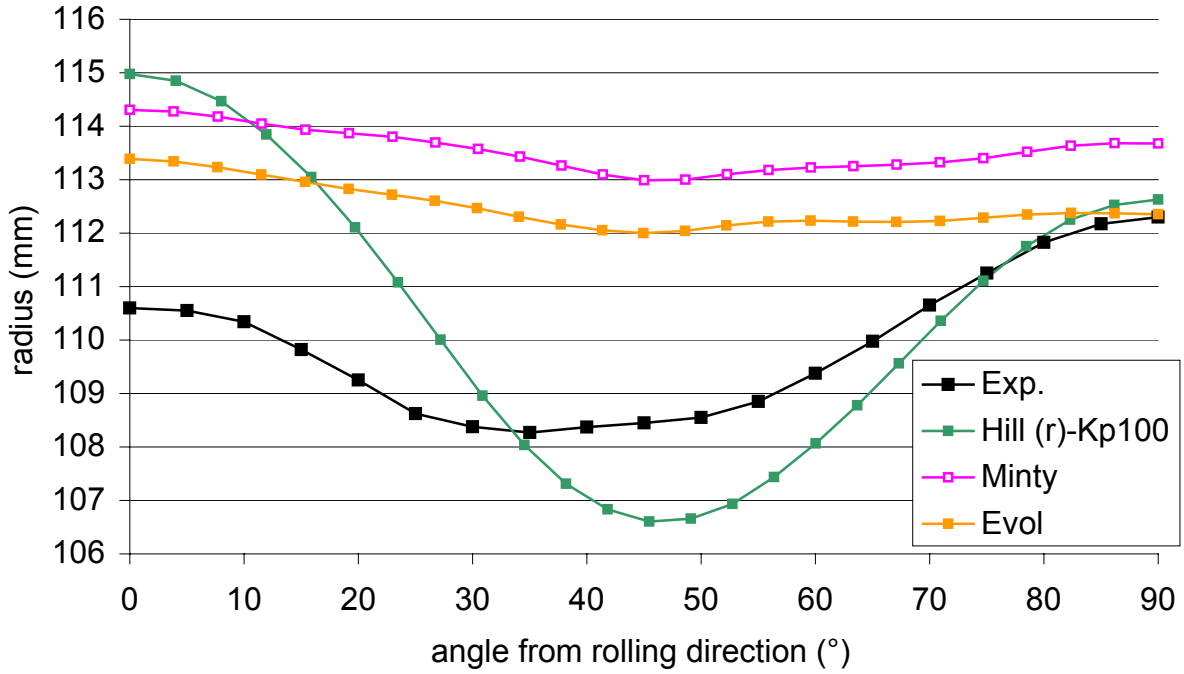

Figure 91: Earing profile for ULC Ti steel with oil lubricant

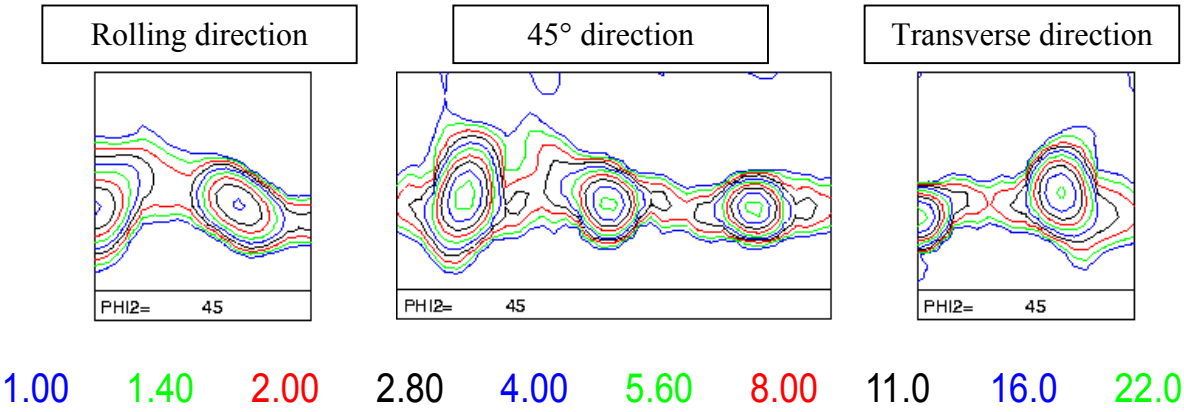

Figure 92: Predicted textures along the rolling, 45° and transverse directions (ULC Ti steel with oil lubricant)

Figure 91 presents the earing profile for the ULC Ti steel with the oil lubricant. The shape of the computed curves is, contrarily to the SPXI 250 steel, in agreement with the experimental curve. The amplitude is too low for the Minty and Evol laws but it is too large with the Hill law.
The prediction of the earing profile from the Lankford coefficient gives the following results. From Table 7, the Lankford coefficients for the ULC Ti steel can be ordered:

$$r_{45°} = 1.85 < r_{0°} = 2.08 < r_{90°} = 2.59 \tag{207}$$

With all the numerical models, the prediction is fulfilled (example of the Hill law):

$$radius_{45°} = 106.6mm < radius_{90°} = 112.6 < radius_{0°} = 115.0 \tag{208}$$

As no texture measurement on the deformed cup has been performed for this steel, Figure 92 presents only the predicted texture. The graphs are similar to those of the SPXI 250 steel.

3.5 Sensitivity study

To check the validity of the results presented in the previous paragraph, the influence of some important numerical parameters has been investigated. These parameters refer to the finite element mesh, the finite element type, the friction constitutive law or the steel sheet constitutive law.

A NUMBER OF ELEMENT LAYERS

The deep drawing simulations presented in paragraph 3.4 have been performed with 3 layers of finite elements through the thickness of the steel sheet. The same deep drawing process with only one layer of elements has been tested to check the influence of the number of layers on the results. From a computation time point of view, the case with one layer is better; the computation time is indeed more or less proportional to the number of finite elements.
Figure 93 presents the earing profile when 1 or 3 layers of elements are used. The earing profile with only one layer is almost opposite to the experimental one. The bending and the unbending of the steel sheet on the curved part of the matrix cannot be accurately modelled with only one layer (remember that only one integration point per element is used).

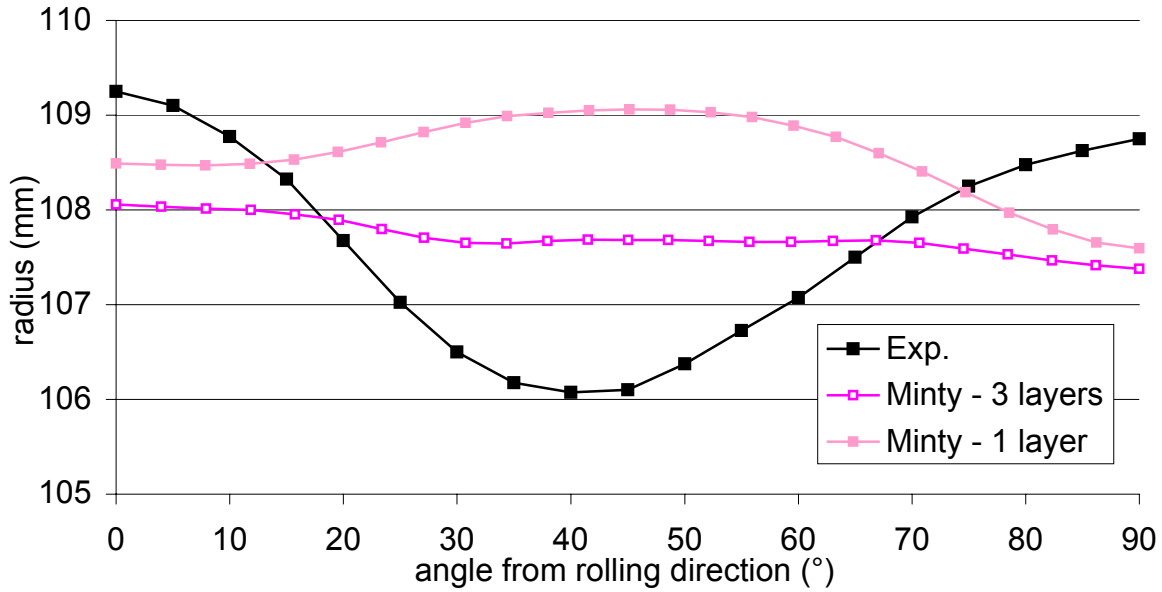

Figure 93: Influence of the number of element layers on the earing profile (SPXI 250 with nylon film lubricant)

Figure 94 presents the punch force with 1 and 3 element layers. When a lower number of finite elements is used, the maximum force is larger and becomes closer to experimental values.

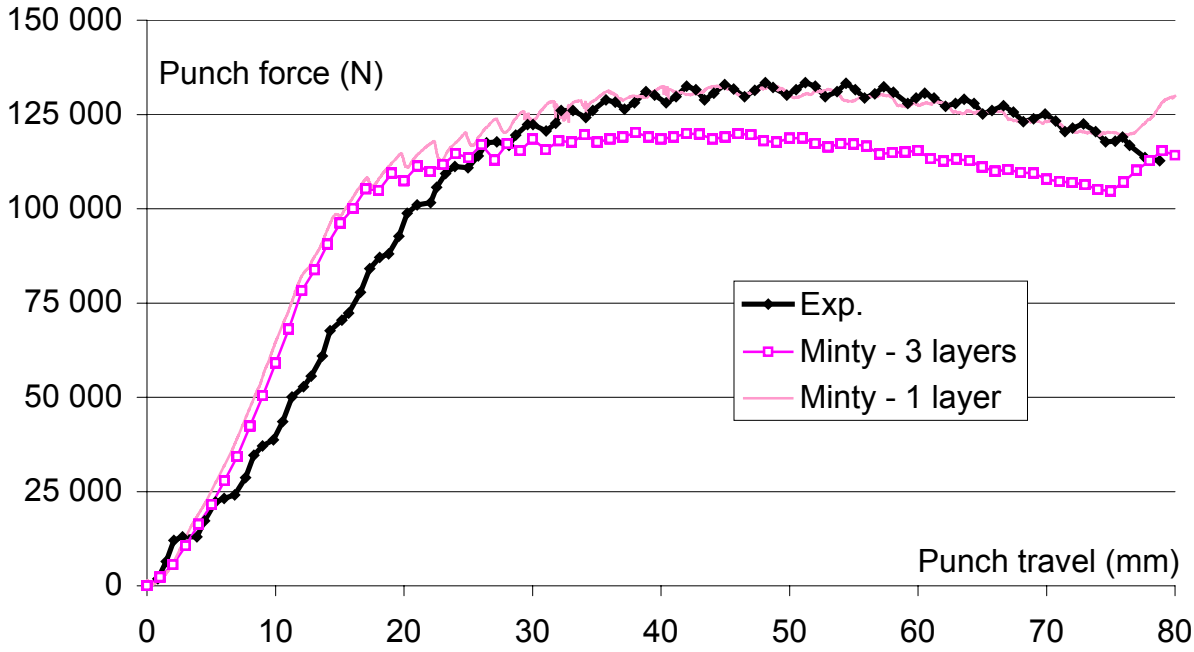

Figure 94: Influence of the number of element layers on the punch force (SPXI 250 with nylon film lubricant)

B COULOMB FRICTION COEFFICIENT

The influence of the Coulomb friction coefficient has already been treated in paragraph 3.4 by comparing the cases with oil lubricant or nylon film lubricant for the SPXI 250 steel. A large influence of the friction coefficient has been noticed on the punch force and on the earing profile. The shape of the earing profile is a bit influenced by the friction coefficient but the mean radius of the cup is more sensitive: the mean radius is 107.7mm for the nylon film lubricated case and 112.6mm for the oil lubricated case (with the SPXI 250 steel and 'Minty' law).
A lower influence has been noted on the principal strain distributions, especially under the punch. The influence of the friction coefficient is mainly due to its effect on the efficiency of clamping of the steel sheet between the blankholder and the matrix. The friction of the steel sheet on the shoulder of the matrix and the punch is also an important parameter.

Thanks to its large influence on the punch force, it is possible to adjust the Coulomb friction coefficient so as to fit the maximum of the experimental punch force. As shown by Figure 95, it seems that a Coulomb friction coefficient of 0.062 is more adapted than the nominal value of 0.02 if we focus on the maximum of the punch force.
However, if we focus on the mean radius of the cup, the nominal friction coefficient (0.02) leads to a mean radius of 107.7mm with the Minty law, which is very close to the experimental value: 107.6mm. While the friction coefficient of 0.062 leads to a mean radius of 109.3mm (an increased value due to an increased clamping of the steel sheet).

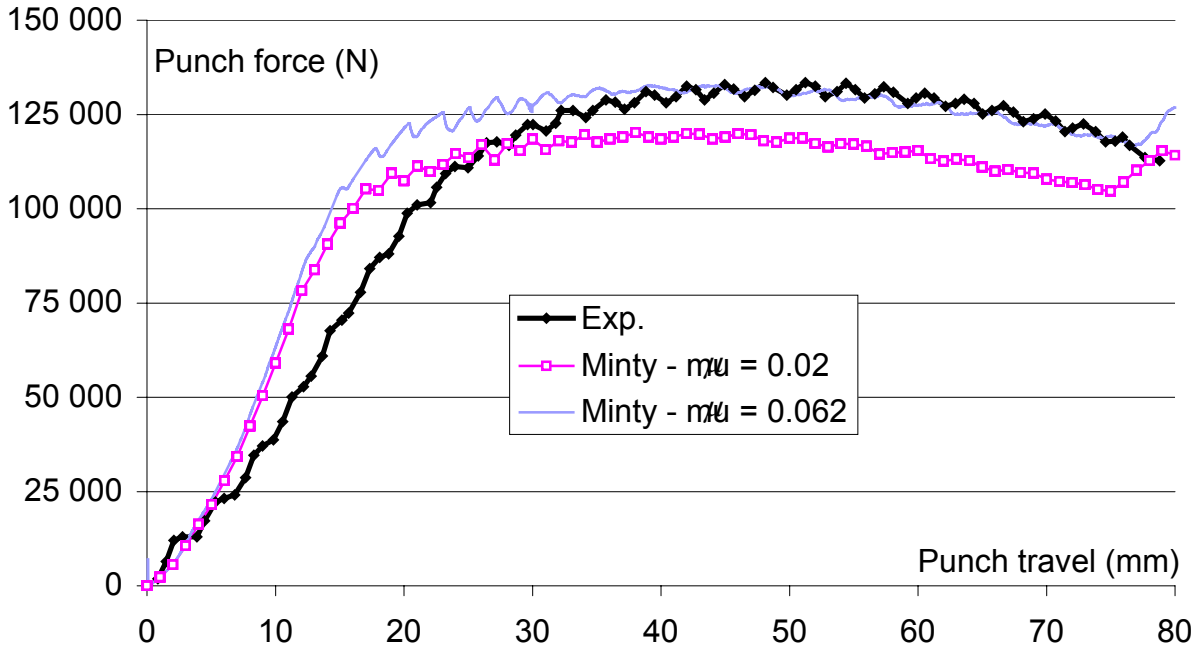

Figure 95: Influence of the Coulomb friction coefficient on the punch force (SPXI 250 with nylon film lubricant)

C PENALTY COEFFICIENT

The value of the penalty coefficient must result from a compromise: a too low value leads to a prohibitive penetration of the blank into the tools and a too high value yields convergence problems.

Two sets of penalty coefficients have been tested: the value generally used in paragraph 3.4 is 1000 N/mm^3 for the contact between the blank and the matrix and 500 N/mm^3 for the contact with the punch and the blankholder. These values are referred to as 'Kp 1000' in Figure 96 and Figure 97. For comparison, a value of 100 N/mm^3 is also tested for the contact between the blank and the 3 tools ('Kp 100' in the figures).

With a lower penalty coefficient, the pressure between the blank and the tool in a contact zone is more uniformly distributed. In addition to the reduction of the risk of convergence problems, a lower penalty coefficient reduces the risk of strain localisation during the simulation.

However, the 'Kp 100' case yields to large penetration: on the curved part of the tools, where the contact pressure is high, almost the half thickness of the blank has penetrated inside the tool. Beside the non accurate position of the blank during the simulation, such penetrations modify the effective curvature radii of the tools.

Figure 96 shows the influence of the penalty coefficient on the punch force. A first remark is that the oscillations that have already been discussed in paragraph 3.4 for the case K_p=1000, are almost eliminated with K_p=100. With a lower penalty coefficient, the difference in the bending stiffness of one element compared to the bending stiffness between 2 elements is smoothed thanks to the more uniform pressure distribution. Another remark is the lower punch force observed for a lower penalty coefficient. This can be explained by the apparent modification of the curvature radii of the tools: the radii are larger for a lower penalty

coefficient (this point is shown in Figure 109 of paragraph 4.4 for another deep drawing process) and by the more uniform distribution of the pressure under the blankholder.

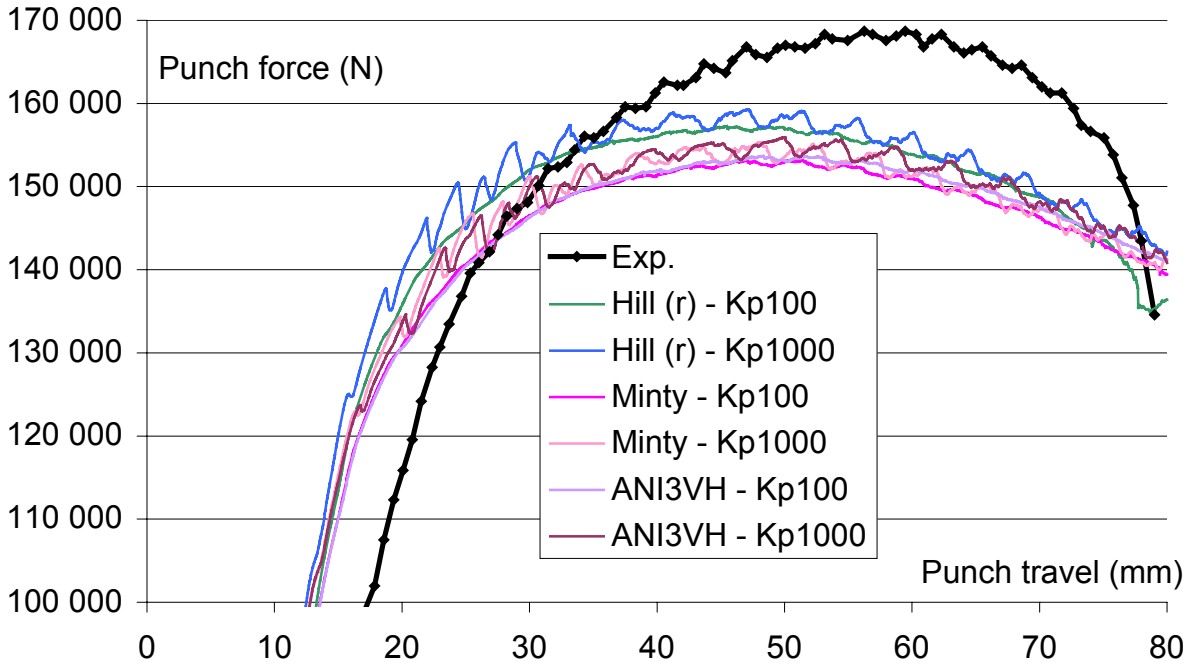

Figure 96: Influence of the penalty coefficient on the punch force (SPXI 250 with oil lubricant)

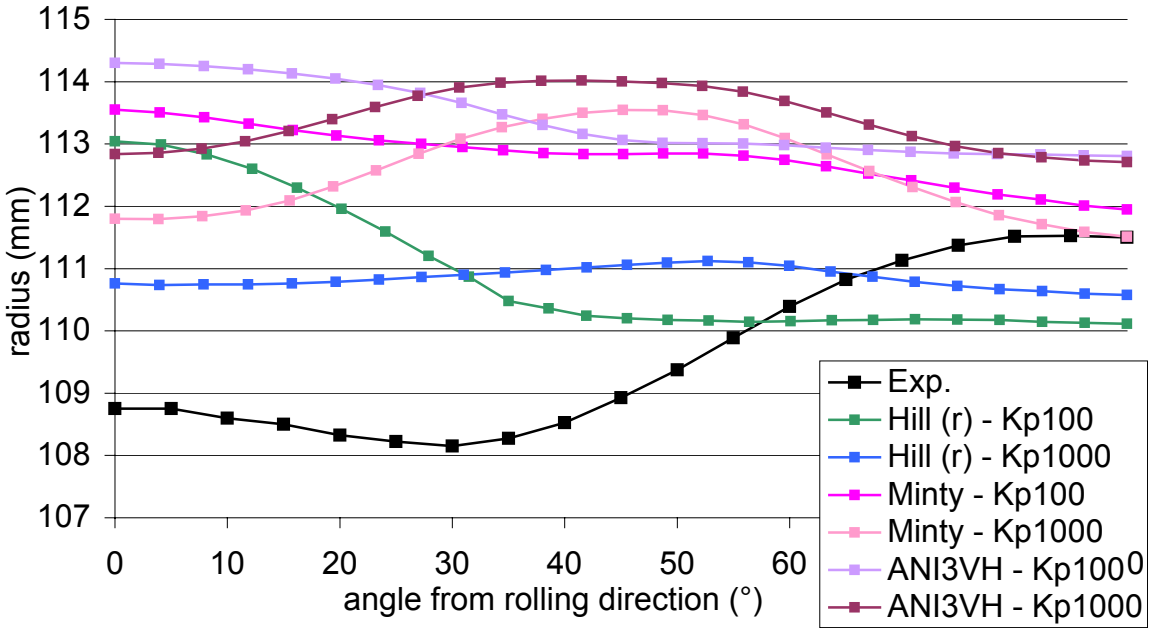

Figure 97: Influence of the penalty coefficient on the earing profile (SPXI 250 with oil lubricant)

Figure 97 presents the influence of the penalty coefficient on the earing profile. The earing profile has already proved to be a very sensitive result. Indeed, the shape of the earing profile is completely different according to the penalty coefficient.
It appears that for K_p =1000, the initial anisotropy of the steel sheet is hidden by the friction behaviour. The link between the earing profile and the Lankford coefficient can indeed be checked for the 'Kp 100' cases (for all the numerical constitutive laws) but not for the 'Kp 1000' cases.

D COMPARISON BETWEEN CONSTITUTIVE LAWS

The constitutive laws have already been compared in paragraph 3.4. Very small differences between the laws have been noted on the principal strain distributions. As the hardening behaviour is based on the same power-type evolution for all the constitutive laws presented here and furthermore fitted identically, the punch force is not noticeably influenced by the constitutive law.
On the other hand, the earing profile is more sensitive (see for instance Figure 72 for the SPXI 250 steel with oil lubricant) but the shape remains nevertheless identical for all laws.

With our model, the influence of the texture updating ('Evol' in the figures) compared to the case using the initial texture throughout the simulation ('Minty') can be analysed. Here again, the principal strain distributions and the punch force are not largely influenced. The earing profile is more influenced: the shape remains more or less identical but a shift can always be noticed. For each case, the radius of the deformed cup is lower when the texture is updated during the simulation.
A relatively small influence of the texture updating on the mechanical behaviour is then observed whereas the final texture is largely different to the initial one.

E THE REPRESENTATIVE SET OF CRYSTAL ORIENTATIONS

The ODFLAM procedure has generally been used to compute the discrete sets of crystallographic orientations representative of the continuous textures. The ODFTAY procedure has also been used for comparison purpose. These procedures are two versions of the software developed by the team of professor Van Houtte for the selection of the representative crystals.
The influence of these procedure on the mechanical behaviour of the steel sheet is very small for the deep drawing simulations presented here. The biggest difference has been noted on the earing profile and is presented in Figure 98.
We have however noticed that the representative sets of crystals obtained with ODFLAM reflects more accurately the anisotropy of the steel sheet. In Figure 99, the Lankford coefficient as a function of the angle from the rolling direction is computed with our texture based model using a representative set obtained with ODFLAM and another one obtained with ODFTAY. The Lankford coefficients directly computed from the continuous texture (referred to as 'Texture' in Figure 99) and 2 sets of experimental values are also plotted.
The Lankford coefficients computed on the basis of the discrete set obtained with ODFLAM are almost perfectly superimposed to the values directly computed from the continuous texture. The ODFTAY procedure is largely less accurate for the computation of the Lankford coefficients. As the Lankford coefficient is an important point for deep drawing processes, the ODFLAM procedure should be preferred here.

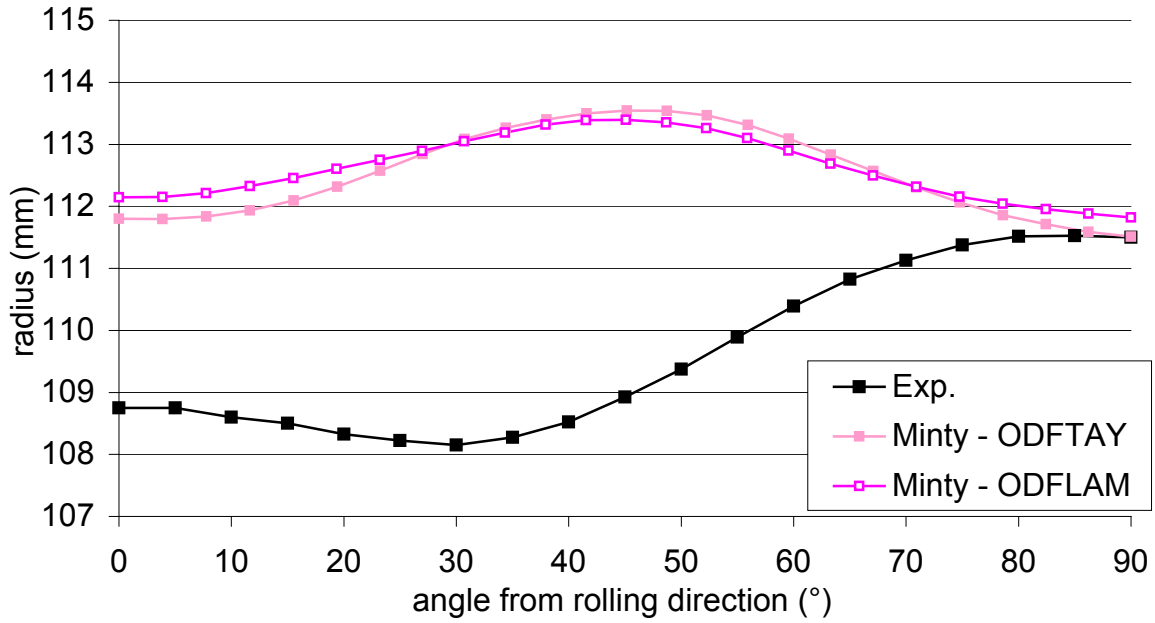

Figure 98: Influence of the procedures used to compute the representative set of crystals on the earing profile (SPXI 250 with oil lubricant)

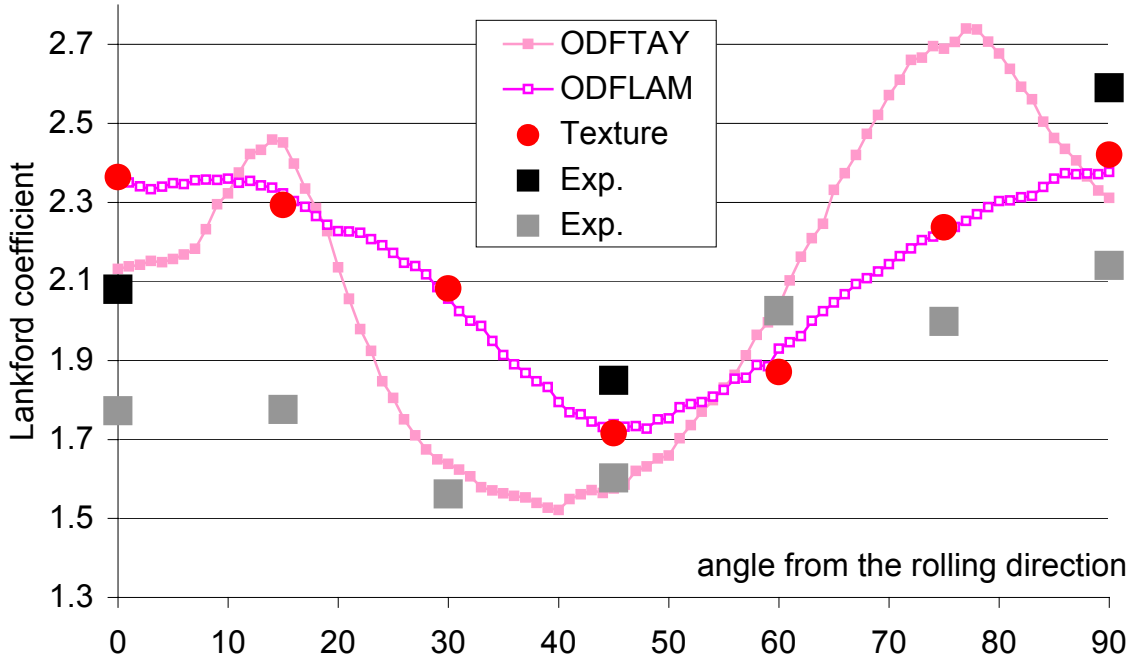

Figure 99: Comparison of the procedures used to compute the representative set of crystals (Lankford coefficient of the ULC Ti steel)

F THE FITTING OF THE HILL PARAMETERS

As explained in paragraph 3.3, the Hill constitutive law can be fitted either on the basis of the Lankford coefficients of the steel sheet or on the basis of the yield stresses. A mixed fitting procedure has also been investigated.

The case of a fitting only based on the Lankford coefficients ('Hill (r)' in the figures) and the case of a fitting allotting the same importance between Lankford coefficients and yield stresses ('Hill (sig+r)') are compared. Figure 100 shows the influence of the fitting procedure on the earing profile. The amplitude of the earing profile is larger when a Lankford coefficients based fitting is used.

The earing profile being closely linked to the Lankford coefficients, a Hill law fitted on the Lankford coefficients should be more accurate for the prediction of the earing profile.

The influence of the fitting procedure on the principal strain distributions is very low as presented by Figure 101.

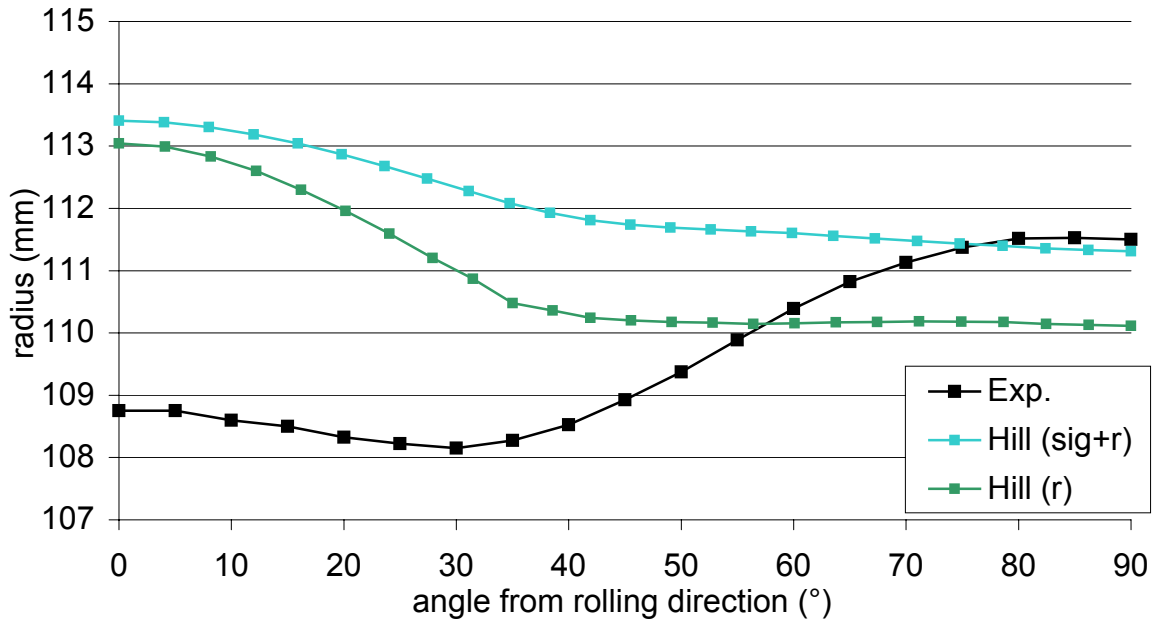

Figure 100: Influence of the fitting of the Hill parameters on the earing profile (SPXI 250 with oil lubricant)

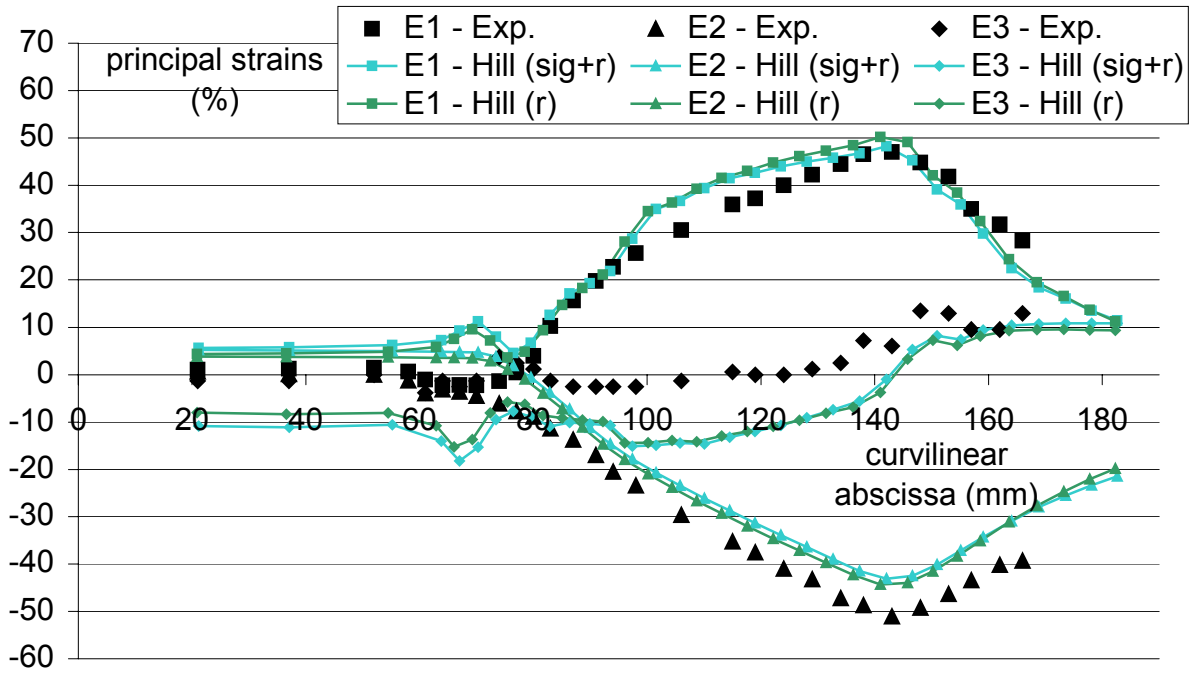

Figure 101: Influence of the fitting of the Hill parameters on the principal strains (SPXI 250 with oil lubricant)

G INFLUENCE OF THE FINITE ELEMENT TYPE

Finally, the influence of the finite element type on the deep drawing simulation is investigated. As already announced in paragraph 3.4 A (2), the finite element type has an influence on the bending behaviour of the modelled steel sheet. The slope of the punch force versus punch travel curve at the beginning of the simulation is then affected.

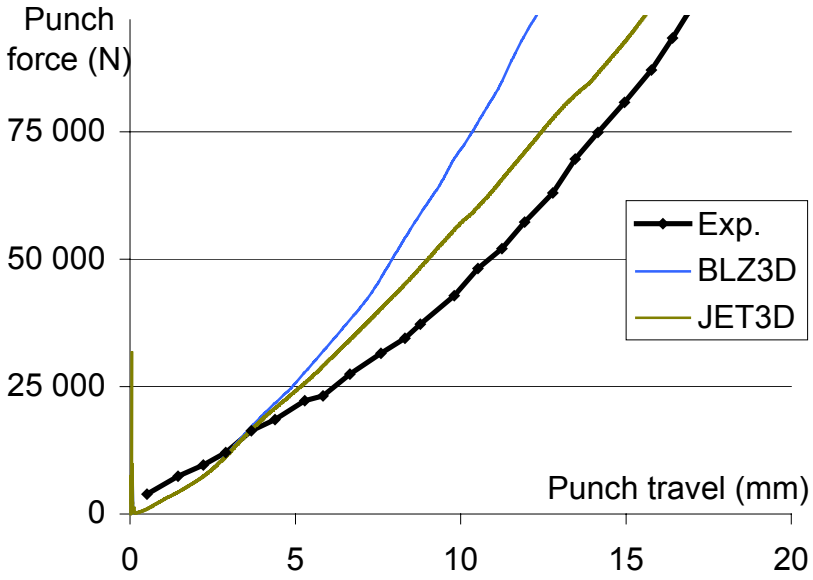

Figure 102: influence of the finite element type on the punch force (SPXI 250 with oil lubricant)

Figure 102 shows the punch force as a function of the punch displacement with BLZ3D elements (see Zhu and Cescotto (1994)) used up to now and with JET3D elements (see Li et al. (1992) and Li et al. (1995)).
The JET3D element and the BLZ3D element are both 8-node brick 3-D solid elements with one integration point (the BLZ3D element can also be used with 2, 4 or 8 integration points). They are mixed elements based on the Hu-Washizu principle (see Simo and Hughes (1986)) with hourglass control. Both elements make use of 3 fields: the stress field, the strain field and the displacement field. The main differences between the BLZ3D and the JET3D elements are the hypothesis used for the strain field and the treatment of the locking.

For both simulations of Figure 102, the identical Hill law is used. The finite element mesh is also identical. As we focus on the slope of the curve during the increasing punch force stage, only the beginning of the simulation is plotted in Figure 102.
The slope obtained with the JET3D elements is lower compared to the one of the BLZ3D elements showing a lower stiffness of the modelled material behaviour during the steel sheet bending stage. The JET3D element is in better agreement with experimental results.

A significant different behaviour is obtained between both finite element types even if they are very similar elements. If shell elements would have been tested, a different behaviour would also be expected.

3.6 Concluding remarks concerning the deep drawing tests performed by RDCS

The results predicted with the numerical models are generally in good agreement with experimental results. The exception case is the prediction of the earing profile with the SPXI 250 steel. For this steel, the weak anisotropy is suspected to be at the origin of the poor accuracy of the numerical results. The earing profile prediction is very sensitive, the anisotropy of the steel sheet is therefore hidden by perturbing numerical parameters. This point has been analysed in paragraph 3.5 and is summarized in Table 13.

Table 13: Summary of the sensitivity study for the earing profile prediction

Numerical parameter	Effect on the mean amplitude	Effect on the shape
Number of element layers	0.87mm	yes
Friction coefficient	4.9mm	yes
Penalty coefficient	0.25mm	yes
Constitutive law	2.5mm	no

It appears that the influence of the constitutive law is relatively small compared to other parameters. Furthermore, the shape of the earing profile is almost not influenced by the constitutive law while other numerical parameters affect the shape.

Table 14 summarises the influence of the numerical parameters on the punch force. The constitutive law used is here again not the most influential parameter.

The finite element model used for the simulations is not accurate enough so that the quality of the constitutive law implemented is the dominant parameter. Even if a significant texture evolution is noted according to the measurements (see for instance Figure 79 showing the evolution of the Lankford coefficients computed from the initial and the final texture

measurements), the prediction of the texture evolution seems not to be an interesting feature for the SPXI 250 steel.

Table 14: Summary of the sensitivity study for the punch force

Numerical parameter	Effect on the value of the maximum	Effect on the initial slope	Effect on the oscillations
Number of element layers	10%	no	no
Friction coefficient	27%	no	no
Penalty coefficient	Small	no	yes
Constitutive law	Small	no	no
Finite element type		yes	

On the other hand, the influence of the constitutive law is quite larger for the ULC Ti steel. The earing profile predicted with the Hill law is quite different from the texture based law as shown by Figure 91.
The implementation of an accurate yield locus representation is then more interesting.

4 *Deep drawing test proposed by KUL*

The prediction of the earing profile in paragraph 3 is in poor agreement with the experimental measurements. It is assumed that the low anisotropy of the SPXI 250 steel is at the origin of this problem. Indeed, the earing profile, which should be induced by the anisotropy of the steel sheet, is largely influenced by secondary features. These features can be experimental inaccuracies or numerical parameters (penalty coefficient, number of element layers…).
The earing profile predicted with the ULC Ti steel, which is more anisotropic, are indeed in better agreement with experimental values (see Figure 91). In the current paragraph, another very anisotropic steel is used to confirm the model validity. It is an interstitial free (IF) steel produced by rolling; the thickness of the steel sheet is 0.84mm.

4.1 Steel used

This steel sheet and the deep drawing process presented here have previously been investigated by Li et al. (2001). Experimental measurements of the earing profile are available and have been extracted from Li et al. (2001). These authors also gave us the parameters required to achieved the deep drawing simulations: characterisation of the IF steel (elastic and plastic parameters and texture measurement of the steel sheet), geometry of the process, friction behaviour…

The texture of the IF steel has been measured at mid-thickness and shows a strong γ fibre typical of rolled steel sheet. The maximum value of the ODF is 12.7. This high value (compared to 5.86 for SPXI 250 steel and 10.91 for the ULC Ti steel) proves the high anisotropy of this IF steel.
Figure 103 presents the Lankford coefficient of the IF steel. The values are computed from the texture measurement; no experimental values were available.
The high Lankford coefficients (from 1.8 to 2.7) also prove the anisotropy of the IF steel. For comparison, the Lankford coefficients of the SPXI 250 steel go from 1.05 to 1.45; for the ULC Ti steel, the Lankford coefficients are between 1.7 and 2.45.

The hardening behaviour is obtained through a tensile test along the rolling direction. The isotropic hardening law described by equation (31) is used. The hardening parameters are fitted on the experimental tensile test. The values are:

$$\begin{aligned} K &= 574MPa \\ \varepsilon_0 &= 0.00626 \\ n &= 0.326 \end{aligned} \tag{209}$$

Finally, the elastic parameters are:

$$\begin{aligned} E &= 210000MPa \\ \nu &= 0.3 \end{aligned} \tag{210}$$

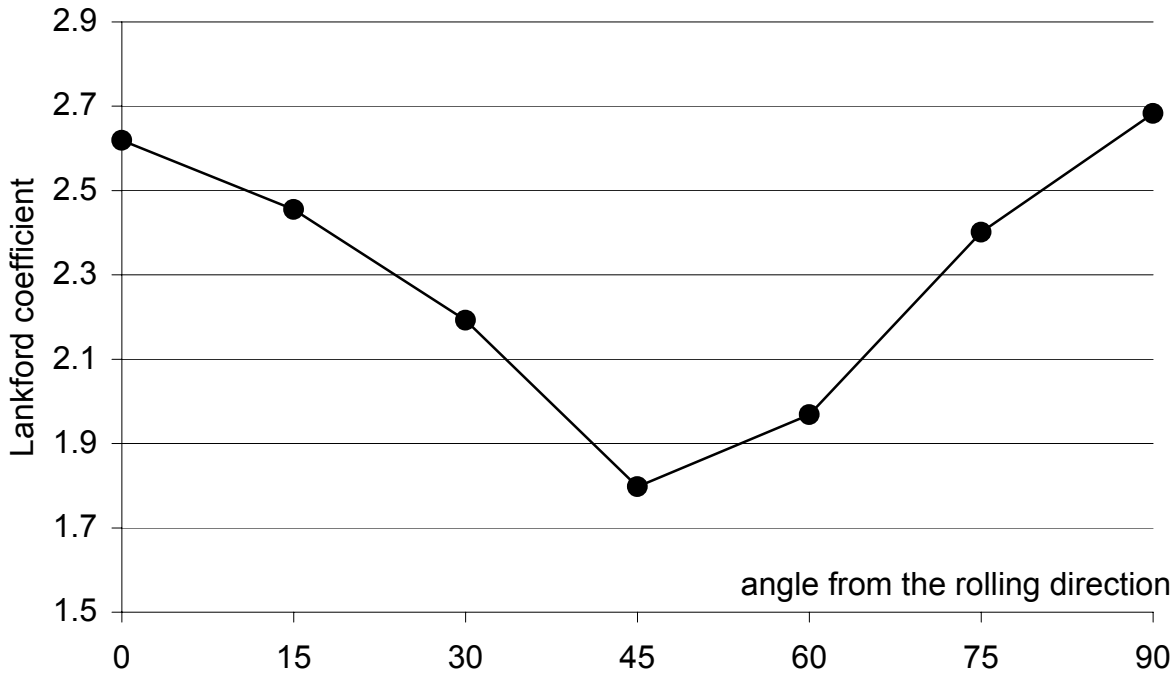

Figure 103: Lankford coefficient of the IF steel (computed on the basis of the texture measurement)

4.2 Geometry and finite element mesh

The geometry of the deep drawing process proposed by Li et al. (2001) is similar to the one of paragraph 3. It consists in an axisymmetric deep drawing process with a punch having a flat bottom. However, the dimensions are not identical: the diameter of the blank is 100mm, the punch diameter is 50mm (the drawing ratio is then 2.0), the punch fillet radius is 5mm, the matrix opening is 52.5mm and the matrix fillet radius is 10mm. The overall size of this deep drawing process is one third of the case treated in section 3 (except for the curvature radii and the blank thickness).

The blankholder force is prescribed to 5 kN.
The Coulomb friction coefficient between the blank and the tools obtained with the experimental lubrication method is μ=0.05.
A major difference from the deep drawing process of section 3 is that the punch travel is not stopped before the whole blank has passed along the matrix curvature. The flat part of the deformed cup which is clamped between the blankholder and the matrix at the end of the process is not present here. The deformed cup is composed of 3 zones (instead of 5): the flat part under the punch, a curved part applied against the curved part of the punch and the flange.
As a consequence, the earing profile does not correspond anymore to the radius of the deformed cup. The earing profile is measured as the height of the drawn cup as a function of the angle from the rolling direction.

The geometry is axisymmetric; but, as the IF steel sheet is orthotropic, a quarter of the process is meshed. To obtain a mesh similar to the one used by Li et al. (2001), the blank is meshed with one layer of 531 BLZ3D elements (see Zhu and Cescotto (1994)). The tools are meshed with triangular facets. Figure 104 presents a 3D split view of the blank and the 3 tools at the

beginning of the simulation. The curved parts of the punch and the matrix are meshed with a large number of triangular facets to model correctly the curvature while the flat parts and especially the blankholder are meshed with less triangular facets.

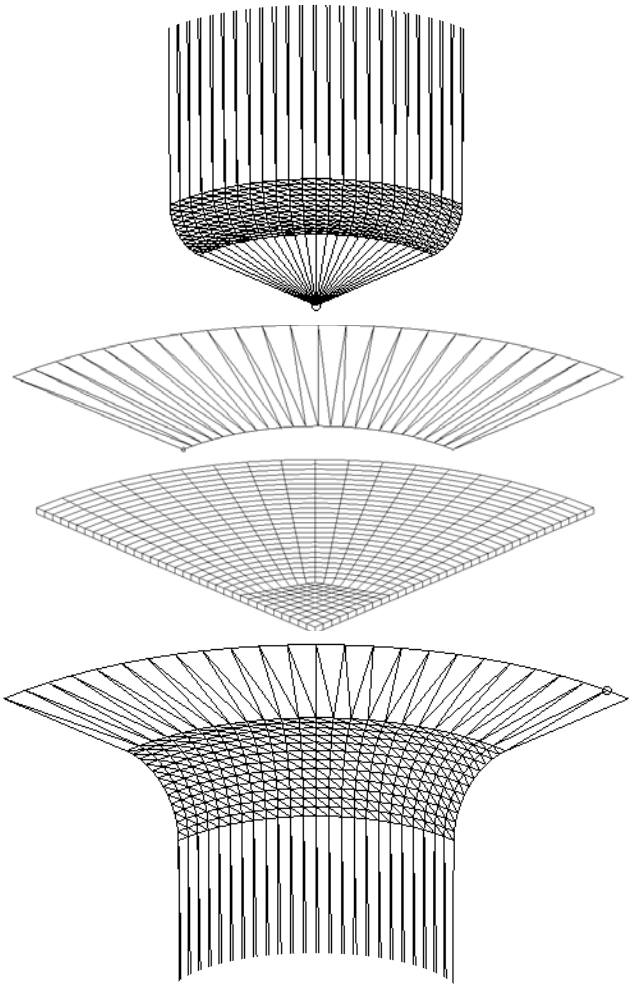

Figure 104: Mesh of the blank and the 3 tools (the punch and the matrix are truncated)

4.3 Constitutive laws

The constitutive laws used in the finite element code are the same than previously:

- 'Minty': our stress-strain interpolation method using the mechanical parameters and the measured texture of the IF steel. The size of the interpolation domains (angle ϑ in equation (47)) is 5° and the 24 slip systems of the bcc metals are used. The texture is not updated and the initial texture converted by ODFLAM into a representative set of 2000 crystals is used throughout the simulation.
- 'Evol': idem but the texture is updated during the simulation.
- 'Hill': the Hill (1948) constitutive law is used. As we focus here on the prediction of the earing profile, which is closely linked to the Lankford coefficients, the Hill parameters are fitted on the Lankford coefficients. The values are:

$$
\begin{aligned}
F &= 0.5395 \\
G &= 0.5526 \\
H &= 1.4474 \\
N &= L = M = 2.5091
\end{aligned}
\qquad (211)
$$

- The Coulomb friction constitutive law COU3DC (see Charlier and Cescotto (1988) and Habraken and Radu (1992)) is used with a friction coefficient of 0.05. The penalty coefficients used are 1000N/mm^3 between the blank and the matrix and 500N/mm^3 between the blank and the punch and the blankholder.

The computation time needed to achieve the simulation is highly dependent on the constitutive law used:

- 'Hill': 44 minutes
- 'Minty': 29 hours
- 'Evol': 130 hours

4.4 Results

For this deep drawing process, we focus on the prediction of the earing profile. The prediction of the punch force and the principal strains are less sensitive to experimental and numerical parameters and are then not investigated here. Figure 105 presents a 3D view of the deformed cup. The earing profile can clearly be visualised on this graph.
A more quantitative representation of the earing profile is the cup height plotted as a function of the angle from the rolling direction. Figure 106 presents the cup height for the 3 constitutive laws used and obtained from experimental measurements.

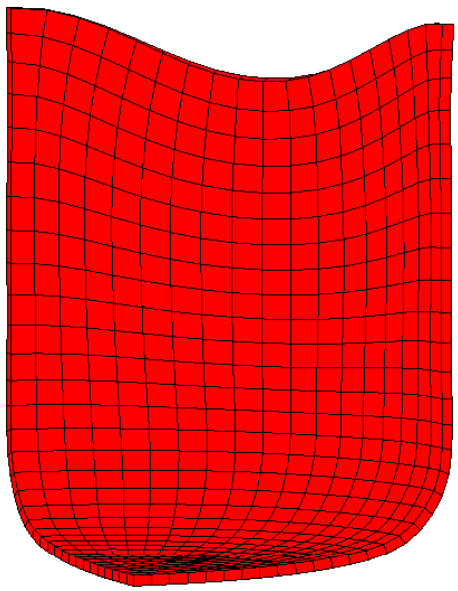

Figure 105: View of the deformed cup

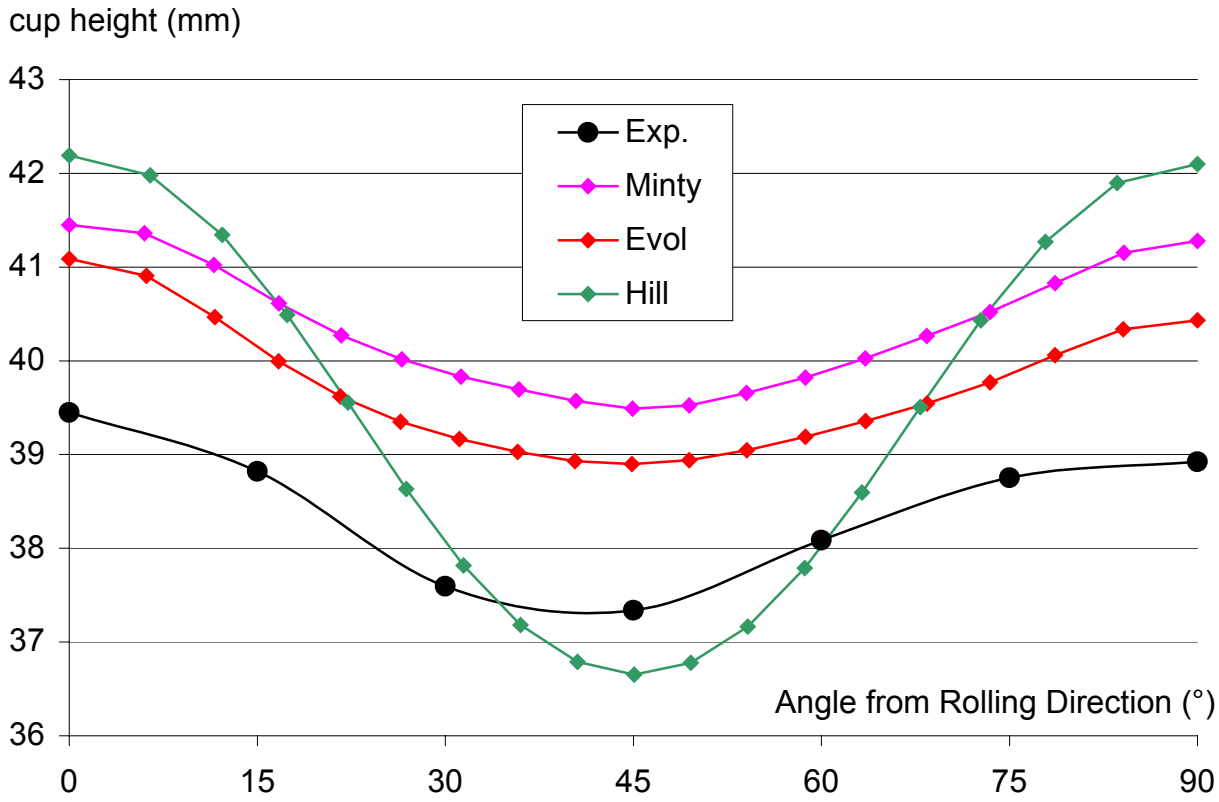

Figure 106: Comparison of predicted and measured cup height (the experimental measurements are extracted from Li et al. (2001))

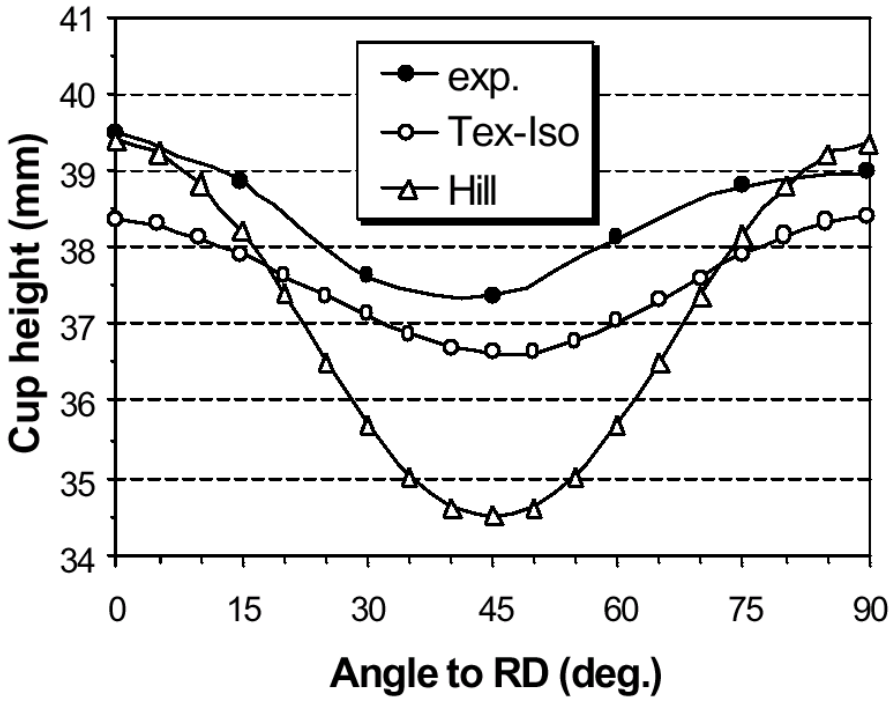

Figure 107: Cup height predicted by Li et al. (2001)

The earing prediction obtained with the 'Minty' law is very similar to the experimental one. Only a shift of around 2mm can be noticed. This shift could certainly be reduced by adjusting the Coulomb friction coefficient or the blankholder force. The predicted cup height is too high meaning that the blank is too much retained between the blankholder and the matrix. A lower blankholder force or a lower friction coefficient would then improve the earing prediction.
The shift can also be reduced by updating the texture during the simulation. The shift is indeed of 1.5mm for the 'Evol' case of Figure 106.
The Hill (1948) law yields a good prediction of the shape of the cup height but the amplitude is too high.
The high anisotropy of the IF steel is better represented on these earing profile graphs (Figure 106) than the small anisotropy of the SPXI 250 steel (see Figure 72).

The results obtained by Li et al. (2001) are presented in Figure 107. The finite element code ABAQUS is used. A Hill (1948) constitutive law is investigated; the amplitude of the earing profile predicted with the Hill law is too large as we have also noted. The 'Tex-iso' label refers to a texture based model in which the anisotropy of the material is described by a plastic potential in strain rate space. An isotropic hardening is used. As the same initial texture is used to represent the material behaviour as for our model, the shape of the earing profile is also correctly predicted but a shift from the experimental curve is present. The difference in the direction of the shift can be explained by the different finite element code used.

The prediction of the earing profile on the basis of the Lankford coefficients gives a cup height versus the angle from the rolling direction in agreement with the experimental and the numerical results. The comparison of Figure 103 showing the Lankford coefficients and Figure 106 showing the earing profile fulfils the link explained by Figure 85 between these 2 graphs. The Lankford coefficients can indeed be put in order:

$$r_{45°} = 1.80 < r_{0°} = 2.62 < r_{90°} = 2.68 \tag{212}$$

and the cup height is in agreement with the link proposed by Figure 85:

$$cup\ height_{45°} < cup\ height_{90°} < cup\ height_{0°}$$

'exp.'	37.34	38.92	39.45	
'Minty'	39.49	41.28	41.45	(213)
'Evol'	38.90	40.43	41.09	
'Hill'	36.65	42.10	42.19	

The friction coefficient and the blankholder force were cited as parameters able to reduce the shift observed between the numerical and the experimental earing profiles. Even if the value of these parameters effectively acting during the experimental deep drawing process are certainly not exactly equal to the prescribed values proposed Li et al. (2001), the adjustment of the blankholder force and the friction coefficient to fit the experimental earing profile is not investigated.
On the other hand, the penalty coefficient is not linked to any experimental value. Its value is chosen on the basis of numerical considerations. The values proposed in paragraph 4.3 (1000N/mm^3 for the matrix contact and 500N/mm^3 for the punch and the blankholder) has proved to be a good compromise: no particular convergence problems were noticed and the penetration is acceptable. However, the influence of the penalty coefficient was tested with a view to reduce the shift on the earing prediction.

As shown by Figure 106, the cup height predicted with the 'Minty' law is too high. This means that the steel sheet clamped between the matrix and the blankholder is retained too much. A reduction of the penalty coefficient would allow a more uniform distribution of the pressure on the clamped part of the steel sheet and then induce a lower predicted cup height. Figure 108 shows the case 'Kp(500,250,250)' where all the penalty coefficients are respectively divided by 2 compared to the initial case: 'Kp(1000,500,500)'. The cup height reduction expected is not observed: at 45° from the rolling direction, the cup height remains approximately constant and along the rolling and the transverse directions, the cup height even increases.
The reasoning proposed above is not wrong but another consequence of the reduction of the penalty coefficient arises and masks the expected effect. The reduction of the penalty coefficients induces a penetration of the blank into the curved part of the punch. The effective curvature radius of the punch is then increased as shown by Figure 109. As a consequence, the shape of the deformed cup under the punch is modified and induces a not desired increasing of the cup height (see Figure 109).
A simulation with higher penalty coefficients was then tested: 2000N/mm^3,1000N/mm^3 and 1000N/mm^3 for the contact with respectively the matrix, the punch and the blankholder. Unfortunately, convergence problems arose and did not allow us to complete this simulation.

Thanks to the observation presented above, it appears that, in order to reduce the predicted cup height, a high penalty coefficient should be used between the blank and the punch (2000N/mm^3 is tested) and a low penalty coefficient should be used for the contact with the matrix and the blankholder (250N/mm^3). The results obtained with the case 'Kp(250,2000,250)' are presented in Figure 108. A small improvement of the predicted cup height is obtained but the shift from the experimental results remains large.
The influence of the penalty coefficient on the cup height seems to have reach its limits. Further modifications of the penalty coefficients to reduce the shift is not reasonably interesting and is not investigated.

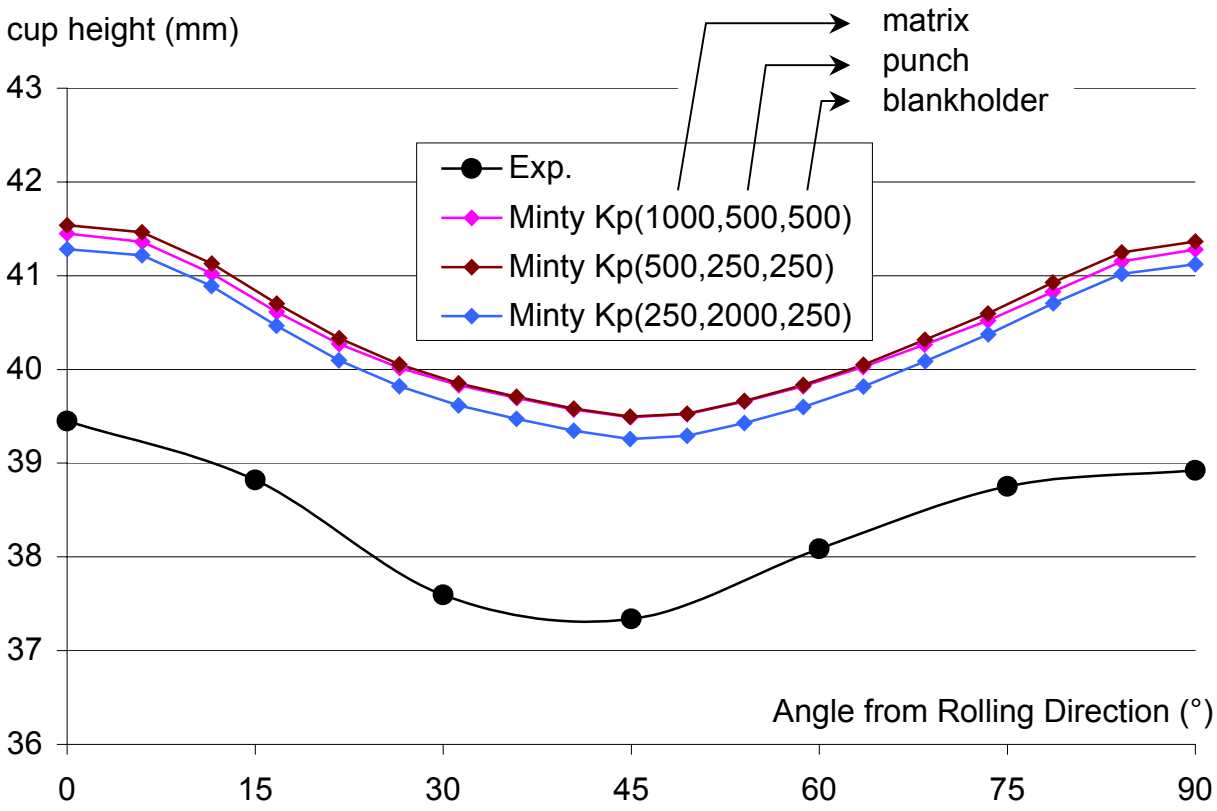

Figure 108: Influence of the penalty coefficient on the cup height

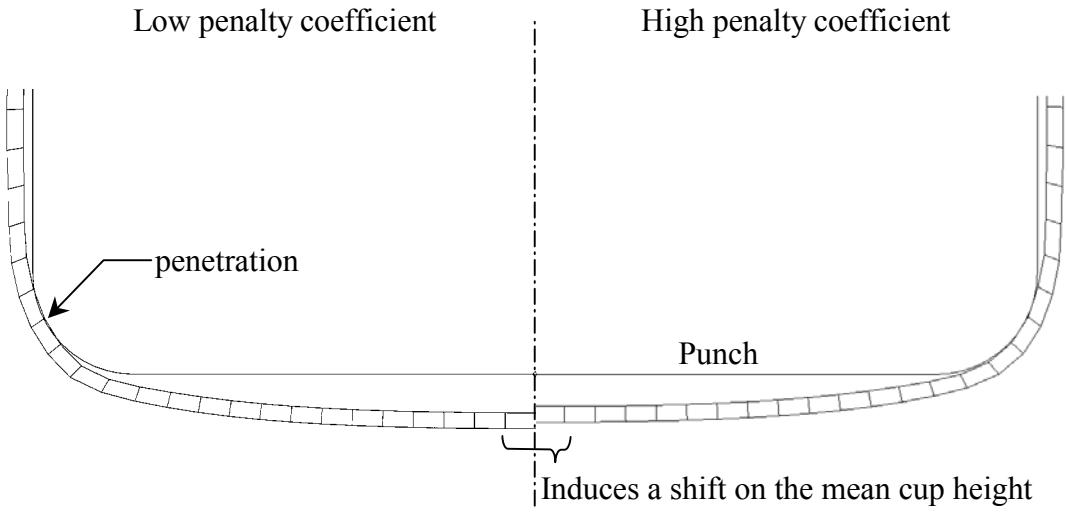

Figure 109: Influence of the penalty coefficient on the curvature of the cup along the punch

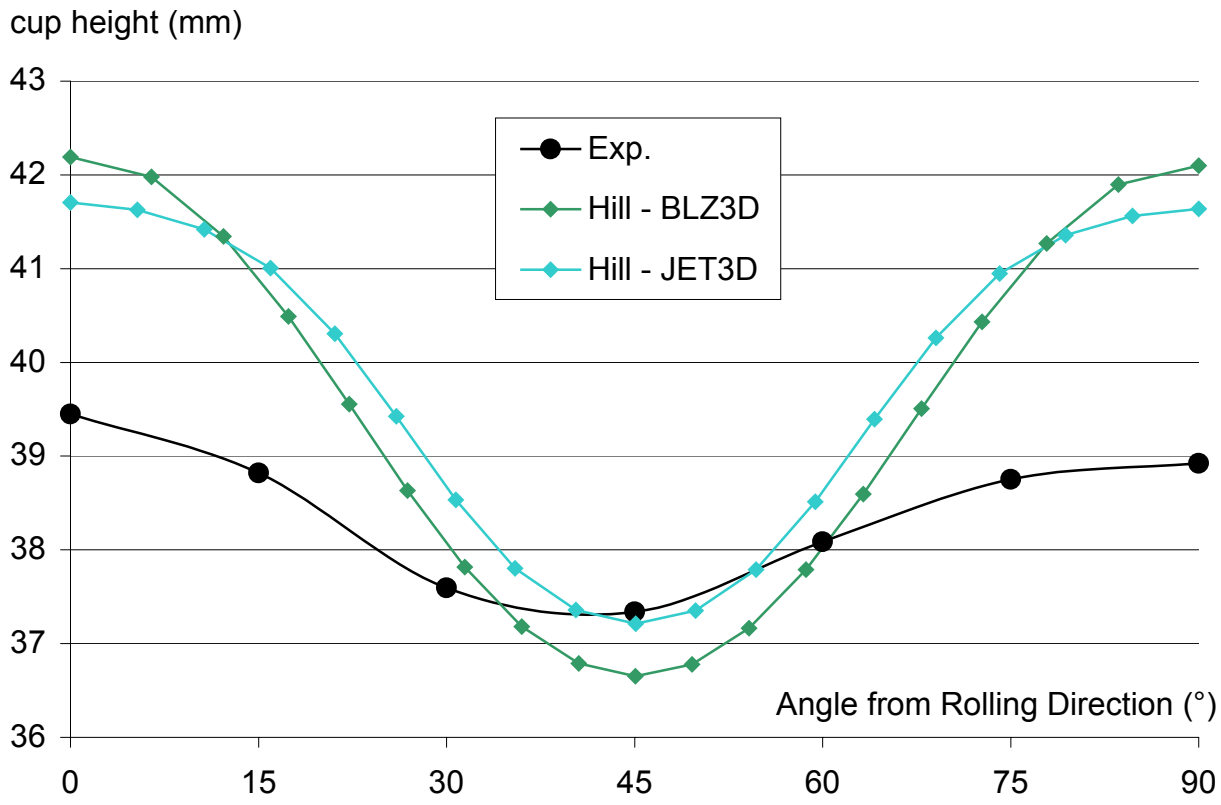

Figure 110: Influence of the element type on the cup height

The influence of the finite element type on the prediction of the cup height is presented by Figure 110 where the BLZ3D element used for most simulations presented here is compared to the JET3D element (see Li et al. (1992)). The same Hill (1948) constitutive law is used in both cases.
A significant influence of the element type can be noticed on the cup height: the amplitude, which has been found to be too large with the Hill law, is reduced when the JET3D element is used. The mean cup height remains approximately constant.

4.5 Removing of the tools

For the deep drawing simulations presented up to here, the computation is stopped when the punch has reached its final position. The deformed cup, at the end of the simulation, remains in contact with the tools. The presented results are then computed on the basis of a constrained configuration. Contrarily, the experimental results are always measured when the tools are removed and the cup is released.
The influence of the removing of the tools through the relaxation of elastic strains, i.e. the springback, is investigated.

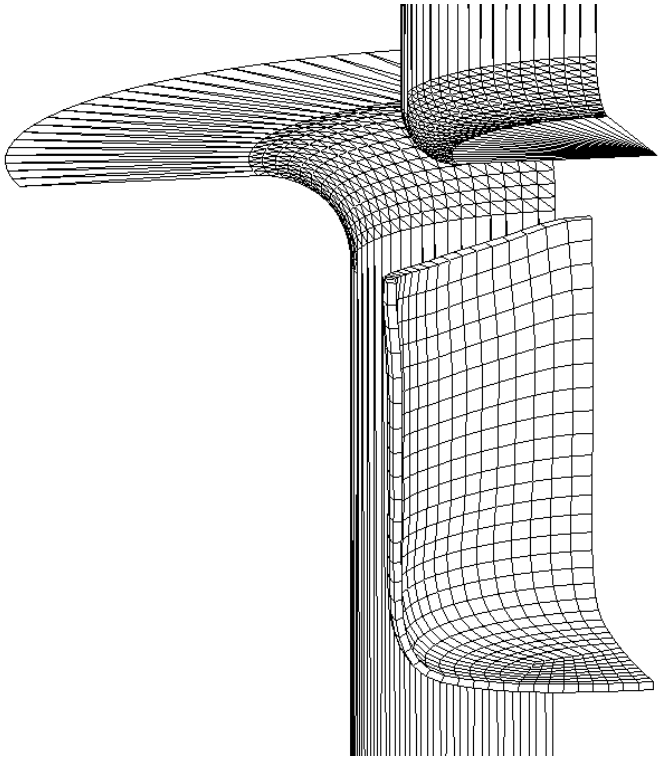

Figure 111: 3D view of the deformed cup with the tools removed

After the deep drawing simulation is achieved, the punch is moved back into its initial position. Its displacements along the Z-axis first go down to draw the steel sheet and then go up to release the cup.
The X and the Y global axes being the symmetry axes of the simulation and the Z-axis being the punch displacement direction, after the punch is removed, the matrix is moved away along the (1,1,0) direction. A gap of around 4mm is managed between the cup and the matrix.
Note that the blankholder is applied against the matrix at the end of the deep drawing simulation and therefore does not need to be removed.
Figure 111 shows a 3D view of the deformed cup and removed tools. The blankholder is not plotted in the figure for clarity purposes.

The influence of the removing of the tools on the cup height is presented by Figure 112. A small increasing of the cup height can be noticed from 30° to 70° from the rolling direction; but the influence is rather small.

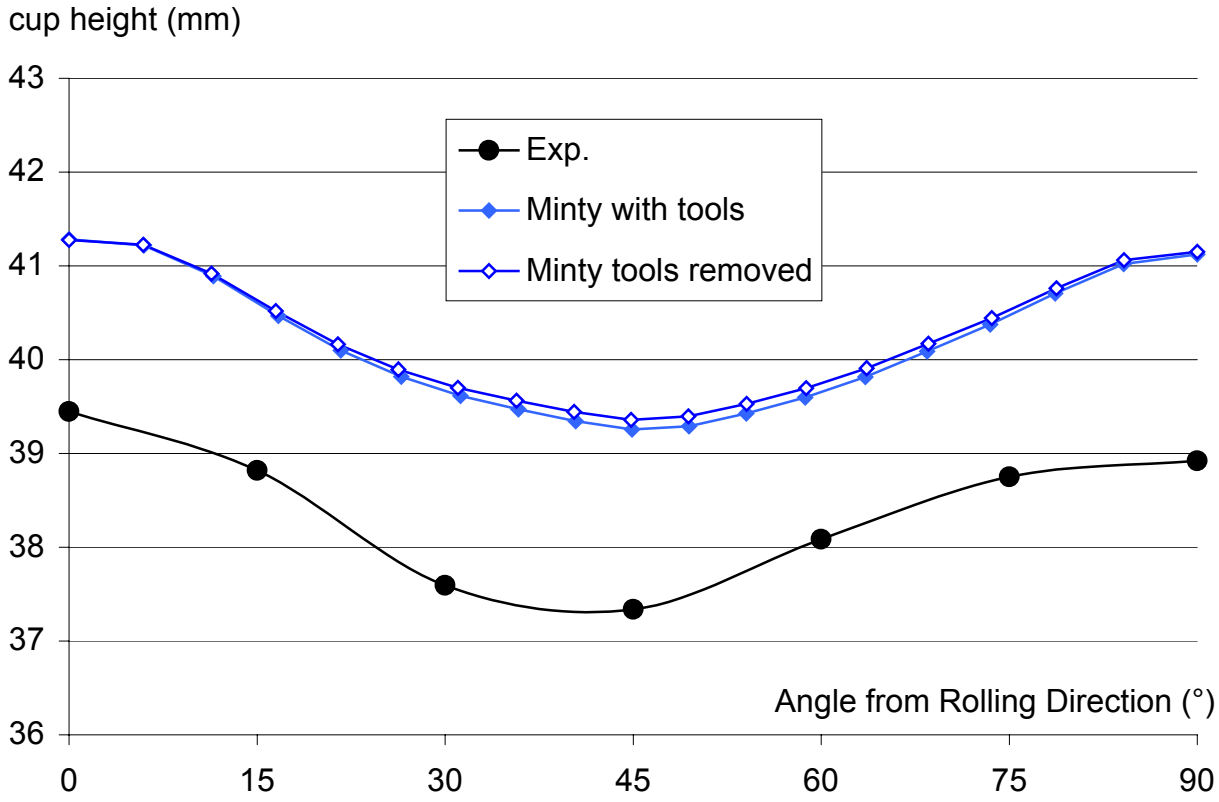

Figure 112: Influence of the removing of the tools on the cup height (the case Kp(250,2000,250) is investigated)

Chapter 5: Conclusion and topics for future researches

The results obtained in chapter 4 with our local yield locus approach are generally in good agreement with the experimental results (prediction of the strain distribution over the deformed cup, prediction of the punch force as a function of the punch travel). However, the prediction of the earing profile is very sensitive to numerical parameters. The earing profile predicted for the most isotropic steel grade investigated (SPXI 250) is in poor agreement with experimental earing profile. The weak anisotropy of this steel is partly hidden by other parameters such as friction or penalty coefficients, the finite element mesh (number of element layers), the constitutive law used. The earing profiles predicted for the ULC Ti steel grade and especially for the IF steel of chapter 4 paragraph 4 are less influenced by perturbing parameters and are in relatively good agreement with experimental results.
The final textures of the steel sheet predicted by the stress-strain interpolation method with Taylor's model are qualitatively in good agreement with measured final textures. Nevertheless, the predicted amplitudes of the ODF maximums are too low compared to measurements.

However, the accuracy of the model in one particular case is not the main interest of the thesis. We particularly focus on the importance of taking texture evolution into account throughout the finite element simulations. The final texture (either predicted or measured) represented by sections of its ODF is in all cases very different from the initial texture. This conclusion is of course only valid on the parts of the cup where large plastic strains occurred. Under the punch, the final texture is almost identical to the initial one.
The different texture evolution from one material point to another according to their strain history makes the models, able to predict the texture evolution, difficult to use from a computational point of view (high CPU time and large memory storage required).
The goal of the local yield locus approach is to reduce the memory storage (only the few parameters necessary to represent a small part of the yield locus must be stored for each integration point) and particularly the computation time required to predict the texture evolution and to take it into account throughout the simulation.
The larger computation time required for one simulation is almost 300 hours. However, thanks to parallel computation, such a simulation can be performed in around 50 to 60 hours which is already a more reasonable duration. Note that the implementation of the parallel computation has been achieved in such a way to be very efficient for the stress-strain interpolation model.

The accuracy of the constitutive law implemented is linked to the accuracy of Taylor's model. The accuracy of the local yield locus compared to Taylor's model is indeed very good. As presented by Figure 30 of chapter 3, the relative error of the local yield locus computed by the stress-strain interpolation method compared to Taylor's model is around 10^{-4} for a size of the domain: ϑ=5°. This size of the domain has been used for most of the simulations presented in chapter 4. A relative error of 10^{-5} can be obtained with a size of the domain of ϑ=1°. Such a small value would however lead to higher computation time due to a larger number of domain updatings required for a complex finite element simulation.
To improve the yield locus accuracy of our model, microscopic Taylor's model should be replaced by a more accurate model. The use of another assumption than equality of microscopic and macroscopic strain rate (Taylor's assumption) should also improve the prediction of texture evolution.

The flowchart of the code was really oriented in such a way that the routine providing the macroscopic stress when the macroscopic strain rate is known can be easily replaced. One can think to replace Taylor's module by self-consistent method (see Nikolov and Doghri (2000)) or LAMEL model (see Liu et al. (2002) and Delannay et al. (2002))…

The implementation of a local yield locus approach is not straightforward. A lot of theoretical developments had to be performed; several numerical tests have been achieved. Nevertheless, the first local approach: the hyperplanes method to which a non negligible part of the research work has been devoted had to be replaced.
On the other hand, the fitting of the material parameters is relatively simple compared to recently developed phenomenological models. Such models increase their complexity to be able to reproduce experimental observation, this yields to high number of material parameters difficult to identify. Our texture based model only requires the measurement of the initial texture to represent the anisotropy of the steel sheet and the fitting of the hardening behaviour on one tensile test. While several complicated and expensive tests must be achieved to fit some sophisticated phenomenological models.

Another finite element simulation has been investigated with the stress-strain interpolation method. It is the benchmark of the conference NUMISHEET 1999 and ESAFORM 2001. It consists in a deep drawing process with a hemispherical punch (see Duchêne et al. (2001) and Duchêne et al. (2002)). Several numerical and experimental results were obtained thanks to the participants to the benchmark.
A relatively good agreement of the results of our simulations compared to experimental results was obtained. Large differences on the final predicted texture was noticed from one point to another of the deformed cup.

If the texture evolution is small for one particular forming process, a global yield locus approach would lead to accurate numerical results within small computation time. A local yield locus approach is not interesting for such a case. However, we have noticed significant texture evolutions for the investigated deep drawing processes. The use of a local yield locus approach is then clearly justified for the presented validations. For instance, the earing profile predicted for the deep drawing process of chapter 4 paragraph 4 is quite better if the texture is updated throughout the simulation.

The gain of our local yield locus approach compared to the direct use of the micro-macro model (Taylor's model in our case) is very good. As presented in paragraph 9.3 of chapter 3, as a mean value, the Taylor's model is called once while the yield locus is explored 158 times by the finite element code, if the texture evolution is not computed. If the texture evolution is desired, the gain is reduced to 62 which remains however an appreciable value.

For future researches about the local yield locus approach, several topics can be investigated. As already mentioned, the replacement of microscopic Taylor's model and the micro-macro Taylor's assumption will be carried out within IAP project (IAP P5/08 From microstructure towards plastic behaviour of single and multiphase materials). Several more sophisticated micro-macro transition models can be investigated, the computation of the texture evolution by Taylor's model being subject to critique.
The implementation of a kinematic hardening to replace the simple isotropic one is also under investigation. The kinematic hardening behaviour proposed by Bouvier et al. (2003) should be implemented.

For the prediction of the Swift effect, a microscopic hardening based on the slip system activity should be investigated. Such a hardening without physical roots has been tested. However, to be able to predict quantitatively the Swift effect for an actual material, an accurate slip system activity based hardening should be implemented.

At this stage, the strategy for the texture updating is rather simple, a texture updating is achieved after a predetermined number of time step. A more physical criterion for texture updating should be investigated; a criterion based on the accumulated plastic work seems interesting.

To decrease the numerical perturbing parameters inducing inaccurate earing predictions, some research could be conducted:

- comparison of Lagrange-contact approach and penalty contact approach,
- comparison of mixed finite element behaviour with real bending experiments to provide guidelines concerning the number of layers necessary to obtain good accuracy.

References

Anand L., Balasubramanian S., Kothari M. (1997), *Constitutive modelling of polycrystalline metals at large strains: application to deformation processing, large plastic deformation of crystalline aggregates*, International Centre for Mechanical Sciences, Courses and Lectures n°376, Springer Ed, 109-172.

Bachu V., Kalidindi S.R. (1998), *On the accuracy of the predictions of texture evolution by the finite element technique for fcc polycrystals*, Materials Science and Engineering A257, 108-117.

Banabic D., Comsa D.S., Kuwabara T., Iizuka E., Hira T., Wagner S., Siegert K. (2002), *Description of the plastic behaviour of sheet metals using a new orthotropic yield criterion*, Proc. of the 7th ICTP, Advanced Technology of Plasticity, vol. 2, Yokohama, Japan

Beaudoin A.J., Dawson P.R., Mathur K.K., Kocks U.F., Korzekwa D.A. (1994), *Application of polycrystal plasticity to sheet forming*, Comp. Methods Appl. Mech. Eng., 117, 49-70.

Berveiller M., Zaoui A. (1984), *Modeling of the plastic behaviour of inhomogeneous media*, J. Engng. Mater. Technol., Vol. 106, pp. 295-298.

Bille J.P., Habraken A. M., Charlier R. (1994), *Numerical Approach of Contact Using an Augmented Lagrangian Method,* 3e Congrès National belge de mécanique théorique et appliquée, Liège, Belgium.

Bishop J. F. W., Hill R. (1951), *A theoretical derivation of the plastic properties of a polycrystalline face-centred metal*, Philosophical Mag., Ser. 7, 42, 1298-1307.

Bouvier S., Teodosiu C., Haddadi H., Tabacaru V. (2003), *Anisotropic work-hardening behaviour of structural steels and aluminium alloys at large strains*, J. Phys. IV France, 105.

Bunge H.-J. (1982), *Texture analysis in materials science*, Butterworths, London.

Cela J. M. (2001), Library CAESAR, Centro Europeo de Paralelismo de Barcelona.

Charlier R., Cescotto S. (1988), *Modélisation du phénomène de contact unilatéral avec frottement dans un contexte de grande déformation*, J. Theoret. Appl. Mech., Special issue, Suppliment No. 1 to Vol. 7.

Crumbach M. et al. (2001), *Recrystallization and grain growth*, vol. II, ed. Gottstein G. and Molodov D. A., Springer Verlag, Berlin, pp. 1053-1060 (part I) and pp. 1061-1068 (part II).

Daniel D., Savoie J., Jonas J. J. (1993),*Textures induced by tension and deep drawing in low carbon steel sheets*, Acta metall. mater., 41(6), 1907-1920.

Dawson P.R., Boyce D. (2002), *Tools for polycrystal plasticity analyses*, Materials Science Forum Vols. 408-412 pp. 67-74.

Dawson P.R., Kumar A. (1997), *Deformation process simulations using polycrystal plasticity, large plastic deformation of crystalline aggregates*, International Centre for Mechanical Sciences, Courses and Lectures n°376, Springer Ed, 247.

Dawson P.R., Miller M.P., Turner T.J. (1998), *Quantification and interpolation of texture and its gradients in rolled aluminium plate*, Proceedings of the second symposium held at the 1998 TMS Fall Meeting, Rosemont, Illinois.

de Montleau P. (2003), *Isotropic and kinematic hardening – law HILL3D_KI*, internal report, M&S department.

de Montleau P., Cela J.M., Moto Mpong S., Godinas A. (2002), *A parallel computing model for the acceleration of a finite element software*, The 4th International symposium on high performance computing, Wompei, Japan.

Delannay L., Logé R.E., Chastel Y., Van Houtte P. (2002), *Prediction of intergranular strains in cubic metals using a multisite elastic-plastic model*, Acta Materialia, 50, pp. 5127-5138.

Duchêne L. (1998), *Modifications et améliorations apportées à la loi MIPAY3*, convention RW n°2748, intermediate report n°26.

Duchêne L. (1999 a), *Description de la programmation de la méthode d'interpolation de la relation de Taylor*, convention RW n°2748, intermediate report n°30.

Duchêne L. (1999 b), *Etude de la précision, de la convergence et de la stabilité de la méthode des hyperplans et de la méthode d'interpolation*, convention RW n°2748, intermediate report n°31.

Duchêne L. (2000) *Implementation of a yield locus interpolation method in the finite element code Lagamine*, DEA graduation work, University of Liège, Belgium.

Duchêne L., Godinas A., Cescotto S., Habraken A. M. (2002), *Texture evolution during deep-drawing processes*, Journal of Materials Processing Technology, 125-126, pp. 110-118.

Duchêne L., Godinas A., Habraken A. M. (1999), *Metal plastic behaviour linked to texture analysis and FEM method*, Proc. 4th Int. Conf.: NUMISHEET'99.

Duchêne L., Habraken A. M., Cescotto S. (1998), *Elastoplastic anisotropic model based on texture analysis to simulate steel sheet behavior*, Proc. 7th Int. Symp. (Cancun, Mexico).

Duchêne L., Habraken A. M., Godinas A. (2000), *Validation of a FEM Model Coupled with Texture Applied to Deep Drawing Process*, Proc. 3rd Int. Conf.: ESAFORM'00.

Duchêne L., Habraken A. M., Godinas A. (2001), *Influence of steel sheet anisotropy during deep-drawing processe*, Proc. 4th Int. Conf.: ESAFORM'01.

Franciosi P. (1988), *On flow and a work hardening expression correlation in metallic single crystal plasticity*, Revue Phys. Apll., 23, pp 383-394.

Frénois S. (2001), *Modélisation polycristalline du comportement mécanique du tantale. Application à la mise en forme par hydroformage*, Ph. D. Thesis, Ecole Centrale des Arts et Manufactures, Ecole Centrale Paris.

Gahbiche A., Ammari L., Benameur T., François M., Guelorget B., Dogui A. (2002), *Evolution des textures de déformation en fonction de la nature des sollicitations de tôles d'emboutissage en acier Fe P04 (C.C)*, Proc. JSTMM'02, Monastir, Tunisie.

Gil Sevillano J., Van Houtte P., Aernoudt E. (1980), *Large strain work hardening and textures*, Prog Mater Sci. 25: 69-412.

Godinas A. (1998 a), *Définition locale de la surface de plasticité – partie1: théorie*, convention RW n°2748, intermediate report n°22.

Godinas A. (1998 b), *Définition locale du comportement plastique d'un matériau*, convention RW n°2748, intermediate report n°27.

Habraken A. M. (2000), *Modelling the plastic anisotropy of polycrystalline materials by FEM*, Grasmech course, February 2000.

Habraken A. M., Cescotto S. (1998), *Contact between deformable solids, the fully coupled approach*, Mathematical and Computer Modelling, 28, No. 4-8, pp. 153-169.

Habraken A. M., Munhoven S. (1996), *Schema d'implantation d'une version simplifiée du couplage micro-macro: texture – éléments finis*, convention RW n°2748, intermediate report n°10.

Habraken A. M., Radu J. P. (1992), *Numerical approach of contact with friction between two bodies in large deformations and rotations*, presented at Contact Mechanics Int. Symp., Lausanne, Switzerland.

Hill R. (1948), *A theory of the yielding and plastic flow of anisotropic metals*, Proc. Roy. Soc. London A193, 281-297.

Hoferlin E. (2001), *Incorporation of an accurate model of texture and strain-path induced anisotropy in simulations of sheet metal forming*, Ph. D. thesis, Katholieke Universiteit Leuven.

Imbault D., Arminjon M. (1993), *Theoretical and numerical study of the initial and induced plastic anisotropy of steel sheets, using a texture-based methodology*, final report of contract Univ. J. Fourier n° 17191401, Laboratoire 3S, Université Joseph Fourier, France.

Jonas J. J., Shrivastava S., Toth L. S. (1998), *The inverse swift effect: experiments and theory*, Acta mater., Vol. 46, No. 1, 51-60.

Kalidindi S.R., Anand L. (1992), *an approximate procedure for predicting the evolution of crystallographic texture in bulk deformation processing of fcc metals*, Int. J. Mech. Sci., Vol. 34, No. 4, pp. 309-329.

Kalidindi S.R., Anand L. (1994), *Macroscopic shape change and evolution of crystallographic texture in pre-textured fcc metals*, J. Mech. Phys. Solids, 42/3,459-490.

Khan A.S., Cheng P. (1996), *An anisotropic elastic-plastic constitutive model for single and polycrystalline metals. I – theoretical developments*, Int. J. Plasticity, 12/2, pp 147-162.

Li K.P. (1995-1996), *Contribution to the Finite Element Simulation of Three-Dimensional Sheet Metal Forming*, Ph. D. Thesis, ULG, Liege.

Li K.P., Cescotto S., Jetteur P. (1992), *An element with hourglass control for the large deformation analysis in three-dimension*, Proc. of 3rd Int. Conf. on Computational Plasticity, Fundamentals and Applications, Barcelona, Spain.

Li K.P., Habraken A. M., Bruneel H. (1995), *Simulation of square-cup deep-drawing with different finite elements*, Journal of Materials Processing Technology, 50, pp. 81-91.

Li S., Hoferlin E., Van Bael A., Van Houtte P. (2001), *Application of a texture-based plastic potential in earing prediction of an IF steel*, Advanced Engineering Materials, 3, No. 12, 990-994.

Liu Y.S., Delannay L., Van Houtte P. (2002), *Application of the Lamel model for simulating cold rolling texture in molybdenum sheet*, Acta Materialia 50, 1849-1856.

Lorrain J.P., Ben Zineb T., Abed Meraim F., Berveiller M. (2002), *Modélisation du comportement élastoplastique de monocristaux de structure cubique. Comparaison théorie/expérience*, Quatrièmes Journées Scientifiques et Techniques en Mécanique et Matériaux, Monastir, Tunisie.

Magnée A., *Cours de métallurgie structurale théorique*, Notes de cours, Faculté des Sciences Appliquées, Université de Liège, Belgium.

Mathur K.K., Dawson P.R. (1989), *On modeling the development crystallographic texture in bulk forming processes*, Int. J. Plasticity, 5, pp. 67-94.

Maudlin P.J., Wright S.I., Kocks U.F., Sahota M.S. (1996), *An application of multisurface plasticity theory : yield surfaces of textured materials*, Acta mater. Vol. 44, No. 10, pp. 4027-4032.

Miller M. P., McDowell D. L. (1996a), *The effect of stress-state on the large strain inelastic deformation behavior of 304L stainless steel*, ASME J. Engng Mater. Technol., 118, 28-36.

Miller M. P., McDowell D. L. (1996b), *Modeling large strain multiaxial effects in fcc polycrystals*, Int. J. Plast., Vol. 12, No. 7, 875-902.

Moto Mpong S., de Montleau P., Godinas A., Habraken A. M. (2002a), *Acceleration of finite element analysis by parallel processing*, The 5th international ESAFORM Conference on Material Forming edited by M.Pietrzyk, Z. Mitura, J. Kaczmar, Krakow Poland, pp. 47-50.

Moto Mpong S., de Montleau P., Godinas A., Habraken A. M. (2002b), *A parallel computing model for the acceleration of a finite element software*, International conference on parallel and distributed processing techniques and applications, Las Vegas, USA.

Munhoven S. (1995), *Velocity gradient and local axes in three-dimensional finite element simulations*, Internal report n° 219, M&S department.

Munhoven S., Habraken A. M., Van Bael A., Winters J. (1996), *Anisotropic finite element analysis based on texture*, Proc. 3rd Int. Conf.: NUMISHEET'96, pp.112-119.

Munhoven S., Habraken A.M., Winters J., Schouwenaars R., Van Houtte P. (1995), *Application of an anisotropic yield locus based on texture to a deep drawing simulation*, NUMIFORM 95, Simulation of Materials Processing: Theory, Methods and Applications, Ed. Shen & Dawson, BALKEMA, 767-772.

Nakamachi E., Chen Y. P., Hirose M., Morimoto H. (2002), *Crystal plasticity finite element and experimental analyses of plastic deformation induced crystal rotations of fcc and bcc single crystal sheets*, Proc. 7th ICTP, Yokohama, Japan.

Nakamachi E., Dong X.H. (1997), *Study of texture effect on sheet failure in a limit dome height test by using elastic/crystalline viscoplastic FE analysis*, ASME Journal of Applied Mechanics, 64, pp. 519-524.

Nikolov S., Doghri I. (2000), *A micro-macro constitutive model for the small deformation behaviour of polyethylene*, Polymer, 41, 1883-1891.

Radhakrishnan B., Sarma G., Zacharia T. (1998), *Coupled finite element-Monte Carlo simulation of microstrucutre and texture evolution during thermomechanical processing*, Proceedings of the second symposium held at the 1998 TMS Fall Meeting, Rosemont, Illinois.

Radu J.-P., Munhoven S., Habraken A. M. (1997), *Amélioration de la version simplifiée du couplage micro-macro: texture – éléments finis. Tests de validation*, convention RW n°2748, intermediate report n°11.

Reuss A. (1929), *Berechnung der Fließgrenze von Mischkristallen auf Grund der Plastizitätsbedingung für Einkristalle*, Z. Angew. Math. Mech., 9, 49-58.

Rohatgi A., Jonas J. J., Shrivastava S. (1995), *Effect of stress-relief annealing on the inverse Swift effect in steel and iron*, Scripta Metallurgica et Materialia, Vol. 32, No. 5, 737-741.

Sachs G. (1928), *Zur ableitung einer fliessbedingung*, Z. Verein Deutscher Ing, 72, 734-736.

Sarma G., Radhakrishnan B., Zacharia T. (1998), *Polycrystal simulations of texture evolution during deformation processing*, Proceedings of the second symposium held at the 1998 TMS Fall Meeting, Rosemont, Illinois.

Simo J.C., Hughes T.J.R. (1986), *On the variational foundations of assumedstrain methods*, J. Appl. Mech., ASME, Vol. 53, pp. 51-54.

Stout M. G., Chen S. R., Fred Kocks U., Schwartz A. J., MacEwen S. R., Beaudoin A. J. (1998), *Mechanisms responsible for texture development in a 5182 aluminium alloy deformed at elevated temperature*, Proceedings of the second symposium held at the 1998 TMS Fall Meeting, Rosemont, Illinois.

Swift H.W. (1947), *Length changes in metals under torsional overstrain*, Engineering 163, 253-257.

Takashima Y., Kopp R. (2002), *Microstructure evolution in hot H-shape rolling simulated by finite element method*, Proc. 7th ICTP, Yokohama, Japan.

Taylor G.I. (1938), *Plastic strain in metals*, J. Inst. Met 62:307-324.

Teodosiu C. (1997), *Dislocation modelling of crystal plasticity, Large plastic deformation of crystalline aggregates*, International Centre for Mechanical Sciences, Courses and Lectures n°376, Springer Ed, 21-80.

Toth L.S., Dudzinski D., Molinari A. (1996), *Forming limit predictions with the perturbation method using stress potential functions of polycrystal viscoplasticity*, Int. J. Mech. Sci., Vol. 38, No. 8-9, pp. 805-824.

Toth L.S., Van Houtte P. (1992), *Discretization techniques for orientation distribution function*, Textures and Microstructures, Vol. 19, pp.229-244.

Turkmen H.S., Dawson P.R., Miller M.P. (2002), *The evolution of crystalline stresses of a polycrystalline metal during cyclic loading*, International Journal of Plasticity 18, 941-969.

Vacher P., Arrieux R., Tabourot L. (1998), *Analysis of a criterion of deep drawing operation capability for thin orthotropic sheets*, Journal of Materials Processing Technology, 78, 190-197.

Van Bael A. (1994), *Anisotropic yield loci derived from crystallographic data and their application in finite element simulations of plastic forming processes*, Ph. D. Thesis, KUL, Leuven.

Van Houtte P. (1988), *A comprehensive mathematical formulation of an extended Taylor-Bishop-Hill model featuring relaxed constraints, the Renouard-Wintenberger theory and a strain rate sensitivity model*, Textures and Microstructures, Vols. 8 & 9, pp.313-350.

Van Houtte P. (1994), *The "MTM-FHM" software system, Version 2*, user's Manual, KUL, Leuven.

Van Houtte P. (1995), *Micromechanics of polycrystalline materials*, Chaire Francqui, Université de Liège.

Van Houtte P., Delannay L., Kalidindi S.R. (2002), *Comparison of two grain interaction models for polycrystal plasticity and deformation texture prediction*, International Journal of Plasticity 18, 359-377.

Van Houtte P., Delannay L., Samajdar I. (1999), *Quantitative prediction of cold rolling textures in low-carbon steel by means of the LAMEL model*, Textures and Microstructures 31, 109-147.

Van Houtte P., Rabet L. (1997), *Generalisation of the relaxed constraints models for the prediction of deformation textures*, Revue de Métallurgie-CIT/Science et Génie des matériaux, pp. 1483-1494.

Voigt W. (1928), *Lehrbuch der kristallphysik*, B.G. Teubner Verlag, Leipzig.

Weber L., Moser B., Künzi H. U., Mortensen A. (2000), *Swift and inverse swift effect in alumina fiber reinforced aluminium wires*, Acta mater., 48, 2451-2459.

Winters J. (1996), *Implementation of Texture-Based Yield Locus into an Elastoplastic Finite Element Code*, Ph. D. Thesis, KUL, Leuven.

Wu H-C (2003), *On finite plastic deformation of anisotropic metallic materials*, Int. J. Plast., 19, 91-119.

Wu P. D., Neale K. W., Van der Giessen E. (1996), *Simulation of the behaviour of fcc polycrystals during reversed torsion*, Int. J. Plast., Vol. 12, No. 9, 1199-1219.

Xiao H., Bruhns O. T., Meyers A. (2001), *Large strain responses of elastic-perfect plasticity and kinematic hardening plasticity with the logarithmic rate: Swift effect in torsion*, Int. J. Plast., 17, 211-235.

Zhu Y.Y., Cescotto S. (1994), *Transient thermal and thermomechanical analysis by F.E.M.*, Computers and Structures, 53(2), pp. 275-304.